

Universidad Politécnica de Madrid

Escuela Técnica Superior de Ingenieros de Telecomunicación

Departamento de Ingeniería Electrónica



Luminescent Ru(II) Dyes and Materials for GaN-Based Gas Microsensors

PhD Thesis

Guido Ielasi

M.Sc. in Materials Science

2021

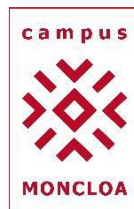
Universidad Complutense de Madrid

Facultad de Ciencias Químicas

Departamento de Química Orgánica



UNIVERSIDAD
COMPLUTENSE
MADRID



Universidad Politécnica de Madrid

ETSI de Telecomunicación

Departamento de Ingeniería Electrónica



POLITÉCNICA

Luminescent Ru(II) Dyes and Materials for GaN-Based Gas Microsensors

PhD Thesis

Guido Ielasi

M.Sc. in Materials Science

Supervisors:

Guillermo Orellana Moraleda, Full Professor/Catedrático (UCM)

Elías Muñoz Merino, Full Professor/Catedrático (UPM)

2021

Luminescent Ru(II) dyes and materials for GaN-based gas microsensors

Guido Ielasi - 2021

Ai miei genitori e a Silvia

Acknowledgments

This work was funded by the European Union through the EU Marie Skłodowska-Curie Innovative Training Network “SAMOSS” (Sample In-Answer Out Optochemical Sensing Systems), and the Spanish MINECO.

First, I would like to thank my advisors Prof. Guillermo Orellana Moraleda and Prof. Elías Muñoz Merino. Thanks for accepting my candidature in the first place, for helping developing my scientific mind, for believing in me when I doubted, and for pushing me forward when it was needed.

Quiero también agradecer el Prof. Andrés Rodríguez Domínguez por haberme aceptado en el Programa de Doctorado en Ingeniería de Sistemas Electrónicos.

Quiero agradecer todos los miembros del grupo GSOLFA, sobre todo a las Prof. M^a Cruz Moreno Bondi por sus constructivas sugerencias y por ser tan divertida en el labo como fuera del trabajo.

Nuria Martín, merci beaucoup pour tes cours de culture espagnoles et de philosophie, et pour ta sympathie.

Prof. Javier Lucas Urraca Ruiz, gracias por tu ayuda en campo científico, por el apoyo psicologico en los momentos duros del PhD, y también por las escapadas fuera de trabajo.

Dr. Maximino Bedoya Gutiérrez, gracias por tus soluciones a todos los problemas y toda la ayuda, tenemos todavía que hacer nuestro partido de padel...

Dr. Nieves Fresno López and Dr. Pramiti Hui, thanks for your help in organic synthesis.
Prof. Ana Belén Descalzo por tu ayuda y sugerencias.

Dra. Irene Núñez González, gracias por ser siempre amable y divertida.

Dr. José Ángel de la Torre González, gracias por como siempre me hiciste morir de risa.

Dr. Keurison Figueiredo Magalhaes, obrigado pela amizade, você foi o melhor colega de laboratório que alguém poderia esperar. E obrigado por nos dar junto com a Renata a melhor viagem da nossa vida. Espero que muitos mais venham.

Dra. Francesca Salis grazie per tutto il supporto che mi hai dato dal primo giorno nel lab.

Prof. Francisco Amaro Torres, gracias por tus divertidas charlas y informaciones interesante sobre el mundo de los microorganismos. Ahora se cuantas amebas pueden matarme...

Dra. M^a Victoria González de Vallejo y Dra. Idoia Urriza Arsuaga por vuestra simpatía

Dra. Lidia N. Gómez Arribas, Dr. Alberto Rico Yuste, Prof. Fernando Navarro Viloslada, Dr. Sergio Carrasco Garrido Prof. M^a Concepción Pérez Conde, Dra. Ana Bettina Glahn Martínez, Beatriz Bedoya Gutiérrez, y la Prof. Elena Benito Peña gracias por vuestra ayuda y colaboración.

Then I would like to thank all the SAMOSS family. Sergio, Mengyun, Maria, Leena, Konstanze, Monika, Ola, Sruj, Heman, Riikka, Sandro, and Laura, it was a huge pleasure to share this journey with you all... And a special thank to my bruv Frank, for all the adventures we had together.

También quería dar las gracias a mis amigos de Madrid. Gracias Jorge y Mauri por haberme dado la bienvenida, ha sido muy guay ser vuestro compañero de piso. Maria, gracias por haber hecho de Mauri un hombre mejor ;).

Lele, che divertido averti ritrovato a Madrid, magari tra qualche anno ci vedremo back in Turin. Gracias Vlad por tu gran simpatía y todos los platos Mexicanos.

Enza y David, grazie per la vostra compagnia e tutta la festa juntos, ci vediamo presto in Spagna o in Italia.

Tia Elena, gracias por haber sido la mejor casera del mundo y mucho más.

Edu, you were the first friend I made in Madrid and the last that helped me packing the car to come back to Italy... Thanks for being such a fantastic friend, I enjoyed so much our time together.

Grazie Alberto Maulu e Simone Lavarini per la nostra amicizia dai tempi dell'Uni ed in giro per l'Europa e il Mondo. Thanks Aziz Nairi for our friendship in France and Spain.

Grazie Jac per essere sempre stato un modello per migliorarmi, un supporto nei momenti difficili ed un esempio di forza. Mi sento molto fortunato ad averti come fratello. Grazie al mio gemello Edo per le nostre discussioni sempre di crescita personale e per tutti momenti di grande gioia e baldanza. Grazie Davi per avermi sempre supportato e per mostrarmi ogni giorno come dare il meglio 8e per avermi trovato un lavoro 😊).

Grazie a mia madre e a mio padre, questa tesi la dedico a voi. Grazie a tutti i sacrifici che avete fatto per darmi la possibilità di arrivare fino a questo traguardo, e grazie a tutto quello che mi avete insegnato e a tutto l'amore che mia avete dato.

Silvia, he tenido muchísima suerte de tenerte a mi lado por esta aventura española que ha sido hasta ahora la más bella de mi vida. Mucho más nos espera... Gracias.

INDEX

RESUMEN

ABSTRACT

Lista de publicaciones emanadas de esta Tesis	XVI
List of publications from this Thesis so far	XVIII
Glossary of symbols used in this Thesis	XIX
1. INTRODUCTION.....	1
1.1. Background	3
1.1.1. The senses of electronics	3
1.1.2. Optical chemical sensors	4
1.1.3. Phase-shift measurements.....	8
1.1.4. Ru(II)-polyazaheteroaromatic indicator dyes	10
1.1.5. GaN-based LEDs – the light source.	20
1.1.6. The sensor as a whole: optics and electronics.	23
1.1.7. Smartphone-as-sensor concept.....	26
1.2. Objectives	29
1.3. Motivation	31
1.3.1. GaN-based hybrids	31
1.3.2. Polarity sensing.....	33
1.3.3. Ethanol sensing.....	34
1.3.4. Cell cultures.....	34
1.4. Work plan and methodology	36
1.4.1. Manufacturing GaN-based organic-inorganic hybrids for O ₂ sensing....	36
1.4.2. Luminescent ethanol (polarity) sensing	37
1.4.3. Sensitive elements inside microfluidic cell cultures for in situ monitoring of the O ₂ partial pressure.....	38
References	41
2. GAN-SILANE-DYE HYBRID MATERIALS FOR LUMINESCENT CHEMICAL SENSING	53

Luminescent Ru(II) dyes and materials for GaN-based gas microsensors

2.1.	Introduction	55
2.2.	Materials and methods	62
2.2.1.	Materials	62
2.2.2.	Silanization of the n-GaN Surface	63
2.3.	Results and discussion.....	66
2.3.1.	Silanization of the GaN Surface.....	66
2.3.2.	Effect of the silane coating on the photochemistry of the tethered luminescent indicator dye	72
2.3.3.	Effect of the silane coating on the O ₂ -sensing performance	77
2.4.	References.....	81
3.	DEVELOPING AN OPTODE FOR ETHANOL SENSING BASED ON Ru(II) INDICATOR DYES	87
3.1.	Introduction	89
3.1.1.	Luminescence-based ethanol sensing.....	89
3.1.2.	Ruthenium(II) polypyridyl dyes as polarity probes.....	92
3.1.3.	Aim	92
3.2.	Materials and methods	93
3.2.1.	Materials	93
3.2.2.	Measurements and instrumentation.....	96
3.3.	Results and discussion.....	99
3.3.1.	Spectral features of the three novel indicator dyes.....	100
3.3.2.	Manufacturing the EtOH-sensitive luminescence films	105
3.3.3.	Analytical features – EtOH in gas stream	117
3.3.4.	Analytical features – Headspace of H ₂ O-EtOH solution	122
3.4.	Appendix I.....	125
3.5.	Annex	127
3.6.	References.....	145
4.	APPLICATION OF LUMINESCENCE-BASED MICROSENSORS TO MICROFLUIDIC CELL CULTURES AND ORGAN-ON-A-CHIP DEVICES	155
4.1.	Introduction	157
4.2.	Dioxygen sensors for HUVECs culture in PDMS-glass microfluidic chips...	159
4.2.1.	Aim of the study	159

4.2.2.	Materials and methods	159
4.2.3.	Results and discussion	167
4.2.4.	Results discussion.....	182
4.2.5.	Acknowledgements.....	182
4.2.6.	Annex I.....	183
4.3.	Dioxygen and temperature sensors for glass organ-on-a-chip devices	185
4.3.1.	Aim of the study	188
4.3.2.	Materials and methods	188
4.3.3.	Results and discussion	192
4.3.4.	Results discussion.....	196
4.3.5.	Acknowledgements.....	197
4.3.6.	Annex II.....	198
4.4.	References.....	199
5.	HIGHLIGHTS, CONCLUSIONS, AND OUTLOOK.....	205
5.1.	GaN-silane-dye hybrid materials for luminescent chemical sensing.....	207
5.1.1.	Summary of obtained results	207
5.1.2.	Conclusions	207
5.2.	Optodes for EtOH monitoring based on polarity-sensitive Ru(II) indicator dyes	208
5.2.1.	Summary of obtained results	208
5.2.2.	Conclusions	209
5.3.	O₂ and T luminescent microsensors for microfluidic devices.....	210
5.3.1.	Summary of obtained results	210
5.3.2.	Conclusions	210
5.4.	Outlook	211
5.5.	References.....	213

RESUMEN

Esta tesis presenta la investigación realizada como parte de la red EU Marie Skłodowska-Curie Innovative Training Network "SAMOSS" (Sample In-Answer Out Optochemical Sensing Systems), que involucró a otros nueve doctorados en cinco universidades (Univ. Complutense de Madrid, Univ. of Applied Sciences of Jena, Ben-Gurion Univ. of the Negev, Austrian Inst. of Technology, Univ. of Groningen, Univ. of Technology of Compiègne) y dos investigadores que trabajan en dos empresas (Micronit Micro Technologies en Enschede, NL, y Biosensor en Roma, IT). El trabajo se llevó a cabo en los laboratorios del grupo "GSOLFA (Sensores Químicos Ópticos y Fotoquímica Aplicada)" en el Departamento de Química Orgánica de la Universidad Complutense (UCM), en el ISOM (Instituto de Sistemas Optoelectrónicos y Microtecnología) de la Escuela Técnica Superior de Ingenieros de Telecomunicación de la Universidad Politécnica de Madrid (UPM) y en un estancia de cuatro meses en los Países Bajos, una parte en la Universidad de Groningen (RUG) y una en Micronit Micro Technologies.

El objetivo de este proyecto ha sido desarrollar elementos sensibles que, con la electrónica integrada adecuada, podrían conectarse a un smartphone para obtener instrumentación capaz de detectar especies químicas de interés en seguridad personal y laboral (e.g. etanol y oxígeno). Los elementos sensibles desarrollados han sido materiales híbridos orgánico-inorgánicos fabricados por funcionalización directa de GaN o por fijación de una capa delgada de polímero teñido a la superficie de un LED de GaN. Se han abordado algunos problemas básicos relacionados con la selección de colorantes luminiscentes adecuados y el dopado óptimo del GaN, para comprender y controlar el transporte de electrones desde las moléculas luminiscentes al semiconductor. Además, se han explorado aplicaciones complementarias de los dispositivos sensores.

La tesis está organizada como sigue:

- I. INTRODUCCIÓN. Se discute el estado del arte, motivación para el trabajo, objetivos principales y plan de I+D.
- II. MATERIALES HÍBRIDOS GaN-SILANO-COMPLEJO DE Ru(II) PARA SENSORES QUÍMICOS LUMINISCENTES. Se describe la fabricación de materiales híbridos orgánico-inorgánicos basados en GaN para la detección de O₂ y el énfasis está principalmente en la optimización del material que constituye el elemento sensible. El indicador sensible al O₂ se unió químicamente a las superficies de GaN a través de una capa intermedia de aminosilano para una máxima estabilidad y durabilidad. El principal interés

fue estudiar la influencia en la luminiscencia de los híbridos y en la respuesta a las especies de interés (O_2) 1) del tipo de dopaje del semiconductor y 2) de la composición y espesor de la capa de acoplamiento.

- III. DESARROLLO DE UN OPTODO PARA LA DETECCIÓN DE EtOH BASADO EN COMPLEJOS LUMINISCENTES DE Ru(II). El trabajo comprende el diseño computacional, la síntesis química y la caracterización de complejos luminiscentes para detección de etanol. El mejor indicador, utilizado por teñir soportes poliméricos, fue calibrado en fase gas con diferentes concentraciones de EtOH y H₂O para investigar selectividad y características analíticas, enfocándose en la aplicación específica de monitorear plantas de producción de etanol.
- IV. APLICACIÓN DE MICROSENSORES LUMINISCENTES EN EL MONITOREO DE CULTIVOS CÉLULARES EN ESTRUCTURAS MICROFLUIDICAS. Se describe la aplicación de los sensores desarrollados para monitorear el O₂ en cultivos de células en canales microfluídicos de PDMS-vidrio (en la Univ. de Groningen), y monitorear temperatura y O₂ en dispositivos de órgano-en-chip de vidrio (en Micronit).
- V. ASPECTOS DESTACADOS, CONCLUSIONES Y PERSPECTIVAS FUTURAS.

Los tres capítulos principales contienen material que ya ha sido publicado. Se adaptaron al formato de tesis, pero se escribieron como capítulos independientes con una breve introducción y conclusión.

Lista de publicaciones emanadas de esta Tesis

-
- Ielasi, G.; Hui, P.; Palacio, C.; Muñoz, E.; Orellana, G. Silane control of the electron injection and oxygen sensitivity of dye-silane-GaN hybrid materials for luminescent chemical sensing. *Sens. Actuator B-Chem.* **2018**, 254, 926–934.
-
- Bustamante, N.; Ielasi, G.; Bedoya, M.; Orellana, G. Optimization of Fiber-Optic Temperature Sensing with Polymer-Embedded Luminescent Ru(II) Complexes. *Polymers* **2018**, 10, 234.
-
- Ielasi, G.; Alcover, G.; Casellas, J.; de Graaf, C.; Orellana, G.; Reguero, M. Computer-aided design of short-lived phosphorescent Ru(II) polarity probes. *Dyes & Pigments* **2019**, 162, 168–176.
-
- Urriza-Arsuaga, I.; Ielasi, G.; Bedoya, M.; Orellana, G. Luminescence-Based Sensors for Bioprocess Applications. In *Fluorescence in Industry. Springer Series on Fluorescence (Methods and Applications)*; Pedras B., Ed.; Springer: Cham, **2019**; https://doi.org/10.1007/4243_2019_10.
-

ABSTRACT

This thesis presents the research carried out as part of the EU Marie Skłodowska-Curie Innovative Training Network “SAMOSS” (*Sample In-Answer Out Optochemical Sensing Systems*), involving other 9 early stage researchers at PhD programs in 5 universities (Univ. Complutense de Madrid, Univ. of Applied Sciences of Jena, Ben-Gurion Univ. of the Negev, Austrian Inst. of Technology, Univ. of Groningen, Univ. of Technology of Compiègne) plus two experienced researchers working at two companies (Micronit Micro Technologies B.V. in Enschede, NL, and Biosensor S.r.l. in Rome, IT). This work has been carried out in the laboratories of the “GSOLFA” (Chemical Optosensors and Applied Photochemistry) group at the Organic Chemistry Department of Universidad Complutense de Madrid (UCM), at the ISOM (Instituto de Sistemas Optoelectrónicos y Microtecnología) of the School of Telecommunications Engineering of Universidad Politécnica de Madrid (UPM) and, in a four-month long secondment in The Netherlands, in RUG (University of Groningen) and in Micronit Micro Technologies B.V.

The aim of this project has been to develop sensitive elements that, with the proper miniaturized large-scale integration electronics, could be plugged to provide smartphones the capability for detecting chemical species of interest for personal and workplace safety (e.g. ethanol and oxygen). The sensitive elements have been organic-inorganic hybrids fabricated either by direct functionalization of GaN or by attachment of a thin dyed polymer layer to the surface of the GaN LED. Some basic issues regarding selection of proper luminescent dyes and optimum doping of GaN, in order to understand and control the electron transport from the dye to the GaN device, have been addressed as well. Besides, complementary applications of the sensor devices have been explored.

The thesis is organized as follows:

- I. INTRODUCTION. The state-of-the art, motivation for the work, main goals and work plan are explained.
- II. GaN-SILANE-DYE HYBRID MATERIALS FOR LUMINESCENT CHEMICAL SENSING. The third part reports the manufacturing of GaN-based organic-inorganic hybrids for O₂ sensing, with an emphasis on the optimization of the sensitive element material. The O₂-sensitive dye has been tethered to GaN surfaces via an aminosilane-coupling layer for utmost stability and durability. The main interest has been to study 1) the influence of the GaN substrate doping and 2) the effect of the intermediate layer

composition and thickness on the hybrids luminescence and response to the analyte (O_2).

- III. DEVELOPING AN OPTODE FOR EtOH SENSING BASED ON Ru(II) INDICATOR DYES. This section focuses on the preparation of novel luminescent indicator dyes and indicator/polymer layers for ethanol sensing. The work started with computer-aided design, followed by chemical synthesis and characterization of the dyes. Subsequently, the best luminescent probe has been supported in perm-selective polymers and calibrated in gas phase with different concentrations of EtOH and H_2O to investigate selectivity and analytical features, focusing on the specific application of monitoring ethanol production and storage plants.
- IV. APPLICATION OF LUMINESCENCE-BASED MICROSENSORS TO MICROFLUIDIC CELL CULTURES AND ORGAN-ON-A-CHIP DEVICES. Finally, the work focused on a particular application of the developed sensors, namely to monitor microfluidic cell cultures. In RUG, O_2 sensors have been implemented in human umbilical vein endothelial cells culture into PDMS-glass microfluidic chips while, at Micronit, O_2 and temperature sensors have been used in organ-on-a-chip glass devices.

V. HIGHLIGHTS, CONCLUSIONS, AND OUTLOOK.

The three main chapters contain material that has already been published. They were adapted to the thesis format but written as independent chapters with a short introduction and conclusion.

List of publications from this Thesis so far

-
- Ielasi, G.; Hui, P.; Palacio, C.; Muñoz, E.; Orellana, G. Silane control of the electron injection and oxygen sensitivity of dye-silane-GaN hybrid materials for luminescent chemical sensing. *Sens. Actuator B-Chem.* **2018**, *254*, 926–934.
-
- Bustamante, N.; Ielasi, G.; Bedoya, M.; Orellana, G. Optimization of Fiber-Optic Temperature Sensing with Polymer-Embedded Luminescent Ru(II) Complexes. *Polymers* **2018**, *10*, 234.
-
- Ielasi, G.; Alcover, G.; Casellas, J.; de Graaf, C.; Orellana, G.; Reguero, M. Computer-aided design of short-lived phosphorescent Ru(II) polarity probes. *Dyes & Pigments* **2019**, *162*, 168–176.
-
- Urriza-Arsuaga, I.; Ielasi, G.; Bedoya, M.; Orellana, G. Luminescence-Based Sensors for Bioprocess Applications. In *Fluorescence in Industry. Springer Series on Fluorescence (Methods and Applications)*; Pedras B., Ed.; Springer: Cham, **2019**; https://doi.org/10.1007/4243_2019_10.
-

Glossary of symbols used in this Thesis

A	Absorbance
α_c	Critical angle of the total internal reflection
β	Coupling constant (electron transfer)
B_i	Pre-exponential factor
c	Concentration /mol dm ⁻³
c	Speed of light in vacuum (3×10^8 /m s ⁻¹)
$\delta(\alpha)$	Penetration distance (Eq. [11])
f	Light modulation frequency (Eq. [7])
G	Substituent
$I(z;\alpha)$	Evanescence field intensity (Eq. [10])
I_{exc}	Intensity of the excitation light
I_L	Luminescence intensity (Eq.[1])
$I_L(t)$	Emission decay profile (Eq. [2])
K_a	Association constant
k_B	Boltzmann constant ($1.38064852 \times 10^{-23}$ m ² kg s ⁻² K ⁻¹)
k_{et}	Electron transfer deactivation rate constant (Eq.[16])
k_q	Bimolecular quenching constant
k_r	Radiative rate
k_{nr}	Non-radiative rate
$K_{\text{SV}} = k_Q \tau_{M0}$	Stern-Volmer quenching constants
l	Optical pathlength /cm
L	Ligand
μ	Dipole moment
n	Refractive index
η_c	Escape ratio
R	Gas constant (8.314 J mol ⁻¹ K ⁻¹)
δ	NMR chemical shift /ppm
Δf	Solvent-specific orientation polarizability term (Eq. [6])
ε	Relative permittivity, or dielectric constant, of the material
$\varepsilon\lambda$	Molar absorption coefficient /dm ³ mol ⁻¹ cm ⁻¹
h	Planck constant ($6.62606957(29) \times 10^{-34}$ /J s)
κ	Emission collection efficiency
k_d	Excited state deactivation rate constant
λ	Wavelength /nm
Λ	Attenuation length of the N 1s photoelectrons (2.3 nm)
ν_{abs}	Wavenumber of the absorption maximum /cm ⁻¹
ν_{em}	Wavenumber of the emission maximum /cm ⁻¹
τ	Luminescence lifetime (Eq.(4) and Eq.[7])
τ_M	Pre-exponential weighted mean lifetime (Eq. [14])
T	Temperature in °C
ϕ	Phase shift (Eq. [3])
φ	Photoelectrons collection angle in XPS measurement
Φ_L, Φ_{em}	Luminescence quantum yield
Φ_{ISC}	Intersystem crossing quantum yield

1. INTRODUCTION

If we can see further, it is only by standing on the shoulders of giants.

– Bernard of Chartres, XII century

Chapter 1 - Introduction

1.1. Background

1.1.1. The senses of electronics

Sensors are regarded as “*the senses of electronics*” [Grandke 1989]. Sight (vision), hearing (audition), taste (gustation), smell (olfaction), and touch (somatosensation) are the human’s five traditionally recognized senses and they all function in the same way: a receptor responds to a particular stimulus, and this receptor interacts with a transducer leading to a signal cascade ultimately reaching the brain. Equally, artificial sensors are used to collect information and trigger responses from stimuli. There are many examples of such devices in our everyday life, such as the temperature control of the oven in our kitchen, the IR sensors for operating the television remote, LDR – Light Dependant Resistor – sensors used for controlling the street lighting system, and the lambda sensor that monitors oxygen entering the car’s catalytic converter. *Chemical* sensors have been an extraordinary step forward in the 20th century, starting from the pH-sensitive glass electrode by Haber and Klemensiewicz [Haber 1909], because they completely revolutionized the analytical chemistry world (**Figure 1**).

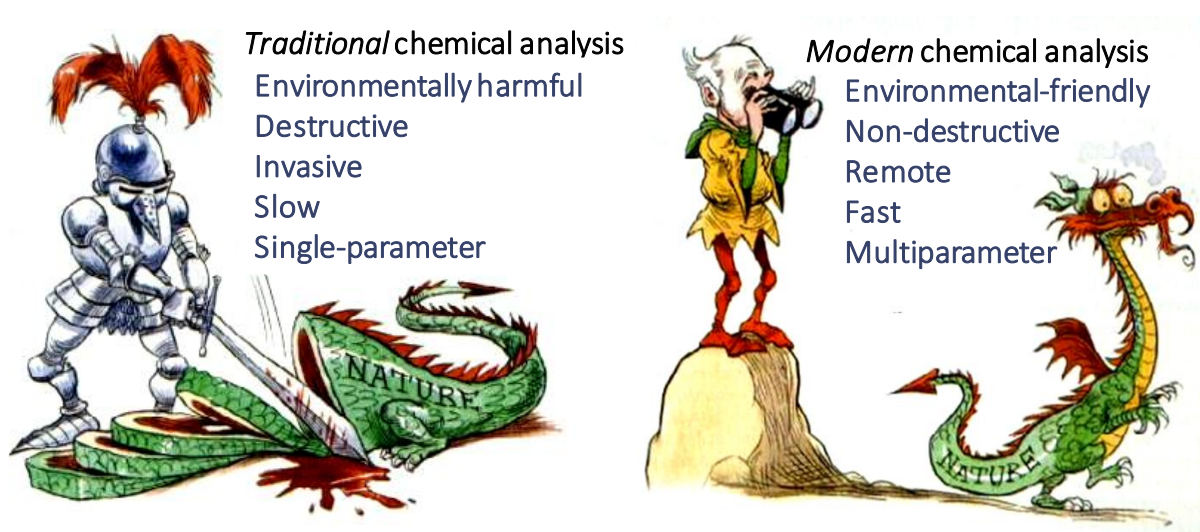


Figure 1. The evolution of analytical chemistry. (Copyright: Chris Riddell. Adapted with permission).

1.1.2. Optical chemical sensors

Specifically, a chemical sensor is “a device that transforms chemical information, ranging from the concentration of a specific sample component to total composition analysis, into an analytically useful signal” [Hulanicki 1991]. It is composed of two basic functional units. The first part is the “receptor”, the task of which is to convert the chemical information into a form of energy. The second is the “transducer”, capable of transforming the energy carrying the chemical information about the sample into the final signal (see **Figure 2**).

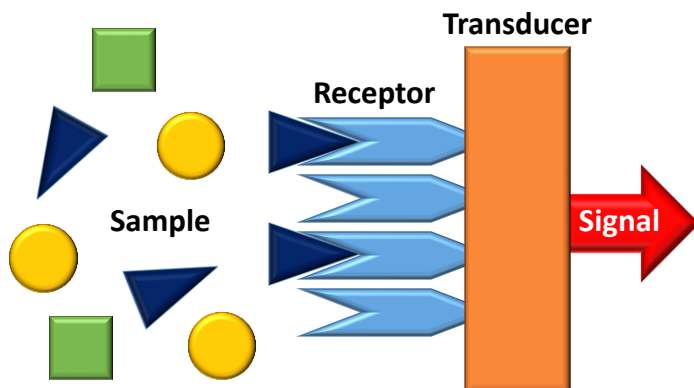


Figure 2. Chemical sensor or biosensor structure. The recognition element (receptor) selectively interacts with the analyte of interest, producing the analytical response.

Chemical sensors may be classified according to the operating principle of the transducer: optical, electrochemical, electrical, mass sensitive, magnetic, thermometric, or other depending on its physical properties. Every transduction method has its strong points. Optical sensors are particularly valuable in many applications due to their unique features, e.g. contactless monitoring, remote sensing, high detection sensitivity, wavelength selectivity, absence of electrical interference or risks, lack of analyte consumption, and ease of miniaturization, among others [Narayanaswamy 2004]. Optical chemical sensors may exploit various optical properties [Hulanicki 1991]: absorbance, reflectance, refractive index change (including also surface plasmon resonance effect), optothermal effect, light scattering, and luminescence. The last term comprises every phenomenon involving “cold” (i.e. other than black body radiation), spontaneous emission (i.e.: transition of a quantum mechanical system from an excited energy state to a lower energy state with emission of a quantum in the form of a photon) of light by a substance [Wiedemann 1888].

The use of *luminescence*-based sensors offers particular advantages over other conventional photometric techniques. First, they use a non-differential detection method, unlike absorption- or reflectance-based techniques: the emitted light has a

different,-higher-, wavelength than the incident one used for excitation, which leads to higher signal-to-noise ratio and lower limits of detection (i.e. greater sensitivity), down to the single photon or single molecule. Secondly, most molecules do not produce luminescence; this allows background-free measurements also when analyzing a complex sample containing many components (i.e. high selectivity, **Figure 3**) [Lakowicz 2006].

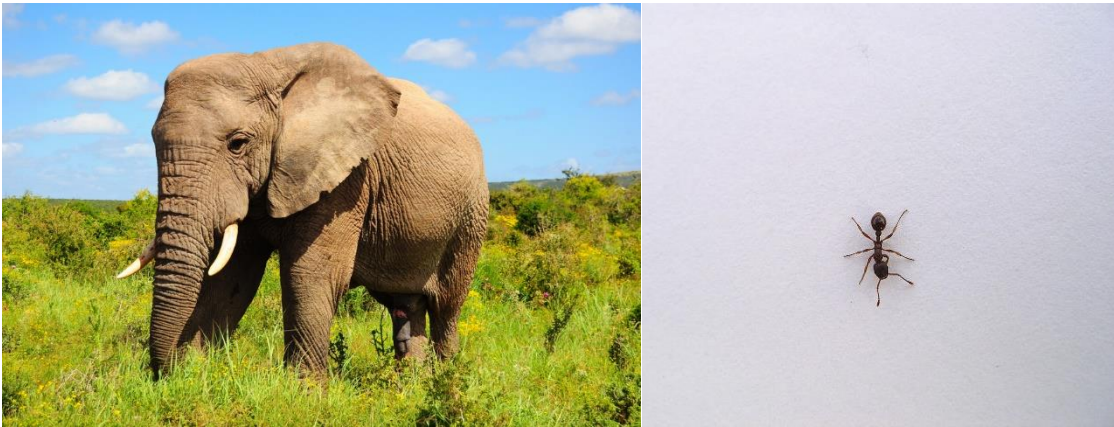


Figure 3. The advantages of luminescence over absorption for sensing purposes: Can you see the ant on the back of the elephant? An ant (the signal) is less distinguishable when placed on the back of an elephant (i.e. in presence of a strong background) than on a white sheet of paper (i.e. in background-free conditions).

Depending on the energy source that provides the energy to reach the electronic excited state, one can sub-divide in [Valeur 2011]:

- a) Chemiluminescence (chemical reaction)
- b) Triboluminescence (crystal fracture)
- c) Electroluminescence (electric current)
- d) Mechanoluminescence or piezoluminescence (mechanical/pressure stress)
- e) Radioluminescence (ionizing radiation)
- f) Thermoluminescence (temperature)
- g) Photoluminescence (photons).

In this work, the optical chemical sensors developed were based on photoluminescence.

Photoluminescence. Under the general term of photoluminescence, two different phenomena are considered: fluorescence and phosphorescence (see **Figure 4**). This distinction comes from the spin parallelism of the electrons after photon absorption. In

In the case of fluorescence, the photoexcited electron in the singlet excited orbital possesses opposite spin respect that of the electron in the ground state – i.e. the spin of the two electrons is anti-parallel (as it was in the corresponding ground state). The transition from the excited state to the ground state is, therefore, spin-allowed. For this reason, the emission rates are high, typically on the order of 10^8 – 10^9 s $^{-1}$, so that the fluorescence lifetime is on the order of 1–10 ns. In phosphorescence, conversely, the spins of the photoexcited (triplet) and ground state electrons are the same – i.e. the spin is parallel. Therefore, electrons need more time to relax to the ground state because the re-emission of photons involves quantum mechanically forbidden energy state transitions. Emission rates are lower (10^3 to 1 s $^{-1}$), so that phosphorescence lifetimes are typically milliseconds to seconds. An intermediate case is typical of transition metal-ligand complexes, which contain a heavy metal atom and one or more organic ligands. In these complexes the excited state is a singlet, but because of the presence of the central heavy atom, a facilitated intersystem crossing (ISC) process takes place [IUPAC Gold Book 1997]. Displaying mixed singlet-triplet states, the lifetime of the excited state is intermediate between those of fluorescence and phosphorescence, and spans from hundreds of nanoseconds to several microseconds (see Table 1. Luminescence phenomena and typical time scale).

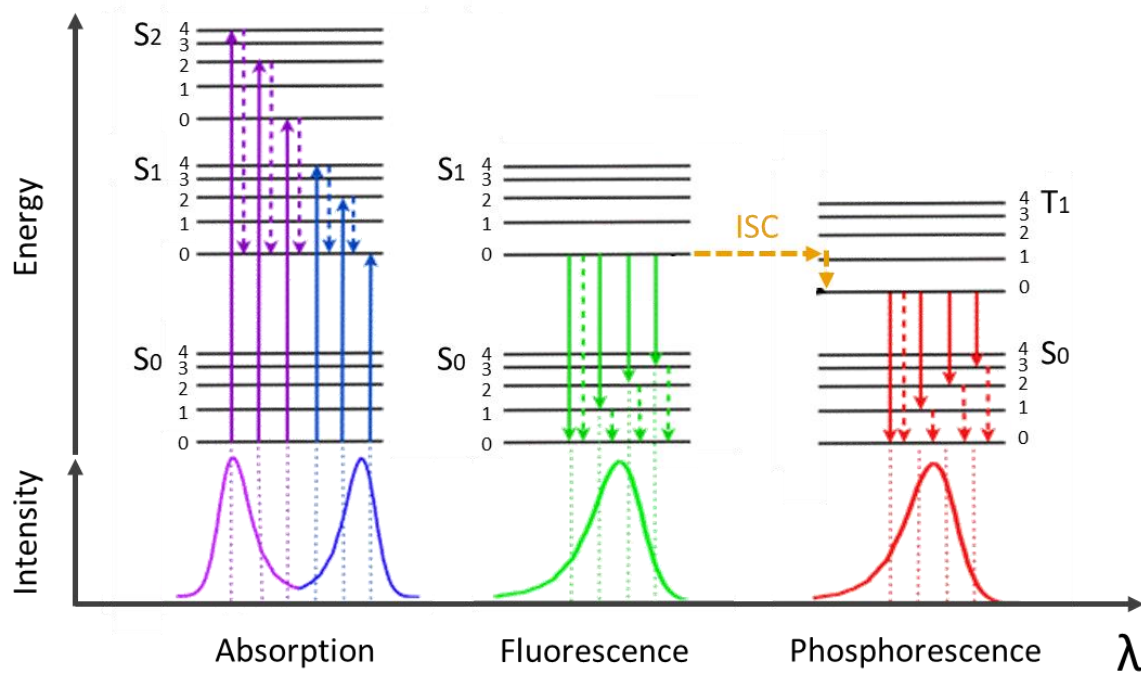


Figure 4. Representation of the energy transitions relative to absorption, fluorescence and phosphorescence. Adapted from [Web photobiology.info], licensed under an open access license.

Table 1. Luminescence phenomena and typical time scale

Phenomenon	Time /s
Absorption	10^{-15}
Vibrational relaxation/Internal conversion	10^{-12}
Fluorescence	10^{-9}
Phosphorescence	$>10^{-3}$

Which is the measuring principle? The intensity of luminescence I_L from a luminophore solution can be expressed as follows (eq.1):

$$I_L = \Phi_L I_0 \kappa \varepsilon_\lambda l c \quad [1]$$

being Φ_L the luminescence quantum yield of the luminophore, I_0 the intensity of excitation source, κ a parameter depending on the instrumental setup, ε_λ the absorption coefficient of the luminophore, l the optical path length of the absorbing material, and c the luminophore concentration.

If the analyte is **intrinsically** luminescent, it is possible to *directly* interrogate the species of interest. This is done, for example, in the measurement of the NO_x levels for air quality assessment, or chlorophyll determination in water for algal bloom tracking. In these examples, the change in chlorophyll or NO concentration is linearly related to their I_L variation. However, due to the small number of luminescent chemical species, usually **indicator-mediated** sensors are required. In this case, an indicator dye responds to the analyte of interest (*directly* or *indirectly* by way of a “relay” species, the concentration of which is related to that of the analyte), through a photochemical “quenching” process, which is a decrease of the luminescence of the indicator species due to the presence of an external agent. In this case, the presence of the analyte lowers the Φ_L in eq [1]. Quenching may involve different phenomena such as energy, electron or proton transfer in competition with the spontaneous deactivation of the excited state of the indicator dye by radiative and non-radiative pathways (Figure 5). Alternatively, but less often, the interaction of the indicator dye with the analyte (reversibly) removes a pre-existing quenching leading to enhanced luminescence

("turn-on sensors"). This Thesis will deal exclusively with indicator-mediated luminescent chemical sensors.

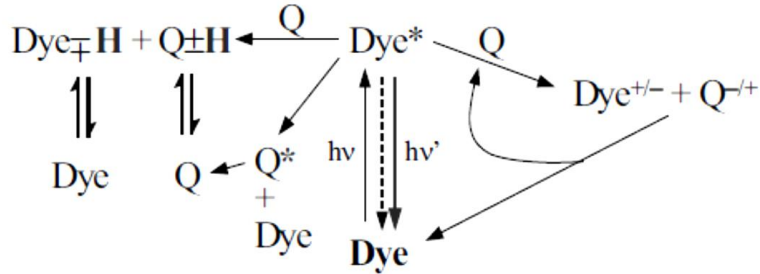


Figure 5. The different principles of (reversible) luminescence sensing based on photochemical quenching processes (electron, proton, or energy transfer). Dye = luminescent indicator; Q = quencher species; dotted arrow: non-radiative deactivation processes. The luminescence intensity (and excited state lifetime) of the indicator dye decreases in the presence of the quencher [Orellana 2006].

1.1.3. Phase-shift measurements.

The main strengths of the luminescence technique, namely high sensitivity and selectivity, can be insufficient for producing sensors working under "real life" conditions (i.e. outside a controlled environment), because they may lack a third fundamental component: stability. The weakness they often suffer is that many undesired and out-of-control factors may influence the luminescence intensity. Examples are instability or waning of the excitation source, detector aging, photobleaching of the dye during operation due to the strong excitation light, indicator dye leaching out of the supporting matrix, and irreproducibility of the sensitive layer fabrication. Using sensors based on the luminescence lifetime (i.e. the electronic excited state decay kinetics monitoring after an excitation light pulse) can avoid these issues. There are many important advantages of lifetime- over intensity-based methods; particularly, for sensing purposes, the fact that the emission *decay* kinetics is not dependent on the number of luminescent molecules involved in the phenomenon and, hence, all of the undesirable interferences listed above are eliminated (as far as a sufficient number of indicator molecules is left to detect their luminescence!). The price to pay for this increase in reliability over time is the need of high-speed excitation and detection systems, which made emission lifetime measurements an expensive and complex methodology 30 years ago. Nowadays, however, technological advances have led to cheaper robust electronic components such as excitation sources (especially LEDs) and photodiode detectors, so that luminescence decay kinetics-based sensors eventually became affordable.

There are two possible ways of measuring the excited state lifetime: using a time-resolved luminescence signal or a phase-based signal (**Figure 6**).

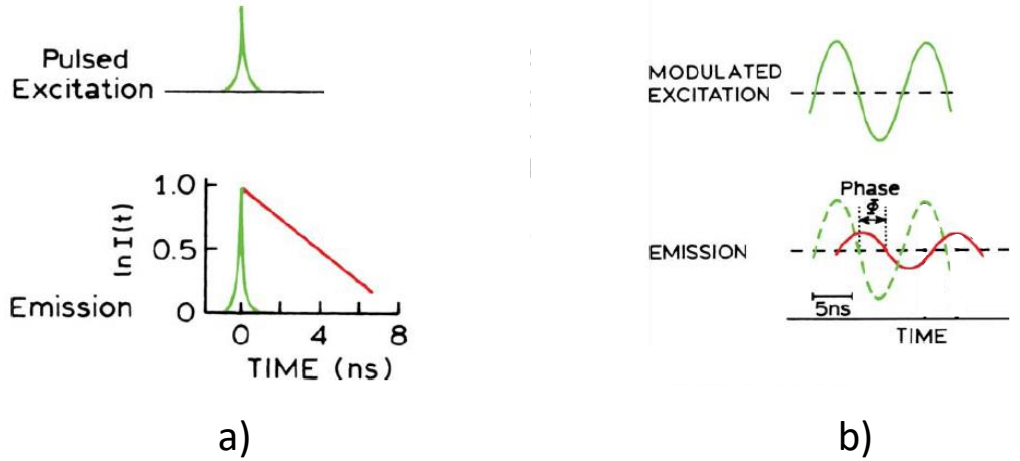


Figure 6. a) Time-domain (or pulse luminometry) vs b) frequency-domain (or phase-modulation) detection. Adapted from [Lakowicz 2006] with permission.

In the **time-resolved technique**, the excitation pulse of the light source is significantly shorter than the luminescence decay time. After absorption of light, the population of the resulting luminescent excited state decreases following first order kinetics. Consequently, the luminophore emission I_L decays exponentially over time, as in eq. 2:

$$I_L(t) = \sum_i I_{0i} e^{-t/\tau_i} \quad [2]$$

where I_0 is the intensity at $t = 0$ after the (ultrashort) excitation pulse and τ is the so-called luminescence lifetime (reciprocal of the rate constant of the emission decay, i.e. the sum of the unimolecular radiative and non-radiative deactivation rate constants k_r and k_{nr}). τ corresponds by definition to the time the population of emitter excited states takes to decrease to $1/e$ times its initial value. In the presence of a single type of emitting species in an isotropic homogeneous environment, $i = 1$ and thus the decay is exponential. More often than not, when *indicator dyes* are embedded into *polymer supports*, a tandem required for fiber-optical chemical sensing, the luminescence decay profile obeys a multi-exponential function. The decay profile is measured by either laser kinetic spectrometry (LKS) or single photon timing (SPT) techniques, both requiring expensive and usually bulky instrumentation, and the luminescence lifetime is extracted from the experimental data fit [Ceroni 2012].

However, the **phase-resolved technique** is based on a continuous, (usually sinusoidally) modulated, illumination. In this way, the emission of the luminescent dye or material becomes modulated accordingly but with a certain delay, $-\text{phase}$

shift –, due to the finite lifetime of the emissive excited state. The instrumentation required with this technique is a lot less demanding than with the time-resolved one, both in cost and size, making it more suitable for sensing purposes. The phase shift (ϕ), at a particular modulation frequency of the excitation light (f), is a function of the indicator dye luminescence lifetime (τ), according to eq. 3 [Ceroni 2012]:

$$\tan \phi = 2\pi f \tau \quad [3]$$

Very many optical sensors based on luminescence measurements –both in time and phase domains– have been reported in the literature. However, only few of them have made it to *commercial* applications. This gap is due, amongst other reasons, to the different properties of the luminescence of the diverse indicator dyes employed, for which every application needs a different setup and set of excitation source, filters, detector, electronics, etc... The solution to this problem was pioneered by the UCM Chemical Optosensors & Applied Photochemistry Group (GSOLFA, <https://www.gsolfa.info/>), by using a plurality of robust indicator dyes of the same family having similar excitation/emission properties but each one just being sensitive to a single chemical parameter [Orellana 1998, Orellana 2004]. This approach would allow using a single optoelectronic instrumentation that, by simple exchanging the sensitive *terminal* placed at the distal end of an optical fiber for convenience, can sense a wide range of chemical species. Luminescent polypyridyl ruthenium(II) complexes can be used as probes in a system of this kind [Orellana 2004, Marcélis 2013, Martí 2015].

1.1.4. Ru(II)-polyazaheteroaromatic indicator dyes

These photoactive metal complexes have a wide range of applications, spanning from photocatalysis [Puntoriero 2011] to photovoltaics (in the so-called dye-sensitized solar cells [Nazeeruddin 2011]) and organic light-emitting diodes [Evansa 2006, Gao 2000], to chemical sensors (as luminescent indicator dyes) [Orellana 2004]. For the latter application, a judicious selection of the coordinating **ligands** around the metal core and the sought **photochemical quenching mechanism** has allowed so far the development of luminescent sensing materials (polymer-embedded dye) for numerous analytes and physical parameters. A shortlist includes O₂ (energy transfer), pH, CO₂ and NH₃ (proton transfer), hydrogen sulfide (electron transfer), metal ions such as Fe(II) and Cu(II) (electron transfer), temperature and humidity (via excited state switch), ethanol, glucose and cholesterol (coupling the O₂ sensor to the respective enzymes), and biological oxygen demand (BOD) or herbicides (using the O₂ sensor as transducer of the status of membrane-immobilized living microorganisms).

Chapter 1 - Introduction

Their strengths, compared to purely organic dyes usually employed for developing luminescence-based sensors, are numerous:

1. They are much more photochemically and thermally stable.
2. Their luminescence lifetime is in the μs range. On the one hand, it is shorter than that of phosphorescent molecules, meaning that they are less quenched by dioxygen and so they can be used as luminescent probes under atmospheric conditions. On the other hand, it is longer than fluorescence, so their emission can be collected using unexpensive, “slow” electronics.
3. Their absorption and emission of light are far away in energy, allowing using cheap colored glass filters to separate the intense scattered excitation light from the emitted signal. Moreover, they can be excited with GaN-based blue LEDs and their red luminescence can be efficiently detected with photodiodes, both cheap optoelectronic elements.

Moreover, suitable **functional groups** placed in the periphery of the metal complex enable their immobilization on different supports by electrostatic, hydrophobic or covalent binding procedures [Orellana 2004].

The strong red-orange luminescence of a solution of tris(bipyridine)ruthenium(II) chloride was reported for the first time by Paris and Brandt in 1959 [Paris 1959]; since then, this phenomenon has been widely studied and this one and related compounds have found many applications in different fields, from electrochemistry to photocatalysis, to cancerous cell killing and to sensors, just to name a few.

Ruthenium(II) is a transition metal ion with a d^6 configuration. Its five d orbitals are partially filled, so that they can accept or donate electrons readily. It can form stable metal complexes in presence of six σ -donor ligands with octahedral arrangement. This is especially true if the ligands are also π -acceptors, called strong- or high-field ligands: two classical examples are the polyazaaromatic chelating compounds 2,2'-bipyridine (bpy) and 1,10-phenanthroline (phen). In this thesis, the focus will be on complexes containing ligands of these families, most famous member of which is the forefather $[\text{Ru}(\text{bpy})_3]^{2+}$ (**Figure 7**).

In this ruthenium complex (and similar ones), two d orbitals –the $d_{x^2-y^2}$ and the d_{z^2} – are directed towards the ligands occupying the six vertices of the octahedron. The three remaining d orbitals d_{xy} , d_{xz} and d_{yz} are directed between the bonds with the ligands. Therefore, the octahedral crystal field due to the ligands coordination to the metal ion provokes splitting of its electronic levels, so that a doubly degenerated e_g level is found at higher energy and a triply degenerated t_{2g} level lies at lower energy (**Figure 8**).

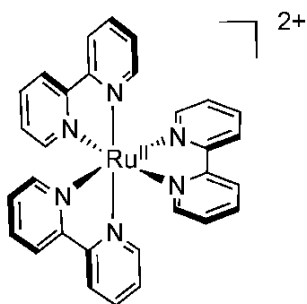


Figure 7. $[\text{Ru}(\text{bpy})_3]^{2+}$ molecular structure.

The two e_g , the s and three of the p metal orbitals, linearly combined with the symmetry-matched orbitals of the ligands, generate the σ metal-ligand (M-L) complex orbitals; the remaining three p and the three t_{2g} orbitals, also combined with the symmetry-matched ligands' orbitals, generate the π M-L molecular orbitals (MO). In case of $[\text{Ru}(\text{bpy})_3]^{2+}$, $[\text{Ru}(\text{phen})_3]^{2+}$ and similar complexes, the strong ligand field causes the (π bonded) t_{2g} to be the highest occupied MO (HOMO), filled with six paired electrons. This is the complex ground state and possesses singlet multiplicity. Different ligands have different energy orbitals. Their linear combination leads to different levels in the M-L complex, which are typically distinguishable in its absorption spectrum.

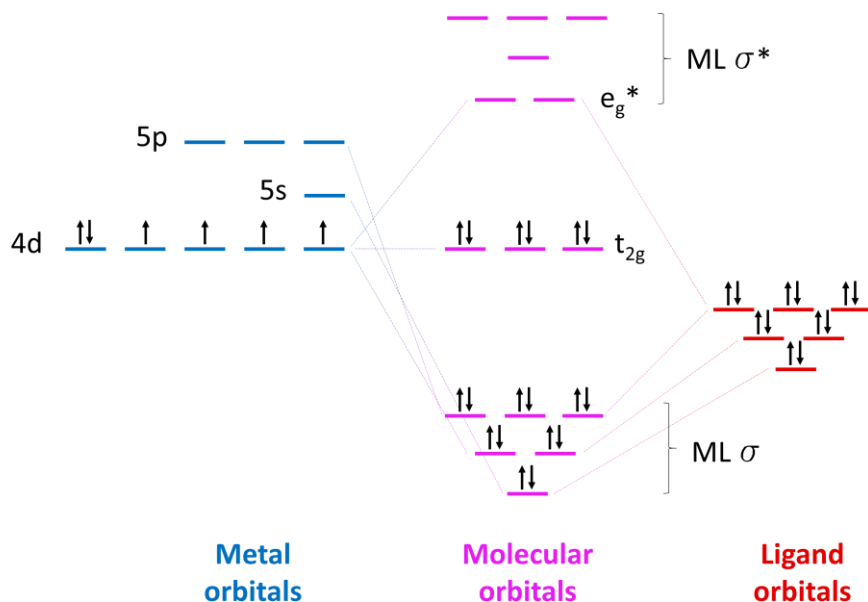


Figure 8. Schematic MO diagram and electronic transitions for a Ru(II) complex in octahedral coordination.

Absorption spectra. 2,2'-Bipyridine absorbs only in the UV region, with two sharp bands at 230-250 nm and 280-320 nm. These features are observed, similarly, in case of $\text{Ru}(\text{bpy})_3^{2+}$ and are hence associated with ligand-centered (LC) or intraligand (IL) $\pi-\pi^*$ transitions. Small differences are introduced in the region, partly because of the weak effect of the metal and partly because of the appearance of transitions between ligand-centered orbitals and metal-centered orbitals (ligand-to-metal charge transfers, LMCT). The striking difference between the free ligand and the metal complex absorption spectra is the appearance in the latter of a broad structured absorption band in the visible region, the maximum of which is situated at 450-500 nm. This band is related to the lowest, spin-allowed energy transition in the ML complex system from the d orbital of metal nature to the π^* orbital of ligand nature, so that it is a metal-to-ligand charge transfer (MLCT) transition. Other less intense absorptions bands are usually present, and they are associated with forbidden transitions.

As a result of the energy position of bonding and anti-bonding orbitals, different homoleptic (i.e. with three identical ligands) ruthenium complexes may display differences in shape and position of the absorption bands (compare $\text{Ru}(\text{nbpy})_3^{2+}$ and $\text{Ru}(\text{nody})_3^{2+}$ absorption spectra, Figure 9). Considering the MLCT band:

- stronger σ -donating ligands lead to an energy raise of the metal-based $d(\pi)$ orbitals;
- stronger electron-withdrawing ligands lower the energy of the ligand-centered π^* orbitals.

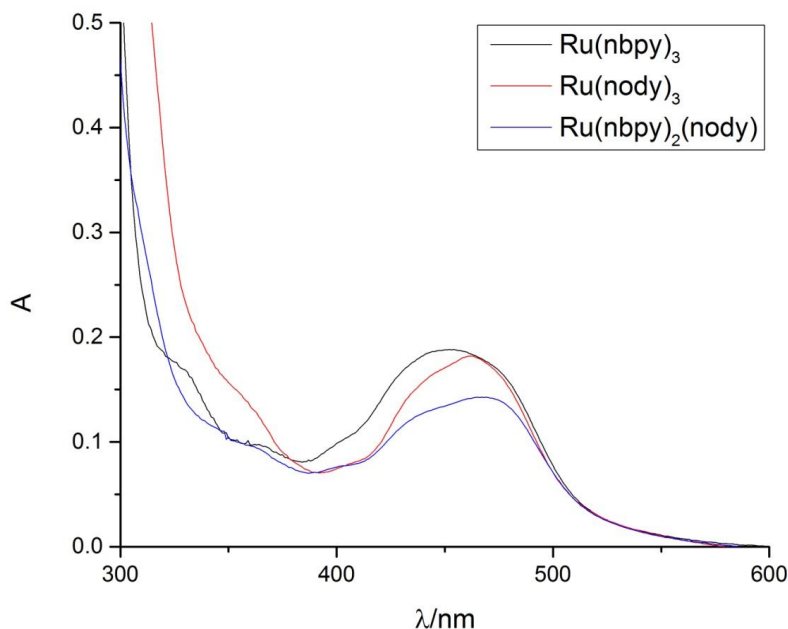


Figure 9. $\text{Ru}(\text{nbpy})_3^{2+}$, $\text{Ru}(\text{nody})_3^{2+}$ and $[\text{Ru}(\text{nbpy})_2(\text{nody})]^{2+}$ absorption spectra in THF.

In case of heteroleptic (i.e. those lacking three identical ligands) Ru(II) complexes, their absorption spectrum appears as the weighted sum of the spectra of the homoleptic complexes containing the respective ligands (i.e. the absorption spectra of $[\text{Ru}(\text{L})_2(\text{L}')]\text{ }^{2+}$ correspond to $2/3 \text{ } [\text{Ru}(\text{L})_3]\text{ }^{2+}$ plus $1/3 \text{ } [\text{Ru}(\text{L}')_3]\text{ }^{2+}$) (**Figure 9**).

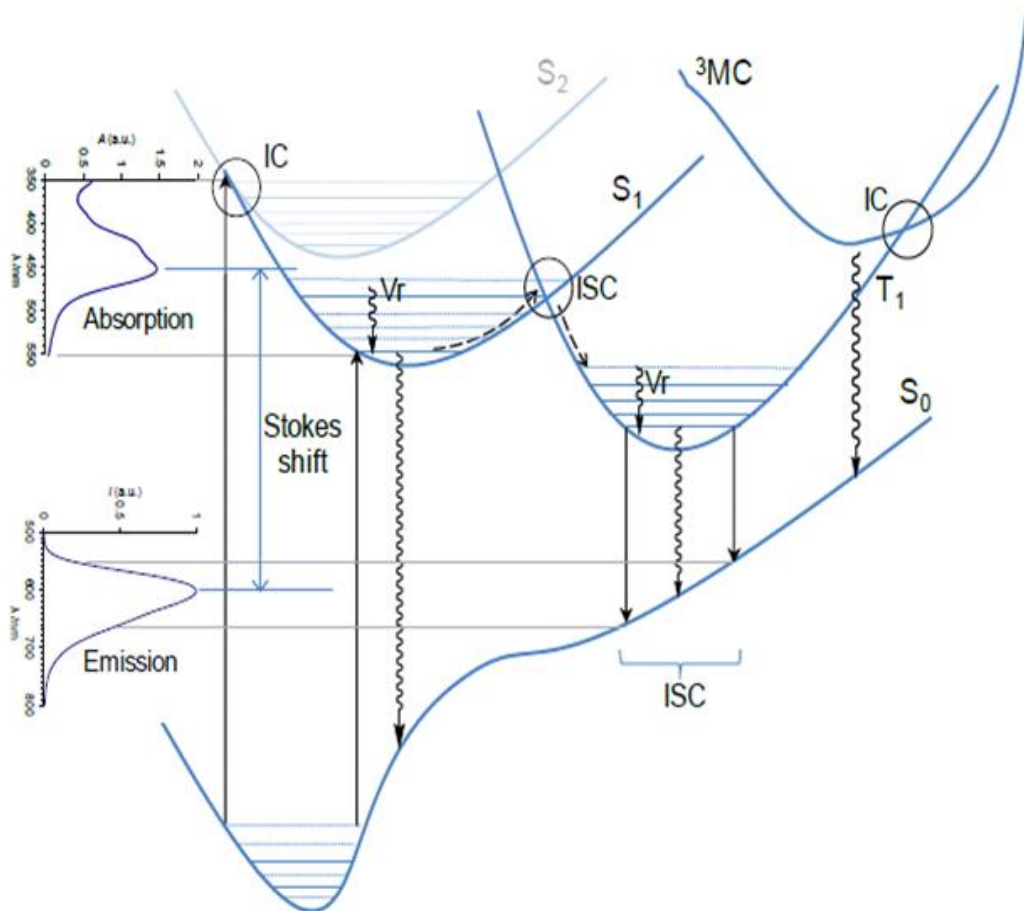


Figure 10. Energy diagram of a prototypical ruthenium(II) polypyridyl complex. The represented electronic levels are the ground state (S_0), the first and second singlet excited states (S_1 and S_2 , respectively), the triplet excited state (T_1), and the thermally-activated metal-centred excited state (${}^3\text{MC}$). IC stands for internal conversion, Vr for vibrational relaxation and ISC for intersystem crossing. See text for details. From [Ribeiro dos Santos 2014] with permission.

How does the spatial charge density change during the MLCT? Upon absorption of a photon of UV or blue light, the $[\text{Ru}(\text{bpy})_3]\text{ }^{2+}$ dye is excited to ${}^1\text{MLCT}$ state. Regardless the excitation, the electron quickly relaxes to the lowest ${}^1\text{MLCT}$ (Kasha's rule; $\text{IC}_{S_2 \rightarrow S_1}$ in Figure 10). Due to the large spin-orbit coupling in transition metal complexes, a fast intersystem crossing takes place thereof, populating the ${}^3\text{MLCT}$ state (Figure 10, ISC).

In this way, a metal $4d(t_{2g})$ electron is promoted to one of the three equivalent π^* orbitals of the coordinated ligands [Chen 1998]. Coupling with the surrounding solvent dipoles induces localization of the electron on a single ligand [Campagna 2007]. In the case of coordination of the Ru(II) to three identical ligands, the ${}^3\text{MLCT}$ state becomes “randomized” by interligand hopping [Wallin 2005]. All these steps take place on a timescale of a few hundreds of femtoseconds. Finally, the dye can relax from the ${}^3\text{MLCT}$ to the ground state by both non-radiative and radiative pathways (Figure 10).

Luminescence. Ru(II) complexes radiative relaxation is typically a broad band that peaks around 600 nm. The emission quantum yield of the forefather $[\text{Ru}(\text{bpy})_3]^{2+}$ is around 0.04 (in air-equilibrated water). Since the lowest-lying excited state has triplet nature while the ground state is a singlet, the deactivation is relatively slow, and its room temperature emission lifetime is about 400 ns (in air-equilibrated water). Dyes of the same family can display a longer luminescence lifetime: $[\text{Ru}(\text{dpp})_3]^{2+}$ (dpp = 4,7-diphenyl-1,10-phenanthroline), for example, has a τ of around 7 μs (deoxygenated acetonitrile solution). Luminescence-based sensors rely on the variation of their luminescence in the presence of an analyte of interest. There are several possible **deactivation mechanisms of the ${}^3\text{MLCT}$ excited state of Ru(II) polypyridyls:**

1. Förster resonance energy transfer (FRET) (**Figure 11**). FRET is a process based on classical dipole-dipole interactions between the transition dipoles of the donor and the acceptor (nonradiative dipole-dipole coupling) and is strongly dependent on the donor-acceptor distance, R , falling off at a rate of $1/R^6$ (FRET can typically occur over distances up to 10 nm). FRET also depends on the donor-acceptor spectral overlap and on the relative orientation of the donor and acceptor transition dipole moments (in the case of rigid systems). Examples of Ru(II) luminescent dyes quenching via FRET are reported in [Descalzo 2013, Sujitraj 2019].
2. Dexter energy transfer (DET) (**Figure 12**). DET is another excited state quenching mechanism. An excited electron is transferred from one molecule (the absorber of light) to a second molecule while, at the same time, an electron is transferred from the latter to the former (electron exchange mechanism). This process requires a wavefunction overlap between the donor and acceptor, which means it can only occur at short distances, typically within 1 nm (it falls off exponentially with distance, proportional to e^{-kR}). A recent example of the DET quenching in Ru(II) polypyridyls is [Urriza-Arsuaga 2019a] and references therein.

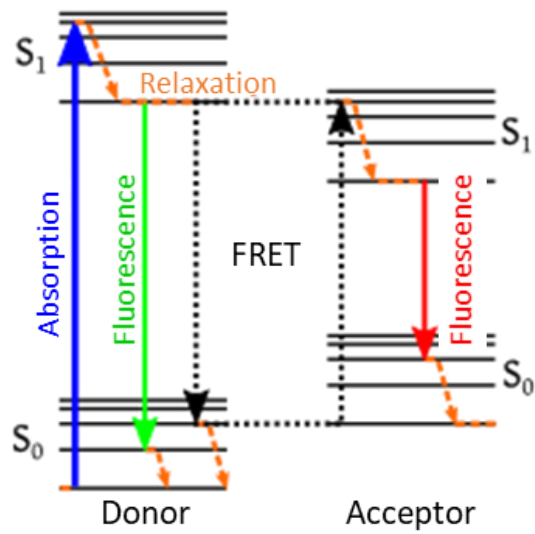


Figure 11. Jablonski diagram of FRET with typical timescales indicated. The black dashed horizontal lines indicate a virtual photon.

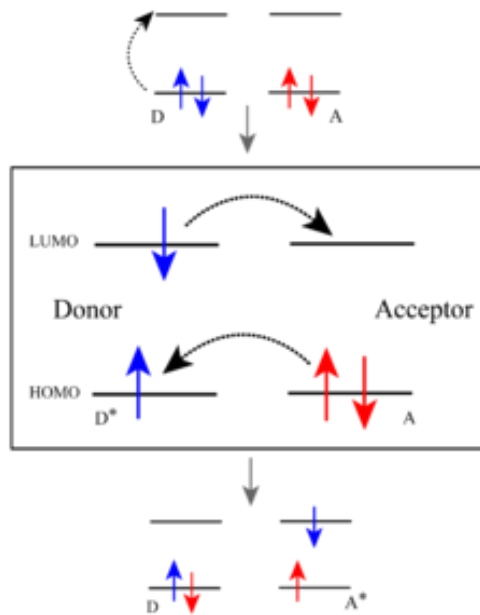


Figure 12. Scheme of Dexter energy transfer mechanism.

3. Photoinduced electron transfer (PET) (**Figure 13**). PET is an excited state electron transfer process by which an excited electron is transferred from donor to acceptor. The electron can reach the acceptor in a single step (*tunneling* in case of direct donor-acceptor coupling, *superexchange* in case of bridge-mediated electron transfer) or by means of subsequent steps through intermediate redox active species (*hopping*). Tunneling and superexchange mechanisms require again wavefunction overlap between the donor and acceptor, and the electron transfer probability decreases exponentially with the donor-acceptor distance ($e^{-\beta r}$, where β is a parameter that characterizes the distance dependence of the coupling). Examples of PET quenching in Ru(II) complexes are those of [Ribeiro Santos 2015, Urriza-Arsuaga 2019b].

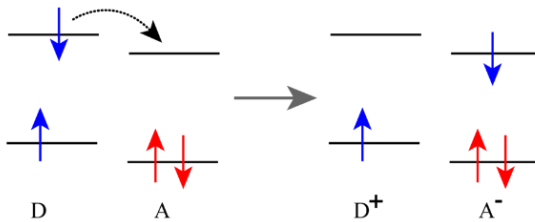


Figure 13. Scheme of photoinduced electron transfer mechanism.

Several additional external factors can influence the luminophores spectroscopic and/or photophysical features. Two of them will be analyzed in detail due to their importance for the developed sensors: temperature and environmental polarity.

1.1.4.1. Dependence of the luminescence lifetime on temperature

In the absence of emission quenchers, the excited state lifetime of luminescent dyes depends on the competition between radiative and non-radiative deactivation processes. In the case of Ru(II) polypyridyl complexes, it has been demonstrated [Lumpkin 1990, Pourtois 2004, Sun 2013] that thermal activation can promote the photoexcited electron of the metal dye, located in a luminescent metal-to-ligand charge transfer (³MLCT) manifold of three closely spaced states (Figure 14), to a nearby ³MLCT excited state (so-called “fourth ³MLCT”), and often also to a higher lying non-emissive metal-centered state (³MC) (**Figure 14**). The non-radiative constant corresponding to the thermal activation process follows Arrhenius-type kinetics, so that the temperature dependence of the luminescence lifetime (τ , i.e. the inverse of the excited state deactivation rate constant, k_d) for a Ru(II) complex can be expressed according to eq. (4) [Van Houten 1976],

$$\tau = 1/k_d = [A + B \exp(-\Delta E/k_B T)]^{-1} \quad (4)$$

where A represents the temperature-independent term that includes both radiative and non-radiative deactivation constants from the ${}^3\text{MLCT}$ excited state, and B is the pre-exponential factor in the Arrhenius equation. The ΔE parameter stands for the energy gap (if the crossing is a *reversible* process) or the activation energy (if it is *irreversible*) between the ${}^3\text{MLCT}$ manifold and the thermally accessible excited state, k_{B} is the Boltzman constant, and T is the absolute temperature.

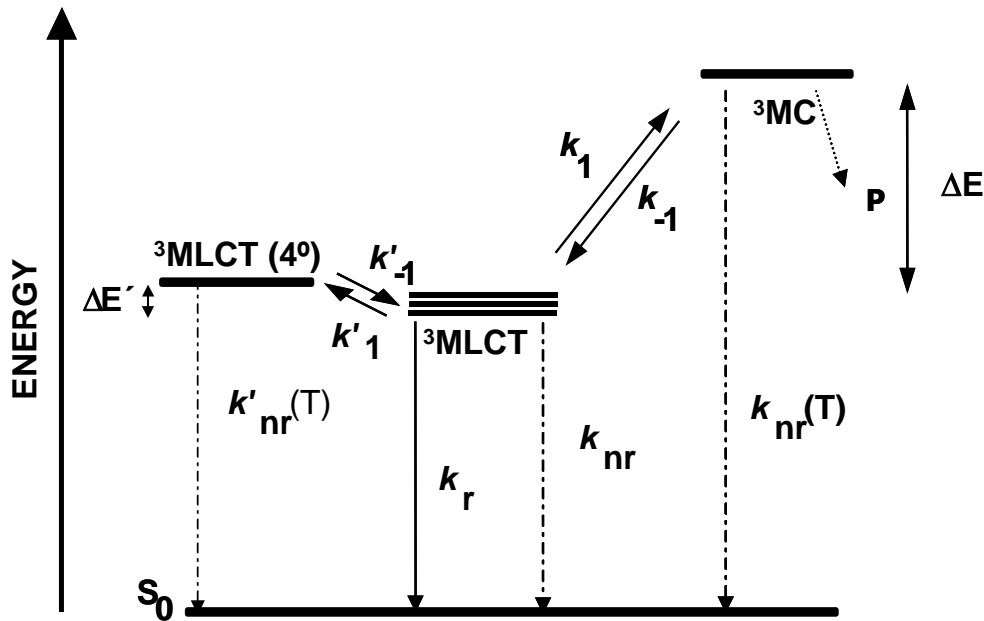


Figure 14. Simplified excited state deactivation diagram for a Ru(II) complex with polyazaheterocyclic chelating ligands. The picture depicts only the emitting and the thermally activated (dark) excited states. From [Bustamante 2018], licensed under an open access Creative Commons CC BY 4.0 license.

From eq. (4) it can be inferred that the temperature sensitivity of the luminescent Ru(II) complexes increases with the accessibility to their ${}^3\text{MC}$ state. However, a very efficient crossing to this excited state leads to photolabile species, due to the anti-bonding nature of σ -type ${}^3\text{MC}$ states ($e(\text{d}^*)$) [Seddon 1984]. The relative energy of the metal-centered level depends on the σ -donor features of the chelating ligands (*average* ligand field strength), while the position of the luminescent ${}^3\text{MLCT}$ manifold is determined by the energy of the lowest-lying π^* orbital of the ligand set.

These considerations will be of extreme importance later on, when the development of luminescent probes for temperature sensing will be discussed (chapter 4).

1.1.4.2. Dependence of the luminescence on environment polarity

From the different theoretical and experimental studies of the effects of the environment on the luminescence of organic molecules, numerous mathematical relationships have been developed [Valeur 2001]. Most of them are based on a linear correlation between the difference in wavenumbers (energy) separating the absorption and fluorescence maxima of the luminophore (Stokes shift, $\Delta\nu = \nu_a - \nu_e$), and a property of the solvent related to its “polarity”. The most popular is probably the relationship found independently by Lippert [Lippert 1957] and Mataga [Mataga 1956] for a model assuming that the solvent is a continuous medium and the solute is into a “spherical cavity” within it (eq [5]),

$$\Delta\nu = \frac{1}{4\pi\varepsilon_0} \frac{2}{hca^3} (\mu_e - \mu_g)^2 \Delta f + \text{const.} \quad [5]$$

where a is the cavity radius of the reaction field model [Onsager 1936] and Δf is the solvent orientation polarizability as described by eq [6].

$$\Delta f = \frac{\varepsilon - 1}{2\varepsilon + 1} - \frac{n^2 - 1}{2n^2 + 1} \quad [6]$$

Eq. [5] reveals that the Stokes shift increases linearly with increasing Δf , and that the slope is positive and proportional to the square of the difference in dipole moment between the ground and the excited state. Due to its simplicity and success in the absence of specific interactions between the solvent and solute, the Lippert-Mataga (L-M) relationship has been widely used.

Important *solvatochromic* effects on the electronic emission band can be produced by various excited state processes, being intramolecular charge transfer (ICT) the most common one. The main feature of ICT dyes is the presence of electron-withdrawing and electron-releasing moieties in specific positions of the molecule. Following absorption of a photon, an electron is transferred from the donor to the acceptor moieties in a so-called “push-pull” mechanism, leading to transient charge separation within the molecule and to an important increase of the dipole moment. Therefore, polarity effects are particularly noticeable on the luminescent properties due to the large change of dipole moment between the absorbing and the luminescent state.

Unfortunately, the simplicity of the L-M model does not account properly for this type of systems. The applicability of the L-M equation is also severely limited because all the solvent-solute *specific* interactions are completely left out. To overcome it, many authors have developed empirical ways to evaluate the polarity of the microenvironment. For instance, Zelinskii et al. studied the solvatochromism of 4-amino-N-methylphthalimide, the fluorescence of which was reported to shift bathochromically with the solvent polarity [Zelinskii 1956]. Dimroth et al. set the so-called $E_T(30)$ scale, based on the energy of the longest-wavelength solvatochromic

absorption band of a pyridinium *N*-phenoxide betaine dye [Dimroth 1963]. Nakajima reported the effect of polarity on the vibronic structure of the fluorescence spectrum of pyrene [Nakajima 1971], later used by Dong and Winnik for experimental solvent polarity evaluation with the so-called "Py" scale [Dong 1982]. Amongst all these methods, luminescence measurements have many advantages compared to absorption determinations because of the higher sensitivity and selectivity of the former. These features are essential for fluorescence-based imaging, single-molecule, nanoprobes and quantitative analysis.

Optical probes have also been used for evaluating the "empirical polarity" of many different environments. The $E_T(30)$ parameter has been determined for as many as 270 solvents [Cerón-Carrasco 2014], as well as for solvent mixtures, ionic liquids, surface of solids, and microheterogeneous systems, e.g. surfactants and polymers [Machado 2014]. The Py scale has been particularly useful for investigating micelles [Capek 2002, Piñeiro 2015], polymers [Winnik 1993], proteins [Bains 2011], and biological membranes [Bains 2011]. In spite of all the progress in the field, these methods also have weaknesses. First of all, as they are empirical, they cannot be used for obtaining parameters such as the dipole moment or hydrogen donating-accepting features of the immediate environment around the probe. Secondly, the estimated polarity degree is strongly dependent on the probe molecule [Reichardt 2010]. Additional polarity scales have been developed, trying to combine the strengths of the Lippert-Mataga and of the empirical methods. An extensive review of the work carried out in this area has been documented by Reichardt and Welton [Reichardt 2010].

The absorption and emission features of transition metal complexes are dependent on the microenvironment polarity as long as their lowest lying electronic excited state has charge transfer (CT) nature [Chen 1998]. Therefore, these molecules should be suitable polarity probes because the metal center, its oxidation state, and the nature and number of ligands allow a fine-tuning of their spectroscopic properties. In particular, the readily accessible long-lived (triplet) metal-to-ligand CT ($^3\text{MLCT}$) excited state of highly photostable ruthenium(II) polypyridyl dyes may be a good candidate to develop robust polarity probes if the underlying factors that influence their response are mastered. The effect of the microenvironment polarity on the photophysics of some Ru(II) complexes has been studied [Caspar 1983], mostly on the highly symmetric forefather of the family, $[\text{Ru}(\text{bpy}_3)]^{2+}$ (bpy = 2,2'-bipyridine).

1.1.5. GaN-based LEDs - the light source.

Gallium nitride and the rest of group III nitride semiconductors belong to group III-V compound semiconductors (III-Vs). The Nitrogen compounds, however, differ from the other III-Vs in ways that are heavily influenced the history of their development.

Chapter 1 - Introduction

GaN was reported in 1932 [Johnson 1932]. Conversely, P- and As- based III-Vs were first developed only in 1952 [Welker 1952], but the progress of the research on the latter was very fast. Ten years later, in 1962, while GaN had still no practical use, Holonyak and Bevacqua realized a visible red GaAsP laser diode (LD) [Holonyak 1962], which triggered the remarkable progress in the development of technologies ranging from crystal growth to device fabrication. Thanks to this progress, various devices have been realized and are enriching our lives today, including infrared LDs for high-speed optical communications, infrared and visible red LDs for optical recording, photovoltaic cells, high-electron-mobility transistors, and heterojunction bipolar transistors. In a relatively short time, a wide spectrum of red to green LEDs were invented through bandgap engineering and doping of materials based on Ga, As, P and dopants such as Zn, Mg, O, etc. [Grimmeiss 1961, Gershenson 1961, Holonyak 1962, Starkiewicz 1962]. On the other hand, blue LEDs, 'the final piece of the puzzle' to create LEDs of all primary colors, remained elusive.

To produce blue light emitting devices, it is required a material with energy bandgap corresponding to about 2.6 eV. Historically, it was known that GaN could be used for blue light emission. The polytypes of GaN, AlN, and InN form a continuous alloy system whose direct bandgaps span, according to literature, from about 0.78 eV for InN [Pankove 1973] to 3.42 eV for GaN, and to 6.0 eV for AlN. Thus, the III-V nitrides could potentially be fabricated into optical devices, which are active at wavelengths ranging from the red well to the ultraviolet. The obstacle was that crystalline GaN with controlled surface roughness was hard to grow on known substrates [Pankove 1973]. Growing high-quality crystalline GaN was challenging because it required: (1) a substrate underneath with small lattice mismatch; (2) an uniform surface to have low defect density [Maruska 1969]. Also, producing p-type GaN was extremely difficult as adding dopants introduces defects into the host material [Pankove 1973] and the elements added to obtain p-doping underwent inactivation [Amano 1988].

From the late sixties, many groups started focusing their efforts towards GaN LEDs. The first reported GaN single crystal was grown on a sapphire substrate by the hydride vapor phase epitaxy (HVPE) method, which uses the chemical reaction between GaCl_3 and NH_3 , in 1969 by Maruska and Tietjen [Maruska 1969]. After two years, the first blue LED using GaN was reported [Pankove 1971].

In the 70s some researchers adopted new techniques such as molecular beam epitaxy (MBE) and metalorganic chemical vapor deposition (MOCVD), and added an intermediate layer onto the sapphire substrate for growing GaN crystals. Firstly, Akasaki, Amano and other co-workers introduced a buffer of polycrystalline AlN (30 nm) on sapphire and obtained high quality crystalline GaN with good optical properties [Akasaki 1989]. Later, Shuji Nakamura produced high quality GaN onto a thin layer of GaN grown at low temperature [Nakamura 1991]. This process is still in use today for fabrication.

Chapter 1 - Introduction

The last obstacle for developing p-n junctions was obtaining p-doped GaN. Nakamura and colleagues realized that Mg-doped GaN would invariably make Mg-H complexes leading to inactivity of Mg in GaN. The researchers found that electrons irradiation or thermal annealing in N₂ ambient of Mg-doped GaN frees up Mg from Mg-H complexes, thus enabling p-type doping in GaN [Richman 1963].

Thanks to all this development, high quality crystals of GaN with clean interfaces and successful p-doping were finally obtained, and they were proved to be the cornerstone of blue LED mass development [Amano 1986].

In the following years, many other structures for manufacturing devices were built based on that progress: the blue-violet LDs used for Blu-ray® discs were realized on thick-film GaN substrates grown from seed sapphire or GaAs crystals. High-power high-frequency high-electron mobility transistors (HEMTs), in widespread use in base stations for cell phones, were obtained on SiC substrates. Also AlGaN/GaN heterojunction field-effect transistors (HFETs), grown on Si substrates, would shortly become available for use as mid-voltage switching devices. All these devices are changing our world helping to reduce energy consumption. For example, LED lamps may be used in 55% of households worldwide by 2025, and the worldwide reduction in power consumption is estimated to be 1,100 TWh per year, assuming a luminous efficacy of 150 lm/W [Haitz 2011]. This value is almost five times the total power consumption of Spain (234 TWh as of 2014). High expectations are also being placed on scanning laser displays including head-mounted displays in terms of reducing power consumption, because they require neither polarizers nor In-containing transparent electrodes, both of which are currently used in liquid crystal displays.

Some of their physical properties made them arduous to achieve, but others have to be acknowledged as important strengths. For example, the fact that group III nitride semiconductors are poorly affected by crystal defect and to their short diffusion length of excited (injected) carriers (compared to that for As- and P-based compound semiconductors) [Kaneta 2006]. It is astounding to realize how much our lives have been (and will be) improved by the many devices that came from these non-perfect crystals grown on non-native substrates.

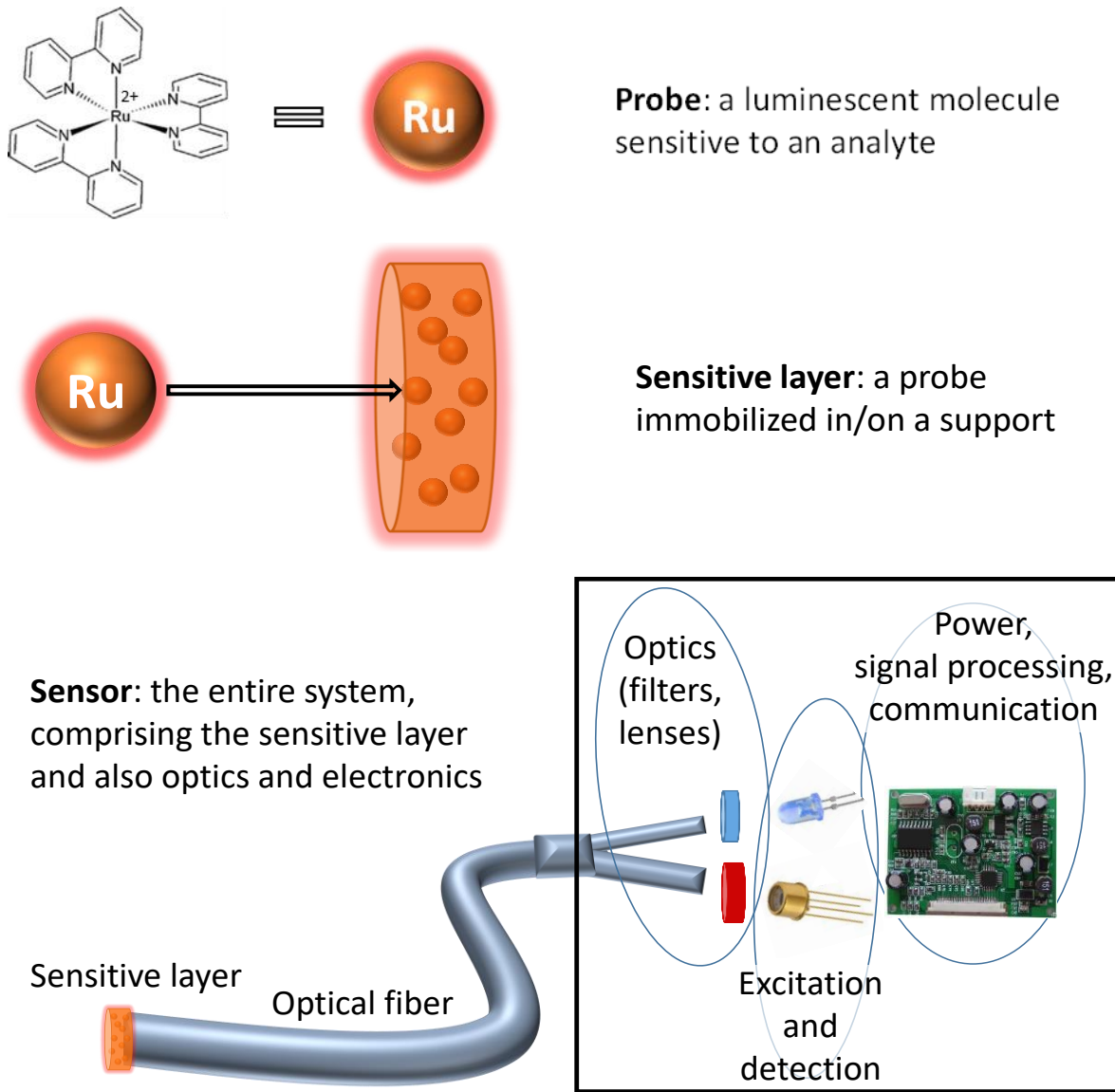


Figure 15. Artistic depiction of the differences between probe, sensitive element, and sensor in luminescent chemical sensing.

1.1.6. The sensor as a whole: optics and electronics.

We started from the definition of sensor and dig into the features of the probe. Sometimes in the literature, these two terms (sensor and probe) are interchanged. Herein we used the so-called 'Cammann 1996': "Chemical

sensors are *miniaturized* devices which can deliver real-time and *on-line* information on the presence of specific compounds or ions even in *complex samples*." This definition is useful to shed light on the (generally accepted) differences between chemically-sensitive probe, sensitive element and optical chemical sensor: the latter is the entire instrument, which comprises also the light source, detector, signal-processing unit and the required optical components (optical filters, lenses, optical fiber) (Figure 15).[†]

For performing luminescent sensing measurements, rather than measuring the absolute intensity of the emission from the sensitive layer as a function of the analyte concentration, the output of the excitation LED is sinusoidally modulated so that the emission of the luminescent probe becomes modulated accordingly, but *phase-shifted* due to the finite lifetime of the excited state (see Figure 16). The resulting phase shift (ϕ) depends on the modulation frequency (f) and on the luminescence lifetime of the probe molecule (τ), as in eq [7] [Valeur 2012]:

$$\tau = \frac{\tan \phi}{2\pi f} \quad [7]$$

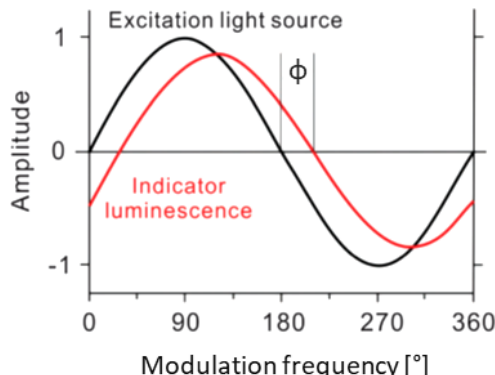


Figure 16. Frequency-domain luminometry: the intensity of the excitation LED is sinusoidally modulated in time so that the emission of the luminescent probe is modulated accordingly. The phase shift is related to the probe luminescence lifetime.

If the emission decay is perfectly exponential (e.g. in isotropic solutions of the luminophore), the observed ϕ can be used to determine the τ instead of using digitalization of the luminescent decay profile after a short excitation light pulse. However, if the excited state decay is an ensemble of luminophore molecules in different microenvironments, the value of τ calculated from ϕ is an averaged one, which also depends on the modulation frequency and is not always coincident with

[†] Still, nowadays many authors differentiate between a "sensor" and a "probe" [device] according to the reversibility or irreversibility of its response to the analyte [Wolfbeis 2013].

Chapter 1 - Introduction

the pre-exponentially weighted emission lifetime determined from the luminescence decay analysis (see 3.2.2.2) [Lakowicz 2006].

The luminometer modulation frequency needs to be optimized for achieving the maximum response according to the probe emission lifetime. It is important to select the optimum value of f for maximizing the sensitivity, i.e. to achieve the largest variation in ϕ when τ changes as a function of the analyte concentration. The highest sensitivity is obtained when the phase shift approaches 45°, because the tangent function is steeper at this value. In case of multi-exponential decays (e.g. coming from a probe molecule sitting in different microenvironments within the sensitive layer), the measured τ value is only an “*apparent lifetime*” as it changes when the modulation frequency is varied, because it weights differently the various components of the emission. When the modulation frequency has been selected, it is kept constant so that eq [7] can be used to calculate the (apparent or real) decay time of the analyte-sensitive luminophore.

Some of the sensors based on luminescent Ru(II) complexes are already commercialized, most notably the O₂ optical sensors, because they compete advantageously with the 60+ years old amperometric Clark sensor [Orellana 2014, Wang 2014]. Some examples of marketed sensors based on luminescence phase shift measurements:

- Pyroscience GmbH (<https://www.pyroscience.com/en/products/theory/optical-oxygen-sensors>)
- PreSense GmbH (<https://www.presens.de/>)
- Anton Paar O₂ Meter: OxyQC (<https://www.anton-paar.com/corp-en/products/details/o2-meter-oxyqc-oxyqc-wide-range/>)
- Ocean Insight (<https://www.oceaninsight.com/support/knowledge-hub/measurement-techniques/oxygen-sensing/>)
- NEOFOX by Spectrecolgy (<https://www.spectrecolgy.com/optical-o2-sensors/>)
- InPro6860i by METTLER TOLEDO (<https://www.mt.com/es/en/home/products/Process-Analytics/DO-CO2-ozone-sensor/dissolved-oxygen-meter/optical-dissolved-oxygen-sensor/optical-inpro-6860i.html#overviewpm>)

The sensors’ low cost and reduced size are pivotal features for field applications and for developing hand-held devices. In the area of biological and chemical sensors, much work has focused on *miniaturization* in order to accomplish devices that can be both portable and work *in situ* and in real-time. Thanks to the advances in microfabrication, amazing progress has been achieved, obtaining miniaturized sensors down to micro- and even nano-scale, coupled with microfluidic devices for unattended complex

sampling handling of minute liquid samples. However, most of these micro-/nano-sensors still require bulky instrumentation for detecting signals and computers to analyze data and display results. Moreover, there is additional room required for pumps, amplifiers, controllers, power suppliers and so on, leading to the paradox of eventually using chips-in-a-lab (miniaturized devices that need an entire laboratory in order to work) instead of the sought miniature *lab-on-a-chip*. One possible solution to these challenges may come also from the *smartphone-as-sensor* concept, which allows coupling these micro/nano-sensors to miniaturized electronics for device control and power supplying, software execution, imaging and data transmission [Vashist 2014, Vashist 2015, Roda 2016, McCracken 2016].

1.1.7. Smartphone-as-sensor concept

Current smartphones can perform instructions millions of times faster than the computer that brought the Man on the Moon in the Apollo mission of 1969. Over the past decade, plummeting prices have led to widespread adoption of these useful handy devices, nowadays surpassing 3 billion globally. There are rural areas where more people have access to a mobile device than to a toilet or sanitized water [Orellana 2012, Web un.org 2013]. Moreover, smartphones possess other features such as small size, access to GPS and data communication, which might allow them to provide a unique (bio)sensing network for monitoring hazardous chemicals or microorganisms over very wide areas for personal safety and national security applications. Researchers and manufacturers alike recognized the attractiveness of both integrating sensors into smartphones and designing smartphone-enabled point-of-care (POC) sensors. The first approach has been widely used for physical sensors: many have already been implemented in the marketed models, such as those for detecting position, proximity, incident light, and magnetic fields and, more recently, also temperature and pressure [Web developer.android.com 2017]. However, the second type is more interesting for complex (bio)chemical sensors, either for electrical or optical sensors [Vashist 2014, Vashist 2015]. Amongst the latter, devices based on microscopy, scattering, spectroscopy, colorimetric and luminescence have all been developed (see Figure 17 for examples) [Roda 2016, McCracken 2016].

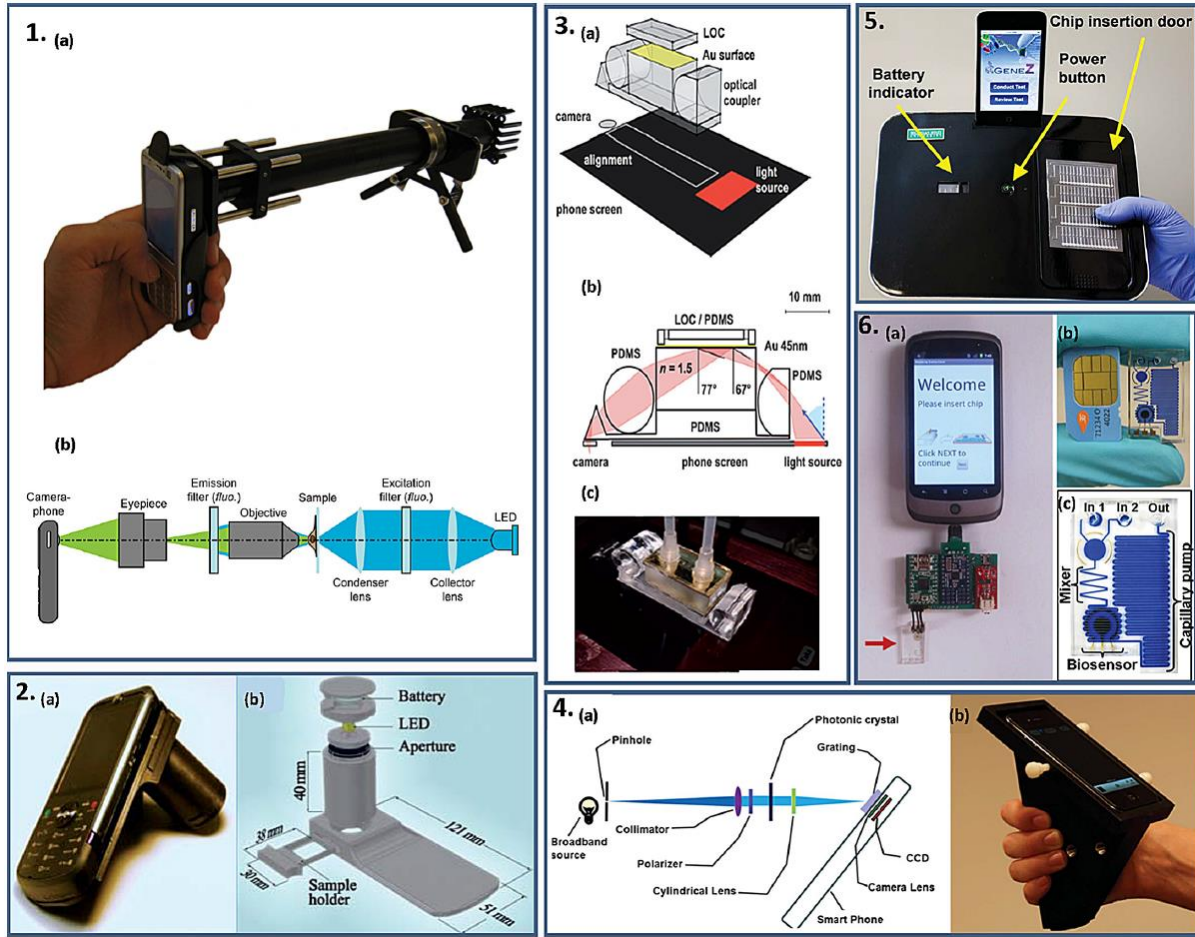


Figure 17. Panel 1: (a) a prototype, with filters and LED installed, for fluorescence imaging, and (b) cellphone microscopy optical layout for fluorescence and bright-field imaging. **Panel 2:** (a) lens-free cellphone microscope based on incoherent in-line holography, and (b) schematic diagram of its microscope attachment. **Panel 3:** (a) 3D scheme of a representative setup for angle-resolved SPR using screen illumination and front camera detection optically coupled with a disposable device; (b) 2D raytrace of the experimental arrangement showing the light path from screen to camera, and (c) picture of the actual experimental arrangement. **Panel 4:** (a) scheme of the optical components within a smartphone-based detection instrument for label-free photonic crystal biosensing; (b) cradle with the detection slot for the biosensor slide. **Panel 5:** picture of the Gene-Z, a prototype for genetic analysis on microRNAs working with disposable chips and interfaced to an iPod Touch. **Panel 6:** (a) photograph of a prototype composed of smartphone, additional electronics and a microfluidic chip (indicated with the arrow); (b) picture of the chip and a cellphone SIM card for comparison, and (c) enlarged image of the chip with labeled components (the channels are filled with blue dye for improved visualization of the fluidic network).

Reproduced from [Roda 2016] with permission.

Chapter 1 - Introduction

As a collaboration between UPM-ISOM-B105ESL and UCM-GSOLFA, a preliminary O₂ sensor as a piggyback module connected to an Android-based smartphone, was fabricated and tested [Muñoz 2014]. It was fabricated by using a Ru(II) dye functionalized n-type GaN sensor chip and miniaturized low-cost digital LSI electronics for phase detection (**Figure 18**). This experience generated some issues on the GaN surface functionalization that we address and try to clarify in the present Thesis.



Figure 18. Picture of the smartphone-controllable O₂ sensor with included optical fibers for remote sensing in solution or the gas phase.

1.2. Objectives

Since their inception, UV to green light-emitting diodes (LEDs) based on GaN (and other III-nitride semiconductors) have revolutionized areas as diverse as illumination, medical treatments and biophotonics. Chemical sensing also benefited, as many fluorophores that provide extreme sensitivity and selectivity absorb light in that region. Additionally, integration and smartphone-based sensing allow the sought portability and miniaturization for optosensor development. For manufacturing intrinsically responsive GaN-based LEDs, we modified n-doped GaN substrates to tether a luminescent Ru(II) indicator dye. These complexes are, in fact, optimal for developing luminescence-based sensors as they can be excited with the blue light of GaN-based LEDs.

The common thread of this thesis will be the development of luminescent Ru(II) polypyridyl complexes (and materials containing these indicator dyes) that can be used to manufacture GaN-based microsensors, i.e. sensitive elements that, with the proper miniaturized LSI electronics, can be plugged to current **smartphones** to achieve instrumentation for detecting chemical species of interest for personal and workplace safety (e.g. ethanol and oxygen). The sensitive elements will be organic-inorganic hybrids fabricated either by *direct functionalization* of GaN or by *attaching of a thin dyed polymer layer* to the surface of the GaN LED. Some basic issues regarding selection of proper luminescent dyes and optimum doping of GaN, in order to understand and control electron transport from the dye to the GaN device will be addressed. Besides, complementary applications of the sensor devices will be explored. Thus, the above objectives will be divided in three main subparts:

- 1) In the first part, *GaN-based organic-inorganic hybrids* for O₂ sensing will be manufactured, and the emphasis will be mainly on the *optimization of the material* constituting the sensitive element. The O₂-sensitive dye will be tethered to GaN surfaces via an aminosilane-coupling layer for utmost stability and durability. The main interest is to study the effect of the intermediate layer thickness and composition on the hybrids luminescence and response to the species of interest (O₂), and to determine the proper doping type of the GaN surface. Answering these key questions will allow selecting the proper LEDs to obtain the sought Ru(II) dye-GaN LED luminescent chemical sensors.
- 2) The second section will focus on the *preparation of novel luminescent indicator dyes* for ethanol, –essentially, polarity–, sensing. The work will start with computer-aided design, followed by chemical synthesis and characterization. Subsequently, these indicator dyes will be supported in perm-selective polymers and calibrated with different concentrations of EtOH and H₂O to investigate their selectivity and analytical features.

Chapter 1 - Introduction

- 3) Finally, the O₂ partial pressure will be monitored *in situ* inside *microfluidic cell cultures* and *organ-on-chip devices* using polymer materials dyed with either O₂- or T-sensitive dyes. This part is hence focused on this particular exciting *application of luminescence-based sensors*.

1.3. Motivation

Numerous are the reasons behind the election of these objectives; hereafter the most relevant motivations are outlined.

1.3.1. GaN-based hybrids

Inorganic semiconductors have often been used in hybrid functional materials development, particularly in applications such as light harvesting and chemical sensing [Gründler 2007, Potje-Kamloth 2008, Ren 2011]. Silicon, due to the advanced degree of its manufacturing technology, has been the predominant one so far, but many others are also of strong interest. *GaN* is among the leading ones because it is exceptionally suited for high-speed/high-power electronics [Flack 2016], high efficiency power transmission [Ueda 2017], and light-emitting devices [Nakamura 2000]. Moreover, it is biocompatible [Jewett 2012] and chemically stable under physiological conditions [Steinhoff 2003], making it very interesting for biosensing applications. Although chemically inert, it is possible to functionalize its surface with complex molecules (indicator dyes, peptides, proteins or DNA) following a suitable surface activation [Baur 2005, Arranz 2008, Makowski 2011a, Makowski 2011b].

In a close collaboration with UPM-ISOM, the GSOLFA group at UCM recently developed a route to *directly tether* luminescent Ru(II) dyes for optochemical sensing onto the surface of GaN wafers and GaN-based blue LED chips [Lopez-Gejo 2011]. The functionalization route (**Figure 19**) includes: i) hydroxylation of the GaN wafers or LEDs by oxygen plasma treatment; ii) aminosilanization of the activated surface; iii) reaction of the aminated surfaces with the hexa(sulfonyl chloride) derivative of the tris(4,7-diphenyl-1,10-phenanthroline)ruthenium(II) indicator dye.

Blue LEDs are the usual light sources used for optical sensors that make use of Ru(II) indicator dyes, and so direct functionalization of the LED surface allows the *highest possible miniaturization*, being the light source in direct contact with the sensitive layer, which is also in the thinnest possible format – a nanolayer growth on the GaN surface. Coupling these functionalized LEDs with miniaturized detectors and electronics should lead to the development of integrated microcircuits with intrinsic gas-sensing features [Lopez-Gejo 2011]. Moreover, GaN surface functionalization helps to extract more efficiently the emitted light from the semiconductor. Light extraction increases for two reasons: refractive index matching and interaction with the evanescent field.

- 1) Refractive index matching. Because of the very high refractive index of GaN (2.54 at $\lambda = 400$ nm), the percentage of emitted photons able to escape from the GaN chip is very low [Seong 2013]. Given the *critical angle* of the total internal reflection α_c (Eq. [8]), the *escape ratio* (η_c), is described as Eq. [9]

$$\alpha_c = \sin^{-1} \left(\frac{n_2}{n_1} \right) \quad [8]$$

$$\eta_c = \frac{(1 - \cos \alpha_c)}{2} \quad [9]$$

The critical angle and escape ratio at the GaN/air interface are equal to 23° and 0.040, respectively. The refractive index of silanes self-assembled layers is 1.46 [Terracciano 2013] – for comparison, PDMS-based encapsulating polymers have a refractive index of 1.41 at $\lambda=400$ nm [Zhang 2020]. Hence, the critical angle and escape ratio calculated at the GaN/silane layer interface are equal to 34° and 0.085, respectively, higher than those at the the GaN/air interface.

- 2) Interaction with the evanescent field. In the theory of wave propagation, evanescent fields most often play a secondary role since they are usually much lower than non-evanescent fields. Obviously, this is not the case at the interface between two media by a totally reflected field incident from the optically denser side, where the evanescent fields represent the entire field contribution [Felsen 1976]. The field intensity ($I(z;\alpha)$) decreases exponentially with the distance from the interface z , (Eq. [10]), with a parameter $\delta(\alpha)$ called *penetration distance* reported in Eq. [11]):

$$I(z; \alpha) = I_0 \exp[-z/\delta(\alpha)] \quad [10]$$

$$\delta(\alpha) = \frac{\lambda}{4\pi\sqrt{n_2^2 \sin(\alpha) - n_1^2}} = \frac{\lambda}{4\pi n_2 \sqrt{\sin^2(\alpha) - \sin^2(\alpha_c)}} \quad [11]$$

Where λ is the wavelength, n_2 is the refractive index of the material from where the radiation comes, n_1 is the refractive index of the material in which the radiation is penetrating, α and α_c are the incident angle and the critical angle of total internal reflection, respectively. The penetration distance for the GaN/silane interface ranges between 31 nm (incident angle tending to 90°) and 3656 nm (incident angle equal to 34° – the critical angle of total internal reflection for the GaN/silane interface); this distance is always higher than the distance expected between the luminophore molecules and the interface. For a very useful graphical representation of the evanescent field, visit <https://www.olympus-lifescience.com/en/microscope-resource/primer/java/tirf/penetration/>.

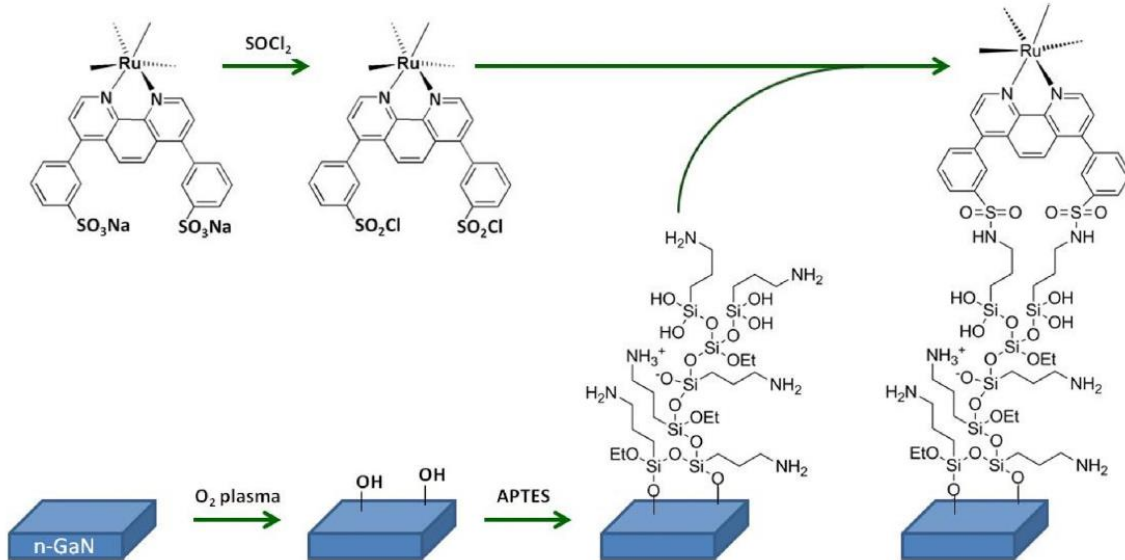


Figure 19. Fabrication of the luminescent $\text{Ru}(\text{pbbs})_3$ -silane-GaN surface. Reprinted from [Ielasi 2018] with permission.

1.3.2. Polarity sensing

Environmental polarity measurements are of high interest in numerous fields. In biology, for example, *micropolarity molecular probes* are widely used for distinguishing and imaging different microenvironments because, although the typical solvent in biological systems is water, there are significant variations of polarity within proteins, vesicles, cells, and tissues [Demchenko 2015]. In addition, the presence and concentration of molecules in solution may dramatically change the local polarity in a solvent [Zhou 2016]. Polarity probes may also detect biomolecular interactions [Klymchenko 2013]. Important macroscopic applications of environmentally-sensitive dyes are relative humidity sensors (atmosphere, food storage) [Moreno-Bondi 2004] and monitoring hydrocarbons in water (e.g., fuel leaks) [Orellana 2011] or, conversely, water in organic solvents used in industrial processes (e.g., during solvent and chemicals production or purification) [Jung 2016].

Luminescent organic dyes have been widely used as molecular probes. The basis for their usefulness is that the probe luminescence features – position and intensity of its maximum, vibronic fine structure, quantum yield, lifetime and/or polarization – are dependent on the environment directly around the probe if the lowest-lying electronic excited state is of the so called “*intramolecular charge transfer*” type [Valeur 2001, Reichardt 2011]. The use of *optical sensors to monitor micropolarity* has particular advantages, especially because it allows easy miniaturization, imaging, and unbeatable spatial resolution down to the nanosize [Lee 2014].

1.3.3. Ethanol sensing

Ethanol (EtOH, ethyl alcohol) has been known for long time in human history. Most cultures have independently discovered the processes of producing beer and wine (fermentation), and spirits (distillation) [Arnold 1911] and, as a matter of fact, alcohol has been described in important antique pieces like Confucius Analects, Homer poems, the Bible and the Koran. Measuring the ethanol levels is of great interest for a variety of applications and industrial processes [Lam 2009], both in gas and in liquid phase. One example is during ethanol production via yeast fermentation, in order to control the reaction progress. Another important application is the measurement of the EtOH concentration in alcoholic beverages [Heymann 2017] (for taxation purposes) or in fuel, in which ethanol is currently used as an additive for octane booster in unleaded gasoline, making for about 25% and 10% in Brazil and USA, respectively, of the total volume in the gasoline consumption [Web eia.gov 2016, Belincanta 2016, Iodice 2017]). In addition, because of its prominence in car accidents, breath analyzers are very often used for assessing blood alcohol concentration (given the demonstrated correlation between the ethanol amount in the blood and driving unfitness). Finally, the lower explosive limit (LEL) and upper explosive limit (UEL) of ethanol are 3.3 and 19.0% v/v (33000 – 190000 ppm) in air (at atmospheric pressure and 298 K), respectively [Zabetakis 1965, DrysdaleBrandes 2007]. For this reason, the United States of America institute for occupational safety and health (NIOSH) set the immediately dangerous to life and health (IDLH) concentration as 10% of the LEL, or 3300 ppm [NIOSH 1995]. Therefore, measuring ethanol vapor concentration in air is of primary importance in ethanol production plants or storehouses.

1.3.4. Cell cultures

Cell culturing is of paramount importance in many fields of research, such as cellular and molecular biology, medicine and pharmacology. Many vaccines (e.g., against polio, chickenpox) are obtained thanks to mass culturing of animal cell lines [Perdue 2011, Milián 2015], and tissue engineering allows development of substitutes for biological tissue or whole organs [MacArthur 2005, Lanza 2014, Phelan 2017].

For growing cells in vitro, control of culture conditions is of great importance in order to recreate in vivo-like environment, because they affect cellular function and behavior. Microfluidic cell cultures are especially interesting because they permit close mimicking of in vivo conditions, e.g. allowing continuous perfusion of the culture, creating physical or chemical gradients, controlling cells number and volume available, and growing different cells in close contact to allow exchanging material or signals [Huh 2012, Bhatia Halldorsson 2015]. Moreover, it is possible to continuously perfuse living cells arranged in 3D structures to simulate tissue- and organ-level

physiology, in the so-called organ-on-a-chip (OOAC) devices [Bhatia 2014]. This is especially important when dealing with preclinical drug testing, for which traditional 2D cell-cultures, even though able to provide valid information about the substance efficacy and toxicity, fail to represent precisely cells function and physiology [Breslin 2013, Edmondson 2014]. The 3D structures found in an intact organ or its simulation can instead add fundamental information about tissue–tissue interactions [Huh 2012].

One of the most important parameters in cell culture is dioxygen (O_2) tension [Semenza 2007, Jagannathan 2016]. While it is known since long time that atmospheric dioxygen pressure is not the “normal” condition for human cells [Cooper 1958, Jagannathan 2016], cell cultures are still kept majorly under 19.95–21% O_2 . These values are much higher than in the human body, where O_2 varies between 0.5 to 16%. In the case of endothelial cells, for example, normoxia is considered about 10% O_2 for arterial environment and 5% O_2 for venous environment [Tsai 2003], and hence in these conditions cells should be cultured for biologically relevant results. Another fundamental cell culture parameter is temperature (T) [Kretzmer 1998] that, since the 60s, is known to have a dramatic effect on cells growth kinetics [Watanabe 1967]. While human cells are always cultured in incubators at 37 °C, the required handling is usually done at 20–25 °C. These mild temperature shocks are commonly neglected, but recent studies revealed that changes in mammalian gene expression could be detected after one hour already at 32 °C, without recovery at 37 °C [Fujita 1999]. Further undesired effects are induced when cells are exposed to lower temperatures [Kaufmann 1999, Neutelings 2013]. For all these reasons, there is a growing interest on monitoring O_2 and T in cell cultures. Microfluidic chip-based cell cultures enable control of these parameters at a microscopic level, although their monitoring can be challenging due to the chips small size. Moreover, real time measurements as well as high spatial resolution of PO_2 and T are usually required [Abaci 2014, Brennan 2014, Oomen 2016]. Optical O_2 and T sensors are thus the most suitable, giving their aptness for miniaturization and imaging (and, in case of dioxygen sensors, avoiding analyte consumption in such tiny volumes [Sun 2015]).

1.4. Work plan and methodology

1.4.1. Manufacturing GaN-based organic-inorganic hybrids for O₂ sensing

Glass (as a control), p-doped and n-doped GaN surfaces were activated with O₂ plasma and then coated with different ω -aminosilane layers. The obtained pendant amine groups were used to covalently tether a strongly luminescent O₂-sensitive Ru(II) dye to the various surfaces.

From previous results [López-Gejo 2010], significantly dimmed luminescence from the dye was expected if the silane intermediate layer coating n-GaN substrates is thin (a few nm). This quenching, which is reflected as a shortening of the emission lifetime, was hypothesized to be caused by efficient competition of a *photo-induced electron transfer* (PET) process from the photoexcited dye to the n-type semiconductor valence band. Such hypothesis came from the fact that it was not observed in either underlying glass or p-type GaN substrates because of the absence or higher-lying position of the conduction band of the latter, respectively.

The aim of our research was twofold: to confirm the PET phenomenon and to find ways to overcome the disturbing associated luminescence quenching. Because most electron transfer processes are dependent on distance, we studied the occurrence of the PET process by investigating how this unwanted process was influenced by the *aminosilane layer thickness* and, eventually, suppressed it by using tailored thick layers. The structure of the aminoalkyl trialkoxysilane determines its O-substitution rate and hence the thickness of the GaN surface coating. Two factors play a key role [Zhu 2012, Vashist 2014]:

- the “goodness” of the leaving group (hydroxylation of ethoxy groups is 6–10 times slower than that of methoxy groups) and
- the presence of an amine group in a distal position that favors intramolecular nucleophilic catalysis.

These two features guided the selection of the aminosilanes in order to obtain layers ranging from monolayer (sub-nanometers) to several nanometers. We studied also the influence of the silane coating thickness on the O₂ sensing features of the hybrid materials.

Dicing, cleaning and O₂-plasma activation of the glass and GaN substrates were performed in the clean room of the Instituto de Sistemas Optoelectrónicos y Microtecnología, Universidad Politécnica de Madrid (ISOM, UPM). Silanization and attachment of the O₂-sensitive indicator dye was carried out at the UCM-GSOLFA laboratories. For characterization of the hybrid materials surface, X-ray photoelectron spectroscopy (Universidad Autónoma de Madrid) and atomic force microscopy (National Center for Electron Microscopy, UCM, Madrid) was used to evaluate the

thickness and morphology of the layers. Confocal luminescence microscopy with single-photon-timing detection (UCM-GSOLFA) provided the emission lifetime (τ) of the resulting dye-silane-GaN hybrid sensing materials, allowing investigation of the effect of the silane layer thickness on the emission lifetime of the hybrids as well as their response to molecular oxygen.

1.4.2. Luminescent ethanol (polarity) sensing

Once succeeded in the optimization of miniaturized GaN-Ru(II) luminescent sensors for monitoring dioxygen concentration, the focus shifted towards developing similar microsensors for different species. Ethanol was selected as target analyte.

The work started with the design of the luminescent Ru(II)-polypyridyl *polarity probes* with the help of computational modeling. Various mechanisms can be exploited to produce the *solvatochromic* behavior, being intramolecular charge transfer (ICT) in the excited state the most common one [Zhou 2016]. The main feature of all ICT dyes is the presence of electron-withdrawing (EW) and electron-releasing (ER) moieties in suitable positions of their molecular structure. Following absorption of a photon, an electron is transferred from the donor to the acceptor groups in the so-called “push-pull” mechanism, leading to charge separation within the molecule and an important increase of its dipole moment in the electronic excited state. The luminophore response to the microenvironment polarity is proportional to the change in dipole moment from the ground to the excited state [Mataga 1956, Lippert 1957, Zhou 2016]. For metal complexes, the absorption and emission features are dependent on the microenvironment polarity as long as their lowest lying electronic excited state has charge transfer (CT) nature [Thompson 2013], so that Ru(II)-polyazaheteroaromatic dyes should be *suitable polarity probes*.

The selected Ru(II) dyes were synthesized in the UCM-GSOLFA laboratories of the Dpm't. of Organic Chemistry and properly characterized therein, both for their structural and spectroscopic features in different solvents to confirm their fitness-to-purpose. The sensitivity to polarity can be exploited for preparing EtOH-sensitive polymers if the dye is supported in a *perm-selective polymer* film that allows preferential permeation of EtOH while blocking other polar analytes (e.g. H₂O, a possible interference for EtOH sensing). After investigating the effect of alcohols on the luminescence of these novel Ru(II) complexes, they were embedded in different perm-selective polymers to act as support and specially to eliminate the possible interference from water.

Computational modeling was performed in collaboration with the Quantum Chemistry group of Universitat Rovira i Virgili (URV), Tarragona, led by Prof. M. Mar Reguero de la Poza. Synthesis and characterization – ultraviolet/visible absorption spectroscopy, luminescence spectroscopy and single-photon timing decay analysis in

solvents of different polarity – of the Ru(II) dyes for microenvironmental probing were carried out at UCM-GSOLFA laboratories. Once the perm-selective polymers were doped with the indicator dyes, their response to ethanol and water vapors was investigated by using a compact phase shift-based luminescence lifetime monitoring system (developed at former Interlab Electronic Engineering, Madrid, in collaboration with UCM-GSOLFA).

1.4.3. Sensitive elements inside microfluidic cell cultures for *in situ* monitoring of the O₂ partial pressure

Part of this work was carried out during a three-month secondment in The Netherlands. Approximately eight weeks were spent at the Rijksuniversiteit of Groningen (RUG), and about five weeks in Micronit Micro Technologies B.V. in Enschede, thus also satisfying the requirements for the international PhD mention. The local supervisor at RUG was Prof. Dr. Elisabeth M. J. Verpoorte, head of the Pharmaceutical Analysis group. At Micronit, I was supervised by Dr. Monica Brivio and Dr. Sandro Meucci.

At RUG, microfluidic chips for the human umbilical vein endothelial cells (HUVECs) cultures were fabricated following the usual steps for soft lithography processes. The chips were made of poly(dimethylsiloxane) (PDMS), based on a design already tested in the Pharmaceutical Analysis group for the same purpose. The aim was to fabricate an O₂-sensitive layer into the PDMS microfluidic chip by *depositing directly into the microchannels* a “sensor cocktail” containing the liquid pre-polymer, an O₂-sensitive Ru(II) dye, the solvent and the additives. Because of the inert, highly hydrophobic nature of the material surface, a sol-gel strategy was followed in order to obtain a siloxane coating assembled onto the PDMS surface as the layer matrix. Cells were cultured into the functionalized chips, and the biocompatibility of the O₂-sensitive coatings was tested. Finally, a fiber optic-based compact luminescence lifetime monitoring system in the frequency domain developed at UCM was used to interrogate the O₂ levels *in situ*. The instrument was tuned to the excitation/emission wavelengths and luminescence lifetime of these polyazaaromatic ruthenium complexes and equipped with optical fibers for remote sensing into the channels of the microfluidic chip.

At Micronit company, devices for organ-on-chip (OOC) application were made of three layers: a perforated glass slide supporting a gas-permeable PET membrane, sandwiched between two glass slides equipped with perfluorinated elastomeric gaskets. The cells are supposed to be seeded onto the porous membrane. The flow chambers are created by mechanically compressing the three layers using the dedicated (customizable) Micronit’s Fluidic Connect Pro clamp. The aim was to produce O₂- and T-sensitive spots into the glass microfluidic chambers. Again, the

Chapter 1 - Introduction

fiber optic-equipped portable luminometer was used to monitor O₂ and T in situ, contactless.

Design, preparation and characterization – ultraviolet/visible spectroscopy, luminescence spectroscopy and luminescence lifetime imaging – of the O₂-sensitive and T-sensitive polymers were carried out at the UCM-GSOLFA laboratory for laser spectroscopy. Primary HUVECs were obtained from the University Medical Center (RUG), and the additional material for cell culture, as well as the required training, were provided by the personnel of the Pharmaceutical Analysis group (RUG).

Microchip fabrication techniques for PDMS chips were also acquired at the Rijksuniversiteit. Calibration of the O₂-sensitive PDMS chips, cell culturing and O₂ pressure measurements in the microfluidic cell cultures were performed in the thermostated hypoxic workstation of the Pharmaceutical Analysis group laboratory (RUG). Preparation of glass OOC devices and calibration of the O₂-sensitive and T-sensitive spots were carried out at Micronit Microtechnologies B.V.

Chapter 1 - Introduction

References

Abaci	2014	Abaci, H. E.; Shen, Y.-I; Tan, S.; Gerecht, S. Recapitulating Physiological and Pathological Shear Stress and Oxygen to Model Vasculature in Health and Disease. <i>Sci. Rep.</i> 2014 , <i>4</i> , 4951.
Akasaki	1989	Akasaki, I; Amano, H.; Koide, Y. Hiramatsu, K.; Sawaki, N. Effects of AlN Buffer Layer on Crystallographic Structure and on Electrical and Optical Properties of GaN and Ga _{1-x} Al _x N ($0 < x \leq 0.4$) Films Grown on Sapphire Substrate by MOVPE. <i>J. Cryst. Growth</i> 1989 , <i>98</i> , 209–219. https://doi.org/10.1016/0022-0248(89)90200-5 .
Amano	1986	Amano, H.; Sawaki, N.; Akasaki, I.; Toyoda, Y. Metalorganic vapor phase epitaxial growth of a high quality GaN film using an AlN buffer layer. <i>Appl. Phys. Lett.</i> 1986 , <i>48</i> , 353.
Amano	1988	Amano, H.; Akasaki, I.; Kozawa, T.; Hiramatsu, K.; Sawaki, N.; Ikeda, K.; Ishii, Y. Electron Beam Effects on Blue Luminescence of Zinc-Doped GaN. <i>J. Lumin.</i> 1988 , <i>40</i> , 121.
Arranz	2008	Arranz, A.; Palacio, C.; García-Fresnadillo, D.; Orellana, G.; Navarro, A.; Muñoz, E. Influence of Surface Hydroxylation on 3-Aminopropyltriethoxysilane Growth Mode During Chemical Functionalization of GaN Surfaces: An Angle-Resolved X-ray Photoelectron Spectroscopy Study. <i>Langmuir</i> 2008 , <i>24</i> , 8667–8671.
Bains	2011	Bains, G.; Patel, A. B.; Narayanaswami, V. Pyrene: a Probe to Study Protein Conformation and Conformational Changes. <i>Molecules</i> 2011 , <i>16</i> , 7909–7935.
Baur	2005	Baur, B.; Steinhoff, G.; Hernando, J.; Purrucker, O.; Tanaka, M.; Nickel, B.; Stutzmann, M.; Eickhoff, M. Chemical Functionalization of GaN and AlN Surfaces. <i>Appl. Phys. Lett.</i> 2005 , <i>87</i> , 263901.
Belincanta	2016	Belincanta, J.; Alchorne, J. A.; Teixeira da Silva, M. The Brazilian Experience with Ethanol Fuel: Aspects of Production, Use, Quality and Distribution Logistics. <i>Braz. J. Chem. Eng.</i> 2016 , <i>33</i> , 1091–1102.
Bhatia	2014	Bhatia, S. N.; Ingber, D. E. Microfluidic Organs-on-Chips. <i>Nat. Biotechnol.</i> 2014 , <i>32</i> , 760–772.
Brennan	2014	Brennan, M. D.; Rexius-Hall, M. L.; Jane Elgass, L.; Eddington, D. T. Oxygen Control with Microfluidics. <i>Lab Chip</i> 2014 , <i>14</i> , 4305–4318.
Bustamante	2018	Bustamante, N.; Ielasi, G.; Bedoya, M.; Orellana, G. Optimization of Temperature Sensing with Polymer-Embedded Luminescent Ru(II) Complexes. <i>Polymers</i> 2018 , <i>10</i> , 234; doi:10.3390/polym10030234

Chapter 1 - Introduction

Cammann	1996	Cammann, K.; Guibault, E. A.; Hall, H.; Kellner, R.; Wolfbeis, O. S. The Cambridge Definition of Chemical Sensors. In: <i>Proceedings of the Cambridge Workshop on Chemical Sensors and Biosensors</i> . Cambridge University Press, New York, 1996 .
Campagna	2007	Campagna, S.; Puntoriero, F.; Nastasi, F.; Bergamini, G.; Balzani, V. Photochemistry and Photophysics of Coordination Compounds: Ruthenium. In: Photochemistry and Photophysics of Coordination Compounds I, Balzani, V.; Campagna, S. (Eds) 2007 (Springer, Berlin, Heidelberg), Ch. 4, pp. 117–214.
Capek	2002	Capek, I. Fate of Excited Probes in Micellar Systems. <i>Adv. Colloid Interface Sci.</i> 2002 , <i>97</i> , 91–149.
Caspar	1983	Caspar, J. V.; Meyer, T. J. Photochemistry of Ru(bpy) ₃ ²⁺ . Solvent Effects. <i>J. Am. Chem. Soc.</i> 1983 , <i>105</i> , 5583–5590.
Cerón-Carrasco	2014	Cerón-Carrasco, J. P.; Jacquemin, D.; Laurence, C.; Planchat, A.; Reichardt, C.; Sraïdi, K. Solvent Polarity Scales: Determination of New ET(30) Values for 84 Organic Solvents. <i>J. Phys. Org. Chem.</i> 2014 , <i>27</i> , 512–518.
Ceroni	2012	Ceroni, P. The Exploration of Supramolecular Systems and Nanostructures by Photochemical Techniques, Springer Netherlands, 2012 ; DOI 10.1007/978-94-007-2042-8.
Chen	1998	Chen, P.; Meyer, T. J. Medium Effects on Charge Transfer in Metal Complexes. <i>Chem. Rev.</i> 1998 , <i>98</i> , 1439–1477.
Cooper	1958	Cooper, P. D.; Burt, A. M.; Wilson, J. N. Critical Effect of Oxygen Tension on Rate of Growth. <i>Nature</i> 1958 , <i>182</i> , 1508–1509.
Demchenko	2015	Demchenko, A. P.; Duportail, G.; Oncul, S.; Klymchenko, A. S.; Mély, Y. Introduction to Fluorescence Probing of Biological Membranes. <i>Methods Mol Biol.</i> 2015 , <i>1232</i> , 19–43.
Descalzo	2013	Descalzo, A. B.; Somoza, C.; Moreno-Bondi, M. C.; Orellana, G. Luminescent Core-Shell Imprinted Nanoparticles Engineered for Targeted Förster Resonance Energy Transfer-Based Sensing. <i>Anal. Chem.</i> 2013 , <i>85</i> , 5316–5320.
Dimroth	1963	Dimroth, K.; Reichardt, C.; Siepmann, T.; Bohlmann, F. On pyridinium N-phenol betaines and their use for characterizing the polarity of solvents. <i>Liebigs Ann. Chem.</i> 1963 , <i>661</i> , 1.
Dong	1982	Dong, D. C.; Winnik, M. A. The Py Scale of Solvent Polarities. <i>Photochem. Photobiol.</i> 1982 , <i>35</i> , 17–21.
Evansa	2006	Evansa, R. C.; Douglassa, P.; Winscomb, C. J. Coordination Complexes Exhibiting Room-Temperature Phosphorescence: Evaluation of Their Suitability as Triplet Emitters in Organic Light Emitting Diodes. <i>Coord. Chem. Rev.</i> 2006 , <i>250</i> , 2093–2126.

Chapter 1 - Introduction

Felsen	1976	Felsen, L. B. Evanescent waves. <i>J. Opt. Soc. Am.</i> 1976 , <i>66</i> , 751–760
Flack	2016	Flack, T. J.; Pushpakaran, B. N.; Bayne, S. B. GaN Technology for Power Electronic Applications: A Review. <i>J. Electron. Mater.</i> 2016 , <i>45</i> , 2673–2682.
Gao	2000	Gao, F. G.; Bard, A. J. Solid-State Organic Light-Emitting Diodes Based on Tris(2,2'-bipyridine)ruthenium(II) Complexes. <i>J. Am. Chem. Soc.</i> 2000 , <i>122</i> , 7426–7427.
Gershenzon	1961	Gershenzon, M.; Mikulyak, R. M. Electroluminescence at p-n Junctions in Gallium Phosphide. <i>J. Appl. Phys.</i> 1961 , <i>32</i> , 1338.
Grandke	1989	Grandke, T.; Ko, W. H. Sensors: A Comprehensive Survey. Vol. 1: Fundamentals and General Aspects. Wiley-VCH, 1989 .
Grimmeiss	1961	Grimmeiss, H. G.; Koelmans, H. Analysis of p-n Luminescence in Zn-Doped GaP. <i>Phys. Rev.</i> 1961 , <i>123</i> , 1939.
Gründler	2007	Gründler, P. Semiconductor Structures as Chemical Sensors. In <i>Chemical Sensors: An Introduction for Scientists and Engineers</i> ; Gründler, P., Ed.; Springer-Verlag: Berlin Heidelberg, 2007 ; Chapter 3, pp. 115–117.
Haber	1909	Haber, F.; Klemensiewicz, Z. Über Elektrische Phasengrenzkräfte. <i>Z. Phys. Chem.</i> 1909 , <i>67</i> , 385–431.
Haitz	2011	Haitz, R.; Tsao, J.Y. Solid-state lighting: ‘The case’ 10 years after and future prospects. <i>Phys. Status Solidi A</i> 2011 , <i>208</i> , 17–29. https://doi.org/10.1002/pssa.201026349 .
Halldorsson	2015	Halldorsson, S.; Lucumi, E.; Gómez-Sjöberg, R.; Fleming, R. M. Advantages and Challenges of Microcell Culture in Polydimethylsiloxane Devices. <i>Biosens. Bioelectron.</i> 2015 , <i>63</i> , 218–231.
Holonyak Jr.	1962	Holonyak Jr., N.; Bevacqua, S.F. Coherent (Visible) Light Emission From Ga(As _{1-x} P _x) Junctions. <i>Appl. Phys. Lett.</i> 1962 , <i>1</i> , 82.
Huh	2012	Huh, D.; Torisawa, Y. S.; Hamilton, G. A.; Kim, H. J.; Ingber, D. E. Microengineered Physiological Biomimicry Organs-on-Chips. <i>Lab Chip</i> 2012 , <i>12</i> , 2156–2164.
Hulanicki	1991	Hulanicki, A.; Glab, S.; Ingman, F. Chemical Sensors Definitions and Classification. <i>Pure Appl. Chem.</i> 1991 , <i>63</i> , 1247–1250.
Ielasi	2018	Ielasi, G.; Hui, P.; Palacio, C.; Muñoz, E.; Orellana, G. Silane control of the electron injection and oxygen sensitivity of dye-silane-GaN hybrid materials for luminescent chemical sensing. <i>Sens. Actuator B-Chem.</i> 2018 , <i>254</i> , 926–934.
Ielasi	2019	Ielasi, G.; Alcover, G.; Casellas, J.; de Graaf, C.; Orellana, G.; Reguero, M. Computer-aided design of short-lived phosphorescent Ru(II) polarity probes. <i>Dyes Pigm.</i> 2019 , <i>162</i> , 168–176.

Chapter 1 - Introduction

Iodice	2017	Iodice, P.; Senatore, A.; Langella, G.; Amoresano, A. Advantages of Ethanol-Gasoline Blends as Fuel Substitute for Last Generation SI Engines. <i>Environ. Prog. Sustain. Energy</i> 2017 . https://doi.org/10.1002/ep.12545 .
IUPAC Gold Book	1997	IUPAC. Compendium of Chemical Terminology, 2nd ed. (the "Gold Book"). Compiled by A. D. McNaught and A. Wilkinson. Blackwell Scientific Publications, Oxford (1997). XML on-line corrected version: http://goldbook.iupac.org (2006-) created by M. Nic, J. Jirat, B. Kosata; updates compiled by A. Jenkins. ISBN 0-9678550-9-8. https://doi.org/10.1351/goldbook .
Jagannathan	2016	Jagannathan, L.; Cuddapah, S.; Costa, M. Oxidative Stress Under Ambient and Physiological Oxygen Tension in Tissue Culture. <i>Curr. Pharmacol. Rep.</i> 2016 , 2, 64–72.
Jewett	2012	Jewett, S. A.; Makowski, M. S.; Andrews, B.; Manfra, M. J.; Ivanisevic, A. Gallium Nitride is Biocompatible and Non-Toxic Before and After Functionalization with Peptides. <i>Acta Biomater.</i> 2012 , 8, 728–733.
Johnson	1932	Johnson, W.C.; Parsons, J.B.; Crew, M.C. Nitrogen Compounds of Gallium. I, II. <i>J. Phys. Chem.</i> 1932 , 36, 2588.
Jung	2016	Jung, H. S.; Verwilst, P.; Kim, W. Y.; Kim, J. S. Fluorescent and Colorimetric Sensors for the Detection of Humidity or Water Content. <i>Chem. Soc. Rev.</i> 2016 , 45, 1242–1256.
Kaneta	2006	Kaneta, A.; Funato, M.; Narukawa, Y.; Mukai, T.; Kawakami, Y. Direct Correlation Between Nonradiative Recombination Centers and Threading Dislocations in InGaN Quantum Wells by Near-Field Photoluminescence Spectroscopy. <i>Phys. Status Solidi C</i> 2006 , 3, 1897–1901. https://doi.org/10.1002/pssc.200565403 .
Klymchenko	2013	Klymchenko, A. S.; Mely, Y. Fluorescent Environment-Sensitive Dyes as Reporters of Biomolecular Interactions. <i>Prog. Mol. Biol. Transl. Sci.</i> 2013 , 113, 35–58.
Lakowicz	2006	Lakowicz, J. R. Principles of Fluorescence Spectroscopy, 3rd ed.; Springer Science+Business Media, LLC: New York, NY, 2006 , Ch.2; e-ISBN 978-0-387-46312-4.
Lam	2009	Lam, H.; Kostov, Y. Optical Instrumentation for Bioprocess Monitoring. In <i>Optical Sensor Systems in Biotechnology</i> . Rao, G., Ed.; Springer-Verlag: Berlin Heidelberg, 2009 ; Chapter 1, pp 1–28.
Lanza	2014	Lanza, R. P.; Langer, R.; Vacanti, J. P. Principles of Tissue Engineering, 4th ed.; Academic Press: New York, 2014 .
Lee	2014	Lee, Y.-E. K.; Monson, E.; Brasuel, M.; Philbert, M. A.; Kopelman, R. PEBBLE Nanosensors for In Vitro Bioanalysis.

		In <i>Therapeutics and Advanced Biophotonics</i> ; Vo-Dinh, T., Ed.; CRC Press: Boca Raton, 2014 ; Chapter 22, pp 555–574.
Lippert	1957	Lippert, E. Spectroscopic Determination of the Dipole Moment of Aromatic Compounds in the First Excited Singlet State. <i>Z. Elektrochem., Ber. Bunsenges. Phys. Chem.</i> 1957 , <i>61</i> , 962–975.
López-Gejo	2010	López-Gejo, J.; Arranz, A.; Navarro, A.; Palacio, C.; Muñoz, E.; Orellana, G. Microsensors Based on GaN Semiconductors Covalently Functionalized With Luminescent Ru(II) Complexes, <i>J. Am. Chem. Soc.</i> 2010 , <i>132</i> , 1746–1747.
Lopez-Gejo	2011	Lopez-Gejo, J.; Navarro-Tobar, A.; Arranz, A.; Palacio, C.; Muñoz, E.; Orellana, G. Direct Grafting of Long-Lived Luminescent Indicator Dyes to GaN Light-Emitting Diodes for Chemical Microsensor Development. <i>Appl. Mater. Interfaces</i> 2011 , <i>3</i> , 3846–3854.
Lumpkin	1990	Lumpkin, R. S.; Kober, E. M.; Worl, L. A.; Murtaza, Z.; Meyer, T. J. Metal-to-ligand charge-transfer (MLCT) photochemistry: experimental evidence for the participation of a higher lying MLCT state in polypyridyl complexes of ruthenium(II) and osmium(II). <i>J. Phys. Chem.</i> 1990 , <i>94</i> , 239–243. DOI: 10.1021/j100364a039.
MacArthur	2005	MacArthur, B. D.; Oreffo, R. O. C. Bridging the Gap. <i>Nature</i> 2005 , <i>433</i> , 19.
Machado	2014	Machado, V. G.; Stock, R. I.; Reichardt C. Pyridinium N-Phenolate Betaine Dyes. <i>Chem. Rev.</i> 2014 , <i>114</i> , 10429–10475.
Makowski	2011 a	Makowski, M.S.; Zemlyanov, D. Y.; Ivanisevic, A. Olefin Metathesis Reaction on GaN (0001) Surfaces. <i>Appl. Surf. Sci.</i> 2011 , <i>257</i> , 4625–4632.
Makowski	2011 b	Makowski, M. S.; Zemlyanov, D. Y.; Lindsey J. A.; Bernhard, J. C.; Hagen, E. M.; Chan, B. K.; Petersohn, A. A.; Medow, M. R.; Wendel, L. E.; Chen, D.; Canter, J. M.; Ivanisevic, A. Covalent Attachment of a Peptide to the Surface of Gallium Nitride. <i>Surf. Sci.</i> 2011 , <i>605</i> , 1466–1475.
Marcélis	2013	Marcélis, L.; Moucheron, C.; Kirsch-De Mesmaeker, A. Ru-TAP Complexes and DNA: From Photo-Induced Electron Transfer to Gene Photo-Silencing in Living Cells. <i>Phil. Trans. R. Soc. A</i> 2013 , <i>371</i> , 20120131.
Martí	2015	Martí, A. A. Metal Complexes and Time-Resolved Photoluminescence Spectroscopy for Sensing applications. <i>J. Photochem. Photobiol. A</i> 2015 , <i>307–308</i> , 35–47.
Maruska	1969	Maruska, H. P.; Tietjen, J. J. The Preparation and Properties of Vapor-Deposited Single Crystalline GaN. <i>Appl. Phys. Lett.</i> 1969 , <i>15</i> , 327.

Chapter 1 - Introduction

Mataga	1956	Mataga, N.; Kaifu, Y.; Koizumi, M. Solvent Effects upon Fluorescence Spectra and the Dipole moments of Excited Molecules. <i>Bull. Chem. Soc. Jpn.</i> 1956 ; 29; 465–470.
McCracken	2016	McCracken, K. E.; Yoon, J.-Y. Recent Approaches for Optical Smartphone Sensing in Resource-Limited Settings: A Brief Review. <i>Anal. Methods</i> 2016 , 8, 6591–6601.
Milián	2015	Milián, E.; Kamen, A. A. Current and Emerging Cell Culture Manufacturing Technologies for Influenza Vaccines. <i>Biomed. Res. Int.</i> 2015 , Article ID 504831, 11 pages.
Moreno-Bondi	2004	Moreno-Bondi, M.C.; Orellana, G.; Bedoya, M. Fibre Optic Sensors for Humidity Monitoring. In <i>Optical Sensors: Industrial, Environmental and Diagnostic Applications</i> ; Narayanaswamy, R.; Wolfbeis, O. S., Eds.; Springer: Berlin Heidelberg, 2004; Chapter 11, pp. 251–280, and references therein.
Muñoz	2014	Muñoz, P. Diseño e implementación de un sensor óptico de oxígeno ambiental integrable en teléfonos móviles inteligentes. <i>Proyecto Fin de Carrera ETSIT-UPM 2014</i> .
Nakajima	1971	Nakajima, A. Solvent Effect on the Vibrational Structures of Fluorescence and Absorption Spectra of Pyrene. <i>Bull. Chem. Soc. Jpn.</i> 1971 , 44, 3272–3277.
Nakamura	1991	Nakamura, S. GaN Growth Using GaN Buffer Layer. <i>Jpn. J. Appl. Phys.</i> 1991 , 30, 1705.
Nakamura	2000	Nakamura, S.; Pearton, S.; Fasol, G. The Blue Laser Diode: The Complete Story, 2nd ed; Springer-Verlag: Berlin Heidelberg, 2000.
Narayanaswamy	2004	Narayanaswamy, R.; Wolfbeis Otto S. Optical Sensors: Industrial Environmental and Diagnostic Applications (Springer Series on Chemical Sensors and Biosensors) 2004 Edition. Springer;
Nazeeruddin	2011	Nazeeruddin, M. K.; Baranoff, E.; Grätzel, M. Dye-Sensitized Solar Cells: A Brief Overview. <i>Sol. Energy</i> 2011 , 85, 1172–1178.
Onsager	1936	Onsager, L. Electric Moments of Molecules in Liquids. <i>J. Am. Chem. Soc.</i> 1936 ; 58; 1486–1493.
Oomen	2016	Oomen, P. E.; Skolimowski, M. D.; Verpoorte, E. Implementing Oxygen Control in Chip-Based Cell and Tissue Culture Systems. <i>Lab Chip</i> 2016 , 16, 3394–3414.
Orellana	1998	Orellana, G.; García-Fresnadillo, D.; Marazuela, M.D.; Moreno-Bondi, M.C.; Delgado, J.; Sicilia, J.M. Fiber-optic chemical sensors: From molecular engineering to environmental analytical chemistry in the field, in <i>Monitoring of Water Quality: The Contribution of Advanced Technologies</i> , F. Colin, P. Queauviller (Eds.), Elsevier, Amsterdam, 1998 ; pp 103–116.

Chapter 1 - Introduction

Orellana	2004 a	Orellana, G. Luminescent optical sensors, <i>Anal. Bioanal. Chem.</i> 2004 , 379, 344–346.
Orellana	2004 b	Orellana, G.; García-Fresnadillo, D. In <i>Optical Sensors: Industrial, Environmental and Diagnostic Applications</i> ; Narayanaswamy, R.; Wolfbeis, O. S., Eds.; Springer: Berlin Heidelberg, 2004 ; Chapter 13, pp. 309–357, and references therein.
Orellana	2006	Orellana G. FLUORESCENCE-BASED SENSORS. In: <i>Optical Chemical Sensors</i> . NATO Science Series II: Mathematics, Physics and Chemistry, vol 224. Baldini F., Chester A., Homola J., Martellucci S., Eds.; Springer: Dordrecht, NL, 2006 . https://doi.org/10.1007/1-4020-4611-1_6
Orellana	2011	Orellana, G.; Cano-Raya, C.; López-Gejo, J.; Santos, A. R. Online Monitoring Sensors. In <i>Treatise on Water Science</i> ; Wilderer P., Ed.; Elsevier: Oxford, UK, 2011 ; Vol. 3, Chapter 59, pp 221–262.
Orellana	2012	Orellana, G.; Muñoz, E.; Gil-Herrera, L.K.; Muñoz, P.; López-Gejo, J.; Palacio, C. Integrated Luminescent Chemical Microsensors Based on GaN LEDs for Security Applications Using Smartphones. <i>Proc. SPIE</i> 2012 , 8545, 85450J.
Orellana	2014	Orellana, G.; López-Gejo, J.; Pedras, B. Silicone Films for Fiber-Optic Chemical Sensing. In <i>Concise Encyclopedia of High Performance Silicones</i> ; Tiwari, A.; Soucek, M. D., Eds.; Scrivener Publishing: Salem, MA, 2014 ; Chapter 22, pp 339–354.
Pankove	1971	Pankove, J.I.; Miller, E.A.; Richman, D.; Berkeyheiser, J.E. Electroluminescence in GaN. <i>J. Lumin</i> 1971 , 4, 63.
Pankove	1973	Pankove, J. I. Luminescence in GaN. <i>J. Lumin</i> 1973 , 7, 114.
Paris	1959	Paris, J. P.; Brandt, W. W. Charge Transfer Luminescence of a Ruthenium II Chelate. <i>J. Am. Chem. Soc.</i> 1959 , 81, 5001–5002.
Perdue	2011	Perdue, M. L. The Future of Cell Culture-Based Influenza Vaccine Production. <i>Expert Rev. Vaccines</i> 2011 , 10, 1183–1194.
Phelan	2017	Phelan, K.; May, K. M. Mammalian Cell Tissue Culture Techniques. <i>Curr. Protoc. Mol. Biol.</i> 2017 , 117, A.3F.1–A.3F.23.
Piñeiro	2015	Piñeiro, L.; Novo, M.; Al-Soufi, W. Fluorescence Emission of Pyrene in Surfactant Solutions. <i>Adv. Colloid Interface Sci.</i> 2015 , 215, 1–12.
Potje-Kamloth	2008	Potje-Kamloth, K. Semiconductor Junction Gas Sensors. <i>Chem. Rev.</i> 2008 , 108, 367–399.
Pourtois	2004	Pourtois, G.; Beljonne, D.; Moucheron, C.; Schumm, S.; Kirsch-De Mesmaeker, A.; Lazzaroni, R.; Brédas, J.-L. Photophysical properties of ruthenium(II) polyazaaromatic compounds: a theoretical insight. <i>J. Am. Chem. Soc.</i> 2004 , 126, 683–692. DOI: 10.1021/ja034444h.

Chapter 1 - Introduction

Puntoriero	2011	Puntoriero, F.; Sartorel, A.; Orlandi, M.; La Ganga, G.; Serroni, S.; Bonchio, M.; Scandola, F.; Campagna, S. Photoinduced Water Oxidation Using Dendrimeric Ru(II) Complexes as Photosensitizers. <i>Coord. Chem. Rev.</i> 2011 , 255, 2594–2601.
Reichardt	2010	Reichardt, C.; Welton, T. Solvents and Solvent Effects in Organic Chemistry, 4th ed; Wiley-VCH: Weinheim, 2010 .
Ren	2011	Ren, F.; Pearton, S. J. Semiconductor Device-Based Sensors for Gas, Chemical, and Biomedical Applications; CRC Press: Boca Raton, 2011 .
Ribeiro dos Santos	2014	Ribeiro dos Santos, A. Design, Synthesis and Photochemistry of Luminescent Ru(II) Complexes with Polyazaheteroaromatic Ligands for Environmental Sensing Applications. <i>Doctoral dissertation</i> 2014 .
Ribeiro dos Santos	2015	Ribeiro Santos, A.; Escudero, D.; González, L.; Orellana, G. Unravelling The Quenching Mechanisms Of A Luminescent Ru(II) Probe For Cu(II). <i>Chem. Asian J.</i> 2015 , 10, 622–629, DOI: 10.1002/asia.201403340
Richman	1963	Richman, D. Dissociation pressures of GaAs, GaP and InP and the nature of III-V melts. <i>J. Phys. Chem. Solids</i> 1963 , 24, 1131.
Roda	2016	Roda, A.; Michelini, E.; Zangheri, M.; Di Fusco, M.; Calabria, D.; Simoni, P. Smartphone-Based Biosensors: A Critical Review and Perspectives. <i>Trends Analyt. Chem.</i> 2016 , 79, 317–325.
Seddon	1984	Seddon, E. A.; Seddon, K. R. <i>The Chemistry of Ruthenium</i> , vol. 19; Clark, R. J. H., Ed.; Elsevier: Amsterdam, NL, 1984 , pp. 1228-1236. ISBN: 9781483289908 (e-book).
Semenza	2007	Semenza, G. L. Life with Oxygen. <i>Science</i> 2007 , 318, 62–64.
Seong	2013	Seong, T.-Y.; Han, J.; Amano, H.; Morkoç, H. III-Nitride Based Light Emitting Diodes and Applications; Springer: Dordrecht, 2013 .
Starkiewicz	1962	Starkiewicz, J.; Allen, J. W. Injection Electroluminescence at p-n Junctions in Zinc-Doped Gallium Phosphide. <i>J. Phys. Chem. Solids</i> 1962 , 23, 881.
Steinhoff	2003	Steinhoff, G.; Purrucker, O.; Tanaka, M.; Stutzmann, M., Eickhoff, M. Al _x Ga _{1-x} N-A New Material System for Biosensors. <i>Adv. Funct. Mater.</i> 2003 , 13, 841–846.
Sujitraj	2019	Sujitraj, S.; Mengyuan, L.; Qijun, S. New Luminescent Probe For The Selective Detection Of Dopamine Based On In Situ Prepared Ru(II) Complex-Sodium Dodecyl Benzyl Sulfonate Assembly. <i>J. Photochem. Photobiol. A</i> 2019 , 371, 128–135.
Sun	2013	Sun, Q.; Mosquera-Vazquez, S.; Daku, L. M.; Guénée, L.; Goodwin, H. A.; Vauthey, E.; Hauser, A. Experimental

		evidence of ultrafast quenching of the $^3\text{MLCT}$ luminescence in ruthenium(II) tris-bipyridyl complexes via a ^3dd state. <i>J. Am. Chem. Soc.</i> 2013 , <i>135</i> , 13660–13663. DOI: 10.1021/ja407225t.
Sun	2015	Sun, S.; Ungerböck, B.; Mayr, T. Imaging of Oxygen in Microreactors and Microfluidic Systems. <i>Methods Appl. Fluoresc.</i> 2015 , <i>3</i> , 034002.
Terracciano	2013	Terracciano, M.; Rea, I.; Politi, J.; De Stefano, L. Optical Characterization of Aminosilane-Modified Silicon Dioxide Surface for Biosensing. <i>J. Europ. Opt. Soc. Rap. Public.</i> 2013 , <i>8</i> , 13075.
Thompson	2013	Thompson, D. W.; Ito, A.; Meyer, T. J. [Ru(bpy) ₃] ²⁺ and Other Remarkable Metal-to-Ligand Charge Transfer (MLCT) Excited States. <i>Pure Appl. Chem.</i> 2013 , <i>85</i> , 1257–1305.
Tsai	2003	Tsai, A. G.; Johnson, P. C.; Intaglietta, M. Oxygen Gradients in the Microcirculation. <i>Physiol. Rev.</i> 2003 , <i>83</i> , 933–963.
Ueda	2017	Ueda, D. Properties and Advantages of Gallium Nitride. In <i>Power GaN Devices: Materials, Applications and Reliability</i> ; Meneghini, M., Meneghesso, G., Zanoni, E., Eds.; Springer: Cham, 2017 ; Chapter 1, 1–26.
Urriza-Arsuaga	2019 a	Urriza-Arsuaga, I.; Bedoya, M.; Orellana, G. Luminescent sensor for O ₂ detection in biomethane streams. <i>Sens. Actuat. B: Chem.</i> 2019 , <i>279</i> , 458–465.
Urriza-Arsuaga	2019 b	Urriza-Arsuaga, I.; Bedoya, M.; Orellana, G. Unprecedented Reversible Real-Time Luminescent Sensing of H ₂ S in the Gas Phase. <i>Anal. Chem.</i> 2019 , <i>91</i> , 2231–2238
Valeur	2001 a	Valeur, B. Effect of Polarity on Fluorescence Emission. Polarity Probes. In: <i>Molecular Fluorescence: Principles and Applications</i> , 1st ed, Wiley-VCH, 2001 ; 200–225
Valeur	2001 b	Valeur, B. Molecular Fluorescence: Principles and Applications. Wiley-VCH Verlag GmbH: Weinheim, 2001 ; Chapter 7, pp 200–225.
Valeur	2011	Valeur, B; Berberan-Santos, M. N. A Brief History of Fluorescence and Phosphorescence before the Emergence of Quantum Theory. <i>J. Chem. Educ.</i> 2011 , <i>88</i> , 731–738. DOI: 10.1021/ed100182h.
Van Houten	1976	Van Houten, J.; Watts, R. J. Temperature dependence of the photophysical and photochemical properties of the tris(2,2'-bipyridyl)ruthenium(II) ion in aqueous solution. <i>J. Am. Chem. Soc.</i> 1976 , <i>98</i> , 4853–4858. DOI: 10.1021/ja00432a028.
Vashist	2014 a	Vashist, S. K.; Lam, E.; Hrapovic, S.; Male, K. B.; Luong, J. H. T. Immobilization of Antibodies and Enzymes on 3-Aminopropyltriethoxysilane-Functionalized Bioanalytical

Chapter 1 - Introduction

		Platforms for Biosensors and Diagnostics. <i>Chem. Rev.</i> 2014 , 114, 11083–11130.
Vashist	2014 b	Vashist, S. K.; Mudanyali, O.; Schneider, E. M.; Zengerle, R.; Ozcan, A. Cellphone-Based Devices for Bioanalytical Sciences. <i>Anal. Bioanal. Chem.</i> 2014 , 406, 3263–3277.
Vashist	2015	Vashist, S. K.; Luppa, P. B.; Yeo, L. Y.; Ozcan, A.; Luong, J. H. Emerging Technologies for Next-Generation Point-of-Care Testing. <i>Trends Biotechnol.</i> 2015 , 33, 692–705.
Wallin	2005	Wallin, S.; Davidsson, J.; Modin, J.; Hammarström, L.; Femtosecond Transient Absorption Anisotropy Study on $[\text{Ru}(\text{bpy})_3]^{2+}$ and $[\text{Ru}(\text{bpy})(\text{py})_4]^{2+}$. Ultrafast Interligand Randomization of the MLCT State. <i>J. Phys. Chem. A</i> 2005 , 109, 4697–4704.
Wang	2014	Wang, X.; Wolfbeis, O. S. Optical Methods for Sensing and Imaging Oxygen: Materials, Spectroscopies and Applications. <i>Chem. Soc. Rev.</i> 2014 , 43, 3666–3761.
Web developer.android.com	2017	Sensors Overview. (2017, January 24). Retrieved from https://developer.android.com/guide/topics/sensors/sensors_overview.html .
Web eia.gov	2016	Almost all U.S. gasoline is blended with 10% ethanol. (2016, May 4). Retrieved from https://www.eia.gov/todayinenergy/detail.php?id=26092 .
Web photobiology.info	2017	Visser, J. W. G. A.; Rolinski, J. O. Basic Photophysics. Retrieved from http://photobiology.info/Visser-Rolinski.html .
Web un.org	2013	Deputy UN chief calls for urgent action to tackle global sanitation crisis. (2013, March 21). Retrieved from http://www.un.org/apps/news/story.asp?NewsID=44452&Cr=sanitation&Cr1=#.WeNO7zBx1Pb
Welker	1952	Welker, H. Über Neue Halbleitende Verbindungen. <i>Z. Naturforsch</i> 1952 , 7a, 744.
Wiedemann	1888	Wiedemann, E. Über Fluorescenz und Phosphorescenz, I. Abhandlung [On fluorescence and phosphorescence, first paper], <i>Annalen der Physik</i> 1888 , 34, 446–463. From page 447: "Ich möchte für diese zweite Art der Lichterregung, für die uns eine einheitliche Benennung fehlt, den Namen Luminescenz vorschlagen, und Körper, die in dieser Weise leuchten, luminescirende nennen." [For this second type of light excitation, for which we lack a consistent name, I would like to suggest the name "luminescence", and call "luminescing" bodies that glow in this way.]
Winnik	1993	Winnik, F. M. Photophysics of Preassociated Pyrenes in Aqueous Polymer Solutions and in Other Organized Media. <i>Chem. Rev.</i> 1993 , 93, 587–614.

Chapter 1 - Introduction

Wolfbeis	2013	Wolfbeis, O. S. Editorial: Probes, Sensors, and Labels: Why is Real Progress Slow? <i>Angew. Chem. Int. Ed.</i> 2013 ; 52, 9864-9865.
Zelinskii	1956	Zelinskii, V. V.; Kolobkov, V. P.; Pikulik, L. G. The Spectral Relation for Luminescence Yield. <i>Opt. i Spekt.</i> 1956 ; 1; 161-167.
Zhang	2020	Zhang, X.; Qiu, J.; Li, X.; Zhao, J.; Liu, L. Complex Refractive Indices Measurements of Polymers in Visible and Near-Infrared Bands. <i>Appl. Opt.</i> 2020 , 59, 2337-2344.
Zhou	2016	Zhou, J.; Ma, H. Design Principles of Spectroscopic Probes for Biological Applications. <i>Chem. Sci.</i> 2016 , 7, 6309-6315.
Zhu	2012	Zhu, M.; Lerum, M. Z.; Chen, W. How To Prepare Reproducible, Homogeneous, and Hydrolytically Stable Aminosilane-Derived Layers on Silica. <i>Langmuir</i> 2012 , 28, 416-423.

Chapter 1 - Introduction

2. GAN-SILANE-DYE HYBRID MATERIALS FOR LUMINESCENT CHEMICAL SENSING

"I had no confidence in inventing the blue LED, I just wanted my PhD"

Shuji Nakamura

2.1. Introduction

Organic-inorganic hybrids, an intimate synergic mix of two materials with properties that strengthen the sum of the original ones or are even completely new, have been exploited by Nature for a long time (fine examples are bone, teeth and nacre). Mankind also profited from their combined properties, the most famous example of which is probably the so-called Blue Maya pigment (**Figure 20**): a naturally derived organic dye (blue indigo) that, encapsulated into palygorskite, can withstand biodegradation (e.g. from its deposition in *a fresco* painting twelve centuries ago) as well as acids, alkalis and organic solvents [Reyes-Valerio 1993]. This material, similarly to others that have been of high interest for industrial applications in the last 70 years such as paintings or polymer composites, belongs to the “class I” hybrids [Sanchez 1994]. This term encompasses compositions kept together in a physical way by weak bonds. Conversely, materials in which the two components are adjoined by *covalent* bonds are called “class II” hybrids. The latter type, that underlines the fundamental role of the organic-inorganic interface [Gómez-Romero 2004], is attracting more attention lately. Numerous products belonging to this group are already commercially available [Sanchez 2005].

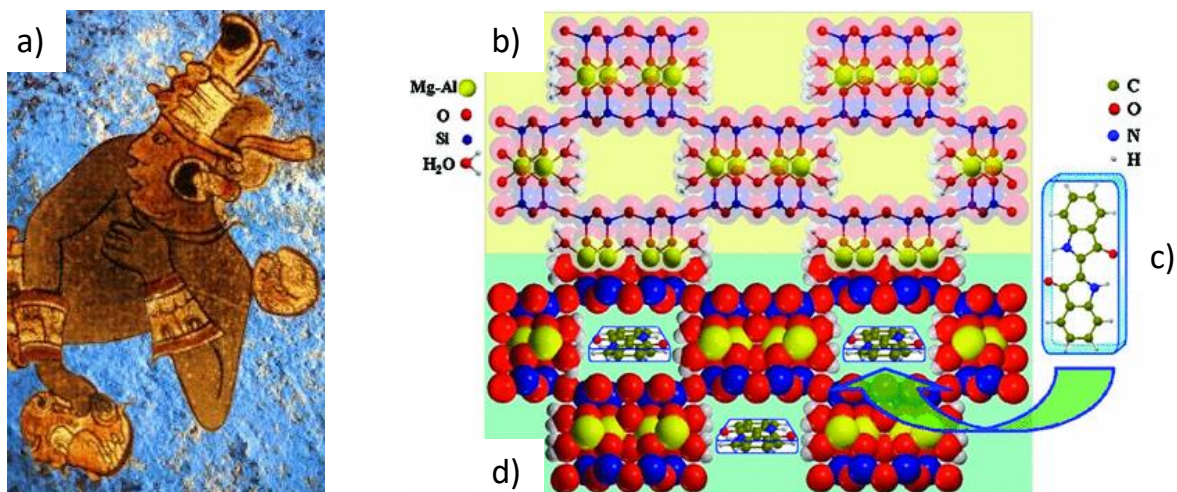


Figure 20. a) Painting of a warrior with Azul Maya on the background. Source: Constantino Reyes, free to use. b) The structure of palygorskite projected on the (001) plane; c) the indigo molecule; d) encapsulation of indigo inside the nano-tunnels of palygorskite forms the Maya Blue pigment (zeolitic H₂O not shown for sake of clarity). Reprinted from [Quartieri 2015] with permission.

Inorganic semiconductors have often been used in hybrid functional materials development, particularly in applications such as light harvesting and chemical sensing [Gründler 2007, Potje-Kamloth 2008, Ren 2011]. Silicon, due to the advanced degree of its manufacturing technology, has been the predominant one so far, but many others are also of high interest. GaN and its alloys are among the leading ones because they are exceptionally suited for high-speed/high-power electronics [Flack 2016], high efficiency power transmission [Ueda 2017], and light-emitting devices due to their very efficient blue electroluminescence (other colors upon proper In alloying) [Nakamura 2000]. Specifically, in the field of optical sensors GaN is especially important because, due to its wide band gap of 3.4 eV, is the material of choice for high energy - UV to green - light emitting diodes (LEDs), which can be used as photoexcitation source of many luminophores. The necessary n-type and p-type doping are obtained, respectively, with silicon or oxygen and with magnesium [Reshchikov 2005]. Moreover GaN is biocompatible [Jewett 2012] and chemically stable under physiological conditions [Steinhoff 2003], making it very interesting for biosensing applications. Although chemically inert, it is possible to functionalize its surface with complex molecules (indicator dyes, peptides, proteins, DNA) following surface activation [Baur 2005, Arranz 2008, Makowski 2011 a, Makowski 2011 b].

Silanes are amongst the most common coupling agents for functionalizing materials. They are widely used in industry as adhesives and sealants, applying μm to mm thick layers for changing the surface properties or increasing adhesion of polymers onto metals, glass, etc [Arkles 1977]... Beside this "macroscopic" applications, materials can be functionalized with thinner coating, down to a subnanometer-thick monolayer, for attaching (bio)molecules for finer control of surface properties [Vashist 2014]. Of the hundreds of commercially available silanes, the majority are based on the general formula $(X)_3\text{SiY}$, where X is an alkoxy (-OCH₃ or -OCH₂CH₃) or halogen (-Cl) ligand and Y is an organofunctional group (aminopropyl, methacryloxy, glycidoxyl, vinyl, etc.). The X part is responsible to the attachment to the inorganic material (metal, oxide, etc...) while the Y side bears the functionality for coupling to the organic part (see **Figure 21**).

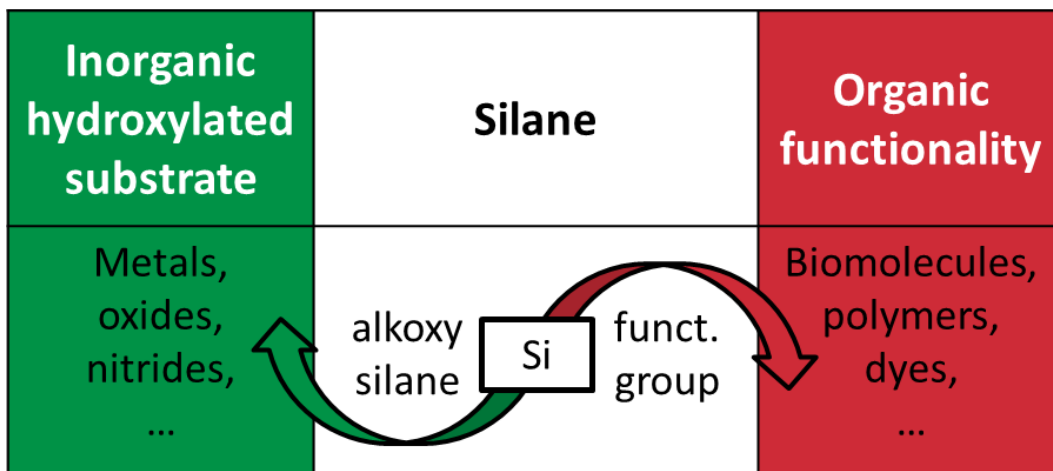


Figure 21. How functional alkoxy silane molecules work. Adapted from [Materne 2006] with permission.

In particular, amino-terminated silanes are widely used because they allow facile coupling (with molecules containing suitable moieties, e.g. COOH), increase surface hydrophilicity and facilitate the formation of siloxane bonds with surface -OH (because of self-catalysis, as explained below) [White 2000].

The most used and studied aminosilane is 3-aminopropyltriethoxysilane (APTES). In general, an APTES molecule is at first hydrolyzed in solution; then, when contacted with a surface rich in hydroxyl groups three possible bonding mechanisms can follow [Vashist 2014] (see **Figure 22**):

- 1) The silanol or the amine of APTES forms a hydrogen bond with the surface hydroxyl groups.
- 2) H-bonded APTES silanols can get covalently attached by SN2 exchange with loss of ethanol. Reaction of free APTES molecules in solution with a surface-bound APTES, leads to vertical polymerization with formation of multilayers.
- 3) If two or more APTES molecules are covalently attached in close proximity, condensation reaction between neighbors leads to horizontal polymerization (an example of the so-called self-assembled monolayer, SAM).

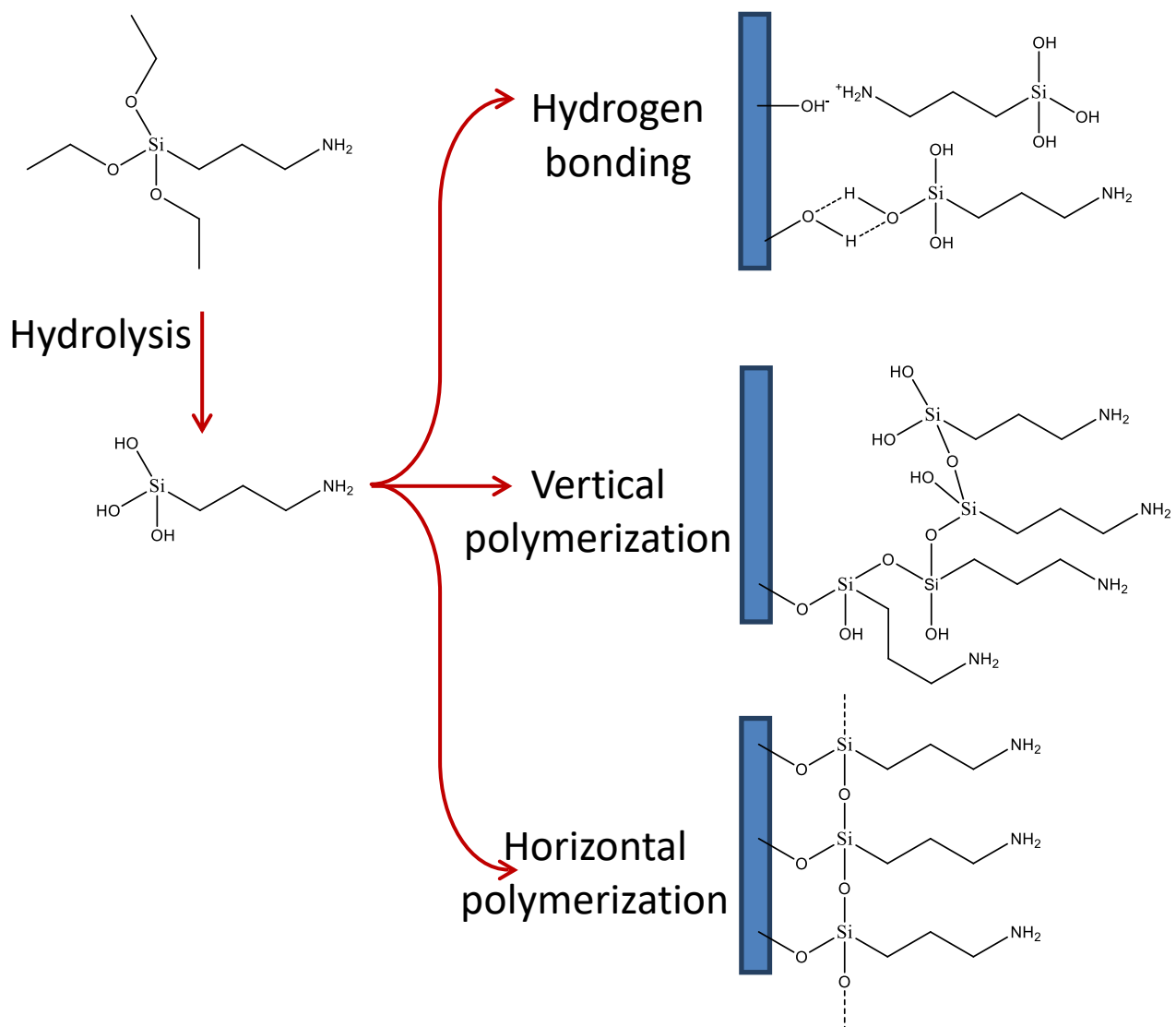


Figure 22. The three possible bonding mechanisms of APTES onto a hydroxylated surface.

While these general mechanisms work for all different aminoalkyl trialkoxysilanes, their particular structure determines their *O*-substitution rate and hence the thickness of the GaN surface coating. Two factors play a key role:

- the goodness of the leaving group (for example hydroxylation of ethoxy groups is 6-10 times slower than that of methoxy groups [Arkles 1992]), and
- the presence of an amino group in a distal position that favors intramolecular nucleophilic catalysis. It is well documented that the amino group of an

aminoalkyl alkoxy silane is sometimes an in-built catalyst for the siloxane bond formation [Kanan 2002, Zhu 2012]. When the amine is located in γ position with respect to the silicon atom, it plays both as an *inter-* and *intra-*molecular catalyst, the latter by formation of a five-membered ring that becomes an excellent leaving group after protonation by traces of water or by the surface OH groups [Chiang 1980].

Particular silanes possess only one or two alkoxy groups in order to limit multilayer formation due to polymerization between silane monomers. Moreover, there are more “advanced” cyclic azasilanes, which exploit the energy difference between the inherent Si-N bond and the Si-O bond that can form with surface O⁻, so as to completely avoid self-polymerization. In our case, however, we need to fully coat with a “thick” layer (more than a monolayer) substrates (GaN) that contain few hydroxyl groups, thus we selected 3-alkoxy silanes (the structure of the six silanes used in this work is depicted below in **Chart 1**) that are expected to show high polymerization for obtaining high surface coverage.

The GSOLFA group recently developed a route to exploit ω -aminosilane coupling agents to directly tether luminescent Ru(II) dyes for optochemical sensing onto the surface of GaN wafers and GaN-based blue LED chips (**Figure 23** and **Figure 24**) [López-Gejo 2011]. The functionalization route includes: i) hydroxylation of the GaN wafers or LEDs by oxygen plasma treatment; ii) aminosilanization of the activated surface; iii) reaction of the aminated surfaces with the hexa(sulfonyl chloride) derivative of the tris[(4,7-diphenyl)-1,10-phenanthroline]ruthenium(II) dye. Direct functionalization of the LED surface allows the highest possible miniaturization, being the light source in direct contact with the sensitive luminescent layer, which is also in the thinnest possible format. Coupling these functionalized LEDs with miniaturized detectors and electronics should lead to the development of integrated microcircuits with intrinsic gas-sensing features [Orellana 2012]. Moreover, GaN surface functionalization helps profiting from the semiconductor emitted light: in planar GaN LEDs, due to the very high refractive index of the semiconductor, more than 60% of the emitted photons remain trapped in the chip [Seong 2013].

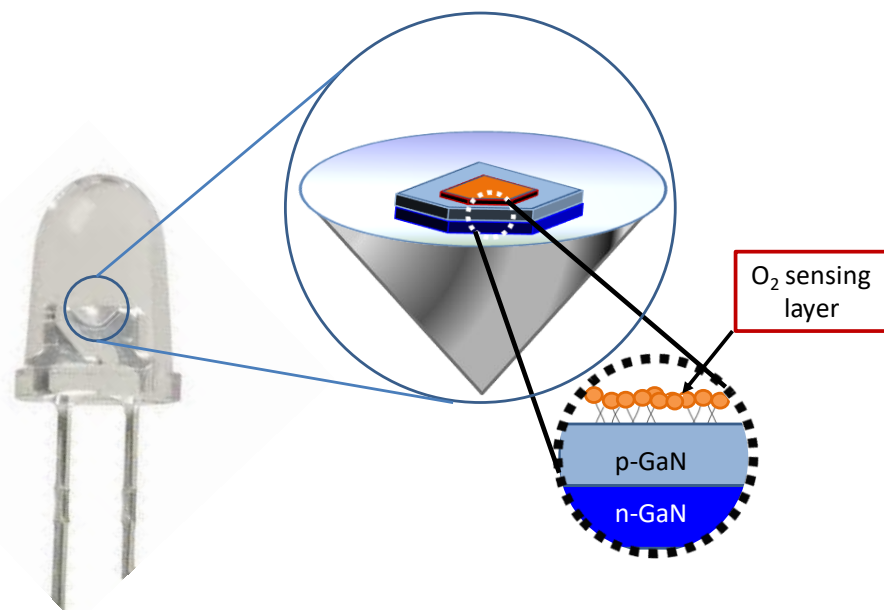


Figure 23. Artistic depiction of the O₂-sensitive LEDs

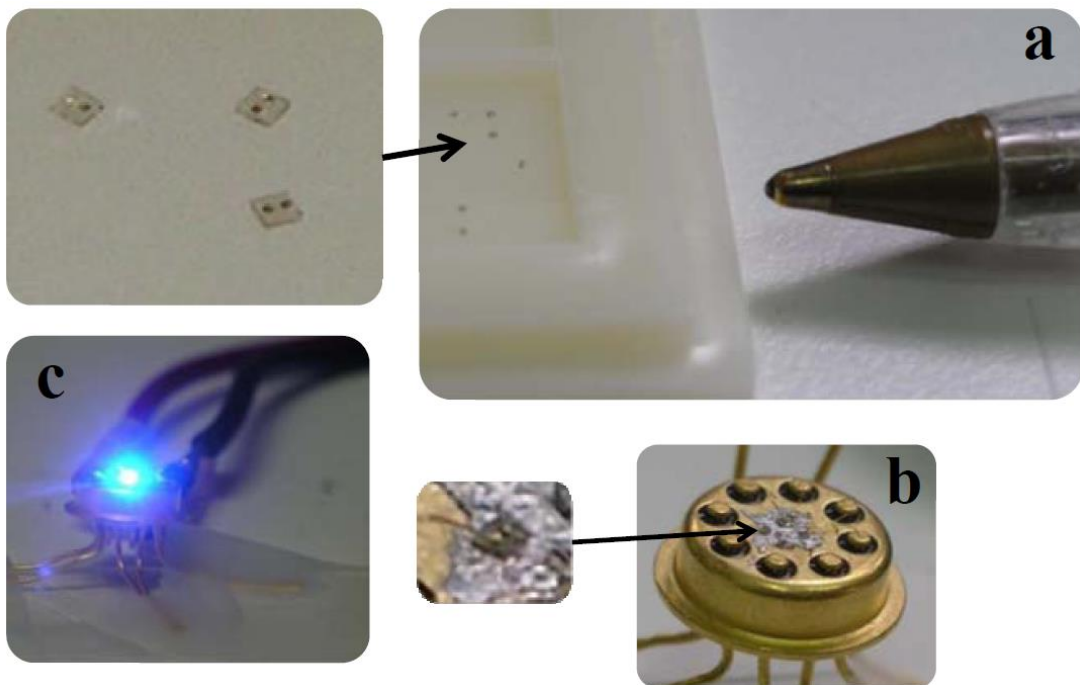


Figure 24. Pictures of the commercial functionalized LEDs before (a) and after (b) attachment of connectors. (c) Operating LED. Reprinted with permission from [López-Gejo 2011]. Copyright 2011 American Chemical Society.

However, we found that while functionalized p-doped GaN yielded hybrids with luminescence lifetimes and response to O₂ similar to known Ru(II) polypyridyl-based sensors [Mingoarraz 1995, McGee 2009], the n-GaN hybrid materials showed much shorter emission lifetime and displayed virtually no O₂ sensitivity. Our hypothesis, based on the estimated relative position of the energy bands of n- and p-GaN *vs* the Ru(II) complex 3+/2+* redox potential, was the occurrence of a photoinduced electron transfer (PET) quenching from the triplet metal-to-ligand d-π* excited state of the dye to the conduction band (CB) of the semiconductor [López-Gejo 2011].

While manufacturing of chemosensitive LEDs was a milestone, the unexpected quenching process observed with n-GaN limits the slate of possible optical sensor structure and applications. For example, the current push for a brightness increase has led to propose coupling of the GaN chip quantum wells with surface plasmons to boost the chip internal quantum efficiency by energy transfer. As p-GaN cannot be doped as highly as n-GaN, the coupling would greatly benefit from deposition of the plasmonic metal on top of the latter and using it as the outermost layer of the chip. This “reverse” structure, with the n-GaN layer on top (**Figure 25**), is characterized of better current injection, good heat dissipation, and enhanced reliability against electrostatic discharge [Kim 2013].

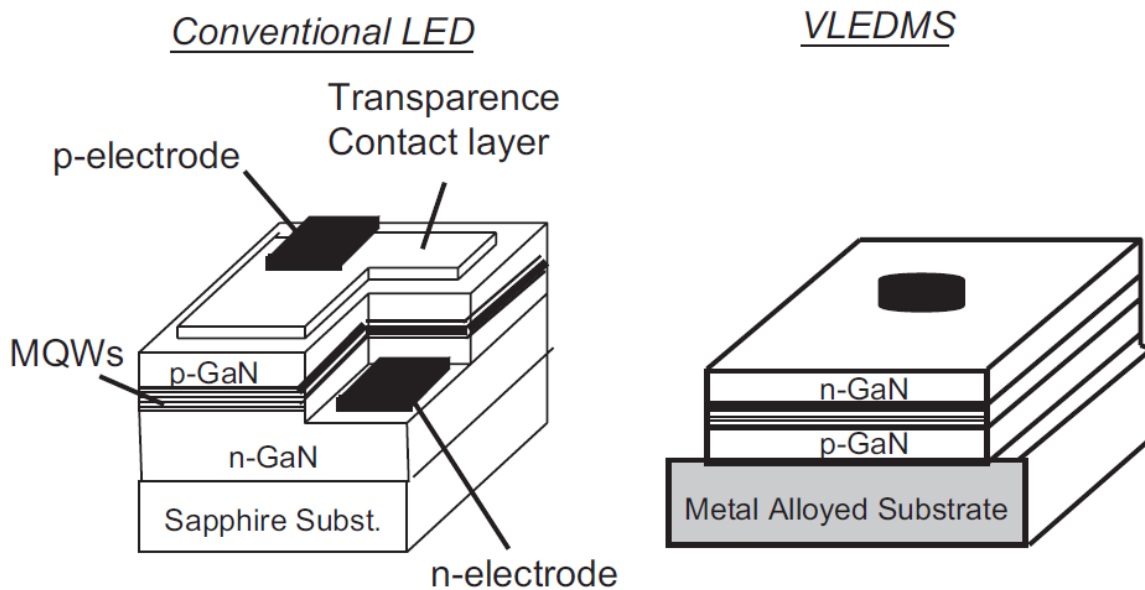


Figure 25. Schematic diagram of conventional GaN LED's on sapphire substrate and high-voltage GaN vertical light emitting diodes on metal alloyed substrate (VLEDMS). Reprinted from [Tran 2007] with permission. Copyright 2007 John Wiley and Sons.

Another interesting application is in the field of fabricating active-matrix GaN microdisplays. The fabrication of high-resolution, small dot pitch, high-brightness microdisplays, of interest for producing wearable devices, has been demonstrated feasible hybridizing using a GaN LED array [Templier 2016]. One of the main problems, namely adding highly saturated green and red emission, can be solved using color converters: using blue emission and down-converting it into green or red by photoluminescence using phosphor materials. It has been shown that using this approach, highly saturated red can be obtained using quantum dots converters [Sanchot 2015]. However, a difficulty to obtain a full color display with this approach is then to achieve patterning such converters with a small pixel pitch. This could be solved using our approach of direct functionalization of the emitting pixels.

Moreover, given the vast election of materials used for LEDs manufacturing, it would be ideal to be able to use as many luminescent indicator dyes as possible with a plurality of electroluminescent semiconductor surfaces. Therefore, the aim of this research is twofold: to confirm the PET phenomenon and to find ways to overcome the associated luminescence quenching. Because most electron transfer processes are dependent on distance, we have confirmed the occurrence of the PET by investigating how our unwanted process is influenced by the aminosilane layer thickness and, eventually, suppressed by using tailored thick layers. Needless to say, the buffer silane thickness also influences the O₂ sensing features of the hybrid LEDs.

2.2. Materials and methods

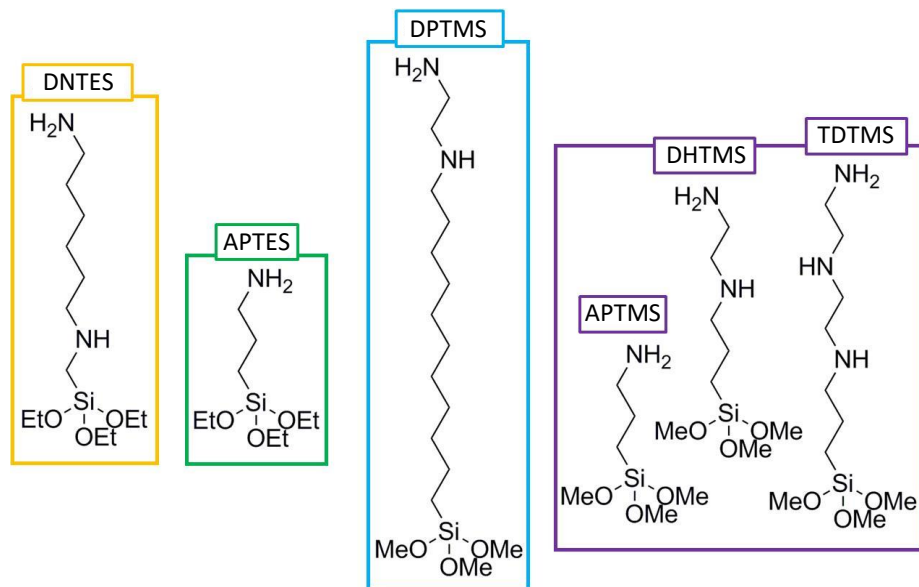
2.2.1. Materials

Water was purified with a Millipore Direct-Q system (Bedford, MA). HPLC grade solvents were purchased from Fisher Scientific (Loughborough, UK) and used without further purification. H₂SO₄ (96–98%), H₂O₂ (30%) and triethylamine (>99%) were purchased from Scharlab (Barcelona, ES); SOCl₂ (>99.7%) was purchased from Alfa Aesar (Haverhill, MA). 3-aminopropyltriethoxysilane (APTES, 98%) and 3-aminopropyltrimethoxysilane (APTMS, 98%) were purchased from Alfa Aesar; 2,9-diazanonyltriethoxysilane (DNTES, 95%) and 12,15-diazapentadecyltrimethoxysilane (DPTMS, 95%) were purchased from Gelest (Morrisville, PA); 4,7-diazzaheptyltrimethoxysilane (DHTMS, 97%) and 4,7,10-triazadecyltrimethoxysilane (TDTMS, 95%) were purchased from Abcr (Karlsruhe, DE).

2.2.2. Silanization of the n-GaN Surface

The procedure sits on our previous work [López-Gejo 2011], with some changes as follows. Si-doped (carrier concentration $> 1 \times 10^{18} \text{ cm}^{-3}$), 4 μm thick, n-type GaN wafers deposited on sapphire (oriented in the C-plane(0001) ($\pm 0.5^\circ$), Light Materials Co., Henan, PRC), were diced into 1- cm^2 samples. The latter were cleaned with “piranha” solution [3:1 $\text{H}_2\text{SO}_4:\text{H}_2\text{O}_2$] for 20 min at 80 °C (caution: “piranha” solution is highly corrosive and an extremely powerful oxidizer. To prevent potential explosions, always add peroxide to acid and use a 30% or less solution of H_2O_2 . The solution reacts violently with plastic containers and organic solvents), and then rinsed thoroughly with ultrapure Type I water under sonication, followed by overnight drying in an oven (Heraeus: Hanau, DE) at 50 °C. To carry out the first step of the functionalization procedure, an oxygen plasma treatment (PlasmaPro NGP80, Oxford Instruments, Abingdon, UK) was applied for 10 min to the substrates (O_2 flow = 7 sccm; radio-frequency applied power = 50 W; pressure = 60 mTorr; time = 10 min; direct-current bias measured under those conditions = 108.9 V). After the plasma treatment, each sample was introduced individually in 3.5 mL of a 10 mM aminosilane (DNTEs, APTES, DPTMS, APTMS, DHTMS or TDTMS; see **Chart 1** for the corresponding structures) solution in dry toluene for 44 h. After silanization, the treated samples were sonicated in anhydrous toluene for 5 min to remove any adhered reactant on the surface. The samples were kept in anhydrous toluene until use (1 day maximum).

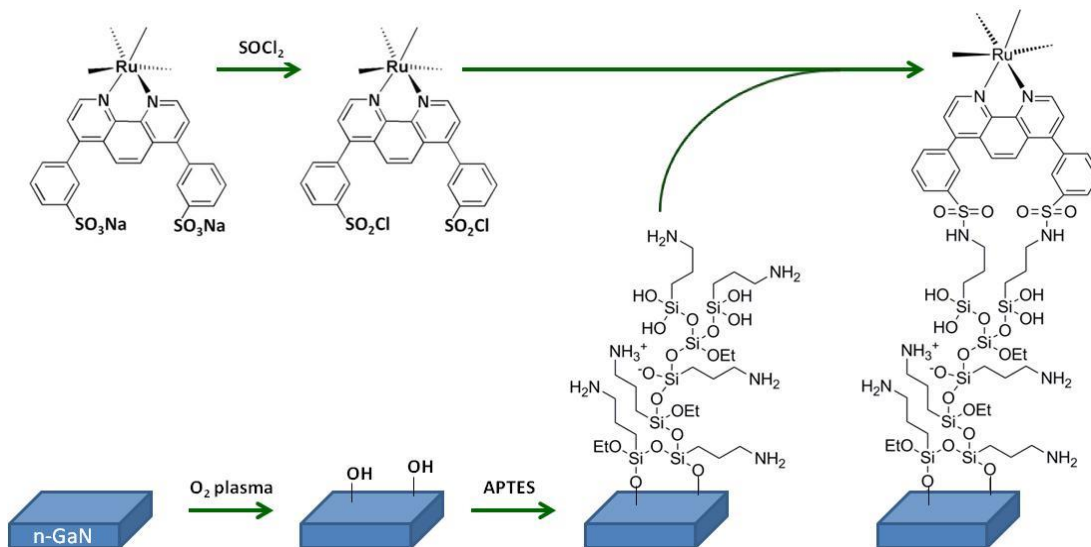
Chart 1. Structure of the aminosilanes selected to build the functionalization layer onto the plasma-treated GaN surface. The four colored boxes separate them into groups with different reactivity (in terms of hydrolysis and condensation), from left (less reactive) to right (more reactive) (see text).



2.2.2.1. Functionalization of the Hybrids with the Luminescent Ru(II) Indicator Dye

The sulfonyl chloride derivative of the ruthenium complex was synthesized by refluxing tetrasodiumtris[(1,10-phenanthroline-4,7-diyl)bis(benzenesulfonate)]ruthenate (abbreviated Na₄[Ru(pbbs)₃]) [Garcia-Fresnadillo 2001] (18 mg) in SOCl₂ (9 mL) containing 3 mL of dry dimethylformamide (DMF) for 3 h. After completion of the reaction, the excess of SOCl₂ was carefully removed by gentle vacuum distillation at ca. 50 °C and the resulting red-orange solid was dissolved in 10 mL of dry DMF. Then, the amino-silanized GaN surfaces were introduced individually into glass vials, and 0.5 mL of the dye solution and 5 drops of dry triethylamine were added to each vial. The reaction mixtures were kept at room temperature for 48 h, leading to the formation of the corresponding sulfonamide upon reaction of one or more sulfonyl chloride groups of the activated indicator dye with the alkylaminesilane tethered to the GaN surface. Next, the dyed surface was thoroughly washed with the following sequence of analytical- or chromatography-grade solvents: DMF, acetone, methanol, ultrapure Type I water (18 MΩcm, Millipore Direct-Q) and acetone. Finally, the samples were allowed to dry under air. The entire functionalization procedure is summarized in **Scheme 1**.

Scheme 1. Route to surface functionalization of n-GaN with Ru(pbbs)₃. The semiconductor surface is hydroxylated with oxygen plasma and the ω-aminosilane layer is grown on top of it (APTES chosen to illustrate the process occurring with any of the selected silanes). In a subsequent step, the pending amino groups react with one or more groups of the sulfonic acid derivative of the luminescent dye. The unreacted sulfonyl moieties are converted back into the original sulfonic acid groups upon the final water wash of the dyed surface.



The original reference [López-Gejo 2011] displayed the chemical structure of the ligands with the sulfonic groups in *para* position. However, we found that the *para/para* isomer is the least abundant one in the commercial mixture of *meta/meta*, *meta/para* and *para/para* isomers of variable composition. Therefore, Scheme 1 depicts the functionalization process with the predominant isomer (i.e., with both sulfonic groups in meta position, which is the one preferred in the sulfonation reaction of the unsubstituted 4,7-diphenyl-1,10-phenanthroline ligand). Separation of the structural isomers has not been attempted.

2.2.2.2. Surface Characterization

To characterize surface morphology, atomic force microscopy (AFM) images were obtained at the ICTS National Center for Electron Microscopy (UCM, Madrid) with a multimode Nanoscope III A (Bruker) equipped with a 15 μm scanner bearing a TESP-SuperSharp (2 nm) silicon tip (Bruker) operated in tapping mode. The roughness of the surface was measured using the Nanoscope Analysis 1.5 software. A RMS value of 0.3 ± 0.1 nm for pristine GaN samples was determined; after the piranha plus O₂- plasma treatments, the RMS increases to 1.0 ± 0.3 nm. Surface analysis was performed by X-ray photoelectron spectroscopy (XPS), also known as electron spectroscopy for chemical analysis (ESCA), accomplished by irradiating a sample with soft X-rays and analyzing the energy of emitted electrons. Experimental details for X-ray photoelectron spectroscopy (XPS) measurements have been given in detail elsewhere [López-Gejo 2010 a] and are only summarized here. Samples were irradiated with MgK α X-rays (photon energy 1253.6 eV, line width 0.7 eV) or AlK α X-rays (photon energy 1486.6 eV, line width 0.85 eV). A hemispherical analyzer (SPECS Phoibos 100 MCD-5) was used to record the spectra with pass energy of 9 eV, yielding a constant resolution of 0.9 eV. The Au 4f $7/2$, Ag 3d $5/2$, and Cu 2p $3/2$ lines of reference samples at 84.0, 368.3, and 932.7 eV, respectively, served to calibrate the binding energies. Although sample charging was observed because of the insulating character of the sapphire substrates on which GaN layers are grown, this effect was corrected, peaking the C 1s band at 285.0 eV and shifting accordingly all other core levels. Core level spectra were recorded using Mg K α radiation except the S 2s and C 1s core level spectra, for which the Al K α radiation was employed to avoid the strong overlapping of those photoemission peaks with the Ga LMM Auger transition.

2.2.2.3. O₂ Sensing Features of the Hybrids

Luminescence lifetime microscopy (LLM) was performed in a Horiba DynaMic (Piscataway, NJ) system consisting of an epifluorescence confocal microscope (Olympus BX51, NY) equipped with a 10 \times objective and a fast red-sensitive PMT detector with thermoelectric cooling (TBX-04, Horiba, NJ). A laser diode (NanoLED-

470LH, Horiba) was used as excitation source (463-nm peak wavelength; 900-ps pulse width; 10-kHz repetition rate). A 470-nm interference filter (Chroma HQ470/20x, Rockingham, VT) as excitation filter, a 490-nm dichroic mirror (Olympus Q490DCXR), and a 500 nm cutoff filter (Chroma HQ 500LP) as emission filter were employed. Luminescence decays were measured by accumulating at least 10000 counts in the peak channel and the emission lifetimes were obtained from single-exponential (solution samples) or tri-exponential (GaN hybrids) curve fittings using the proprietary Horiba hybrid grid-search minimization algorithm (without deconvolution) for stable chi-squared minimization. A full description of the setup is given in [López-Gejo 2010 b].

To obtain the Stern-Volmer O₂ quenching plots, luminescence lifetime measurements under a controlled atmosphere were performed by placing the functionalized GaN samples into a 1-mm pathlength Suprasil® cell (Hellma, Mulheim, Germany) fitted with a rubber septum. This setup allows flowing 0-100% N₂/O₂ mixtures from an electronic mass flow controller manifold (PID Eng&Tech, Madrid, ES) at 100 mL/min before (>10 min) and during the emission lifetime measurements. The cell was placed under the microscope objective on a wedge at a ca. 30° angle to minimize collection of the scattered excitation light.

2.3. Results and discussion

2.3.1. Silanization of the GaN Surface

Many authors have reported that anhydrous silanization of hydroxylated surfaces with APTES for up to a few hours leads to a monolayer of the silane [Arkles 1977, Vashist 2014]. For instance, Baur et al. obtained the latter after a 1.5 h treatment of the oxidized GaN surface [Baur 2005]. Following a similar procedure on a p-GaN substrate, we also verified with XPS the growth of an aminosilane monolayer [Arranz 2008, López-Gejo 2011]. Then we tethered a chemically activated metal-organic Ru(II) dye to obtain red-luminescent GaN-silane-Ru hybrids, with an average emission lifetime of ca. 2.1 μs in the absence of O₂ (pre-exponentially weighted lifetime [Carraway 1991], namely $\tau_M = \sum_i \alpha_i \tau_i / \sum_i \alpha_i$, being the luminescence decay fitted to the multi-exponential function $I(t) = I_0 + \sum_i \alpha_i e^{-t/\tau_i}$) and a sensitivity to this species (calculated as the ratio τ_{N_2} / τ_{O_2}) of about 1.5. We will refer to this hybrid as our “reference” sample. However, when the same functionalization was carried out with n-doped GaN, it led to a slightly thicker layer (~ 2.4 nm [Arranz 2008]), with ca. 3-fold faster excited state deactivation kinetics (τ_M as small as 0.60 μs) [López-Gejo 2011]. We hypothesized that this shorter emission lifetime was due to the efficient competition of

a photo-induced electron transfer process from the dye to the n-type semiconductor. The PET does not occur to the p-type GaN because of the higher-lying position of its conduction band. To lend support to our hypothesis, we have now investigated the effect of the intermediate silane layer thickness on the luminescence decay rate.

We selected six of the numerous commercially available aminoalkylsilanes, most of them well described in the literature. The structure of the selected silanes is depicted in **Chart 1**. Our aim was to coat in full the surface of n-GaN with a layer of variable thickness (from a few monolayers to some nm). As already stated in the introduction, the structure of the aminoalkyl trialkoxysilane determines its O-substitution rate and hence the thickness of the GaN surface coating. Therefore, it is possible to foresee that the least reactive aminosilane will be the DNTEs, because it bears three ethoxy leaving groups and lacks an amine in a suitable position for intramolecular catalysis. APTES displays a γ -amino group but the same weakly leaving ethoxy groups, so that it should be the second least reactive of our silanes. DPTMS contains three methoxy groups, but its amine groups are too far away to be able to form cyclic intermediates. Finally, APTMS, DHTMS and TDTMS possess both reactivity-enhancing features that will lead to the thickest silane layers.

Figure 26 shows the N 1s signals from the uncoated n-GaN surface and coated with the different silane layers. The experimental N 1s spectra can be deconvoluted using three components at 397.4, 399.8 and 401.4 eV, which can be attributed to N-Ga bond, neutral NH_2 , and NH_3^+ amino groups, respectively [Arranz 2008]. The silane coating thickness of the different GaN samples (**Table 2**) was estimated from the XPS results by measuring the attenuation of the N 1s signal from the underlying GaN surface at 397.4 eV (**Figure 26**). Using the simple model of a uniform coating layer, the intensity of the signal emitted by the substrate is given by eq. [12] [Benito 2013],

$$I = I_0 \exp\left(-\frac{d}{\Lambda \cos \varphi}\right) \quad [12]$$

where I is the measured intensity, I_0 is the measured intensity for an uncoated GaN substrate, Λ is the attenuation length of the N 1s photoelectrons (2.3 nm), φ is the photoelectrons collection angle (0° in this case), and d is the coating thickness (in nm).

To verify the resulting d values, we also studied by AFM the n-GaN surfaces coated with the different silanes (**Figure 27**). We looked for areas in which defects (holes/cracks) allowed us to measure directly the silane layer thickness (see **Figure 28**). It should be pointed out that both techniques have pros and cons. On the one hand, measurements by XPS through eq. [12] do not take into account the possible non-uniformity of the coating. However, our XPS probe averages out the sample in a large area (ca. 0.2 cm^2) while AFM focuses on precise positions of interest, so that it is more difficult to select areas that are representative of the entire sample. On the other hand, the density of a silane coating has been reported to increase with its thickness in

the first 2 - 4 nm, reaching a plateau thereafter [Argekar 2013], meaning that the thickness values we obtained by XPS could be slightly underestimated for thin films. It is worth noting that, in those cases where both techniques could be used (APTES and TDTMS), the thickness values we measured were the same within the experimental error (Table 2).

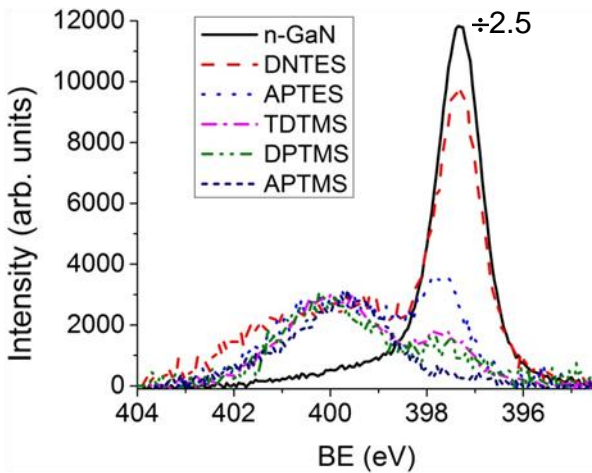


Figure 26. XPS signals (N 1s) from the uncoated GaN surface and coated with different silanes, followed by covalent bonding of $[\text{Ru}(\text{pbbs})_3]$. The N 1s spectra are actually the convolution of three components at 397.4, 399.8 and 401.4 eV, which are attributed to N-Ga bond (substrate), neutral NH_2 and NH_3^+ amino groups, respectively. The spectrum of the uncoated n-GaN has been divided by 2.5 for the sake of clarity.

2,9-Diazanonyltriethoxysilane (DNTES) provides the thinnest coating (3.3 nm) on n-GaN even after 44 h contact time. It was not possible to measure its thickness by AFM, but the typical “stripes” of the GaN surface, resulting from the two-dimensional growth of the semiconductor, are clearly visible underneath the silane layer (**Figure 27A**). The very thin layer growth is in agreement with its molecular structure considerations (see above) and the results reported in literature for silica coatings with DNTES [Zhu 2012, Smith 2008]. Silanization with APTES results in a 5.8 nm thick layer, with a good agreement between the AFM direct measurement (**Figure 27B**) and those by XPS (**Table 2**). The thickness of the TDTMS coating (6.8 nm) is similar to the APTES one, but lacks its uniformity: many islands consisting of silane accumulations are observed (**Figure 27C**), a typical phenomenon observed for many relatively thick silane coatings [Arkles 1977, Arkles 1992, Howarter 2006, Jussila 2010, Shircliff 2013, Vashist 2014, Fischer 2015]. Moreover, it is the thinnest of the methoxy-terminated silane coatings, the reason probably being an intramolecular $\text{NH}\cdots\text{NH}_2$ hydrogen bonding that limits the intramolecular catalysis. A 9-nm thick surface coating (from

XPS) is obtained with DPTMS and it grows with the highest number of islands (**Figure 27D**). This recently commercialized silane is the least reported in the literature. We hypothesize that the long hydrophobic chain of this silane (**Chart 1**) promotes “upside-down” interactions with each other, so that their self-condensation proceeds very rapidly compared to condensation with the surface hydroxyl groups [Wang 2008]. A still thicker surface coating of n-GaN is obtained with APTMS (10.6 nm); it is thicker than that obtained with APTES because of the higher reactivity of the alkoxy groups (MeO) of the former silane. Finally, the thickest coating (ca. 18 nm) is the one achieved with DHTMS (**Figure 27E** and **Figure 28C**). This silane is highly reactive due to the combination of both intra- and inter-molecular nucleophilic catalysis by its amine groups placed in suitable positions. Polycondensation is so favored that it probably starts in solution, generating large clumps that become attached to the surface during the silanization process. These silane polymers appear in the AFM micrograph (**Figure 27F**) as thick fibers of 40 – 50 nm height onto the coating surface.

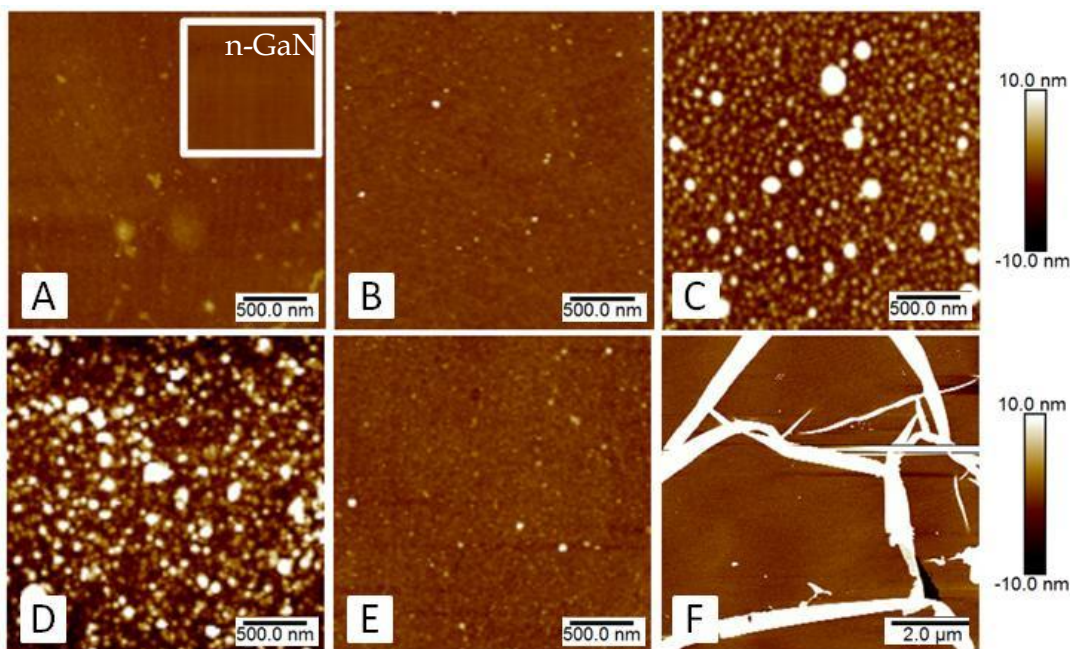


Figure 27. AFM images of the n-GaN surface coated with different silanes, followed by covalent bonding of $[\text{Ru}(\text{pbbs})_3]$: (A) DNTEs (the inset on **Figure 27A** shows the morphology of pristine n-GaN surface); (B) APTES; (C) TDTMS; (D) DPTMS; (E) APTMS; (F) DHTMS. Image size A–E: $2.5 \times 2.5 \mu\text{m}$; F: $8 \times 8 \mu\text{m}$.

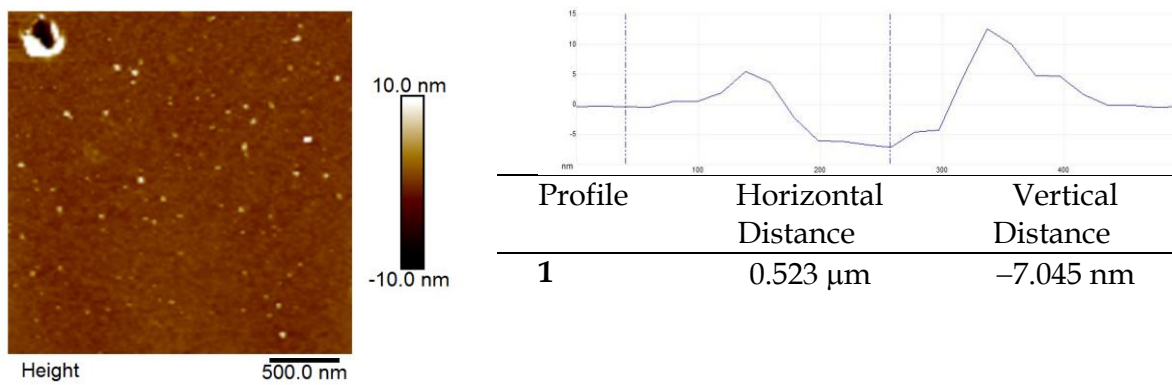


Figure 28 A. GaN-APTES-Ru.

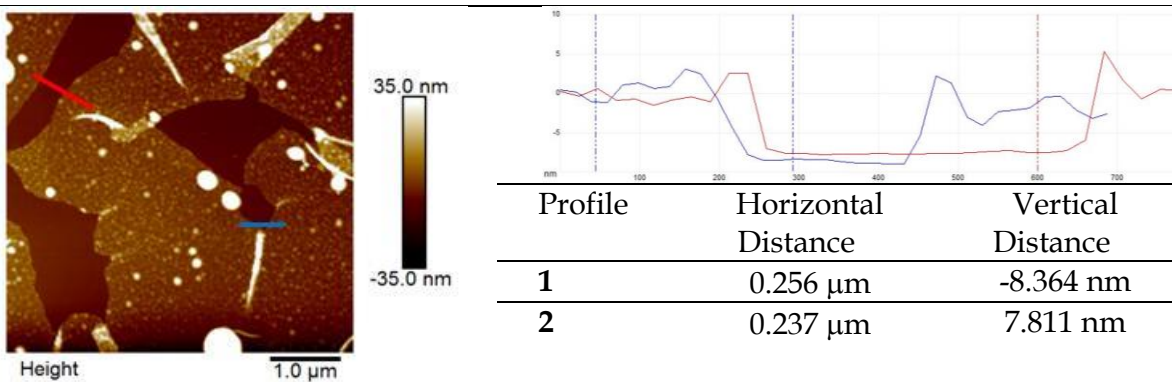


Figure 28 B. GaN-TDTMS-Ru.

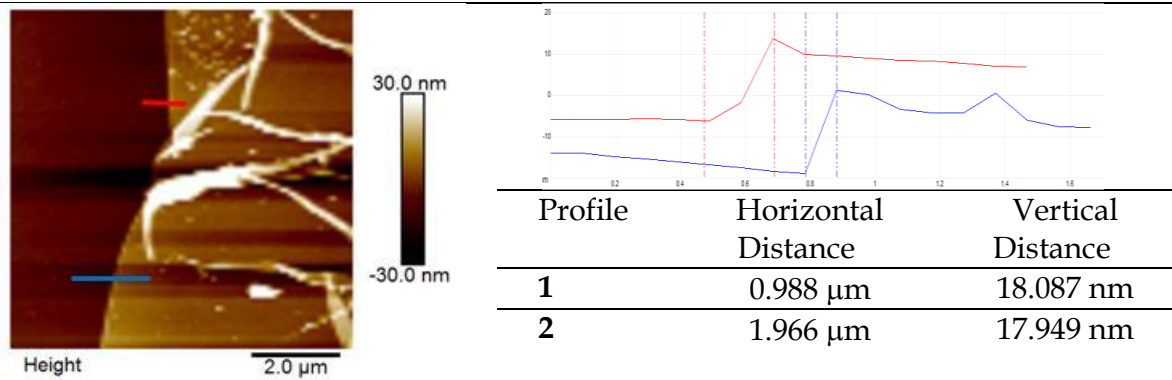


Figure 28 C. GaN-DHTMS-Ru.

Figure 28. AFM images used for measuring thickness of the coating layers obtained after silanization and subsequent covalent bonding of $[\text{Ru}(\text{pbbs})_3]$. Left column: atomic force microographies. Right column: thickness profiles with measured values.

Table 2. Silane coating thickness and pre-exponentially weighted luminescence lifetime of the GaN-silane-Ru(II) dye hybrids.

Silane	GaN type	Silanization time /h	Thickness/nm ^a (ARXPS or XPS)	Thickness/nm ^b (AFM)	$\tau_M/\mu s^c$ (N ₂)	$\tau_M/\mu s^d$ (O ₂)	AFM picture
DNTES	n	44	3.3 (XPS)	Few layers ^e	0.90	0.70	2A
APTES	n	44	5.8 (XPS)	7	1.0	0.74	2B
TDTMS	n	44	6.8 (XPS)	8	1.2	0.97	2C
DPTMS	n	44	9.0 (XPS)	n.d. ^f	0.50	0.50	2D
APTMS	n	44	10.6 (XPS)	n.d. ^f	1.1	0.84	2E
DHTMS	n	44	n.d. ^g	18	2.3	1.3	2F
APTES ^h	n	1.5	2.4 (ARXPS)		0.60	0.60	
APTES ^h	p	1.5	0.8 (ARXPS)		2.1	1.4	

^a Uncertainty: 0.1 nm for ARXPS (angle-resolved XPS) and 0.2 nm for XPS. ^bEstimated maximum uncertainty: 1 nm. ^c Under N₂; uncertainty: $\pm 10\%$. ^d Under O₂; uncertainty: $\pm 10\%$. ^e See text. ^f No holes or cracks were observed in the coating to be used to measure the thickness. ^g The coating is too thick to apply this method. ^h Refs. [Arranz 2008, López-Gejo 2011].

2.3.2. Effect of the silane coating on the photochemistry of the tethered luminescent indicator dye

Verification of actual covalent bonding of the Ru(II) indicator dye is provided by XPS (**Figure 29**). In all samples the sulfonated dye molecules were indeed chemically bonded to the aminosilane intermediate layer, with an average number of three sulfonamide bonds formed per dye molecule (over the six possible bonds) as calculated from the S 2s core level XPS spectra of the samples (see **Table 3**).

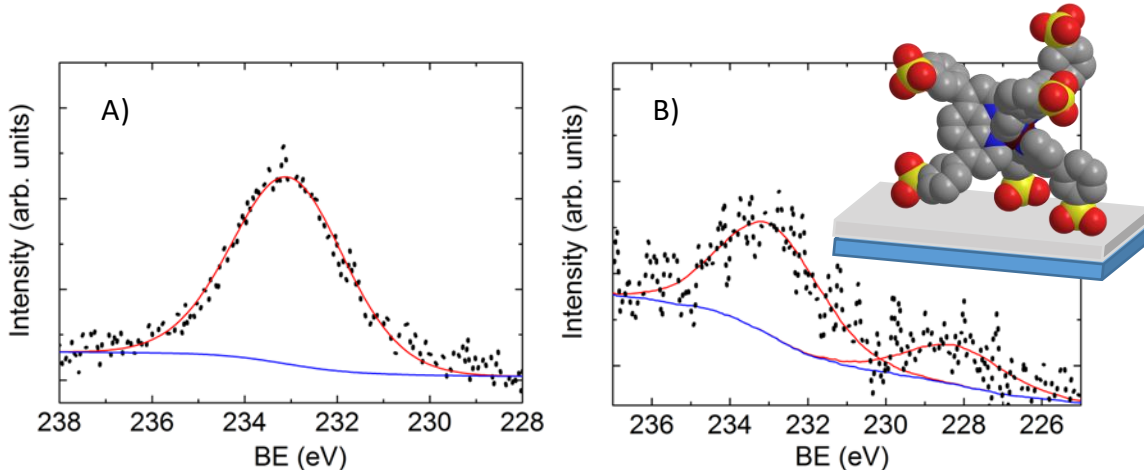
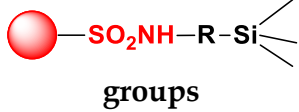


Figure 29. Typical S 2s core level XPS spectra of the samples. A: GaN surface coated with the APTES layer onto which a drop of 10^{-6} M $[\text{Ru}(\text{pbbs})_3]^{4-}$ solution has been deposited (without any chemical pre-activation with SOCl_2) and then the solvent was evaporated. B: GaN surface coated with APTES which was covalently functionalized with $[\text{Ru}(\text{pbbs})_3]^{4-}$ after chemical pre-activation with SOCl_2 (see *Experimental* section); inset: artist depiction of the quasi-octahedral Ru dye tethered to the silane coating.

Additionally, the emission spectrum of the hybrids (**Figure 30B**) obtained by time-resolution emission spectroscopy (**Figure 30A**) shows the usual radiative π^* -d π electronic transition typical of most luminescent dyes of this family [Lees 1987], although the emission maximum (around 600 nm) is 20 nm blueshifted and the band slightly narrower compared to $\text{Ru}(\text{pbbs})_3^{4+}$ in solution [Garcia-Fresnadillo 2001]. These two differences are expected consequences of the lower mobility freedom of the dye molecules following the tethering procedure (rigidochromism) [Lees 1987].

The luminescence decays of the $[\text{Ru}(\text{pbbs})_3]$ -silane-GaN hybrids fabricated with each one of the different silane layers, have been measured both in the absence and in the presence of O_2 by LLM (**Figure 31**). Regardless the O_2 concentration, the extracted emission lifetimes (τ_M) decrease in the order: DHTMS > TDTMS > APTMS > APTES > DNTEs > DPTMS.

Table 3. $S_{\text{ads}}/S_{\text{cov}}$ ratio of the area of the XPS S 2s core level peaks at ~ 233 eV and at ~ 228 eV, and the calculated number of sulfur atoms *covalently* bonded via sulfonamide bond to the aminoalkylsilane (out of the overall 6 sulfur atoms per Ru complex) as a function of the silane used to functionalize the GaN substrate with amine groups.

Intermediate silane layer	DNTES	APTES	TDTMS	DPTMS	APTMS	Ru(II) dye deposited on silane-coated GaN ^a
$S_{\text{ads}}/S_{\text{cov}}^b$	0.5	1.1	2.9	1.0	0.9	
Average no. of  groups	4	~ 3	~ 1.5	3	~ 3	0

^a See text. ^b Uncertainty: ± 0.1 .

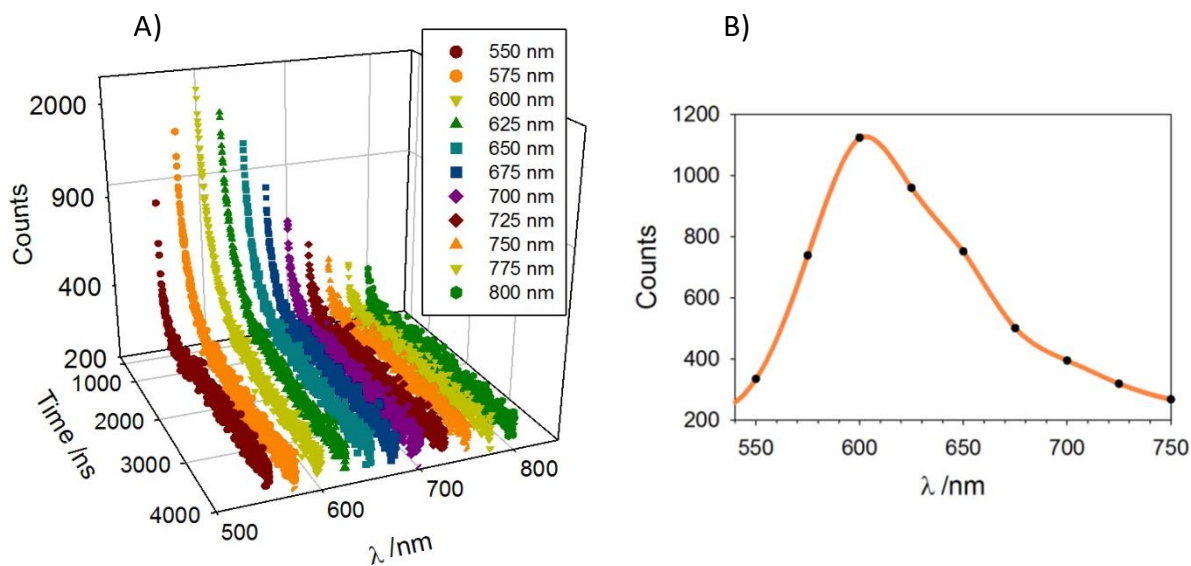


Figure 30. Time-resolved emission spectrum of GaN-APTES-Ru(pbbs)₃. A: Luminescence decays collected at different emission wavelength from 550 nm to 800 nm ($\lambda_{\text{exc}} = 463$ nm). B: Emission spectrum reconstructed from (A) using the data at $t = 400$ ns.

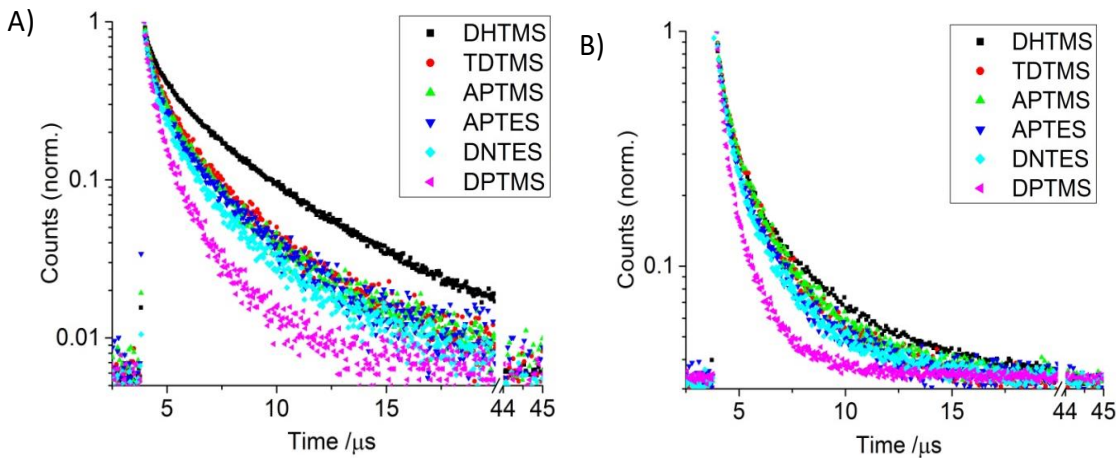


Figure 31. Kinetics of the excited state deactivation of the luminescent Ru(II) indicator dye covalently attached to the silanized n-GaN surface as a function of the aminoalkylsilane intermediate layer. All decays shown have been recorded under pure N₂ (A) or pure O₂ (B).

To rationalize the effect of the distance from the GaN surface to the photoexcited Ru(II) complex, on its deactivation kinetics, our analysis firstly focused on the luminescence of the sensor materials in the absence of O₂ (**Table 2**). It is important to underline that the emission of the [Ru(pbbs)₃]⁴⁻ anion (as the tetra(trihexyltetradecylphosphonium) salt for solubility reasons) in O₂-free solution decays with a lifetime of 5.36 μs in acetonitrile and 3.0 μs in neat APTES. However, the hybrids produced after tethering [Ru(pbbs)₃]⁴⁻ to a *surface* via an aminosilane linker show a shorter, clearly multi-exponential decay. In the absence of O₂, the change from a single-exponential to a multi-exponential decay must be due to the microheterogeneity around the luminescent probe caused by the aminosilane layer to which the Ru complex is covalently bonded. This phenomenon usually occurs when luminescent dyes are embedded in or attached to a solid support [Orellana 2005, Valeur 2012]. Therefore, for the sake of comparison, the pre-exponentially weighted emission lifetimes (τ_M , see above) have always been determined (**Table 2**). Hybrids in which the support was glass were used as control samples. The τ_M values measured in the absence of O₂ using the latter support, which cannot be involved in electron transfer quenching, are on the order of 2.0 ± 0.2 μs [López-Gejo 2011]. A similar result was obtained using just p-GaN as substrate ($\tau_M = 2.1$ μs) [López-Gejo 2011]. This significant decrease of the emission lifetime of [Ru(pbbs)₃]⁴⁻ in going from solution (acetonitrile, APTES) to immobilized onto a solid support is not trivial to explain. Firstly, it is well known that the position of the emissive metal-to-ligand charge transfer (³MLCT) level of Ru(II) polypyridyl complexes depends on the nature of the ligands around the metal core [Juris 1988, Orellana 2004]. The procedure to tether the dye to the aminosilane layer involves conversion of some of the sulfonate moieties into

sulfonamide moieties (see above). The electron withdrawing power of the latter groups is much higher than that of the former [Hansch 1991], so that the new ligand has a lower-lying π^* orbital. Therefore, the luminescence lifetime of the covalently bonded dye will be shorter due to the energy-gap rule effect [Valeur 2012]. Moreover, the shorter emission lifetime could also arise from the significantly less polar microenvironment around the luminescent probe in the aminosilane layer (Lippert-Mataga effect) [Castro 2005]. Unlike glass or p-GaN substrates, the hybrid sensor materials based on n-GaN displayed τ_M values considerably shorter in most of the prepared samples. Radiationless deactivation due to nearby photoexcited dye molecules was excluded, because the extremely weak (diode laser) excitation we used to meet the single photon timing (SPT) detection condition of the LLIM measurements (ca. 7 pJ/pulse) precludes triplet-triplet annihilation processes. Moreover, if so, a similar self-quenching process should also take place when using glass or p-GaN as substrate, a result that was not observed. Our reasoning, therefore, is that a photoinduced electron transfer quenching process from the photoexcited Ru(II) complex to the GaN conduction band occurs in competition with the spontaneous decay [López-Gejo 2010 a]. In this case the emission lifetime of the former (τ_{M0} , Eq. [13]) will further decrease according to Eq. [14],

$$\tau_{M0} = 1/k_0 \quad [13]$$

$$\tau_M = 1/(k_0 + k_{et}) \quad [14]$$

being k_0 the sum of radiative and non-radiative excited state deactivation rate constants, and k_{et} the electron transfer deactivation rate constant, so that the τ_{M0}/τ_M ratio is given by Eq. [15].

$$\tau_{M0}/\tau_M = (k_0 + k_{et})/k_0 = 1 + k_{et}/k_0 \quad [15]$$

The common simplified electron transfer model for rigid media predicts that the excited state quenching decreases exponentially with the donor-acceptor distance r according to Eq. [16] [Beitz 1979, Albinsson 2008, Maeda 2013],

$$k_{et} = k(0) \exp(-\beta r) \quad [16]$$

where $k(0)$ is the electron transfer rate constant when the distance between donor and acceptor is zero and β characterizes the distance dependence of the coupling.

Substituting Eq. [16] into Eq. [15], Eq. [17] is obtained:

$$\tau_{M0}/\tau_M = 1 + (k(0) \exp(-\beta r)) \tau_{M0} \quad [17]$$

Figure 32 depicts the measured relative emission lifetime values (τ_{M0}/τ_M) in the absence of O₂ as a function of the silane layer thickness, together with the best fit of the experimental points to Eq. [17] (parameters of the best fit: $k(0) = 1.9 \pm 0.3 \mu\text{s}^{-1}$; $\beta = 0.025 \pm 0.005 \text{ \AA}^{-1}$; $\tau_{M0} = 2.2 \pm 0.5 \mu\text{s}$; reg. coeff. $r^2 = 0.8944$. The DPTMS was not included in the fit). We can observe that indeed the deactivation constant decreases with the thickness of the intermediate silane layer growth to separate the redox partners,

namely, the photoexcited $[\text{Ru}(\text{pbbs})_3]^{4-}$ and the n-GaN surface. However, the β value obtained from our exponential fit is lower than expected, taking into account that electron transfer (ET) reactions display β parameters spanning from 4 \AA^{-1} (ET through vacuum) to 1 \AA^{-1} for saturated alkane bridges, to 0.02 \AA^{-1} for π -conjugated bridges, and to values as low as 0.001 \AA^{-1} (ET through engineered molecular wires) [Maeda 2013]. Being our β value close to 0.03 \AA^{-1} , we have to conclude that our hybrid materials are not as simple as a donor-bridge-acceptor model predicts. One reason for this discrepancy could be that the intermediate silane layers have some degree of porosity that allows a number of Ru dye molecules to lie closer to the GaN surface than expected for a non-porous coating. Such molecules would be located at a distance short enough to be quenched by PET to a different extent. However, this assumption has to be ruled out because our silanization procedure (in toluene with long contact time) is similar to those used by other groups that have been shown to yield thick dense aminosilane layers [Arkles 1977], with no room for penetration of similar-sized guests [Fischer 2015]. A more plausible explanation is that the ET in our hybrid materials would be enhanced by the presence, in the intermediate layer, of primary and secondary ammonium cations (and their counterions) that are generated by protonation of the aminosilane groups during the washing steps. Moreover, water molecules adsorbed into the silane coating could be responsible of a dramatic increase of the ET, as a boost of the conductivity has been reported for SiO_2 [Anderson 1968] and Si-organic hybrids [Clément 2012] in the presence of those species. DPTMS is an outlier of the fit (**Figure 32**) because of the particular mobile and disordered structure that this extended silane imparts to the resulting layer (see the morphology study, above).

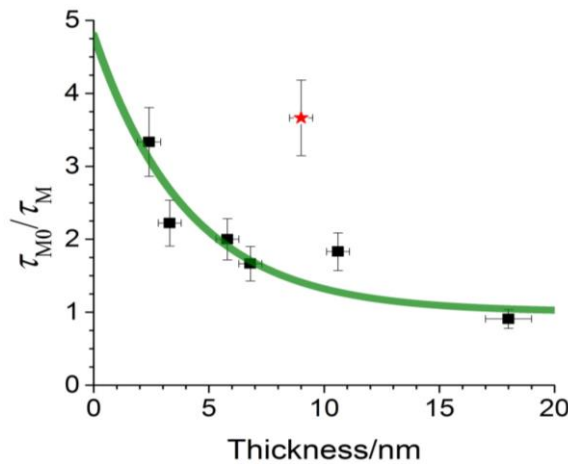


Figure 32. Relative emission lifetime (τ_{M0}/τ_M) of $[\text{Ru}(\text{pbbs})_3]^{4-}$ covalently bonded to an aminosilane layer on top of n-GaN, as a function of the layer thickness. The green line is the best fit of the data points to Eq. [17] (parameters of the best fit: $k(0) = 1.9 \pm 0.3 \mu\text{s}^{-1}$; $\beta = 0.025 \pm 0.005 \text{ \AA}^{-1}$; $\tau_{M0} = 2.2 \pm 0.5 \mu\text{s}$; reg. coeff. $r^2 = 0.8944$). The DPTMS was not included in the fit (see text).

2.3.3. Effect of the silane coating on the O₂-sensing performance

The sensing mechanism of the Ru dye-Silane-GaN hybrid materials is based on collisional quenching of the photoexcited indicator dye by molecular oxygen [Wang 2014]. More precisely, the process involves an energy transfer from the triplet excited state of the dye to the triplet ground state of the quencher [Demas 1977]. The probability of an encounter between the O₂ molecule and the photoexcited Ru(II) complex is lower if the lifetime of the latter is shortened because of its alternative deactivation by photoinduced electron transfer to the underlying semiconductor used as excitation source [López-Gejo 2011]. Therefore, this additional undesired luminescence quenching negatively affects the sensor performance (**Figure 33**). The corresponding experimental emission lifetime data are collected in **Table 2**. Eq. [18] describes a frequently used Stern-Volmer equation for luminophores in microheterogeneous environments based on the so-called “two-site” quenching model [Garcia-Fresnadillo 2001]:

$$\frac{\tau_M^0}{\tau_M} = \left(\frac{f_{01}}{1 + K_{SV1}[Q]} + \frac{f_{02}}{1 + K_{SV2}[Q]} \right)^{-1} \quad [18]$$

where τ_M^0 and τ_M are the pre-exponentially weighted emission lifetimes in absence and in the presence of O₂, respectively, f_{01} and f_{02} are the fractions of the total emission from the luminophore in each one of the two sites on the solid support, in the absence of O₂, while K_{SV1} and K_{SV2} are the Stern-Volmer quenching constants associated to each site ($K_{SV} = k_Q \tau_{M0}$ being k_Q the bimolecular quenching rate constant of the luminophore by O₂). The “two-sites” model does not actually represent two distinct sites where the indicator dye is located, but rather a strategy to get a calibration curve for the sensor by way of a powerful fitting.

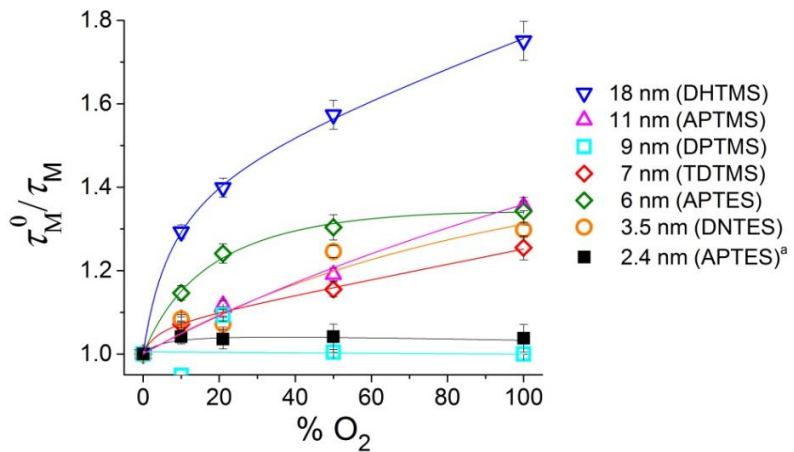


Figure 33. Emission lifetime-based Stern-Volmer plot for the quenching of the photoexcited [Ru(pbbs)₃]⁴⁻ covalently attached to n-GaN by O₂ (in N₂ by volume) as a function of the aminoalkylsilane intermediate layer ($\tau_M = \sum_i \alpha_i \tau_i / \sum_i \alpha_i$). ^a Data from [López-Gejo 2011].

In order to understand the influence of the buffer silane thickness on the hybrids O₂-sensing features, it is useful to compare **Figure 32** and **Figure 33**. The comparison is depicted in **Figure 34**.

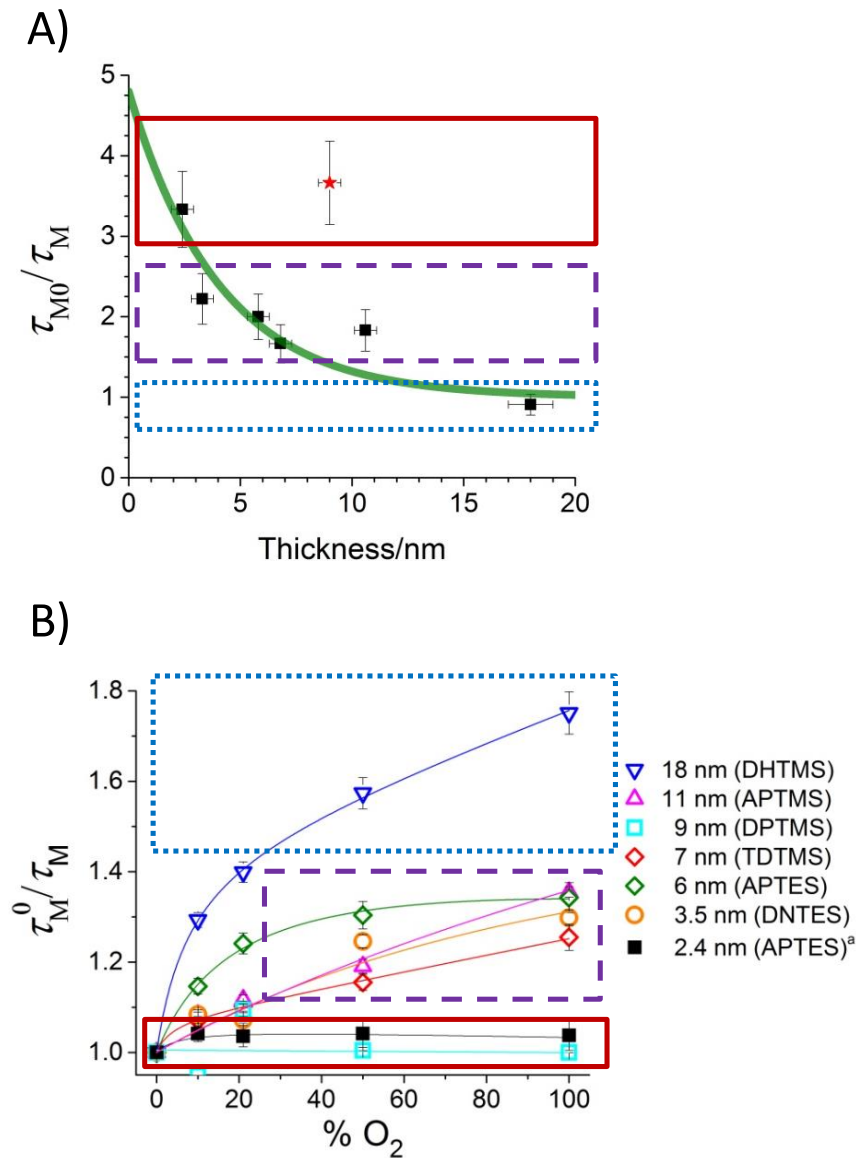


Figure 34. Silane thickness effect on the luminescence lifetime of the attached Ru(II) complex, in the absence (A) and in the presence of different concentrations of O₂ (B).

When the activated GaN surfaces were treated with DHTMS, the obtained silane spacer layer was the thickest one (18 nm), keeping the Ru(II) dye far away from the GaN surface (**Figure 35**). In this case, no PET towards the semiconductor occurs, so that the emission lifetime of the luminophore in the absence of O₂ is the longest one. Therefore, this hybrid sensing material shows always the largest τ_0/τ_M ratio (ca. 1.8 from 0 to 100% O₂) (blue rectangle, **Figure 34**). As a result, Ru(II)-DHTMS-(n-

doped)GaN hybrids could be used as dioxygen sensitive probes. However, when the other silanes are used, the resulting intermediate silane layer obtained thereof is not thick enough to prevent quenching of the photoexcited dye by the n-GaN due to the PET process so that the τ_0^0/τ_M^{100} ratio for all other hybrid materials is smaller. For this reason, the sensing material having the thinnest silane spacing layer (2.4 nm), made by treatment of activated n-GaN with APTES for 1.5 h [López-Gejo 2011], is the most quenched one by PET in the absence of O₂, displaying the lowest sensitivity to O₂ (only a ca. 5% change from 0 to 100% O₂). Also, the hybrid material prepared with DPTMS, which was strongly quenched already in pure N₂, shows virtually no O₂ sensitivity in spite of containing a significant silane layer (red rectangle, Figure 34). Finally, hybrids containing silane coating layer of intermediate thickness between the two extremes, that were slightly quenched because of PET in absence of O₂ (purple rectangle, Figure 34), are characterized by an “intermediate” O₂-sensitivity as per the Stern-Volmer plot.

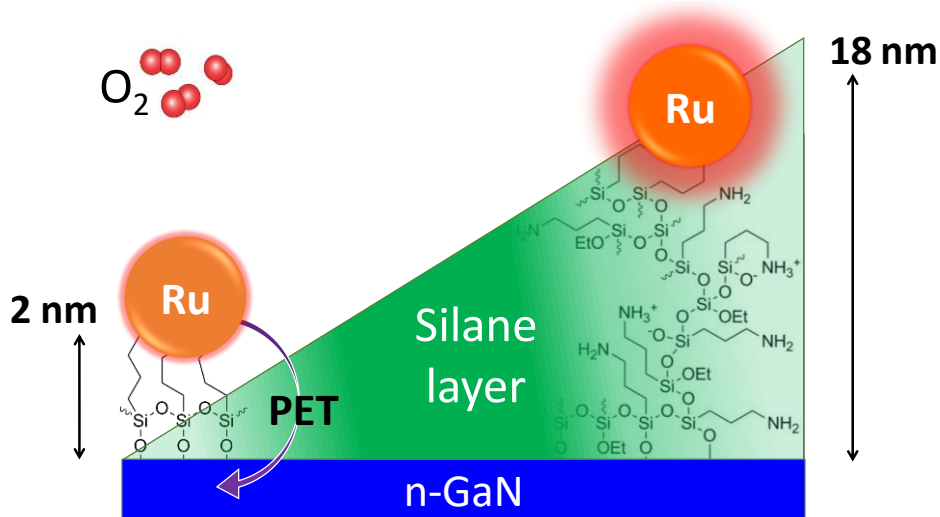


Figure 35. Artistic depiction of different Ru(II)-silane-GaN hybrids. Selecting APTES as the silane linker (left), it was obtained a silane intermediate layer about two nanometer thick. The distance between the Ru(II) luminescent complex and the n-GaN was short enough to allow strong photo-induced electron transfer between the photoexcited Ru(II) indicator dye and the semiconductor. The luminescence of the former was so strongly quenched due to PET that was not influenced by O₂ concentration. Conversely, the thicker 18 nm-layer that was produced using DHTMS (right) separated the dye molecules and the n-GaN, so that PET could not take place. As a result, Ru(II)-DHTMS-(n-doped)GaN hybrids could be used as dioxygen sensitive probes.

2.4. References

Albinsson	2008	Albinsson, B.; Mårtensson, J. Long-Range Electron and Excitation Energy Transfer in Donor–Bridge–Acceptor Systems. <i>J. Photochem. Photobiol. C</i> 2008 , 138–155.
Anderson	1968	Anderson, J. H.; Parks, G. A. Electrical Conductivity of Silica Gel in the Presence of Adsorbed Water. <i>J. Phys. Chem.</i> 1968 , 72, 3662–3668.
Argekar	2013	Argekar, S. U.; Kirley, T. L.; Schaefer, D. W. Determination of Structure–Property Relationships for 3-Aminopropyltriethoxysilane Films Using X-ray Reflectivity. <i>J. Mater. Res.</i> 2013 , 28, 1118–1128.
Arkles	1977	Arkles, B. Tailoring Surfaces with Silanes. <i>Chemtech</i> 1977 , 7, 766–778.
Arkles	1992	Arkles, B.; Steinmetz, J. R.; Zazyczny, J.; Mehta, P. Factors Contributing to the Stability of Alkoxy silanes in Aqueous Solution. <i>J. Adhes. Sci. Technol.</i> 1992 , 6, 193–206.
Arranz	2008	Arranz, A.; Palacio, C.; García-Fresnadillo, D.; Orellana, G.; Navarro, A.; Muñoz, E. Influence of Surface Hydroxylation on 3-Aminopropyltriethoxysilane Growth Mode During Chemical Functionalization of GaN Surfaces: An Angle-Resolved X-ray Photoelectron Spectroscopy Study. <i>Langmuir</i> 2008 , 24, 8667–8671.
Baur	2005	Baur, B.; Steinhoff, G.; Hernando, J.; Purrucker, O.; Tanaka, M.; Nickel, B.; Stutzmann, M.; Eickhoff, M. Chemical Functionalization of GaN and AlN Surfaces. <i>Appl. Phys. Lett.</i> 2005 , 87, 263901.
Beitz	1979	Beitz, J. V.; Miller, J. R. Exothermic Rate Restrictions on Electron Transfer in a Rigid Medium. <i>J. Chem. Phys.</i> 1979 , 71, 4579–4595.
Benito	2013	Benito, N.; Escobar Galindo, R.; Rubio-Zuazo, J.; Castro, R. G.; Palacio, C. High- and Low-Energy X-ray Photoelectron Techniques for Compositional Depth Profiles: Destructive Versus Non-Destructive Methods. <i>J. Phys. D: Appl. Phys.</i> 2013 , 46, 065310.
Carraway	1991	Carraway, E. R.; Demas, J. N.; DeGraff, B. A. Luminescence Quenching Mechanism for Microheterogeneous Systems. <i>Anal. Chem.</i> 1991 , 63, 332–336.
Castro	2005	Castro, A. M.; Delgado, J.; Orellana, G. Hydrocarbon in Water Sensing with PTFE Membranes Doped with a Luminescent Ru(II) Poly(Pyridyl) Complex. <i>J. Mater. Chem.</i> 2005 , 15, 2952–2958.
Chiang	1980	Chiang, C. H.; Ishida, H.; Koenig, J. L. The Structure of γ -Aminopropyltriethoxysilane on Glass Surfaces. <i>J. Colloid Interface Sci.</i> 1980 , 74, 396–404.

Clément	2012	Clément, N.; Guérin, D.; Pleutin, S.; Godey, S.; Vuillaume, D. Role of Hydration on the Electronic Transport through Molecular Junctions on Silicon. <i>J. Phys. Chem. C</i> 2012 , <i>116</i> , 17753–17763.
Demas	1977	Demas, J. N.; Harris, E. W.; McBride, R. P. Energy Transfer from Luminescent Transition Metal Complexes to Oxygen. <i>J. Am. Chem. Soc.</i> 1977 , <i>99</i> , 3547–3551.
Fischer	2015	Fischer, T.; Dietrich, P. M.; Streeck, C.; Ray, S.; Nutsch, A.; Shard, A.; Beckhoff, B.; Unger, W. E. S.; Rurack, K. Quantification of Variable Functional-Group Densities of Mixed-Silane Monolayers on Surfaces via a Dual-Mode Fluorescence and XPS Label. <i>Anal. Chem.</i> 2015 , <i>87</i> , 2685–2692.
Flack	2016	Flack, T. J.; Pushpakaran, B. N.; Bayne, S. B. GaN Technology for Power Electronic Applications: A Review. <i>J. Electron. Mater.</i> 2016 , <i>45</i> , 2673–2682.
Garcia-Fresnadillo	2001	Garcia-Fresnadillo, D.; Orellana, G. Interaction of Sulfonated Ruthenium (II) Polypyridine Complexes with Surfactants Probed by Luminescence Spectroscopy. <i>Helv. Chim. Acta</i> 2001 , <i>84</i> , 2708–2730.
Gómez-Romero	2004	Gómez-Romero, P.; Sanchez, C. In <i>Functional Hybrid Materials</i> ; Gómez-Romero, P., Sanchez, C., Eds.; Wiley-VCH: Weinheim, 2004 ; Chapter 1.
Gründler	2007	Gründler, P. In <i>Chemical Sensors: An Introduction for Scientists and Engineers</i> ; Gründler, P., Ed.; Springer-Verlag: Berlin Heidelberg, 2007 ; Chapter 3, pp 115–117.
Hansch	1991	Hansch, C.; Leo, A.; Taft, R. W. A Survey of Hammett Substituent Constants and Resonance and Field Parameters. <i>Chem. Rev.</i> 1991 , <i>97</i> , 165–195.
Howarter	2006	Howarter, J. A.; Youngblood, J. P. Optimization of Silica Silanization by 3-Aminopropyltriethoxysilane. <i>Langmuir</i> 2006 , <i>22</i> , 11142–11147.
Jewett	2012	Jewett, S. A.; Makowski, M. S.; Andrews, B.; Manfra, M. J.; Ivanisevic, A. Gallium Nitride is Biocompatible and Non-Toxic Before and After Functionalization with Peptides. <i>Acta Biomater.</i> 2012 , <i>8</i> , 728–733.
Juris	1988	Juris, A.; Balzani, V.; Barigelli, F.; Campagna, S.; Belser, P.; von Zelewsky, A. Ru(II) Polypyridine Complexes: Photophysics, Photochemistry, Electrochemistry, and Chemiluminescence. <i>Coord. Chem. Rev.</i> 1988 , <i>84</i> , 85–277.
Jussila	2010	Jussila, P.; Ali-Löytty, H.; Lahtonen, K.; Hirsimäki, M.; Valden, M. Effect of Surface Hydroxyl Concentration on the Bonding and Morphology of Aminopropylsilane Thin Films on Austenitic Stainless Steel, <i>Surf. Interface Anal.</i> 2010 , <i>42</i> , 157–164.

Kanan	2002	Kanan, S. A.; Tze, W. T. Y.; Tripp, C. P. Method to Double the Surface Concentration and Control the Orientation of Adsorbed (3-Aminopropyl) Dimethylethoxysilane on Silica Powders and Glass Slides. <i>Langmuir</i> 2002 , <i>18</i> , 6623–6627.
Kim	2013	Kim, J.-Y.; Jeong, T.; Lee, S. H.; Oh, H. S.; Park, H. J.; Kim, S.-M.; Baek, J. H. Light extraction efficiency part B. Light extraction of high efficient LEDs, in: <i>III-Nitride Based Light Emitting Diodes and Applications</i> ; Seong, T.-Y.; Han, J.; Amano, H.; Morkoc, H., Eds.; Springer: Dordrecht, Netherlands, 2013 , pp. 271–290.
Lees	1987	Lees, A. J. Luminescence Properties of Organometallic Complexes. <i>Chem. Rev.</i> 1987 , <i>87</i> , 711–743.
López-Gejo	2010 a	López-Gejo, J.; Arranz, A.; Navarro, A.; Palacio, C.; Muñoz, E.; Orellana, G. Microsensors Based on GaN Semiconductors Covalently Functionalized with Luminescent Ru(II) Complexes. <i>J. Am. Chem. Soc.</i> 2010 , <i>132</i> , 1746–1747.
López-Gejo	2010 b	López-Gejo, J.; Haigh, D.; Orellana, G. Relationship between the Microscopic and Macroscopic World in Optical Oxygen Sensing: A Luminescence Lifetime Microscopy Study. <i>Langmuir</i> 2010 , <i>26</i> , 2144–2150.
López-Gejo	2011	López-Gejo, J.; Navarro-Tobar, A.; Arranz, A.; Palacio, C.; Muñoz, E.; Orellana, G. Direct Grafting of Long-Lived Luminescent Indicator Dyes to GaN Light-Emitting Diodes for Chemical Microsensor Development. <i>Appl. Mater. Interfaces</i> 2011 , <i>3</i> , 3846–3854.
Maeda	2013	Maeda, H.; Sakamoto, R.; Nishihara, H. Metal Complex Oligomer and Polymer Wires on Electrodes: Tactical Constructions and Versatile Functionalities. <i>Polymer</i> 2013 , <i>54</i> , 4383–4403.
Makowski	2011 a	Makowski, M. S.; Zemlyanov, D. Y.; Ivanisevic, A. Olefin Metathesis Reaction on GaN (0001) Surfaces. <i>Appl. Surf. Sci.</i> 2011 , <i>257</i> , 4625–4632.
Makowski	2011 b	Makowski, M. S.; Zemlyanov, D. Y.; Lindsey J. A., Bernhard, J. C.; Hagen, E. M.; Chan, B. K.; Petersohn, A. A.; Medow, M. R.; Wendel, L. E.; Chen, D.; Canter, J. M.; Ivanisevic, A. Covalent Attachment of a Peptide to the Surface of Gallium Nitride. <i>Surf. Sci.</i> 2011 , <i>605</i> , 1466–1475.
Materne	2006	Materne, T.; de Buyl, F.; Witucki, G. L. Organosilane Technology in Coating Applications: Review and Perspectives. Dow Corning Corporation: Midland (MI), 2006 .
McGee	2009	McGee, K. A.; Mann, K. R. Inefficient Crystal Packing in Chiral [Ru(phen) ₃](PF ₆) ₂ Enables Oxygen Molecule Quenching of the Solid-State MLCT Emission. <i>J. Am. Chem. Soc.</i> 2009 , <i>131</i> , 1896–1902.

Mingoarraz	1995	Mingoarraz, F. J.; Moreno-Bondi, M. C.; García-Fresnadillo, D.; de Dios, C.; Orellana, G. Oxygen-Sensitive Layers for Optical Fibre Devices. <i>Mikrochim. Acta</i> 1995 , <i>121</i> , 107–118.
Nakamura	2000	Nakamura, S.; Pearton, S.; Fasol, G. <i>The Blue Laser Diode: The Complete Story</i> , 2nd ed; Springer-Verlag: Berlin Heidelberg, 2000.
Orellana	2004	Orellana, G.; García-Fresnadillo, D. in <i>Optical Sensors: Industrial Environmental and Diagnostic Applications</i> , Springer Berlin Heidelberg, Berlin, Heidelberg, 2004, DOI: 10.1007/978-3-662-09111-1_13, pp. 309–357
Orellana	2005	Orellana, G.; Moreno-Bondi, M. C.; Garcia-Fresnadillo, D.; Marazuela, M. D. In <i>Frontiers in Chemical Sensors: Novel Principles and Techniques</i> ; Orellana, G., Moreno-Bondi, M. C., Eds; Springer-Verlag: Berlin Heidelberg, 2005 ; Chapter 3, pp 189–225.
Orellana	2012	Orellana, G.; Muñoz, E.; Gil-Herrera, L. K.; Muñoz, P.; López-Gejo, J.; Palacio, C. Integrated Luminescent Chemical Microsensors Based on GaN LEDs for Security Applications Using Smartphones. <i>Proc. SPIE</i> 2012 , <i>8545</i> , 85450J.
Potje-Kamloth	2008	Potje-Kamloth, K. Semiconductor Junction Gas Sensors. <i>Chem. Rev.</i> 2008 , <i>108</i> , 367–399.
Ren	2011	Ren, F.; Pearton, S. J. Semiconductor Device-Based Sensors for Gas, Chemical, and Biomedical Applications; CRC Press: Boca Raton, 2011 .
Reshchikov	2005	Reshchikov, M. A.; Morkoç, H. Luminescence Properties of Defects in GaN. <i>J. Appl. Phys.</i> 2005 , <i>97</i> , 061301.
Reyes-Valerio	1993	Reyes-Valerio, C. <i>De Bonampak al Templo Mayor: El Azul Maya en Mesoamerica</i> ; Siglo XXI: Mexico D. F., 1993 .
Sanchez	1994	Sanchez, C.; Ribot, F. Design of Hybrid Organic-Inorganic Materials Synthesized via Sol-Gel Chemistry. <i>New J. Chem.</i> 1994 , <i>18</i> , 1007–1047.
Sanchez	2005	Sanchez, C.; Julia, B.; Belleville, P.; Popall, M. Applications of Hybrid Organic-Inorganic Nanocomposites. <i>J. Mater. Chem.</i> 2005 , <i>15</i> , 3559–3592 and references therein.
Sanchot	2015	Sanchot, A.; Consonni, M.; Le Calvez, S.; Robin, I. C.; Templier, F. Color conversion using red quantum dots integrated in a sol-gel on high-brightness blue GaN LEDs. <i>Proc. of 2015 MRS Spring Meeting</i> , April 6–10, 2015 , San Francisco, California.
Seong	2013	Seong, T.-Y.; Han, J.; Amano, H.; Morkoç, H. <i>III-Nitride Based Light Emitting Diodes and Applications</i> ; Springer: Dordrecht, Netherlands, 2013 .
Shircliff	2013	Shircliff, R. A.; Stradins, P.; Moutinho, H.; Fennell, J.; Ghirardi, M. L.; Cowley, S. W.; Branz, H. M.; Martin, I. T. Angle-Resolved XPS Analysis and Characterization of Monolayer and

		Multilayer Silane Films for DNA Coupling to Silica. <i>Langmuir</i> 2013 , <i>29</i> , 4057–4067.
Smith	2008	Smith, E. A.; Chen W. How to Prevent the Loss of Surface Functionality Derived from Aminosilanes. <i>Langmuir</i> 2008 , <i>24</i> , 12405–12409.
Steinhoff	2003	Steinhoff, G.; Purrucker, O.; Tanaka, M.; Stutzmann, M., Eickhoff, M. Al _x Ga _{1-x} N-A New Material System for Biosensors. <i>Adv. Funct. Mater.</i> 2003 , <i>13</i> , 841–846.
Templier	2016	Templier, F. GaN-based emissive microdisplays: A very promising technology for compact, ultra-high brightness display systems. <i>J. Soc. Inf. Disp.</i> 2016 , <i>24</i> , 669–675.
Tran	2007	Tran, C. A.; Chu, C.-F.; Cheng, C.-C.; Liu, W.-H.; Chu, J.-Y.; Cheng, H.-C.; Fan, F.-H.; Yen, J.-K.; Doan T. High brightness GaN vertical light emitting diodes on metal alloyed substrate for general lighting application. <i>J. Cryst. Growth</i> 2007 , <i>298</i> , 722–724
Ueda	2017	Ueda, D. In <i>Power GaN Devices: Materials, Applications and Reliability</i> ; Meneghini, M.; Meneghesso, G.; Zanoni, E., Eds.; Springer: Cham, 2017 ; Chapter 1, pp 1–26.
Valeur	2012	Valeur, B.; Berberan-Santos, M. N. <i>Molecular Fluorescence: Principles and Applications</i> , 2nd Edition; Wiley-VCH: Weinheim, 2012 .
Vashist	2014	Vashist, S. K.; Lam, E.; Hrapovic, S.; Male, K. B.; Luong, J. H. T. Immobilization of Antibodies and Enzymes on 3-Aminopropyltriethoxysilane-Functionalized Bioanalytical Platforms for Biosensors and Diagnostics. <i>Chem. Rev.</i> 2014 , <i>114</i> , 11083–11130.
Wang	2008	Wang, W.; Vaughn, M. W. Morphology and Amine Accessibility of (3-Aminopropyl) Triethoxysilane Films on Glass Surfaces. <i>Scanning</i> 2008 , <i>30</i> , 65–77.
Wang	2014	Wang, X.; Wolfbeis, O. S. Optical Methods for Sensing and Imaging Oxygen: Materials, Spectroscopies and Applications. <i>Chem. Soc. Rev.</i> 2014 , <i>43</i> , 3666–3761.
White	2000	White, L. D.; Tripp, C. P. An Infrared Study of the Amine-Catalyzed Reaction of Methoxymethylsilanes with Silica. <i>J. Colloid. Interface Sci.</i> 2000 , <i>227</i> , 237–243.
Zhu	2012	Zhu, M.; Lerum, M. Z.; Chen, W. How to Prepare Reproducible, Homogeneous, and Hydrolytically Stable Aminosilane-Derived Layers on Silica. <i>Langmuir</i> 2012 , <i>28</i> , 416–423.

3. DEVELOPING AN OPTODE FOR ETHANOL SENSING BASED ON Ru(II) INDICATOR DYES

Did you ever measure a smell? Can you tell whether one smell is just twice strong as another? Can you measure the difference between one kind of smell and another? It is very obvious that we have very many different kinds of smells, all the way from the odour of violets and roses up to asafetida. But until you can measure their likeness and differences, you can have no science of odour. If you are ambitious to find a new science, measure a smell.

— Alexander Graham Bell, 1914

3.1. Introduction

3.1.1. Luminescence-based ethanol sensing

Ethanol (EtOH), or ethyl alcohol, has been known for long time in human history. Most cultures have independently discovered the processes of producing beer and wine (fermentation), and spirits (distillation) [Arnold 1911], and as a matter-of-fact alcohol has been described in important antique pieces like Confucius Analects, Homer poems, the Bible and the Koran. Measuring the amount of ethanol is of great interest for a variety of applications and industrial processes [Lam 2009], both in gas and in liquid phase. One example is during ethanol production via yeast fermentation, in order to control the reaction progress. Another important application is the measurement of the EtOH concentration in alcoholic beverages [Heymann 2017] (for taxation purposes) or in fuel, in which ethanol is used as an additive for octane booster in unleaded gasoline, making for about 25% and 10% in Brazil and USA, respectively, of the total volume in the gasoline consumption [Iodice 2017]. In addition, because of its prominence in vehicular accidents, breathalyzers are very often used for assessing blood alcohol concentration (given the demonstrated correlation between ethanol amount in the blood and driving unfitness). Finally, lower explosive limit (LEL) and upper explosive limit (UEL) of ethanol are 3.3 and 19.0% v/v (33000 – 190000 ppm) in air (at atmospheric pressure and 298 K), respectively [Zabetakis 1965, DrysdaleBrandes 2007]. For this reason, the United States institute for occupational safety and health (NIOSH) set the immediately dangerous to life and health (IDLH) concentration as 10% of the LEL, or 3300 ppm [NIOSH 1995]. Therefore, measuring ethanol vapor concentration in air is of primary importance in ethanol production plants or storehouses.

The oldest and simplest method for the determination of alcohol concerned ethanol determination in fermented products and was densitometry-based: described by Gay-Lussac in 1824 [Lussac 1824], it is still utilized in breweries for assessing ethanol concentration in beers. Another measure based on density is the electronic densimetry, which determines the solution density by electronic measurement of the oscillation frequency of a vibrating U-tube [Brereton 2003]. Novel techniques have been developed more recently in order to improve sensitivity and automation. They are based on chromatography (HPLC or GC) or infrared absorption of the EtOH molecules (FTIR or IR), NMR, Raman and MS [Thungon 2017]. These techniques are precise and reliable, but complex, time consuming and require previous separations processes (distillation, pervaporation), expensive instrumentation and trained operators [Thungon 2017]. For overcoming these disadvantages and for applications where in-situ monitoring is necessary, there has been a growing interest in developing *ethanol sensors*.

The most common ethanol sensors are based on two main technologies. On the one hand, there are chemoresistive sensors based on metal oxides (e.g.: tin dioxide) which electrical resistance changes in presence of reducing molecules. Chemoresistive sensors are simple and cheap, but their main disadvantage is their poor response specificity, which makes them very prone to suffer from interference (see **Figure 36**).

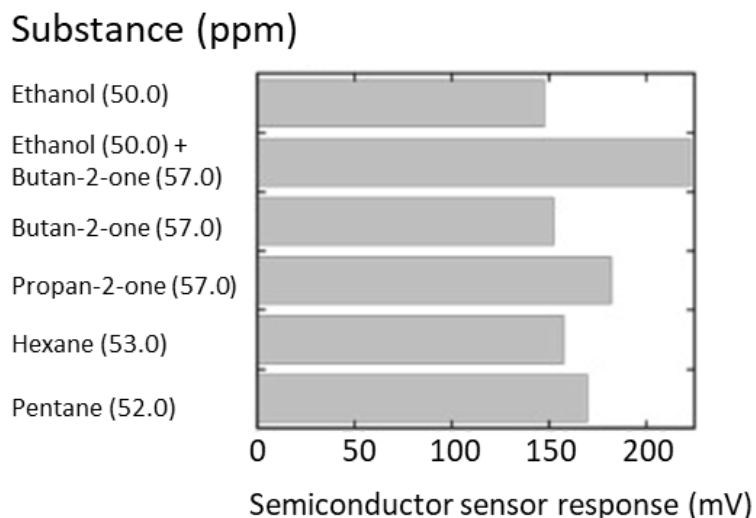


Figure 36. Response of a commercially available semiconductor gas sensor for alcohol testing (type: TGS822, Figaro Engineering Inc., Osaka, Japan), showing interference from other VOCs. Adapted from [Kudo 2010] with permission.

On the other hand, there are electrochemical sensors based on fuel cells, in which ethanol is oxidized at one electrode causing an electric current flow in a circuit [Bay 1972]. Devices belonging to this second family are more expensive but more reliable – portable breath analyzers used by police forces are based on this technology. Both semiconductor-based and fuel cell-based ethanol sensors are widely used but cannot be utilized in some specific applications. For example, they are often not suitable for sensing in presence of flammable or explosive environment, because they must be heated up to high temperatures (usually about 300 °C). Due to the flammability of ethanol vapor, optical sensors are more suitable (sometimes, the only allowed) for sensing applications in these conditions (ATEX directive 2014/34/EU) [DIRECTIVE EU PARLIAMENT 2014, L138 HSE Books 2003].

Amongst all ethanol optical sensors, many are the sensing principles. Some are based on the variation of light interaction with the substance of interest and its ethyl alcohol concentration. Examples are sensors based on acousto-optical phenomena [Askerov 2009] or on changes in the refractive index of different materials, for ex. SnO₂ in different shapes (nanoparticles [Mariammal 2012], nanotubes [Sharifpour-Boushehri 2015]), ZnCdO [Mariammal 2012], carbon nanotubes, fullerene and graphene [Hernaez

2017]. Refractive index-based sensors are very sensitive, but they are weak when it comes to specificity [Sebok 2012, Sharifpour-Boushehri 2015], so they can be no reliable in presence of interfering species.

A strategy to increase selectivity is to exploit the influence of ethanol on the emission of certain luminophores. Some authors took advantage of the fluorescence enhancement of fluorescein (upon hydrogen bond formation) [Zeng 1994] and the fluorescence quenching of polyaromatic-substituted 1,3-oxazoles and -thiazoles when exposed to alcohols (due to intra-molecular charge transfer) [Orellana 1995]. ZnO photoluminescence also is affected by ethanol (which increases the charge carrier density at the semiconductor surface), and hence this oxide has been used for ethanol sensing [Li 2010, Klini 2015]. Additionally, chromo- and fluorophores that interact selectively with alcohols has been reported [Wang 1991, Mohr 2015], exploiting hemiacetal formation reaction of an electron-poor ketone in presence of alcohol.

Ethanol is a polar molecule, so it is possible to manufacture an ethanol sensor based on solvatochromism. Microenvironment surrounding the solvatochromic luminophore causes the changes in position of its ground and excited states. This is normally observed as changes in light absorption and, especially, emission. Simon et al. [Simon 1995] and Carturan et al. [Carturan 2009] reported solvatochromic-based ethanol sensors exploiting fluorescence intensity, whereas Blum et al. [Blum 2001] manufactured sensors based on transreflectance. The sensitivity achieved with these techniques is high, but the dyed polymers were shown to be subject to rapid photobleaching. Moreover, these methods weakness is that they are based on luminescence intensity. With the aim of developing optical sensors with simplified calibration and enhanced signal stability, Mohr et al. [Mohr 2001] experimented coupling a luminophore with long emission lifetime and a chromophore sensitive to ethanol to develop a DLR (dual lifetime referencing)-based system usable for phase shift measurement. The drawback of DLR is that it shares some of the weak points of intensity-based sensors (e.g. photobleaching). For this reason, it should be interesting using luminescence lifetime-based measurements, possibly employing phase shift detection techniques. One example of lifetime-based alcohol sensor is reported in reference [Chang 1997]. The sensor was developed for methanol monitoring in non-polar solvents, but also sensitivity to ethanol and water is shown. However, no attempt to quantify this response and to remove cross-interference due to water or other VOCs was reported.

Theoretically, changes in position of the luminophore ground and excited states due to solvatochromism should be reflected also in its luminescence lifetime, because of the different contribution of non-radiative deactivation pathways (energy gap rule). Experimentally, many other factors influence emission lifetime, so that the correlation between luminescence lifetime and ground - excited state distance is sometimes not trivial to find.

In the following paragraphs, nine Ru(II) complexes which luminescence responds to solvent polarity will be presented. Particularly, three of them have been engineered and synthesized expressly during this thesis. Embedding these dyes in permselective polymers will allow obtain EtOH sensitive materials with increased sensitivity and selectivity.

3.1.2. Ruthenium(II) polypyridyl dyes as polarity probes

Polarity measurements of the microenvironment are of high interest in numerous fields. In particular, fluorescent organic dyes have been widely used as molecular probes of the local environment. The basis is that the probe luminescence features (i.e. position and intensity of its maximum, vibronic fine structure, emission quantum yield, emission lifetime, and polarization) are dependent on the direct environment around the probe [Valeur 2001 a]. In Biology, for example, micropolarity probes are much employed for distinguishing and imaging different microenvironments. Although the typical solvent in biological systems is water, there are significant variations of polarity within proteins, vesicles, cells and tissues [Demchenko 2015, Zhou 2016]. In addition, polarity probes may also detect biomolecular interactions [Klymchenko 2013]. Other important applications of environment-sensitive dyes are monitoring hydrocarbons in water (e.g. fuel leaks [Orellana 2011]) or, conversely, water in non-polar solvents of industrial processes, e.g. during solvents and chemicals production or purification [Jung 2016]. The use of optical sensors to monitor micropolarity has particular advantages, especially because it allows ready miniaturization (with the use of optical fibers), imaging, and unbeatable spatial resolution down to the nanosize [Baù 2011, Lee 2012].

When designing polarity probes, one major complication arises from the loose definition of "polarity". While for a single molecule it generally refers to the internal distribution of its electron density, the interaction between molecules is more complex to describe. In particular, for a minor (solute, probe) and a major component (solvent, surroundings) there are always non-specific interactions that depend mainly on the intrinsic polarity of the solute and on the relative permittivity (ϵ_r) and refractive index (n) of the solvent [Zhou 2016]. In addition, there may be specific interactions such as hydrogen bonding [Kamlet 1976], preferential solvation [Laha 2002, Petrov 2001], acid-base chemistry [Sen Gupta 2016, Tolbert 2002], and induction of charge-transfer [Chen 1998].

3.1.3. Aim

Our aim is to design efficient luminescent polarity probes that can be interrogated with the very same optoelectronic instrumentation currently widespread for O₂ sensing (industrial, environmental, clinical fields, to name a few [Orellana 2004]). The

latter typically uses luminescence lifetime measurements of the indicator dye, normally Ru(II) polypyridyls or porphyrins, most often based on the emission phase shift monitoring. To that end, the goal of this work is to avoid or slow down the interligand hopping, localizing the photoexcited electron on one particular ligand in order to maximize the dipole moment change of the emissive (triplet) excited state, increasing as much as possible the probe response to environmental changes. Electron localization can be achieved by replacing one of the three equivalent bpy moieties of $[\text{Ru}(\text{bpy}_3)]^{2+}$ with another ligand of the 2,2'-bipyridine family bearing electron withdrawing (EW) groups in the 4,4' positions to yield a significantly lower-lying LUMO (lowest unoccupied molecular orbital) [Juris 1988]. The computational methodology exploited to select the most efficient EW groups for this project is reported in the Annex.

The next step will be using the selected luminescent Ru(II) indicator for dying a suitable support in order to manufacture ethanol sensitive spots. The latter will be exploited for monitoring ethanol vapor in air using the portable luminometer. The LOQ has to be lower than 3300 ppm [NIOSH 1995]. The sensor response time must be the shortest possible. Ideally, VOCs and water should not interfere with the signal. The same sensors can be used for monitoring ethanol concentration in alcoholic beverages

3.2. Materials and methods

3.2.1. Materials

3.2.1.1. Indicator dyes

Nine ruthenium complexes have been tested during this thesis for developing ethanol sensors. Three of these indicator dyes were prepared ex novo, while the remaining six had been synthesized previously in our research group.

The three novel heteroleptic indicator dyes (Figure 1) were obtained from the polypyridyl ligands 4,4'-dichloro-2,2'-bipyridine (DCIB), 4,4'-dicyano-2,2'-bipyridine (DCNB), and dimethyl 2,2'-bipyridine-4,4'-dicarboxylate (DCBB) by microwave-assisted synthesis. The ligands were purchased from Fluorochem (Hadfield, UK) and used as received ($\geq 95\%$). The starting cis-Ru(bpy)₂Cl₂ complex has been synthesized following a literature procedure [Sullivan 1978].

- Complex 1: [(4,4'-Dichloro-2,2'-bipyridine)bis(2,2'-bipyridine)]ruthenium(II) bis(hexafluorophosphate), shortened as $[\text{Ru}(\text{bpy})_2(\text{Cl}_2\text{-bpy})]^{2+} [(\text{PF}_6)_2]^{2-}$. Cis-

Ru(bpy)₂Cl₂ (1 eq) and DCIB (1.1 eq) were suspended in a 10 mL 1:1 mixture (v/v) of EtOH and H₂O in a microwave reaction vessel. The latter was capped and purged for 15 min with +99.99% argon. Then the mixture was heated at 110 °C for 30 min in a microwave reactor (Initiator Classic, Biotage®, Uppsala, Sweden). After cooling to room temperature, the EtOH was removed in a rotary evaporator. To the remaining aqueous solution, a saturated aqueous solution of NH₄PF₆ (Alfa Aesar) was added dropwise to precipitate the sought product as its PF₆ salt. After subsequent vacuum filtration, the collected solid was washed with diethyl ether (3 × 10 mL) and dried at 40 °C under reduced pressure (< 1 mbar). Yield: 85%. ¹H NMR (CD₃CN) δ/ppm; J/Hz: 8.59 (H-3^{Cl}-bpy, dd; ⁴J = 1.9, ⁵J = 0.6); 8.49 (H-3,3'-bpy, ddd; ³J = 8.2, ⁴J = 1.5, ⁵J = 0.7); 8.07 (H-4^{bpy}, ddd; ³J = 8.3, ⁴J = 8.1, ⁵J = 2.5); 8.05 (H-4'^{bpy}, ddd; ³J = 8.3, ⁴J = 8.1, ⁵J = 2.5); 7.76 (H-6^{bpy}, ddd; ³J = 5.6, ⁴J = 1.5, ⁵J = 0.7); 7.68 (H-6'^{bpy}, ddd; ³J = 5.6, ⁴J = 1.5, ⁵J = 0.7); 7.66 (H-5^{Cl}-bpy, dd; ³J = 5.8, ⁵J = 1.8); 7.46 (H-6^{Cl}-bpy, dd; ³J = 5.9, ⁴J = 0.6); 7.46 (H-5^{bpy}, ddd; ³J = 8.1, ⁴J = 5.6, ⁵J = 1.5); 7.43 (H-5'^{bpy}, ddd; ³J = 8.1, ⁴J = 5.6, ⁵J = 1.5). The assignment of its NMR data and those of the other luminescent probes followed the work of Orellana et al. [Orellana 1988]. ESI-MS(+) (m/z): Found [M]2+ = 318.9 (calc. for RuC₃₀H₂₂N₆Cl₂₂+ = 319.0); [M]+ = 782.9 (calc. for RuC₃₀H₂₂N₆Cl₂PF₆+ = 783.0).

- Complex 2: [(4,4'-Dicyano-2,2'-bipyridine)bis(2,2'-bipyridine)]ruthenium(II) bis(hexafluorophosphate) shortened as [Ru(bpy)₂((CN)₂-bpy)]²⁺ [(PF₆)₂]²⁻. The same procedure of the 4,4'-dichloro analogue was followed. Yield: 49%. ¹H NMR (CD₃CN) δ/ppm; J/Hz: 9.08 (H-3^{CN}-bpy, dd; ⁴J = 1.8, ⁵J = 0.7); 8.55 (H-3^{bpy}, ddd; ³J = 8.3, ⁴J = 1.3, ⁵J = 0.6); 8.54 (H-3'^{bpy}, ddd; ³J = 8.3, ⁴J = 1.3, ⁵J = 0.6); 8.13 (H-4^{bpy}, ddd; ³J = 8.3, ⁴J = 7.6, ⁵J = 1.4); 8.11 (H-4'^{bpy}, ddd; ³J = 8.3, ⁴J = 7.6, ⁵J = 1.4); 7.98 (H-6^{CN}-bpy, dd; ³J = 5.9, ⁵J = 0.7); 7.85 (H-5^{CN}-bpy, dd; ³J = 5.9, ⁴J = 1.8); 7.74 (H-6^{bpy}, ddd; ³J = 5.6, ⁴J = 1.4, ⁵J = 0.7); 7.69 (H-6'^{bpy}, ddd; ³J = 5.6, ⁴J = 1.4, ⁵J = 0.7); 7.47 (H-5^{bpy}, ddd, ³J = 7.6, ⁴J = 5.6, ⁵J = 1.3); 7.42 (H-5'^{bpy}, ddd; ³J = 7.6, ⁴J = 5.6, ⁵J = 1.3). ESI-MS(+) (m/z): Found [M]2+ = 309.9 (calc. for RuC₃₂H₂₂N₈2+ = 310.0).
- Complex 3: [(4,4'-Dimethoxycarbonyl-2,2'-bipyridine)bis-(2,2'-bipyridine)]ruthenium(II) dichloride, shortened as [Ru(bpy)₂((CO₂CH₃)₂-bpy)]²⁺ [Cl₂]²⁻. The same procedure of the 4,4'-dichloro analogue was followed except that the organic solvent was removed by freeze-drying so that the metal complex was obtained as its chloride salt. Yield: 94%. ¹H NMR (CD₃CN) δ/ppm; J/Hz: 9.08 (H-3^{Ac}-bpy, dd; ⁴J = 1.8, ⁵J = 0.7); 8.94 (H-3^{bpy}, ddd; ³J = 8.3, ⁴J = 1.3, ⁵J = 0.7); 8.93 (H-3'^{bpy}, ddd; ³J = 8.3, ⁴J = 1.3, ⁵J = 0.7); 8.16 (H-4^{bpy}, ddd; ³J = 8.3, ⁴J = 7.6, ⁵J = 1.5); 8.14 (H-4'^{bpy}, ddd; ³J = 8.3, ⁴J = 7.6, ⁵J = 1.5); 8.03 (H-6^{Ac}-bpy, dd; ³J = 5.9, ⁴J = 0.7); 7.86 (H-5^{Ac}-bpy, dd; ³J = 5.9, ⁴J = 1.8); 7.75 (H-6^{bpy}, ddd; ³J =

5.6, $^4J = 1.5$, $^5J = 0.7$); 7.72 (H-6'^{bpy}, ddd; $^3J = 5.6$, $^4J = 1.5$, $^5J = 0.7$); 7.48 (H-5^{bpy}, ddd; $^3J = 7.6$, $^3J = 5.6$, $^4J = 1.3$); 7.44 (H-5'^{bpy}, ddd; $^3J = 7.6$, $^3J = 5.6$, $^4J = 1.3$); 4.01 ($\text{CH}_3\text{Ac-}^{bpy}$, s). ESI-MS(+) (m/z): Found [M] $^{2+} = 342.7$ (calcd for $\text{RuC}_{34}\text{H}_{28}\text{N}_6\text{O}_{42+} = 343.0$); [M] $^{+} = 830.9$ (calcd for $\text{RuC}_{34}\text{H}_{28}\text{N}_6\text{O}_4\text{Cl}_2 \cdot \text{CH}_3\text{CN} \cdot \text{CH}_3\text{OH} = 831.1$).

- Complex 4: [4,4'-(N,N'-dioctadecyl-)dicarboxamide-2,2'-bipyridine]bis(2,2'-bipyridine)ruthenium(II) bis(hexafluorophosphate), shortened as $[\text{Ru}(\text{nbpy})_2(\text{nody})^{2+}] [\text{(PF}_6\text{)}_2]^{2-}$, synthesized as described in [Ribeiro dos Santos 2014];
- Complex 5: tris[4,4'-(N,N'-dioctadecyl-)dicarboxamide-2,2'-bipyridine]ruthenium(II) dichloride, shortened as $[\text{Ru}(\text{nody})_3]^{2+} [\text{Cl}_2]^{2-}$, synthesized as described in [Ribeiro dos Santos 2014];
- Complex 6: tris(4,4'-dinonyl-2,2'-bipyridine)ruthenium(II) dichloride, shortened as $[\text{Ru}(\text{nbpy})_3]^{2+} [\text{Cl}_2]^{2-}$, synthesized as described in [Castro 2005];
- Complex 7: [bis(1,4,5,8-tetraaza-phenanthrene)(1,10-phenanthroline-5,6-dione)ruthenium(II) dichloride, shortened as $[\text{Ru}(\text{tap})_2(\text{pd})]^{2+} [\text{Cl}_2]^{2-}$, (Hall 1995);
- Complex 8: tetrasodium tris(4,4'-Dicarboxy-2,2'-bipyridine)ruthenate, shortened as $[\text{Ru}(\text{dcb})_3]^{4-} [\text{Na}_4]^{4+}$, (Freys 2012).
- Complex 9: tris(4,7-diphenyl-1,10-phenanthroline)ruthenium(II) bis(hexafluorophosphate), shortened as $[\text{Ru}(\text{dpp})_3]^{2+}$, synthesized following [Garcia-Fresnadillo 1996].

3.2.1.2. Reagents, solvents, polymers and additives

Water was purified with a Millipore Direct-Q₃-UV system (Bedford, MA). Organic solvents were of HPLC grade and used without further purification. Sulfonated tetrafluoroethylene based fluoropolymer-copolymer (Nafion[®], 50 μm-thick film), Polyvinyl chloride powder (PVC, average Mw ~80,000), polystyrene beads (PS, average Mw 280,000), Bis(2-ethylhexyl) sebacate (DOS), 2-Nitrophenyl octyl ether (NPOE) were purchased from Merck KGaA (Darmstadt, Germany), poly(1-trimethylsilyl-1-propyne) (PTMSP) was purchased from Gelest (Morrisville, PA), Cyclo-olefin polymer (ZEONOR[®]) was from microfluidic ChipShop GmbH (Jena, DE). One component polydimethylsiloxane (PDMS 3140 RTV COATING) was obtained from DOW CORNING[®] (Midland, MI).

3.2.1.3. Gases

- Nitrogen Premier (purity 5.2, Carburos Metálicos, Barcelona, ES).
- Oxygen, extrapure (purity 4, Praxair, Danbury, CT).
- Air L-50 (purity 4, Praxair).

3.2.1.4. Luminescent film preparation

Luminescent films were made following different methods depending on the polymer:

1. PVC, PS, PTMSP, and Zeonor®: polymer, luminescent indicator dye and additives (e.g. plasticizers for PVC) were dissolved in an apt solvent obtaining a homogeneous gel, which was then poured into a glass vial. A film of controlled thickness was produced after evaporation of the solvent. The film was peeled off with tweezers and then circles (dia. = 0.8 cm) were cut with a biopsy punch (Integra™ Miltex®).
2. PDMS: prepolymer mixture and dye were mixed into a glass vial with the aid of a glass bar and then poured directly onto a sheet of biaxially oriented polyethylene terephthalate (Mylar, 20 × 20 × 0.1 mm, Goodfellow, Huntingdon, UK). It was hence knife-coated with the aid of a mask of known thickness (approx. 100 µm). The film was finally left curing for at least 48 h and then circles (dia. = 0.8 cm) were cut with a biopsy punch.
3. 50 µm-thick Nafion® film (Raynham, MA) was cut into pieces (10 × 10 mm approx). After washing in 1 M HNO₃, it was rinsed with H₂O and then Li-exchanged stirring it in an aqueous solution of LiOH (1 M) overnight. Then, the pieces were introduced individually in 2 ml dye solution in MeOH (5 × 10⁻⁵ M) and left overnight, until the solution was transparent and the film was yellow-orange colored.

3.2.2. Measurements and instrumentation

For spectroscopic characterization, HPLC grade solvents were dried over 3 Å molecular sieve for at least one week prior to use. The ¹H-NMR spectra have been obtained at the UCM Central NMR Instrumentation Facilities with a Bruker DPX 300MHz spectrometer. ESI-MS spectra were recorded at the UCM Central MS Facilities (Madrid, Spain) on a LTQ XL linear ion trap mass spectrometer fitted with an electrospray ionization (ESI) sample inlet.

3.2.2.1. UV-Vis absorption, luminescence spectra and kinetics of the excited state deactivation

Dye solutions. UV-VIS absorption spectra were recorded using a Varian Cary 3-Bio (Palo Alto, CA, USA) at 25 °C. Luminescence was measured using a Horiba Fluoromax-4TCSPC spectrofluorometer (NJ). The dyes solutions were analyzed into 1-cm pathlength Suprasil cells (Hellma, Mülheim, Germany). All emission spectra were corrected, after subtracting the signal of the pure solvent obtained in the same conditions. The correction curve was obtained with a calibrated irradiance lamp (Oriel Instruments). Emission lifetime measurements were carried out with an Edinburgh Instruments FL-980 TCSPC fluorometer equipped with a Horiba NanoLed-470LH laser diode (<1-ns 463-nm pulses at 1.0 MHz). A 470-nm interference filter (Chroma HQ470/20x, Rockingham, VT) as excitation filter, and a 500 nm cutoff filter (Chroma HQ 500LP) as emission filter were employed. Exponential luminescence decays were measured with a 10 or 50 µs window (1,024 channels) by accumulating at least 10,000 counts in the peak channel, and emission lifetimes were extracted from the exponential curve fittings using the proprietary Marquardt-Levenberg non-linear least squares fit algorithm (without deconvolution) for stable chi-squared minimization ($\chi^2 < 1.05$ in all cases).

Dyed polymer films. The same equipment was used for characterizing the dyed films, which were supported on a transparent plastic (Mylar®) and placed in a Suprasil 101-QS cuvette (Hellma). For collecting luminescence spectra and decays, the films were placed in the Horiba Fluoromax-4TCSPC spectrofluorometer in front face configuration, tilted at an angle of 55° with respect to the excitation beam (with a goniometric stage) in order to minimize the scattering light. When recording emission spectra, the excitation wavelength was selected to match the film absorption maximum obtained from UV-Vis absorption spectra. Emission lifetimes were determined as described for the dyes solutions.

3.2.2.2. Phase-sensitive luminescence measurements

Phase-sensitive monitoring was carried out with a field-deployable fiberoptic phase-sensitive luminometer developed in our research group. The instrument is able to determine simultaneously up to four target parameters (e.g. temperature, O₂, moisture, CO₂), or a single parameter in different locations, using common electronic and optoelectronic components but specific Ru(II) polypyridyls immobilized in tailored polymer supports. The system is equipped with four 470 nm LEDs (9600 mcd, RS Amidata, Madrid, Spain) as excitation light sources, digitally modulated at 39, 78 or 156 KHz (user selectable). The optical module contains a 450 nm CS5-60 colored band-pass filter (100 nm FWHM) (Kopp Glass, Pittsburgh, PA) in the excitation channel, a 503 nm dichroic filter (Edmund Optics, York, UK), and a 570 nm long-pass

filter (CS2-73, Kopp), plus a plano-convex lens with 4 mm effective focal length (Edmund) in the emission channel. The excitation light is focused onto a 1000 μm multimode plastic optical fiber (Mitsubishi Cable, Tokyo, JP) fitted with a SMA connector (Ratioplast Optoelectronics, Lübbeke, DE). The luminescence from the four sensitive terminals is monitored with a H11901-01 compact photomultiplier (Hamamatsu Photonics, Hamamatsu, JP). The reference signal is obtained directly from the excitation blue LEDs with one Hamamatsu S5821-03 photodiode per optical channel. The system is also provided with a remote analog output temperature sensor (LM335, Texas Instrument, Dallas, Texas) to correct the possible sensor response for temperature effects. The instrument configuration and data are stored in the unit and can be transferred at any time to and from a laptop computer via the RS232 or USB ports, using our Windows-based software [Orellana 2004b].

EtOH monitoring in gas stream (Figure 37). Luminescent sensitive films were introduced in a thermostated (F12-ED, Julabo GmbH, Seelbach, Germany) stainless-steel flow-through cell. The film response to gas stream, pure or enriched with the analyte of interest, was monitored with the phase-sensitive luminometer unit attaching one of its 3 mm fused silica bifurcated fiber bundles to the flow-through cell via a Teflon® adaptor. Synthetic air or pure N₂, which mass flow rate was controlled by an electronic mass flow controller (MFC) manifold (PIDEng&Tech: Madrid, ES), was enriched flowing through a thermostated (F12-ED, Julabo) bubbler containing ethanol (or water, methanol, acetonitrile, ethyl acetate, acetone, when testing the effect of interferences). In this way, it was possible to generate a known pressure of the species, calculated through the so-called “Antoine equation”, a semi-empirical correlations describing the relation between vapor pressure and temperature for pure components [Antoine 1888]. For calibration purpose, a second (diluent) gas, controlled with a second MFC, was mixed to the saturated (carrier) gas. The setup was monitored with two rotameters to assure no gas was leaching out.

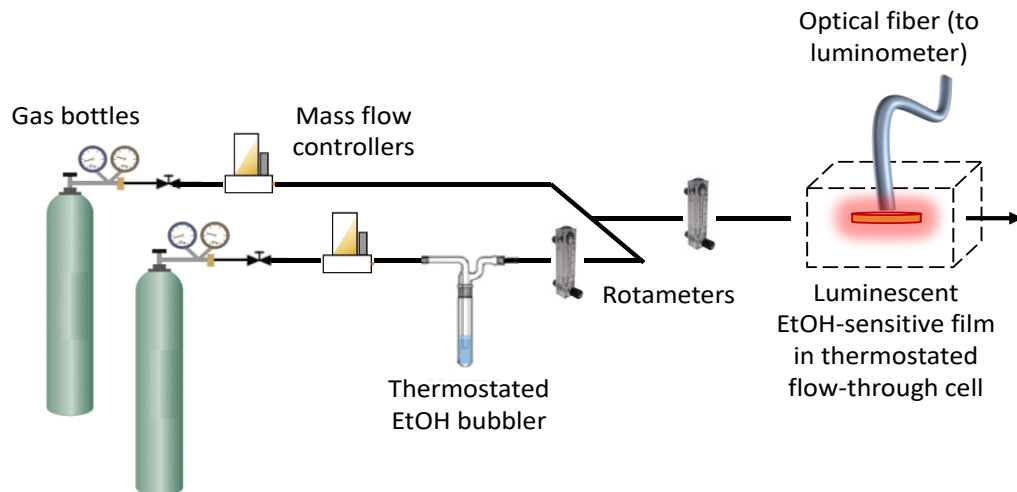


Figure 37. Experimental setup for EtOH monitoring in gas stream.

EtOH monitoring in water-ethanol solutions headspace (monitoring ethyl alcohol in alcoholic beverages or water-saturated environment) (**Figure 38**). 100 ml glass bottles (with B29 orifice) were filled with 50 ml aqueous solutions containing ethanol in different concentration (by volume). The luminescence sensitive film was placed at the distal end of an optical fiber, which was then inserted through a perforated rubber septum (B29). For measuring in the headspace of a bottle, the septum was inserted into the bottle bore as cap.

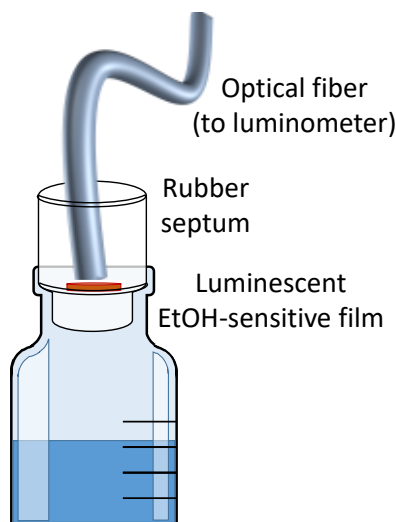


Figure 38. Experimental setup for EtOH monitoring in water-ethanol solutions headspace.

Vapor concentration in the headspace was calculated using the “Dubowski equation” [Dubowski 1975], a derivation of the Raoult’s Law that correlates alcohol concentration in the enriching solution and alcohol concentration in the enriched gas:

$$C_{EtOH}^{gas} = C_{EtOH}^{H2O} k_1 e^{k_2 T} \quad [19]$$

where C_{EtOH}^{gas} is the concentration in mg/l of ethanol in the enriched gas stream, C_{EtOH}^{H2O} is the concentration in g/l of ethanol in the solution, T is the temperature in °C, and k_1 and k_2 are two empirical constants that depend on the compound of interest – in case of ethanol they are 0.04145 (mg/l)/(g/l) and 0.06583 (1/°C), respectively.

3.3. Results and discussion

The work’s goal is the development of a luminescence-based sensor for EtOH monitoring. Particularly, it should be based on portable optoelectronic equipment for luminescence measurements with phase-sensitive detection capable of simultaneous measurement of several parameters for personal interest/safety at the workplace relevance. This task can be fulfilled by using a plurality of robust indicator dyes of the same family having similar excitation/emission properties but each one just sensitive

to a single chemical parameter [Orellana 2004 a]. This approach would allow using a single optoelectronic instrumentation that, by simple exchanging the sensitive terminal at the distal end of an optical fiber, can sense a wide range of chemical species. So far, the indicators that present the most suitable spectroscopic characteristics are ruthenium (II) complexes with polyazaheterocyclic chelating ligands (see Introduction).

3.3.1. Spectral features of the three novel indicator dyes

Because of the presence of the heavy central atom, the multiplicity of the electronic state that absorbs the excitation photon and that of the one that decays from the (triplet) excited state back to the (singlet) ground state is not the same. For this reason, Ru(II) dyes do not always behave as expected from the L-M model. Nevertheless, because these dyes are novel, we found the L-M model useful to characterize the dyes sensitivity to polarity.

Focusing on medium to highly polar solvents, in which the ionic Ru(II) polypyridyls are soluble, the absorption and emission spectra of complexes 1, 2 and 3 generally shift hypsochromically with increasing polarity of the solvents (**Figure 39**, **Figure 40**, **Figure 41**, respectively). The maxima of the longest wavelength transition and of the emission band, together with the corresponding Stokes shifts, are collected in **Table 4**.

The so-called Lippert-Mataga plot (i.e., the plot of Stokes shifts vs the polarizability term, as described in paragraph 1.1.4.2) are plotted in **Figure 42**, **Figure 43**, and **Figure 44** for complexes 1, 2 and 3, respectively. The variation of λ_{abs}^{max} in this range (≤ 6 nm) is small compared to the variations of λ_{em}^{max} (≤ 27 nm) as expected from the much larger change in the dipole moment of the dye in going from the $^3\text{MLCT}$ to the ground state than from the latter to the (initially) delocalized $^1\text{MLCT}$ state (see above).

Protopgenic solvents are not usually included in the Lippert-Mataga theory because they can interact with the probe. In the case of complex 2, for example, the $\text{C}\equiv\text{N}$ group reacts with water, ethyl alcohol and methyl alcohol. For this reason, the values obtained in these solvents have been depicted in the graphs (red dots) but not included in the linear fits.

This characterization proves that these three novel complexes can be used as polarity probes, so that they will be tested in the next paragraph for developing an ethanol sensor.

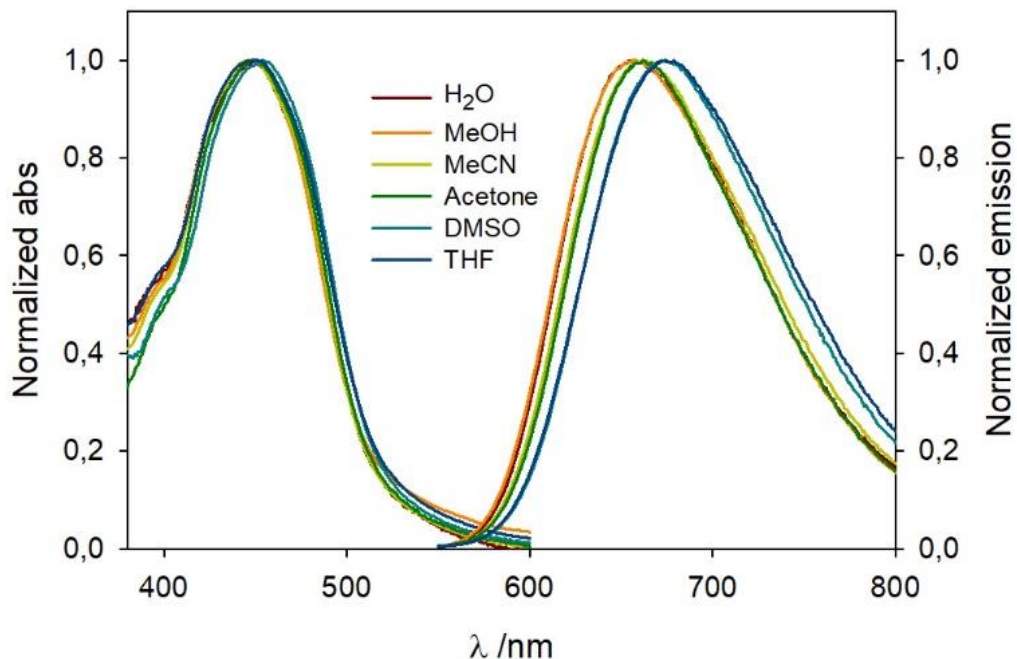


Figure 39. Normalized absorption and emission spectra of $[\text{Ru}(\text{bpy})_2(\text{Cl}_2\text{-bpy})]^{2+}$ in various solvents.

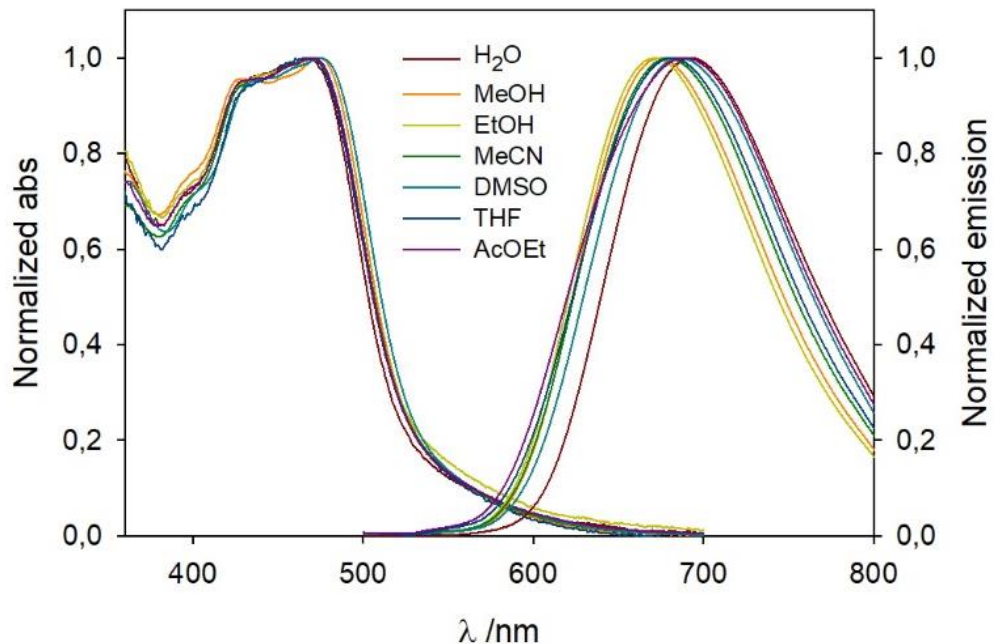


Figure 40. Normalized absorption and emission spectra of $[\text{Ru}(\text{bpy})_2((\text{CN})_2\text{-bpy})]^{2+}$ in various solvents.

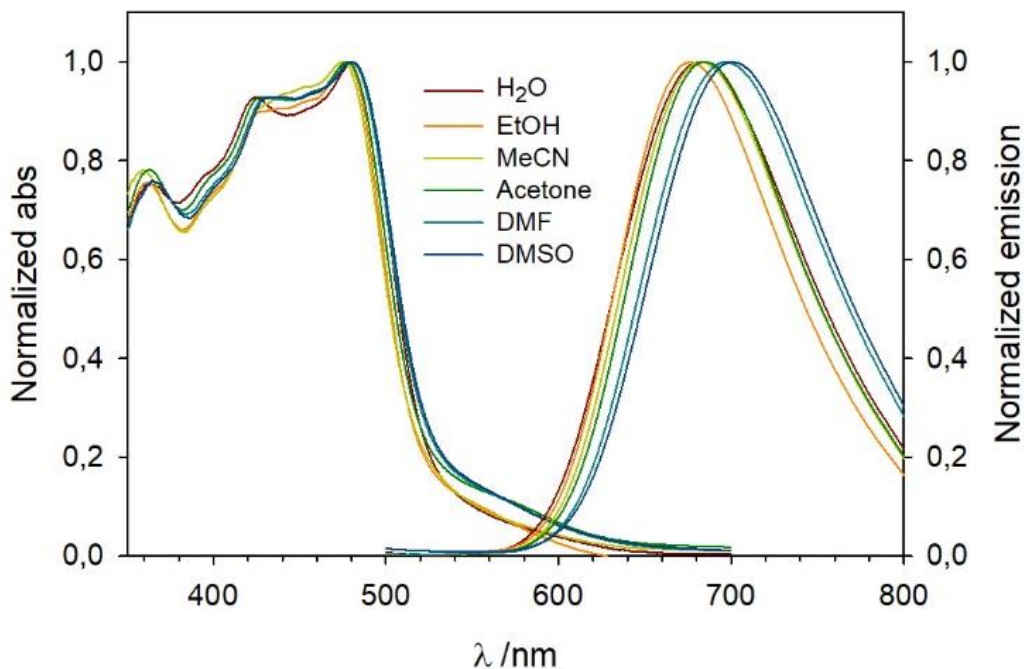


Figure 41. Normalized absorption and emission spectra of $[\text{Ru}(\text{bpy})_2((\text{COOCH}_3)_2\text{-bpy})]^{2+}$ in various solvents.

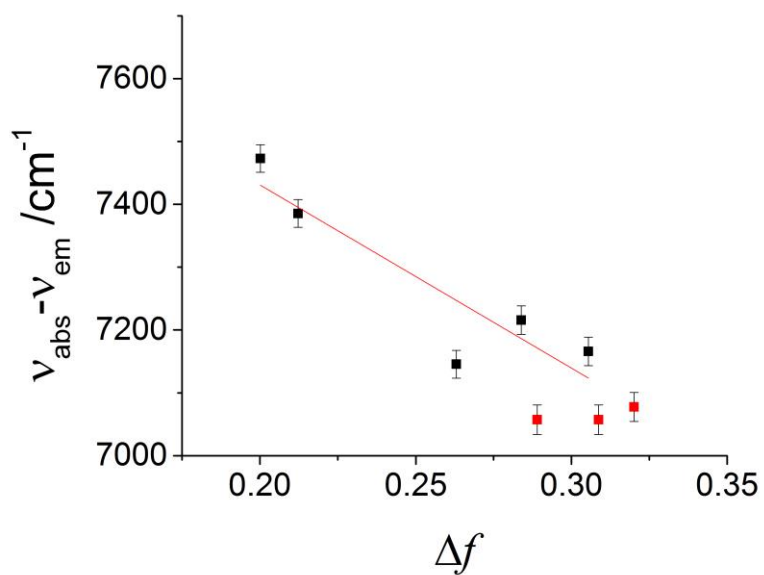


Figure 42. Lippert-Mataga plot for $[\text{Ru}(\text{bpy})_2(\text{Cl}_2\text{-bpy})]^{2+}$. The data depicted in red correspond to the protogenic solvents (EtOH, MeOH, and H₂O). They have not been included in the linear fits to determine the experimental L-M slope (see text).

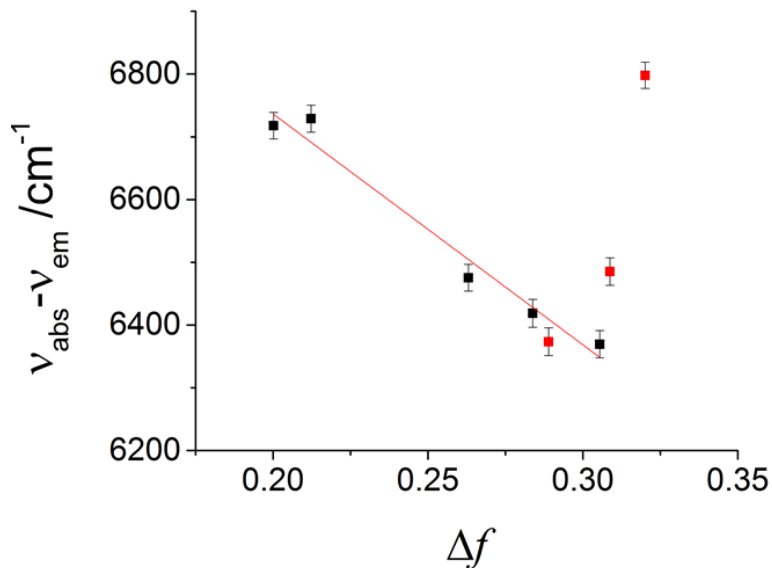


Figure 43. Lippert-Mataga plot for $[\text{Ru}(\text{bpy})_2((\text{CN})_2\text{bpy})]^{2+}$. The data depicted in red correspond to the protogenic solvents (EtOH, MeOH, and H₂O). They have not been included in the linear fits to determine the experimental L-M slope (see text).

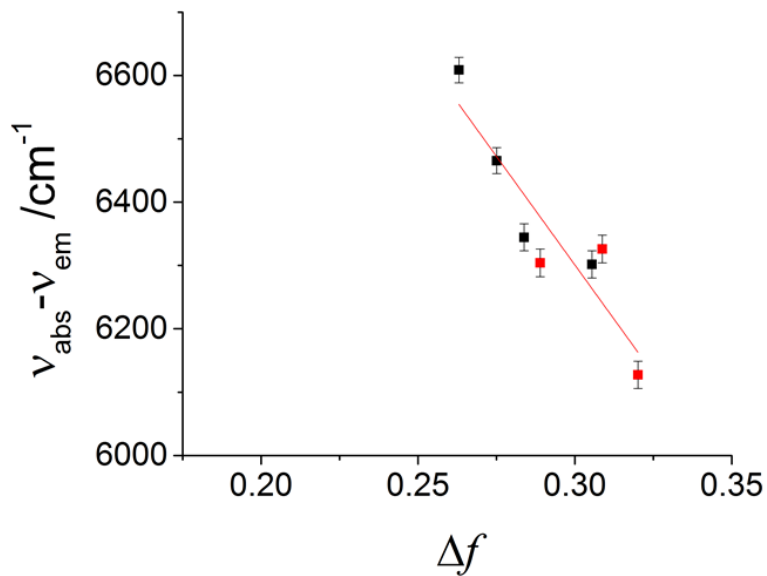


Figure 44. Lippert-Mataga plot for $[\text{Ru}(\text{bpy})_2((\text{COOCH}_3)_2\text{bpy})]^{2+}$. The data depicted in red correspond to the protogenic solvents (EtOH, MeOH, and H₂O). They have not been included in the linear fits to determine the experimental L-M slope (see text).

Table 4. Polarity parameter (Δf), maximum of the visible absorption and emission bands, and Stokes shifts of Ru(II) complexes 1, 2, and 3 in different solvents.

Complex	Solvent	Δf^a	λ_{abs}^{\max} /nm ^b	λ_{em}^{\max} /nm	$\nu_{abs} - \nu_{em}$ /cm ⁻¹	L-M Slope ^c
1	H ₂ O	0.320	448	656	7078	
	Methanol	0.309	447	653	7057	
	Acetonitrile	0.305	449	662	7166	
	Ethanol	0.289	447	653	7057	-2900
	Acetone	0.284	448	662	7216	± 800
	Dimethyl sulfoxide	0.263	454	672	7145	
	Tetrahydrofuran	0.212	450	674	7385	
	Ethyl acetate	0.200	450	678	7473	
2	H ₂ O	0.320	472	695	6798	
	Methanol	0.309	469	674	6485	
	Acetonitrile	0.305	474	679	6370	
	Ethanol	0.289	470	671	6373	-3700
	Acetone	0.284	469	671	6419	± 400
	Dimethyl sulfoxide	0.263	475	686	6475	
	Tetrahydrofuran	0.212	467	681	6729	
	Ethyl acetate	0.200	471	689	6718	
3	H ₂ O	0.320	481	682	6127	
	Methanol	0.309	474	677	6326	
	Acetonitrile	0.305	477	682	6302	
	Ethanol	0.289	474	676	6304	
	Acetone	0.284	477	684	6344	± 1300
	N,N-dimethylformamide	0.275	480	696	6466	
	Dimethyl sulfoxide	0.263	480	703	6609	
	Tetrahydrofuran	0.212	ns ^d	ns ^d	ns ^d	

^a Eq. [6]. ^b Longest wavelength MLCT transition. ^c Slope of the Lippert-Mataga plot, see eq. [5]. ^d Not soluble.

3.3.2. Manufacturing the EtOH-sensitive luminescence films

3.3.2.1. Ru(II) indicator dyes: selection and photophysical properties

Polarity sensitivity can be exploited for preparing EtOH sensitive films if the dye is supported in a permselective polymer film that allows preferential permeation of EtOH while blocking other polar analytes (e.g.: H₂O, a possible interference when applying the sensor to EtOH measurement in breath, alcoholic beverages or fermentation wort). As a first step, the photochemical and photophysical properties of polymer films dyed with nine different Ru(II) luminescent dyes were studied in dry air, ethanol-saturated air and water-saturated air (**Table 5**). Three dyes have been prepared on purpose during this thesis for polarity sensitive application (see previous paragraph). Four had been studied as polarity sensitive indicator dyes in literature: two had been characterized in solvent of different polarity in a previous thesis in our group ([Ru(nbpy)₂(nody)]²⁺ and [Ru(nody)₃]²⁺, [Ribeiro dos Santos 2014]); one had been used, again in our group, for hydrocarbon in water sensing ([Ru(nbpy)₃]²⁺, [Castro 2005]); the last one had been reported by Chang et al. for sensing methanol in apolar environment ([Ru(dcb)₃]²⁺, [Chang 1997]), although it had already been reported in the publication that sensitivity towards EtOH was lower than towards MeOH. Another metal complex studied was [Ru(tap)₂(pd)]²⁺: the reasoning behind this choice was that the aromatic ketone (in the 1,10-Phenanthroline-5,6-dione ligand) could react reversibly with ethanol giving the corresponding hemiacetal. This reaction was expected to influence the optical properties of the compound and allow its use as indicator dye. Finally, [Ru(dpp)₃]²⁺, typically used for O₂ sensing, was taken as a control. The comparison between the different Ru(II) dyes was done in plasticized PVC, because of the ease of preparation of dyed films using this polymer.

The highest difference in absence and presence of the analyte was found for [Ru(dcb)₃]²⁺ (in Nafion®) and [Ru(nbpy)₂(nody)]²⁺ (both in Nafion® and plasticized PVC). The selected indicator dye was the latter, because Nafion® was considered unsuited as polymer matrix (see next paragraph).

Table 5. Selected dyes and pre-exponentially weighted luminescence lifetime of the dyed films (if not stated differently, films are made with 8 mg PVC + 8 mg DOS, and dye concentration is 6×10^{-10} mol of dye/mg of polymer) in air, ethanol-saturated air and water-saturated air. $T = 25^\circ\text{C}$.

Indicator dye	$\tau_M/\mu\text{s}$ air ^a	$\tau_M/\mu\text{s}$ EtOH- saturated air ^{a,b}	$\tau_M/\mu\text{s}$ H ₂ O- saturated air ^{a,c}
[Ru(dpp) ₃] ²⁺	3.44	3.25	3.42
[Ru(nbpy) ₃] ²⁺	0.93	0.60	0.84
[Ru(nody) ₃] ²⁺	0.81	0.81	0.84
[Ru(dcb) ₃] ²⁺	0.55	0.59	0.48
[Ru(nbpy) ₂ (nody)] ²⁺	1.40	1.01	1.31
[Ru(bpy) ₂ (Cl ₂ -bpy)] ²⁺	1.07	0.85	1.01
[Ru(bpy) ₂ ((CN) ₂ -bpy)] ²⁺	0.80	0.71	0.80
[Ru(bpy) ₂ ((CO ₂ CH ₃) ₂ -bpy)] ²⁺	1.32	1.08	0.59
[Ru(tap) ₂ (pd)] ²⁺	1.00	0.79	0.91
[Ru(dcb) ₃] ^{2+,d}	2.99	2.22	2.37
[Ru(nbpy) ₂ (nody)] ^{2+,d}	1.57	0.74	0.89

^a Uncertainty: $\pm 5\%$.

^b 83700 ppm EtOH.

^c 33700 ppm H₂O.

^d The polymer matrix was Nafion® (4×10^{-9} mol indicator dye/mg Nafion®)

3.3.2.2. Selection of the polymer matrix

The selected EtOH-sensitive luminescent dye has to be supported in a permselective polymer film that allows preferential permeation of EtOH. Six different polymers were studied, selected from two groups. On one hand, polymers widely used for manufacturing optical sensors (i.e., PVC, PS and Nafion®), so that the manufacturing strategies were well known. On the other hand, polymers particularly reported in literature for permselective membranes or EtOH/H₂O separation (i.e., PDMS [Vane 2008, Lai 2012, Klini 2015], PTMSP [Masuda 1990, González-Velasco 2002] and COP

Zeonor® [Nagamura 2010]). Important advantages of these polymers for optodes development are their commercial availability, high mechanical stability and ease of preparation.

Dyed films manufactured starting from the different polymers, prepared following the aforementioned methods, have been tested in pure N₂, EtOH-saturated N₂ and H₂O-saturated N₂ (**Table 6**).

Table 6. Luminescence phase shift and response time of [Ru(nbpy)₂(nody)]²⁺ dyed polymer films (6×10^{-10} mol of dye/mg of polymer) in N₂, EtOH-saturated N₂ and H₂O-saturated N₂. $T = 25^\circ\text{C}$.

Polymer matrix (thickness/ μm)	$\phi \text{ N}_2/\%$	$\phi/\%$ EtOH-saturated N ₂ ^a	$t_{90\downarrow} \text{ EtOH}^{\text{b}}/\text{s}$ $t_{90\uparrow} \text{ EtOH}^{\text{c}}/\text{s}$	$\phi/\%$ H ₂ O-saturated N ₂ ^d	$t_{90\downarrow} \text{ H}_2\text{O}^{\text{e}}/\text{s}$ $t_{90\uparrow} \text{ H}_2\text{O}^{\text{f}}/\text{s}$
PVC ^g (160 ± 30)	26.0	17.6	230 ± 30 320 ± 22	23.9	147 ± 19 196 ± 33
PS (80 ± 20)	24.3	22.9	375 ± 32 425 ± 37	23.1	92 ± 7 242 ± 16
PDMS ^h (135 ± 5)	35.2	31.2	105 ± 21 119 ± 21	33.8	61 ± 15 122 ± 18
Nafion® ⁱ (50 ± 3)	28.6	14.5	147 ± 39 1248 ± 120	17.1	169 ± 42 2632 ± 398
PTMSP (160 ± 20)	12.0	13.2	65 ± 8 165 ± 21	13.3	42 ± 4 69 ± 8
Zeonor® (140 ± 10)	6.7	6.0	41 ± 4 40 ± 11	6.5	58 ± 9 40 ± 6

^a 83700 ppm EtOH.

^b response time for 90% signal change from 0 to 83700 ppm EtOH in N₂.

^c response time for 90% signal change from 83700 to 0 ppm EtOH in N₂.

^d 33700 ppm H₂O.

^e response time for 90% signal change from 0 to 33700 ppm H₂O in N₂.

^f response time for 90% signal change from 33700 to 0 ppm H₂O in N₂.

^g with plasticizer (DOS).

^h dye concentration not calculated.

ⁱ 4×10^{-7} mol indicator dye/mg Nafion®. Commercially available films of 50 μm thickness.

PVC was selected as polymer matrix, because it exhibited very high analytical response in presence of ethanol, low water interference, and reasonably fast response and recovery time. Nafion® is actually the polymer that led to the most sensitive optodes: due to its affinity for ethanol, in fact, Nafion® acts as a preconcentration

medium for this species. The drawback is that EtOH preconcentration also leads to long response and recovery time during measurements. Moreover, optodes made with Nafion® are also much more affected by ambient humidity and oxygen, being the permeation of these species significantly higher than in PVC.

3.3.2.3. Photochemical characterization of the dyed films

Absorption and luminescence of $[\text{Ru}(\text{nbpy})_2(\text{nody})]^{2+}$ in solvents of different polarity has been reported in [Ribeiro dos Santos 2014] (Figure 45).

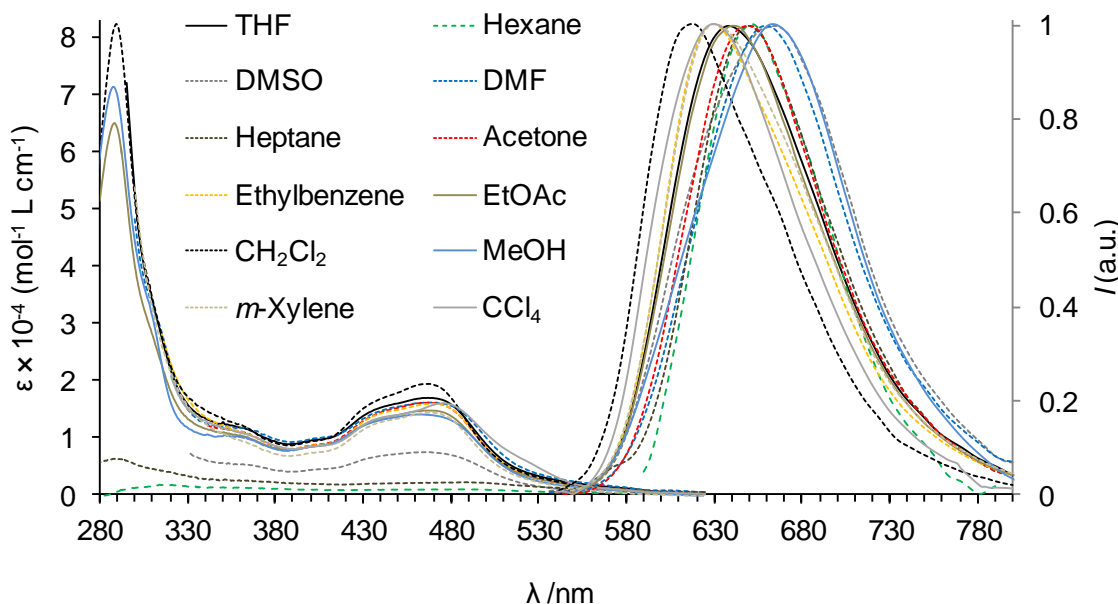


Figure 45. Absorption (left axis) and normalized emission (right axis, corrected for the instrument response) spectra of $10 \mu\text{M} [\text{Ru}(\text{nbpy})_2(\text{nody})](\text{PF}_6)_2$ in tetrahydrofuran (THF), hexane, dimethyl sulfoxide (DMSO), *N,N*-dimethylformamide (DMF), heptane, acetone, ethylbenzene, ethyl acetate (EtOAc), dichloromethane (CH_2Cl_2), methanol (MeOH), *m*-xylene and carbon tetrachloride (CCl_4). Reproduced from [Ribeiro dos Santos 2014] with permission.

From comparison with the spectra in solution, absorption and luminescence of the dye embedded in plasticized PVC (Figure 46, black solid line) resemble those obtained in solution in CH_2Cl_2 , which was expected due to the similarity of the latter and the vinyl chloride monomer. The film luminescence maximum is at 618 nm.

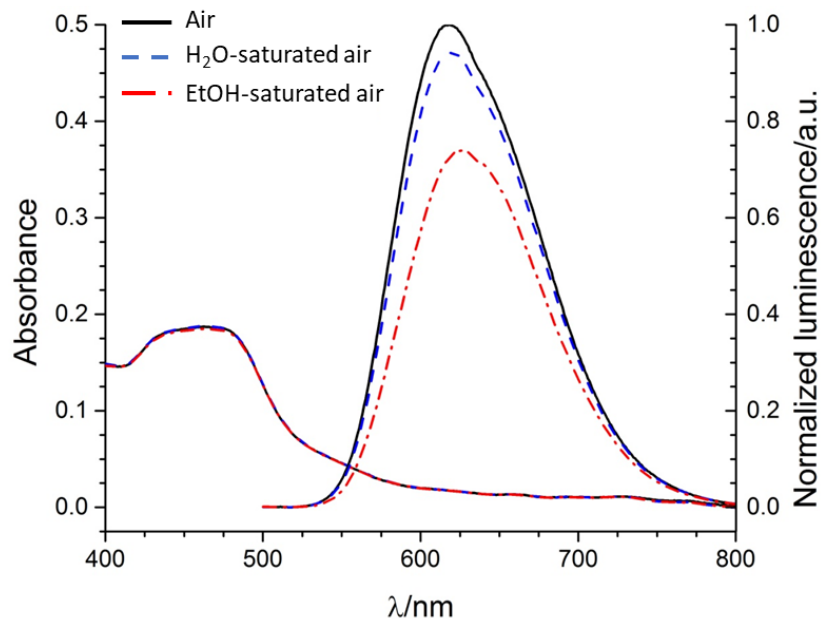


Figure 46. Absorbance and emission spectra (corrected for instrumental response) of a $[\text{Ru}(\text{nbpy})_2(\text{nody})]^{2+}$ /PVC film in air, water-saturated air and ethanol-saturated air ($\lambda_{\text{exc}} = 466 \text{ nm}$, $T = 25^\circ\text{C}$).

Going from air to H_2O -saturated air (about 34000 ppm at 25°C), the film luminescence decreases about 5% and shifts bathochromically 2 nm (Figure 46, blue dashed line). The effect is even greater (decrease about 25% and redshift of 9 nm) when air is saturated with EtOH (about 84000 ppm of ethanol at 25°C) (Figure 2, red dashed-dotted line).

Table 7. Luminescence lifetime obtained from the bi-exponential fit ($i = 2$) of the experimental emission decays of the $\text{Ru}(\text{nbpy})_2(\text{nody})^{2+}$ /plasticized PVC film under air, water-saturated air and ethanol-saturated air. $T = 25^\circ\text{C}$. Atmospheric pressure: $710 \pm 5 \text{ Torr}$. $\lambda_{\text{exc}} = 466 \text{ nm}$; $\lambda_{\text{em}} = > 550 \text{ nm}$.^{a,b}

Atmosphere	$\tau_1/\mu\text{s}$ (%1)	$\tau_2/\mu\text{s}$ (%2)	$\tau_M/\mu\text{s}^c$
Air	0.98 (37)	1.90 (63)	1.56
H_2O sat. air	0.96 (44)	1.83 (56)	1.45
EtOH sat. air	0.77 (48)	1.51 (52)	1.15

^a $I(t) = I_0 + \sum_i \alpha_i e^{-t/\tau_i}$ ($1 \leq i \leq 3$); $\%_i = \alpha_i \tau_i / \sum_i \alpha_i \tau_i$ ($1 \leq i \leq 3$). ^b Estimated maximum uncertainty: 7% for τ_1 , 7% for τ_2 , and 10% for τ_M . ^c $\tau_M = \sum_i \alpha_i \tau_i / \sum_i \alpha_i$ ($1 \leq i \leq 3$).

To shade light onto the occurring phenomena, the luminescence decays of the dyed films have been collected (**Figure 47**).

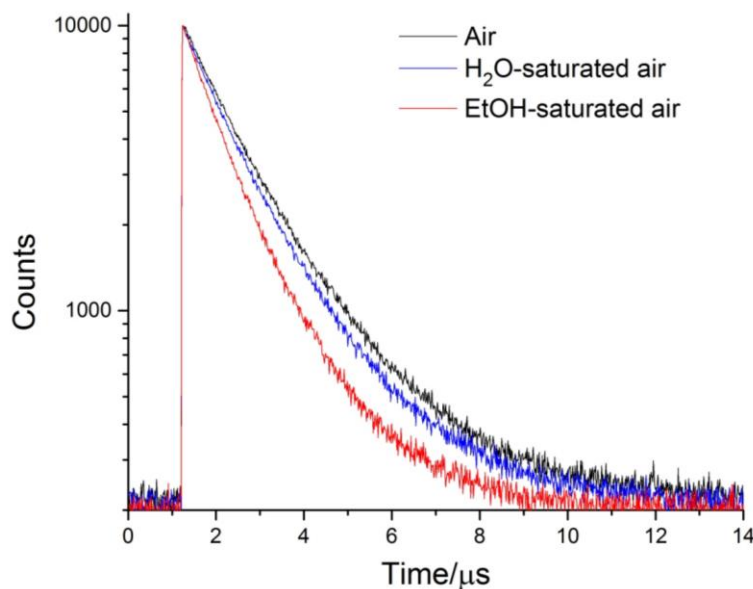


Figure 47. Kinetics of the excited state deactivation of the luminescent $[\text{Ru}(\text{nbpy})_2(\text{nody})]^{2+}$ embedded in plasticized PVC under air, H_2O -saturated air and EtOH-saturated air.

While in solution the dye luminescence decays exponentially, in the polymer the deactivation kinetics is bi-exponential. This phenomenon is frequent when luminescent probes are immobilized into a polymer matrix, since extinction kinetics is influenced by the surrounding media. This indicates the existence of many (at least two, but probably more) different microenvironments. The parameters obtained from multi-exponential fit are reported in Table 7.

The cause of these effects (namely redshift, luminescence intensity decreases and faster deactivation kinetics) can hinge on two mechanisms:

- First, the polar solvents enter the polymer matrix increasing the polarity of the environment surrounding the luminescent indicator, with the resultant emitter excited state stabilization (L-M effect). Consequently, the luminescence maximum will shift to lower frequencies. Due to the energy-gap rule effect [Valeur 2012] the amount of non-radiative deactivation increases, lowering the film luminescence intensity. Water, being more polar than ethanol, should lower the lifetime emission more strongly.
- In addition, luminescence quenching can be due to solvents OH vibration, a phenomenon observed by many authors [García-Fresnadillo 1996]. It is most

probably due to radiationless transition from the triplet MLCT states of the Ru(II) complexes to the oscillating OH of the solvent molecules penetrating between the ligands [Abdel-Shafi 2007]. Also in this case, water should quench the dye luminescence lifetime more than alcohols [Masuda 1998].

The luminescence of $[\text{Ru}(\text{nbpy})_2(\text{nody})]^{2+}$ in PVC films is more efficiently quenched by EtOH than H_2O . The explanation is probably that ethanol can “get closer” than water to the dye molecules, due to the preferential permeation of the former species through plasticized PVC and due to the long non-polar chains of the dye ligands. While the second point explains only weaker luminescence and faster deactivation kinetics, the first one accounts also for the emission redshift.

Next step was studying the influence of dye concentration, type and amount of plasticizer and film thickness in order to improve sensitivity and response time of PVC-based ethanol-sensitive luminescent films.

3.3.2.4. Indicator dye concentration

Plasticized PVC films containing different concentration of luminescent complex were manufactured, as described in the Experimental Part (paragraph 3.3.2.2), in order to evaluate the influence of the indicator dye loading on the optode response. The dyed films luminescence lifetime is not influenced by the amount of immobilized complex into the polymer, considering the uncertainty of the data (**Figure 48**). The use of low concentrations of luminescent dye is thus preferable because it lowers the cost of the indicator film. Therefore, the PVC films selected for further studies have been prepared using 0.1 mg of indicator dye per 100 mg PVC.

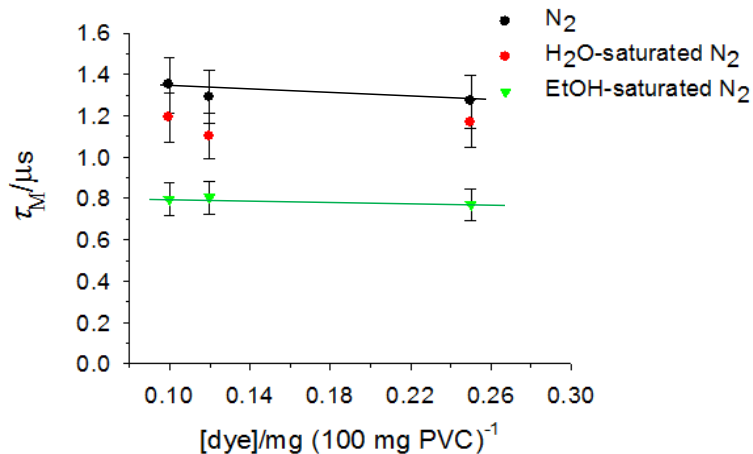


Figure 48. Pre-exponentially weighted luminescence lifetime of $[\text{Ru}(\text{nbpy})_2(\text{nody})]^{2+}$ /plasticized PVC films as a function of the amount of indicator dye immobilized, for successive cycles ($n = 2$) of N_2 , water-saturated N_2 and ethanol-saturated N_2 ($\lambda_{\text{exc}} = 463 \text{ nm}$; long pass emission filters 570 nm and 590 nm). Error bars show 10% of τ_M values.

3.3.2.5. Choice of plasticizers type and concentration

PVC is a stiff material: to increase its workability, the polymer is usually mixed with plasticizers. These additives can also influence permeability of gas into the matrix, but their effect is not easy to foresee. On the one hand, higher amount of plasticizer infers higher chain mobility and increase the free volume inside the material, both features that favor gas permeability. On the other hand, plasticizers are very hydrophobic, thus should decrease the affinity for polar compounds. Moreover, these additives modify the polarity of the environment in proximity of the embedded dye molecules, and this should also influence their luminescence.

Two of the most used plasticizers for PVC sensor films, namely NPOE and DOS, were studied. The amount of the additive has been selected by relying on previous recipes found in literature that reported a ratio plasticizer/polymer (by weight) from 0 to 3 [Wypych 2004, Craggs 1974, Papkovsky 1997], depending on application and sought properties. The pre-exponentially weighted luminescence lifetime of the $[\text{Ru}(\text{nbpy})_2(\text{nody})]^{2+}$ /PVC/plasticizer films as a function of nature and amount of plasticizer in pure N_2 , water-saturated N_2 and ethanol-saturated N_2 is reports in **Figure 49**.

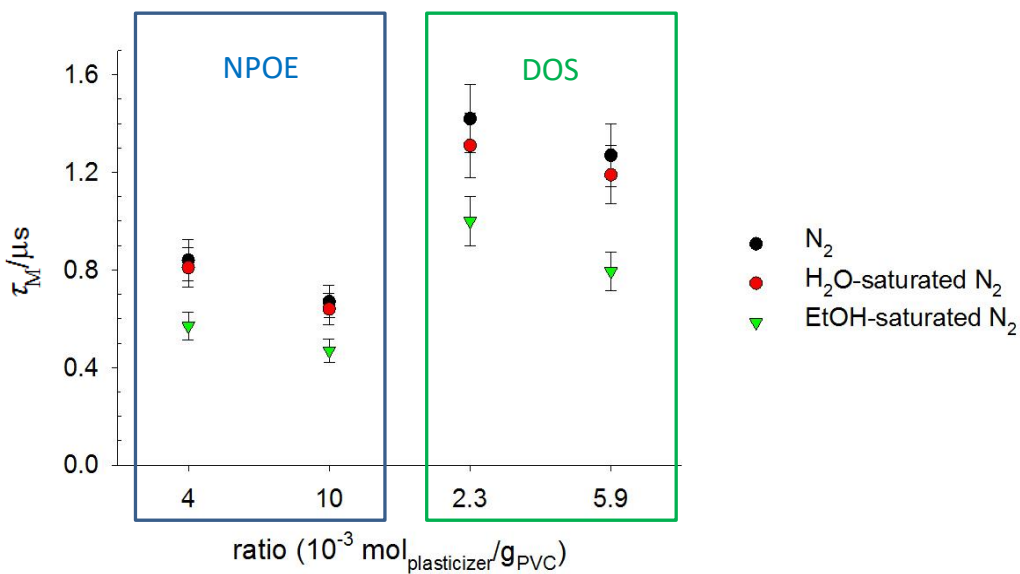


Figure 49. Pre-exponentially weighted luminescence lifetime as a function of the nature and amount (expressed with the ratio between the number of plasticizer millimoles and the polymer mass in grams) of plasticizer in the $[\text{Ru}(\text{nbpy})_2(\text{nody})]^{2+}$ /plasticized PVC films in N_2 , water-saturated N_2 and ethanol-saturated N_2 ($\lambda_{\text{exc}} = 463$ nm; long pass emission filters 570 and 590 nm). Error bars show 10% of the τ_M values.

NPOE appears to quench the indicator dye luminescence, an effect already described by some authors [Papkovsky 1997]. Hence, dioctyl sebacate was selected as plasticizer. On the one hand, the films luminescence lifetime decreases slightly increasing the amount of DOS. On the other hand, the τ_M change due to water-saturated N₂ is a bit lower, while the τ_M change due to ethanol-saturated N₂ is a bit higher. As a result, films manufactured with a ratio DOS:PVC of 2.3 (mmol of DOS / g of PVC) are to some extent more selective to the analyte of interest, probably because of the hydrophobicity of the additive. Using higher amount of plasticizer (i.e. DOS:PVC > 2.3) is not advised because it leads to luminescent sensitive films with poor mechanical properties. For these reasons, this recipe was selected for further characterization.

3.3.2.6. Thickness of the dyed films

A drawback of using PVC as host matrix for the luminophore is the long response and equilibration time of the resulting sensitive films, as shown in paragraph 3.3.2.2. It is possible to reduce the resulting thickness, which influences the response time, lowering the amount of sensor cocktail used for manufacturing the films down to 100 micrometers thick (films of the same composition and lower thickness are fragile and difficult to handle) (**Table 8**).

Table 8. Measured [Ru(nbpy)₂(nody)]²⁺/plasticized PVC film thickness, sensitivity to EtOH and response time.

Film thickness ^a / μm	$\Delta\phi \text{EtOH}^{\text{b}} / ^\circ$	$t_{90\downarrow} \text{EtOH}^{\text{c}} / \text{s}$ $t_{90\uparrow} \text{EtOH}^{\text{d}} / \text{s}$
500 ± 100	5.5 ± 0.1	466 ± 41 357 ± 44
160 ± 30	8.3 ± 0.2	230 ± 30 320 ± 22
130 ± 20	8.0 ± 0.1	90 ± 4 111 ± 6
100 ± 20	7.9 ± 0.1	23 ± 3 19 ± 3

^a Measured with an electronic digital micrometer. Uncertainty: S.D. from measuring 3 different films, 5 different measures each film.

^b Luminescence phase shift difference from 0 to 83700 ppm EtOH in N₂. $T = 25^\circ\text{C}$.

^c Response time for 90% signal change from 0 to 83700 ppm EtOH in N₂.

^d Response time for 90% signal change from 83700 to 0 ppm EtOH in N₂.

As expected, sensitive films of greater thickness show longer response time. Films having thickness of 500 μm also appear to have still many unquenched dye molecules when exposed to gas containing 83700 ppm of EtOH, leading to low sensitivity to the

species of interest. For the dyed films of intermediate thickness (160 and 130 microns), their sensitivity is far better, and it is possible to appreciate a progressively improvement in the response time. Finally, the thinnest films are characterized by short response time (around 20 s) and still high sensitivity (almost the same sensitivity as thicker films, considering the measures uncertainty). Response time is a parameter of paramount importance for the sought application; hence, the 100 μm -thick films have been selected.

3.3.2.7. Other parameters and interfering species

- Temperature.

Once the dyed films were selected, their response as a function of temperature was studied using the portable luminometer. The ambient temperature is highly important, since it can influence EtOH concentration (because the vapor pressure is temperature dependent, as described by Antoine equation [Antoine 1888]), permeability of the species through the polymer (following the Arrhenius relationship [George 2001]), the dyed film photophysical properties (because of the temperature dependence of the luminophore excited state lifetime) and the instrumental response (due to the influence of temperature on the electronics). The $[\text{Ru}(\text{nbpy})_2(\text{nody})]^{2+}/\text{PVC/DOS}$ (2.5:1) film was subjected to successive cycles of 0 ppm and 23800 ppm of EtOH in N_2 (as carrier gas) between 7 °C and 35 °C (Figure 50). The ethanol concentration value is obtained by saturating the carrier gas at 5 °C; this temperature has been chosen to avoid EtOH condensation when reaching the test chamber (which was thermostated at temperature as low as 7 °C). The selected range includes typical environmental temperature in the workplace, temperature of interest for using in breathalyzers, and temperature used in beer fermentation process (which range from 20 to 22.2 °C for ale yeast, from 7 to 12.8 °C for lager yeast [Palmer 2006]).

The sensitivity of the sensor – i.e.: phase shift difference in absence and presence of the analyte – noticeably decreases when the temperature rises. This drop happens because the luminescence lifetime in pure N_2 diminishes increasing temperature due to thermal promotion to the ${}^3\text{MC}$, as already described in [Bustamante 2018]. In presence of EtOH, the luminescence lifetime reduction is less pronounced, because of the competitive radiationless deactivation due to this quencher. This confirms the necessity of including a temperature sensor when monitoring EtOH.

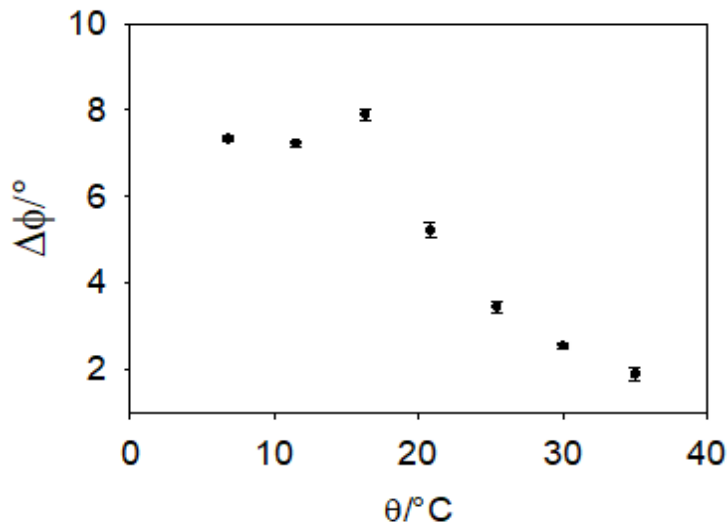


Figure 50. Difference in phase shift from 0 and 23800 ppm of ethanol (in N₂ gas) from 7 °C to 35 °C. Dyed film: [Ru(nbpy)₂(nody)]²⁺/PVC/DOS (2.5:1).

- Dioxygen.

Molecular oxygen is a known deactivator of the triplet excited state of ruthenium complexes. Sensitivity to ethanol - phase shift difference from 0 to 23800 ppm of ethanol (in N₂ gas) - of [Ru(nbpy)₂(nody)]²⁺ dyed plasticized PVC decreases in presence of O₂ (**Figure 51**).

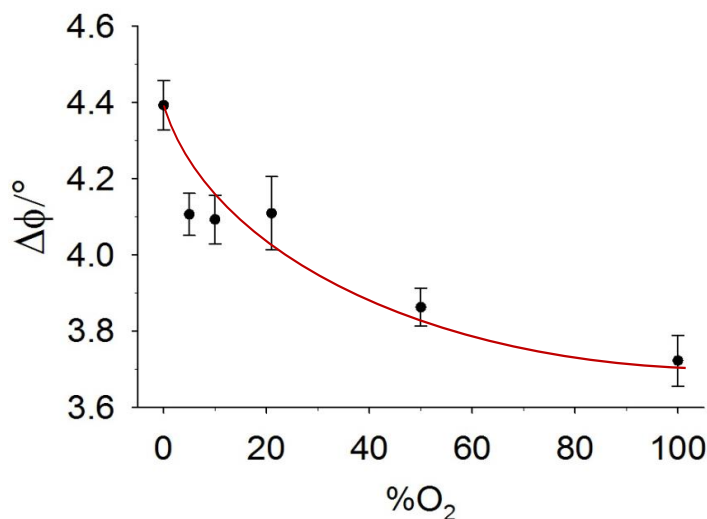


Figure 51. Difference in phase shift from 0 and 23800 ppm EtOH as a function of O₂ concentration (in N₂ by volume). Dyed film: [Ru(nbpy)₂(nody)]²⁺/PVC/DOS (2.5:1). T = (23 ± 1) °C. The red line is only meant to guide the eye.

The sensor shows 0.25% / %O₂ response change at 21% O₂ in pure N₂ at 23 °C, which is smaller than the relative error for a fixed O₂ pressure. Nevertheless, if expecting large variation of O₂ in the location of interest, the sensor can be coupled with an O₂ probe.

- **Water.**

The developed sensor is more sensitive towards EtOH than towards H₂O. Moreover, the ethanol sensitivity is not significantly different in absence of water or in water-saturated gas (see paragraphs *Analytical features – EtOH in gas stream* and *Analytical features – Headspace of H₂O-EtOH solution*). However, the optode response to water saturated N₂ at 25 °C (34000 ppm) is as large as that to 3000 ppm of EtOH (**Figure 52**, $\Delta\phi = 1.95^\circ$). If the working environment is characterized by exceptionally large H₂O vapor pressure variations when monitoring low ethanol concentration, the described EtOH optode must be coupled with a H₂O sensor.

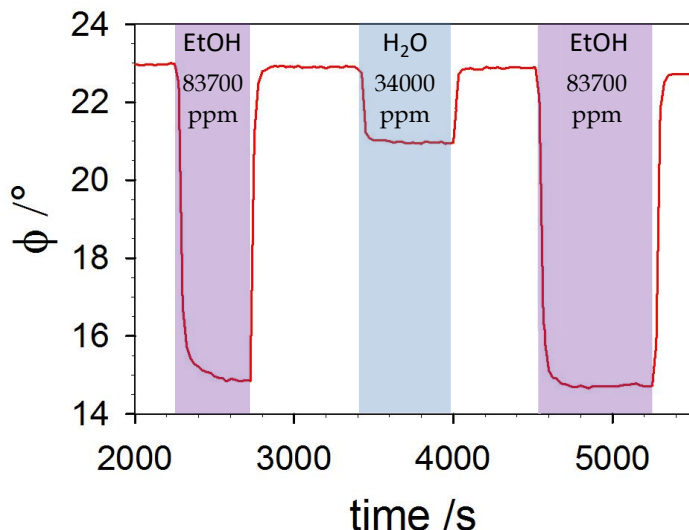


Figure 52. Sensor response to N₂, EtOH saturated N₂ and H₂O-saturated N₂. Dyed film: [Ru(nbpy)₂(nody)]²⁺/PVC/DOS (2.5:1). T = 25 °C.

- **Volatile organic compounds (VOCs).**

The maximum recommended exposure limit (REL) of EtOH is 1000 ppm [NIOSH 1992]. The optode analytical response to such EtOH concentration (in N₂ at 23 °C) is 0.2°. To study the possible interference of other VOCs, the concentration of MeOH, AcOEt, MeCN and acetone causing the same phase shift are compared to the respective RELs in **Table 9**.

For every VOCs considered, the amount causing analytical signal of 0.2° is many times higher than the concentration allowed in the workplace. Thus, these substances will not interfere with the sensor. Contrarily to similar sensors reported in literature (e.g. [Chang 1997]), sensitivity to MeOH is lower than to EtOH, probably because of the plasticized PVC higher affinity for the slightly less polar ethyl alcohol.

Table 9. VOCs and relative concentration (in N₂ at 23 °C) giving analytical signal (i.e., phase shift change) of 0.2°

Analyte	Concentration for 0.2° signal/ ppm ^a	NIOSH REL/ ppm ^b
EtOH	1000	1000
MeOH	6900	200
AcOEt	12000	400
MeCN	12000	40
Acetone	21000	1000

^a Maximum estimated uncertainty (due to the precision of the rotameter scale) = 10% for EtOH, MeOH, AcOEt and MeCN; 20% for acetone. ^b [NIOSH 1992].

3.3.3. Analytical features – EtOH in gas stream

3.3.3.1. Repeatability

First, the sensor repeatability was tested. The luminescent dyed film was exposed to alternate cycles of pure N₂ and EtOH-saturated N₂, which corresponded to 79000 ppm EtOH at the room temperature of 24.0 °C (Figure 53). From the analytical response, the average ϕ and the SD were calculated (Table 10).

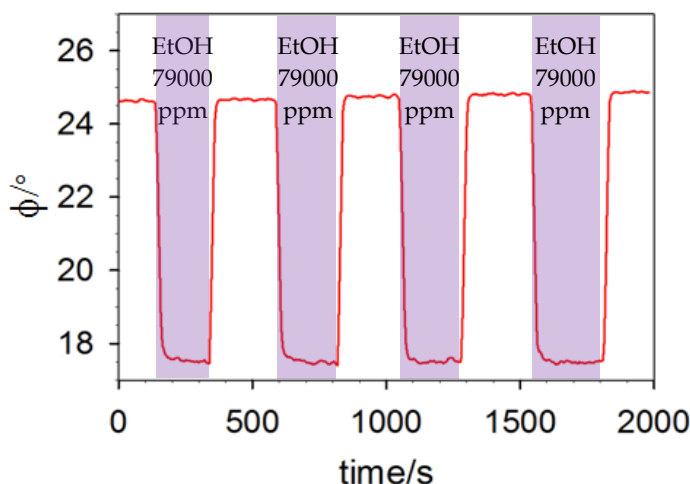


Figure 53. Analytical response of the sensor when the luminescent EtOH-sensitive film was exposed to repeated cycles of pure N₂ and 79000 ppm EtOH in N₂. T = 24.0 °C.

Table 10. Repeatability study of the $[\text{Ru}(\text{nbpy})_2(\text{nody})]^{2+}$ /PVC/DOS (2.5:1) dyed film.

[EtOH]/mmHg	$\phi/^\circ$	SD	n ^a
0	24.75	0.09	5
55.4	17.50	0.02	4

^a number of repeated measurements.

3.3.3.2. Calibration

The luminescent EtOH-sensitive film was exposed to different EtOH concentration in N₂ and the sensor response was collected (Figure 54). The calibration was performed in two temperature conditions: first, the thermostated cell was kept at 10 °C, slightly lower than ethanol flash point (13.0 °C [Liaw 2010]). Secondly, the temperature was set to 24 °C, selected as “room temperature” (see Appendix I, pag. 120). From these data, calibration curves were obtained (Figure 55) and used for calculating the limits of detection (LOD) and quantification (LOQ) (see next paragraph).

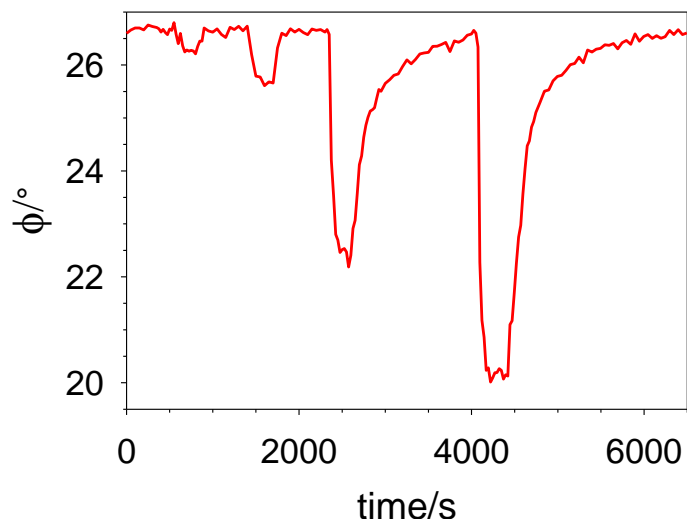


Figure 54. Analytical response of the sensor when the luminescent EtOH-sensitive film was exposed to 1200, 2300, 4800, 9400 ppm EtOH in pure N₂ at 10°C.

At 10 °C, the sensors show longer response time when removing ethanol (Figure 54), compare to higher temperature. This is probably due to the higher condensation/lower evaporation of the analyte onto the luminescent polymer film or/and the steel flow-through cell.

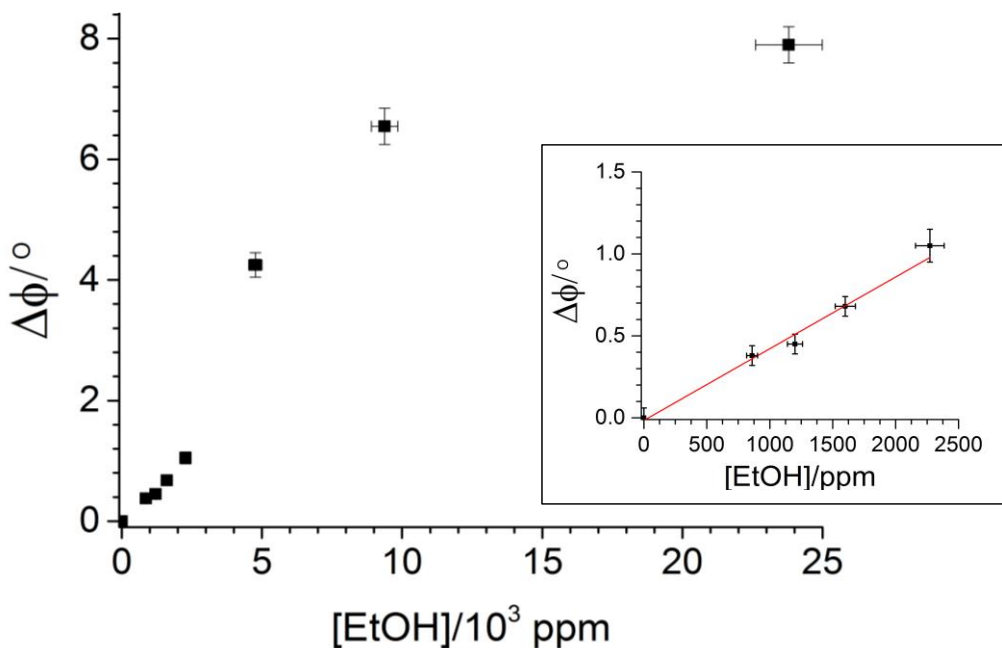


Figure 55. Calibration curve obtained from repeated exposure ($n = 3$) of the sensor to N_2 containing different amount of EtOH at 10°C . In the inset, a magnification of the calibration curve from 0 to 2500 ppm EtOH is shown. The linear fit (red line) is obtained using only the five data points of this shorter range. Equation of the fit: $\Delta\phi/^\circ = a + b \cdot [EtOH]/\text{ppm}$. Parameters of the fit: $a = (-0.02 \pm 0.04)^\circ$; $b = (4.4 \pm 0.3) \times 10^{-4} \cdot \text{ppm}^{-1}$; $R^2 = 0.9794$. x_{error} is estimated from the precision of the rotameters, the higher source of uncertainty; y_{error} is the SD calculated from 3 measurements.

3.3.3.3. Limit of detection and quantification

As reported in the introduction, the ethanol IDLH is 10% of the LEL, which is equivalent to 3300 ppm of ethanol in air [NIOSH 1995]. This is generally the first warning level for investigating the possible source of leakage. Then, if the vapor concentration rises above 20% of the lower explosion limit threshold – 6600 ppm of ethanol in air – primary explosion protection actions are:

- I. concentration limiting (i.e., active dilution, for example by automatically ventilating fresh air into the hazardous area) and
- II. inertization (i.e., removal of oxygen)

If concentration continues to rise because the counter measure is ineffective, at 40% LEL – 13200 ppm ethanol/air mixture – any non-explosion proof instrument or equipment must be switched off.

Table 11 shows the limits of detection (LOD) and quantification (LOQ) obtained from the linear fit to the experimental data points collected at 10.0 and 24.0°C . First, it was estimated the maximum uncertainty in the signal of the blank (pure N_2), equal to 0.05° .

Then, following IUPAC recommendations [Magnusson 2014], LOD and LOQ (**Table 11**) were calculated from the linear fit (inset in Figure 55) as the EtOH concentration corresponding to k times the blank uncertainty with $k_{\text{LOD}} = 3$ and $k_{\text{LOQ}} = 10$, respectively (Figure 56). The LOD and LOQ values decrease lowering the temperature. This result is in agreement with the temperature-dependent response pointed out in section **Other parameters and interfering species**.

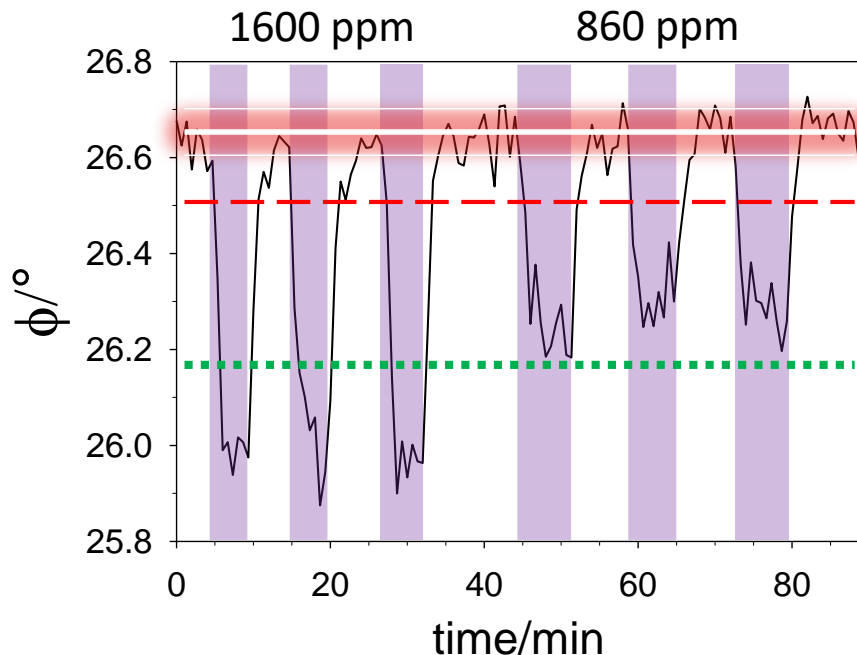


Figure 56. Analytical response of the sensor exposed to 1600 ppm EtOH, slightly higher than the LOQ, and 860 ppm EtOH, lower than LOQ but higher than LOD, in pure N₂ (purple shadow depicts when EtOH was present in the gas feed). T = 10.0 °C. The white continuous line highlights the signal of the blank; the red shadow overlays the uncertainty of the blank. The red dashed line and the green dotted line highlight the LOD and the LOQ, respectively.

These results prove that the developed sensor is very suitable for monitoring explosive atmosphere in ethanol production plant or storing warehouses.

Table 11. LOD and LOQ of the sensor monitoring EtOH in N₂ gas. Sensitive film placed in thermostated flow-through cell. T = 10.0 °C and 24.0 °C.

T/°C	LOD/ppm	LOQ/ppm
10.0	400	1400
24.0	800	2700

3.3.3.4. Reproducibility

To study the films manufacturing reproducibility, two luminescent EtOH-sensitive films belonging to different batches were subjected to 23800 ppm EtOH in N₂ (Figure 57).

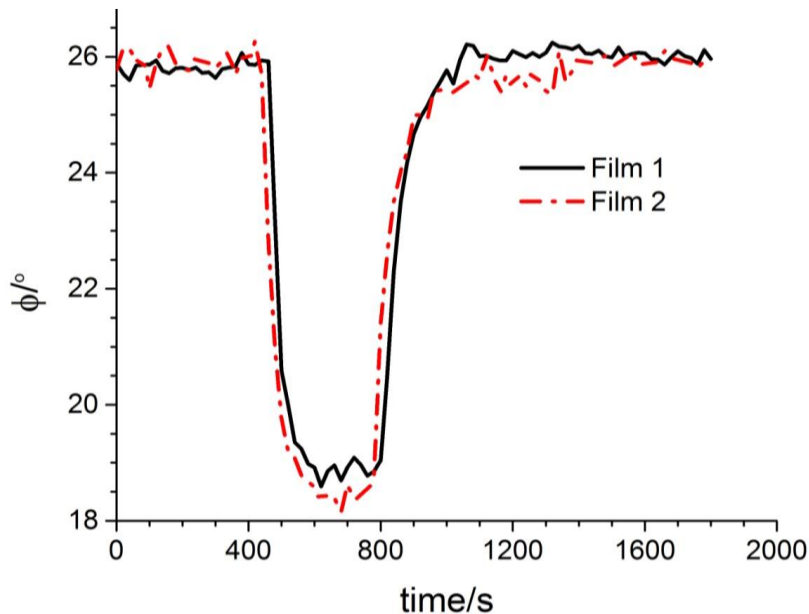


Figure 57. Signal change from 0 to 23800 ppm EtOH in N₂ for two different luminescent EtOH-sensitive films. T = 10 °C.

The sensors response is the same (taking into account the measures uncertainty) in both magnitude and response time (Table 12).

Table 12. Sensor response to 0 and 23800 ppm EtOH in N₂ (T = 10°C).

	φ ₀ /° ^a	φ ₂₃₈₀₀ /° ^b	t _{90↓} /s ^c	t _{90↑} /s ^d
Film 1	25.9	18.8	70	130
Film 2	26.0	18.4	90	160

^a Estimated uncertainty: ± 0.1°.

^b Estimated uncertainty: ± 0.2°.

^c Response time for 90% signal change, when switching from 0 to 23800 ppm EtOH in N₂. Estimated uncertainty: ± 10 s.

^d Response time for 90% signal change, when switching from 23800 to 0 ppm EtOH in N₂. Estimated uncertainty: ± 20 s.

3.3.3.5. Storage stability

The sensitive films were stored in the dark in a closed plastic box at $(24 \pm 3)^\circ\text{C}$. In these conditions, the analytical response towards the analyte of interest remains unchanged for the time tested (1 year). The difference between the two values is well below 3 times the standard deviation. (Figure 58).

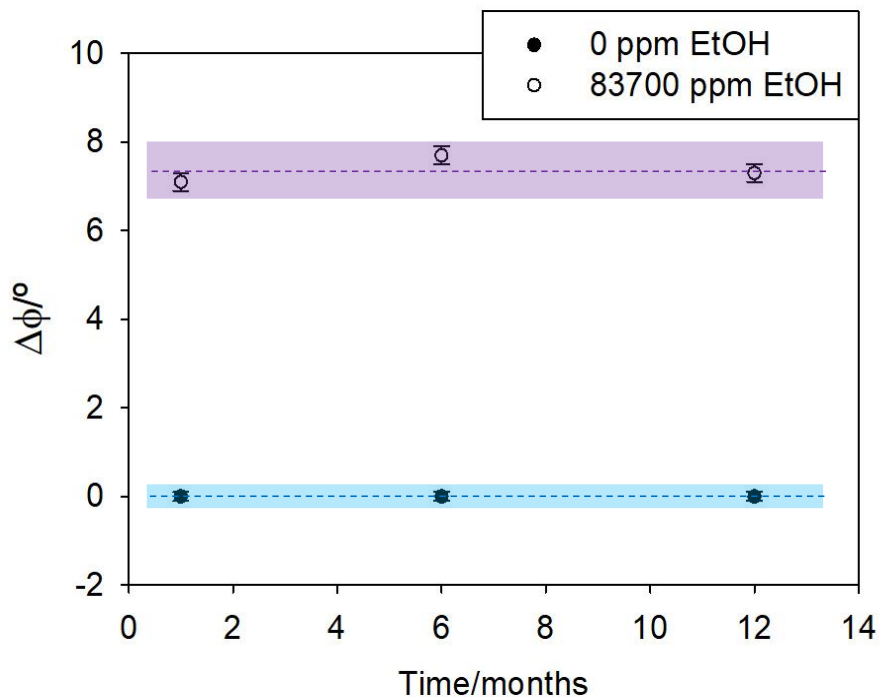


Figure 58. Optode response to 0 and 83700 ppm EtOH in N_2 . $T = 24^\circ\text{C}$. Broken lines and shadows depict mean values and 3 times the SD, respectively.

3.3.4. Analytical features – Headspace of H_2O -EtOH solution

3.3.4.1. Calibration

The response of the sensitive film placed in the headspace of bottles containing 50 ml of aqueous solutions containing from 0 to 40% of EtOH by volume is reported in **Figure 59**. From these data, a calibration curve was obtained (**Figure 60**).

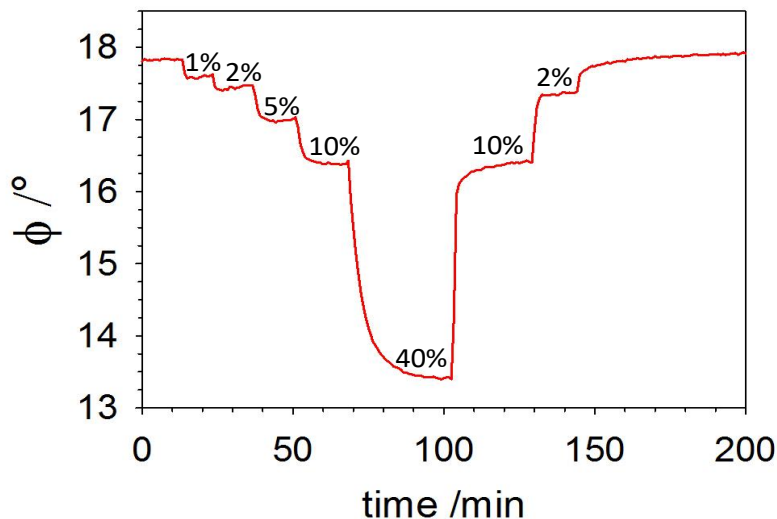


Figure 59. Analytical response of the sensor placed in the headspace of 50 ml aqueous solutions containing 0, 1, 2, 5, 10 and 40% of EtOH by volume. $T = 26\text{ }^{\circ}\text{C}$.

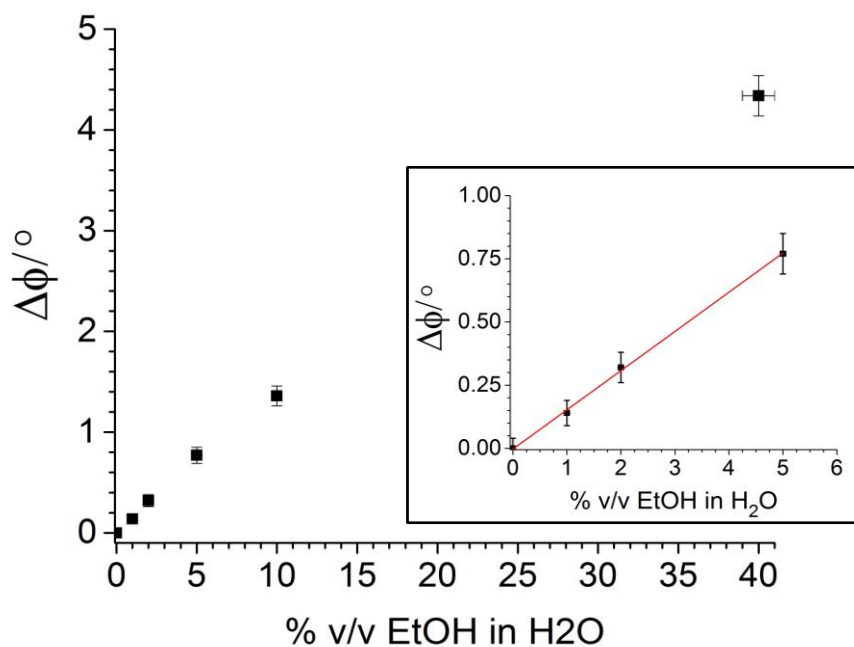


Figure 60. Calibration curve obtained from repeated exposition ($n = 3$) of the sensor to the headspace of EtOH in H_2O solutions. In the inset, a magnification of the calibration curve from 0 to 5% EtOH (in volume) is shown. The linear fit (red line) is obtained using only the four data points of this reduced range. Equation of the fit: $\Delta\phi/^\circ = a + b \cdot \% \text{ EtOH}$. Parameters of the fit: $a = (-0.003 \pm 0.008)^\circ$; $b = (0.155 \pm 0.004)^\circ \cdot \%^{-1}$; $R^2 = 0.9979$. x_{error} is estimated from the solutions preparation uncertainty; y_{error} is the SD calculated from 3 measurements. $T = 26\text{ }^{\circ}\text{C}$.

3.3.4.2. Limit of detection and quantification

The limits of detection (LOD) and quantification (LOQ) obtained from the linear fit to the experimental data points collected at 26 °C are reported in Table 13. First, it was estimated the maximum uncertainty in the signal of the blank (pure H₂O), equal to 0.04°. Then, following IUPAC recommendations [Magnusson 2014], LOD and LOQ were calculated from the linear fit (inset in **Figure 60**) as the EtOH concentration corresponding to k times the blank uncertainty with k_{LOD} = 3 and k_{LOQ} = 10, respectively.

Table 13. LOD and LOQ of the sensor monitoring EtOH in H₂O solutions. Sensitive film placed in the bottle headspace. T = 26 °C.

LOD		LOQ	
Solution % v/v	Headspace / ppm ^a	Solution % v/v	Headspace / ppm ^a
0.8	700	2.6	2300

^a EtOH concentration calculated with the Duboswki equation.

These values show that the developed sensor can be used for monitoring alcohol content in beers, wine, and spirits – beverages with ethyl alcohol concentration usually between 4 and 40% v/v – with an accuracy of ± 0.26%. This sensor is accurate enough for alcohol determination in Europe [Regulation (EU) No 1169/2011]. Some Countries, however, requires higher accuracy in alcohol determination, for example the US where the TTB required standard of measurement of % alcohol within 0.02% accuracy.

3.4. Appendix I

Hereafter is reported the response of the luminescent EtOH-sensitive $[\text{Ru}(\text{nbpy})_2(\text{nody})]^{2+}$ dyed plasticized PVC film at 24.0 °C (**Figure 61**, **Figure 62**) and the obtained calibration curve (**Figure 63**).

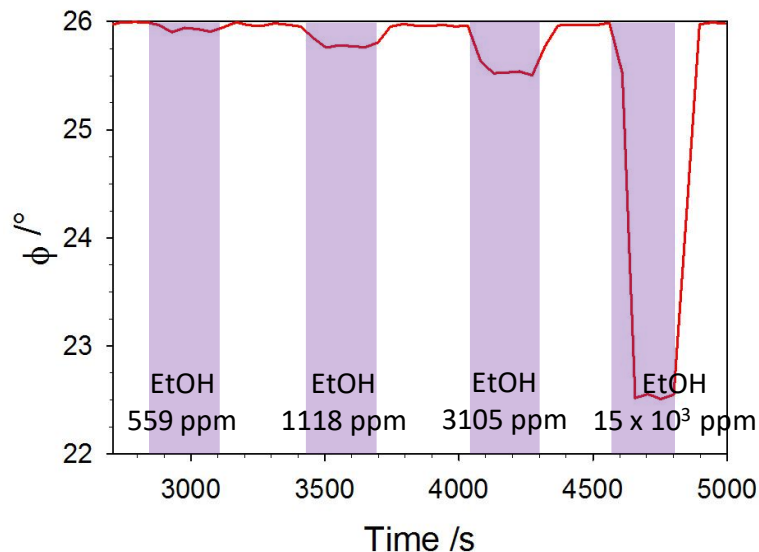


Figure 61. Analytical response of the sensor when the luminescent EtOH-sensitive film was exposed to 559, 1118, 3105, 15000 ppm EtOH in pure N₂ at 24.0 °C.

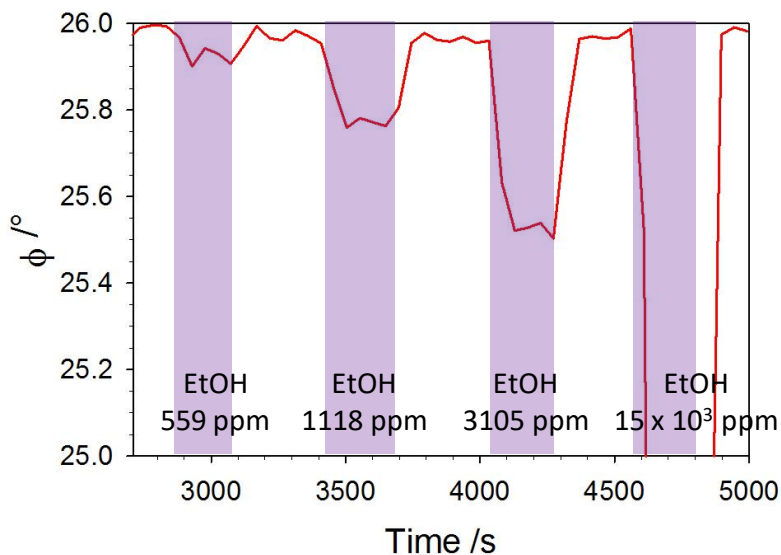


Figure 62. Analytical response of the sensor when the luminescent EtOH-sensitive film was exposed to 559, 1118, 3105, 15000 ppm EtOH in pure N₂ at 24.0 °C. Zoom of the y-axis of the plot at Figure 61.

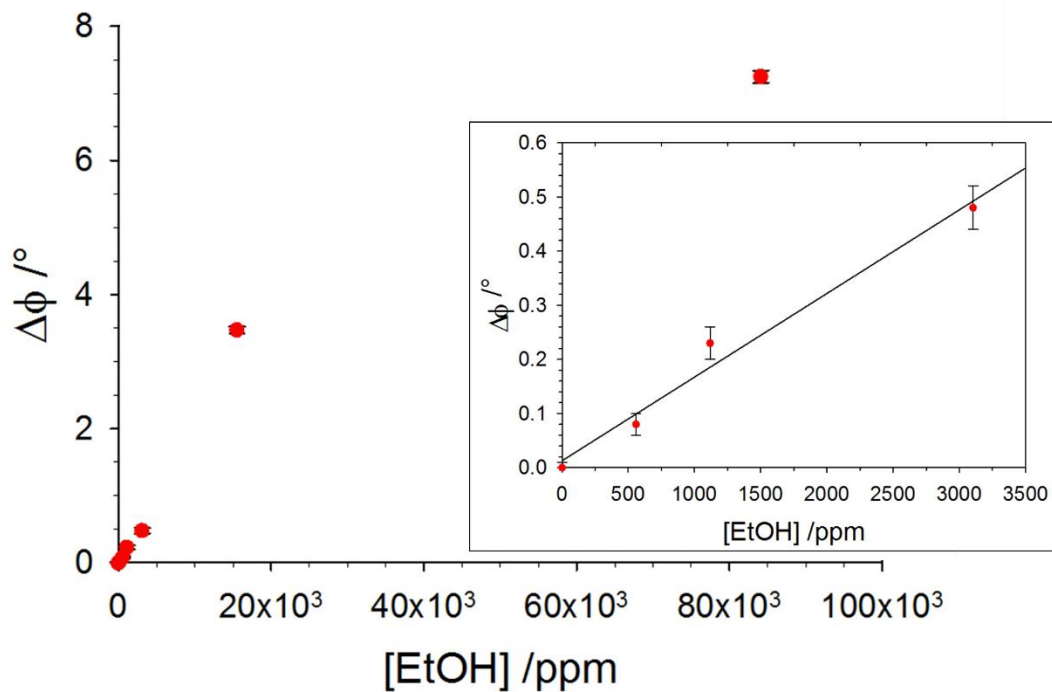


Figure 63. Calibration curve obtained from repeated exposure ($n = 3$) of the sensor to gas mixture based on N_2 as carrier gas and containing different concentration of EtOH at $24 {}^\circ C$. In the inset, a magnification of the calibration curve from 0 to 3500 ppm EtOH is shown. The linear fit (black line) is obtained using only the four data points of this reduced range. Equation of the fit: $\Delta\phi / {}^\circ = a + b \cdot [EtOH] / ppm$. Parameters of the fit: $a = (-0.02 \pm 0.04) {}^\circ$; $b = (4.4 \pm 0.3) \times 10^{-4} {}^\circ \cdot ppm^{-1}$; $R^2 = 0.9794$. x_{error} is estimated from the precision of the rotameters, the higher source of uncertainty; y_{error} is the SD calculated from 3 measurements.

3.5. Annex

Our approach was to use general solvent effects but tuned on the specific molecule, to exploit a computation approach to forecast the behavior of polarity-sensitive Ru(II) complexes without the need to prepare further candidates. The computational study has been extended also to systems with electron-donor substituents in bpy and related ligands to obtain a more general picture of the potential candidates to be used in the polarity probes, to help in its design, and to investigate if a direct relation can be established between electronic properties of substituents and Stokes Shift variation with the microenvironment polarity around the probe [Ielasi 2019].

■ COMPUTATIONAL STRATEGY

The geometries of the S_0 and T_1 states of the Ru(II) complexes have been optimized with density functional theory (DFT) using the Perdew–Burke–Ernzerhof exchange-correlation functional mixed with 25% exact Fock exchange (PBE0) [Adamo 1999]. The Kohn-Sham orbitals are expanded in a basis set of split valence quality (def2-SVP) [Weigend 2005]. The $S_0 \rightarrow S_1$ absorption energy is calculated with time-dependent DFT in the Tamm-Dancoff approximation [Runge 1984, Hirata 1999], whereas the $T_1 \rightarrow S_0$ emission can be determined by standard DFT calculations being the lowest states of the respective spin manifold. Geometry optimizations were performed with the TurboMole 6.6 program package [Furche 2014, TURBOMOLE V6.6 2014] and TD-DFT calculations with Gaussian 09.

The solvent effects are incorporated in the calculations through the Conductor-like solvent model (COSMO) [Klamt 1993] in TurboMole and with the polarized continuum model (PCM) [Tomasi 2005] in Gaussian 09. The solute is placed in a cavity constructed by the superposition of van der Waals spheres around each atom. Point charges are placed on the surface of the cavity, which are brought to self-consistency for the interaction of the electron density of the solute and the solvent, represented as a dielectric continuum with its specific dielectric constant ϵ_r .

The dipole moment of charged molecules depends on the origin of the coordinate system. The fact that the optimal geometry of the complexes in their S_0 and T_1 states is different makes it difficult to define a unique origin for both states. Instead, we have fixed the origin to the center of mass for all species. Other choices lead to important changes in the values of μ , but hardly affect the difference between the dipoles of S_0 and T_1 ($\Delta\mu_{S0-T1}$).

A set of 60 different Ru(II) complexes has been screened. This set contains many complexes of the $[Ru(L1)_2(G_2L2)]^{2+}$ ($L1 = L2 = bpy$) type (Figure 64), but also variants replacing either the L1 or L2 bipyridine ligand with 1,10-phenanthroline (phen), 1,4,5,8-tetraazaphenanthrene (tap), dipyrido[3,2-a:2',3'-c]phenazine (dppz), 2,2'-

bipyrazine (bpz), or 3,4,7,8-tetramethyl-1,10-phenanthroline (tmphen). In addition to the substituents G considered in the probes synthesis, namely Cl (**1**), CN (**2**) and CH₃COO (**3**), the set contains 34 other groups. **Figure 65** displays the structure of the most elaborated groups; the rest is detailed in **Figure 66**. Structure of some substituents and ligands mentioned in **Table 14**, **Table 15** and **Table 16**. Firstly, we only calculated the dipole moments of the S₀ and T₁ states in their optimized geometry in gas phase. Then we selected a subset of complexes mostly looking at the largest $\Delta\mu_{S_0-T_1}$, but also considering the complexity of their synthesis. For this set of 12 complexes, we calculated the Stokes shift in three different solvents of increasing polarity, namely tetrahydrofuran ($\epsilon_r = 7.6$), ethanol ($\epsilon_r = 24.6$) and water ($\epsilon_r = 78.4$).

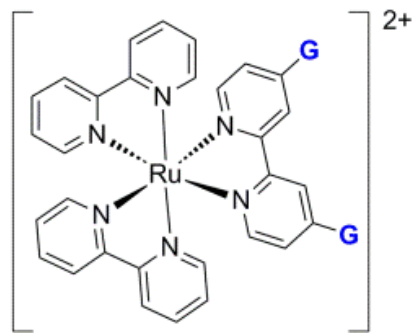


Figure 64. General structure of the luminescent Ru(II) coordination complexes [Ru(bpy)₂(G₂bpy)]²⁺ investigated in this work. G stands for the electron-withdrawing Cl, CN or CO₂CH₃ groups of dyes **1**, **2** and **3**, respectively.

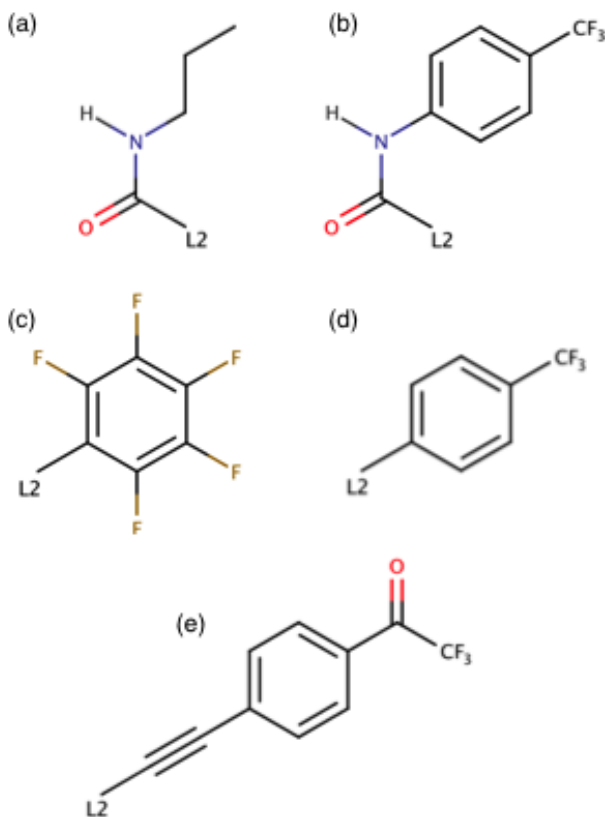


Figure 65. Structure of some of the groups that have been used in the computational study as substituents on the bipyridine ligand L2 at the 4 and 4' positions. a) CONHC_3H_7 ; b) $\text{CONHC}_6\text{H}_4\text{CF}_3$; c) C_6F_5 ; d) $\text{C}_6\text{H}_4\text{CF}_3$; e) $\text{CCC}_6\text{H}_4\text{COCF}_3$.

Chapter 3 - Optode for EtOH sensing based on Ru(II) indicator dyes

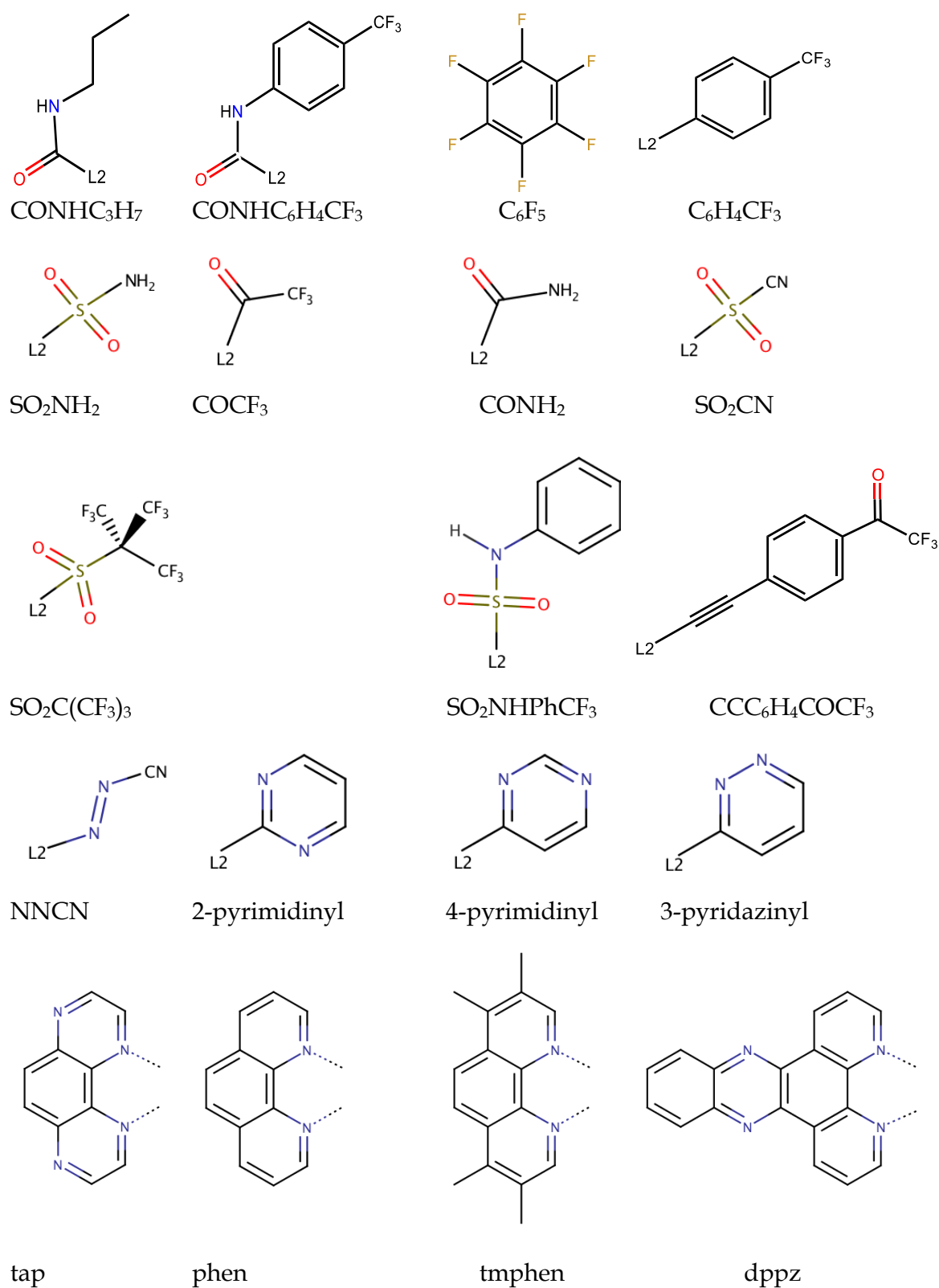


Figure 66. Structure of some substituents and ligands mentioned in **Table 14**, **Table 15** and **Table 16**.

■ RESULTS AND DISCUSSION

COMPUTATIONAL RESULTS

Upon absorption of a photon of UV or blue light, the $[\text{Ru}(\text{bpy}_3)]^{2+}$ dye is excited to $^1\text{MLCT}$ state. Due to the large spin-orbit coupling of transition metal complexes, a fast intersystem crossing takes place, populating the $^3\text{MLCT}$ state. In this way, a metal $4\text{d}(\text{t}_{2g})$ electron is promoted to one of the three equivalent π^* orbitals of the coordinated ligands [Chen 1998]. Coupling with the surrounding solvent dipoles induces localization of the electron on a single ligand [Campagna 2007]. In the case of coordination of the Ru(II) to three identical ligands, the $^3\text{MLCT}$ state becomes “randomized” by interligand hopping [Wallin 2005]. All these steps take place in a timescale of hundreds of femtoseconds. Finally, the dye can relax from the $^3\text{MLCT}$ to the ground state by both non-radiative and radiative pathways. Consequently, the absorption and emission energies have been computed as the $S_0 \rightarrow S_1$ ($^1\text{MLCT}$) and T_1 ($^3\text{MLCT}$) $\rightarrow S_0$ vertical transitions, at the minimum energy structures of the ground state and of the T_1 state, respectively.

Dipole moments of S_0 and T_1 . The D_3 symmetry of the structure of the parent compound, $[\text{Ru}(\text{bpy}_3)]^{2+}$, imposes a zero dipole moment in S_0 . The optimal geometry of the T_1 state is slightly distorted, leading to a MLCT state with an electron localized on one of the bpy ligands and a moderate dipole moment of 4.97 D. In most of the substituted complexes, T_1 is of MLCT character with the excited electron on either L1 or L2. However, in a few complexes the lowest lying triplet state is characterized by a $\pi-\pi^*$ excitation in one of the ligands (“intra-ligand” transition, or IL), without changing the number of electrons on the Ru core (**Table 14**, **Table 15** and **Table 16**). Electron-withdrawing substituents on the L2 ligand induce small dipole moments in the S_0 state and a T_1 state that is localized on the L2 ligand, whereas electron-donating groups tend to localize the excited electron on the L1 (non-substituted) ligands. In this way, the latter groups lead to a change of sign in $\Delta\mu$. Surprisingly enough, the G = $\text{CCC}_6\text{H}_4\text{COCF}_3$ substituent (**Figure 65**, item e) drives also the excited electron on the unsubstituted ligands (L1) and makes the dipole moment of the triplet state smaller than in S_0 ($\Delta\mu = -7.50$ D). Electron withdrawal through resonance leads to the largest changes in the dipole moment (for instance, we calculated $\Delta\mu$ to be 7.43 D for G = $\text{CONHC}_6\text{H}_4\text{CF}_3$) while the inductive effect through σ bonds is less pronounced. A list of the calculated dipole moments of all sixty compounds can be found in **Table 14**, **Table 15** and **Table 16**. Compounds are ordered by their electron-donating/electron-withdrawing and inductive/resonant character.

Table 14. Dipole moments of $[\text{Ru}(\text{L1})_2(\text{G}_2\text{L2})]^{2+}$ in the optimized gas phase geometry of S_0 (μ_{gs}) and T_1 (μ_{exc}), with $\text{L1} = \text{L2} = \text{bpy}$ (see **Figure 65** and **Figure 66** for the structures of selected substituents, G).

G	Excitation	Character	μ_{gs}	μ_{exc}	$\Delta\mu$
CONHC ₃ H ₇	Ru → π*(L2)	MLCT	10.97	18.62	7.65
CONHPhCF ₃	Ru → π*(L2)	MLCT	23.44	31.06	7.62
SO ₂ C(CF ₃) ₃	Ru → π*(L2)	MLCT	32.46	39.73	7.27
COCF ₃	Ru → π*(L2)	MLCT	17.38	24.63	7.26
SiF ₃	Ru → π*(L2)	MLCT	15.74	22.91	7.17
COOCH ₃	Ru → π*(L2)	MLCT	9.47	16.52	7.05
COOH	Ru → π*(L2)	MLCT	8.66	15.65	6.99
NO ₂	Ru → π*(L2)	MLCT	13.97	20.95	6.98
PF ₄	Ru → π*(L2)	MLCT	19.27	26.21	6.93
COCH ₃	Ru → π*(L2)	MLCT	5.15	12.07	6.91
SO ₂ CN	Ru → π*(L2)	MLCT	20.16	27.02	6.86
SO ₃ H	Ru → π*(L2)	MLCT	16.16	23.01	6.85
BF ₂	Ru → π*(L2)	MLCT	10.35	17.15	6.80
CN	Ru → π*(L2)	MLCT	10.70	17.46	6.76
COF	Ru → π*(L2)	MLCT	11.93	18.69	6.77
F	Ru → π*(L2)	MLCT	4.87	11.61	6.74
SO ₂ NH ₂	Ru → π*(L2)	MLCT	13.67	20.39	6.72
Cl	Ru → π*(L2)	MLCT	6.51	13.19	6.68
Br	Ru → π*(L2)	MLCT	11.65	18.30	6.65
SO ₂ NHPhCF ₃	Ru → π*(L2)	MLCT	18.14	24.61	6.47
CF ₃	Ru → π*(L2)	MLCT	13.71	20.16	6.45
H	Ru → π*(L2)	MLCT	0.00	4.97	4.97
NO	L2→L2	IL	3.90	8.29	4.39
NH ₂	Ru → π*(L1)	MLCT	4.30	8.28	3.97

Chapter 3 - Optode for EtOH sensing based on Ru(II) indicator dyes

4-pyrimidinyl	Ru → π*(L1,L2)	MLCT	8.70	12.20	3.50
CH ₃	Ru → π*(L1)	MLCT	0.10	3.55	3.45
3-pyridazinyl	Ru → π*(L1,L2)	MLCT	3.30	5.55	2.25
CONH ₂	Ru → π*(L1,L2)	MLCT	9.80	11.56	1.76
OH	Ru → π*(L1)	MLCT	1.73	2.02	0.29
CCPhCOCF ₃	Ru → π*(L1)	MLCT	34.91	33.67	-1.24
PhF ₅	Ru → π*(L1,L2)	MLCT	20.56	18.54	-2.11
NNCN	L2→L2	IL	15.36	13.14	-2.22
2-pyrimidinyl	Ru → π*(L1)	MLCT	4.10	0.22	-3.88
4-pyridyl	Ru → π*(L1)	MLCT	12.29	8.39	-3.90
CH ₂ COOH	Ru → π*(L1)	MLCT	5.59	1.59	-4.00
NHCOCH ₃	Ru → π*(L1)	MLCT	9.18	4.81	-4.37
PhCF ₃	Ru → π*(L1)	MLCT	22.80	18.36	-4.44
PhCl	Ru → π*(L1)	MLCT	14.25	9.07	-5.18

Table 15. Dipole moments of $[\text{Ru}(\text{L1})_2(\text{G}_2\text{L2})]^{2+}$ in the optimized gas phase geometry of S_0 (μ_{gs}) and T_1 (μ_{exc}) (see **Figure 66** and **Figure 67** for the structures of L1 and L2).

L1	L2	G	Excitation	μ_{gs}	μ_{exc}	$\Delta\mu$
bpy	dppz	-	$\text{Ru} \rightarrow \pi^*(\text{L2})$	7.08	17.08	10.00
tmpphen	bpy	PhCF_3	$\text{Ru} \rightarrow \pi^*(\text{L2})$	19.82	27.56	7.74
tmpphen	bpy	Cl	$\text{Ru} \rightarrow \pi^*(\text{L2})$	4.84	11.82	6.98
tmpphen	bpy	CCPhCOCF_3	$\text{Ru} \rightarrow \pi^*(\text{L2})$	29.71	36.61	6.89
tmpphen	bpy	CN	$\text{Ru} \rightarrow \pi^*(\text{L2})$	9.40	16.25	6.86
tmpphen	tap	-	$\text{Ru} \rightarrow \pi^*(\text{L2})$	4.78	11.13	6.35
bpy	tap	-	$\text{Ru} \rightarrow \pi^*(\text{L2})$	6.10	12.33	6.23
bpy	phen	NO_2	$\text{Ru} \rightarrow \pi^*(\text{L1,L2})$	16.06	22.01	5.95
tmpphen	bpz	-	$\text{Ru} \rightarrow \pi^*(\text{L2})$	4.37	10.22	5.85
bpy	bpz	-	$\text{Ru} \rightarrow \pi^*(\text{L2})$	5.49	11.29	5.80
bpy	py ^(a)	-	$\text{Ru} \rightarrow \pi^*(\text{L1})$	0.62	5.51	4.89
bpy	dppz	NO_2	$\text{Ru} \rightarrow \pi^*(\text{L2})$	15.42	19.84	4.42
bpy	phen	COCF_3	$\text{Ru} \rightarrow \pi^*(\text{L1,L2})$	20.94	24.68	3.74
bpy	dppz	COOH	$\text{Ru} \rightarrow \pi^*(\text{L2})$	10.93	13.66	2.73
bpy	phen	-	$\text{Ru} \rightarrow \pi^*(\text{L1})$	1.03	2.72	1.69
bpy	phen	COOH	$\text{Ru} \rightarrow \pi^*(\text{L1})$	9.17	5.63	-3.54

^a In this case, L2 is formed by two (monodentate) pyridine rings

Table 16. Dipole moments of $[\text{Ru}(\text{C}_3\text{H}_7\text{-L1})_2(\text{G}_2\text{L2})]^{2+}$ in the optimized gas phase geometry of S_0 (μ_{gs}) and T_1 (μ_{exc}).

L1	L2	G	Excitation	μ_{gs}	μ_{exc}	$\Delta\mu$
bpy	bpy	PhCF_3	$\text{Ru} \rightarrow \pi^*(\text{L2})$	18.34	26.31	7.97
bpy	bpy	Cl	$\text{Ru} \rightarrow \pi^*(\text{L2})$	3.57	10.76	7.19
bpy	Bpy	CN	$\text{Ru} \rightarrow \pi^*(\text{L2})$	8.07	15.16	7.09
bpy	Tap	-	$\text{Ru} \rightarrow \pi^*(\text{L2})$	3.53	10.10	6.57
bpy	Bpy	CCPhCOCF_3	$\text{Ru} \rightarrow \pi^*(\text{L2})$	28.05	34.29	6.24
bpy	Bpz	-	$\text{Ru} \rightarrow \pi^*(\text{L2})$	2.65	8.70	6.06

Selection of the final polarity indicator dyes. From the series of 60 complexes, a representative selection of candidates was made for which we have calculated the Stokes shifts in three different solvents. Based on the largest dipole moment difference, synthetic accessibility and on the requirement that the S_1 and T_1 state has MLCT character, we have selected the $[\text{Ru}(\text{L1})_2(\text{G}_2\text{L2})]^{2+}$ complexes with $\text{L1} = \text{L2} = \text{bpy}$ and $\text{G} = \text{NO}_2, \text{CN}, \text{Cl}, \text{CO}_2\text{CH}_3, \text{CF}_3, \text{CONHC}_6\text{H}_4\text{CF}_3, \text{CONHC}_3\text{H}_7, \text{C}_6\text{F}_5, \text{SO}_2\text{NHC}_6\text{H}_4\text{CF}_3, \text{F}$ and Br . Additionally, some other related complexes were considered for the sake of comparison: (i) the parent (i.e. unsubstituted) complex and its 3,4,7,8-tetramethylated derivative to add systems that undergo relatively small changes when going from S_0 to T_1 , and (ii) the $-\text{C}_6\text{H}_4\text{CF}_3$ substituent to study a Ru(II) complex whose CT excitation involves L2. The calculated absorption and emission energies and Stokes shifts for these dyes in solution are collected in Table 17 and Table 18; those Tables encompass bpy ligands bearing substituents with mesomeric or inductive effects, respectively. A plot of the calculated Stokes shifts against the solvent polarity parameter Δf defined in eq. [6] shows a negative linear variation ($R^2 > 0.993$ in all cases). This slope is also listed in the Tables under the entry “L-M (Lippert-Mataga) slope” (eq. [5]).

Table 17. Calculated $S_0 \rightarrow S_1$ absorption energy, $T_1 \rightarrow S_0$ emission energy, Stokes shift, and Lippert-Mataga (L-M) slope (all in cm^{-1}) for $[\text{Ru}(\text{bpy})_2(\text{G}_2\text{bpy})]^{2+}$ complexes with mesomeric electron-donating or electron-withdrawing substituents (G) in water, ethanol and tetrahydrofuran (THF).

G	Solvent	$S_0 \rightarrow S_1$	$T_1 \rightarrow S_0$	Stokes Shift	L-M slope
$\text{C}_6\text{H}_4\text{CF}_3$	THF	20955	16047	4908	
	EtOH	20750	16002	4748	-1880
	H_2O	20684	15982	4702	
$\text{CONH C}_6\text{H}_4\text{CF}_3$	THF	19932	15229	4704	
	EtOH	19786	15221	4564	-1681
	H_2O	19738	15219	4518	
$\text{CONH C}_3\text{H}_7$	THF	20531	15768	4763	
	EtOH	20255	15607	4647	-1383
	H_2O	20166	15555	4611	
NO_2	THF	17235	13457	3778	
	EtOH	16927	13255	3672	-1299
	H_2O	16825	13192	3634	
CO_2CH_3	THF	19714	15360	4354	
	EtOH	19458	15208	4250	-1223
	H_2O	19339	15159	4220	
CN	THF	18375	14236	4139	
	EtOH	18217	14177	4041	-1192
	H_2O	18171	14164	4007	
C_6F_5	THF	20528	15800	4728	
	EtOH	20372	15734	4638	-1127
	H_2O	20327	15726	4602	
H	THF	21896	16614	5262	
	EtOH	21844	16658	5186	-976
	H_2O	21823	16677	5146	

Table 18. Calculated $S_0 \rightarrow S_1$ absorption energy, $T_1 \rightarrow S_0$ emission energy, Stokes shift, and Lippert-Mataga (L-M) slope (all in cm^{-1}) for $[\text{Ru}(\text{bpy})_2(\text{G}_2\text{bpy})]^{2+}$ complexes with inductive electron-donating or -withdrawing substituents in water, ethanol and tetrahydrofuran (THF).

G	Solvent	$S_0 \rightarrow S_1$	$T_1 \rightarrow S_0$	Stokes Shift	L-M slope
H	THF	21876	16617	5258	
	EtOH	21844	16658	5186	-976
	H_2O	21823	16676	5147	
Br	THF	20701	15566	5134	
	EtOH	20562	15507	5055	-935
	H_2O	20519	15487	5032	
Cl	THF	20822	15613	5209	
	EtOH	20705	15568	5137	-855
	H_2O	20669	15553	5116	
F	THF	21280	15805	5475	
	EtOH	21218	15810	5408	-806
	H_2O	21198	15812	5386	
CH_3	THF	21555	16300	5200	
	EtOH	21466	16335	5132	-549
	H_2O	21454	16343	5111	
CF_3	THF	19632	14755	4877	
	EtOH	19539	14712	4827	-536
	H_2O	19519	14700	4820	

The first striking issue observed is that the L-M slope is negative for all complexes, in manifest contradiction to the Lippert-Mataga expression of eq. [5], which predicts a definite positive slope. The origin of this contradiction lies in the fact that the L-M model assumes that the absorbing and emitting states are of the same multiplicity and that the transitions involved do not entail electron transfer. A more detailed analysis of this point will be provided below.

Comparison of the L-M slopes in Table 17 and Table 18 shows that the substituents with mesomeric electronic effects provoke a larger variation of the Stokes shift with increasing solvent polarity, so that they are preferable to develop polarity probes based on Ru(II) complexes. Consequently, the next steps of our study focused mainly on this type of substituents.

In an actual luminescent sensor for polarity monitoring, the Ru complex must be embedded in a hydrophobic film [Castro 2015]. This is usually carried out by attaching long alkyl (e.g., *n*-nonyl) or *tert*-butyl groups in the periphery of the indicator dye. Fortunately, the 4,4'-dinonylbipyridine ligand is commercially available to be used as the ancillary ligands (L1, see above). To model the effect of these chains on the L-M slope, two propyl substituents were additionally introduced in L1 of the complexes listed in **Table 17**, and the L-M slope was recalculated (**Table 19**). Attaching the propyl group as model of the long aliphatic chains has a very small effect on the L-M slopes calculated for the unsubstituted analogues. There is a general tendency to slightly less negative slopes, except for the parent compound and the complexes with the CN and NO₂ substituents (see **Table 19**). This result indicates that the aliphatic chains are not significant for the electronic properties related to the Stokes shifts of the complexes.

Table 19. Calculated Lippert-Mataga slope (in cm⁻¹) and linear correlation coefficients for several Ru[(C₃H₇)₂bpy]₂(G₂bpy)]²⁺ complexes.

G	Slope	R ²
PhCF ₃	-1658	0.997
CONHC ₃ H ₇	-1189	0.998
NO ₂	-1644	1.000
COOCH ₃	-1049	0.997
CN	-1254	1.000
H	-1021	0.993
Cl	-693	0.998

Comparison of the computational and experimental results. The first and most important comparison between experiment and computation concerns the L-M slope or, in other words, how sensitive the different substituted Ru(II) complexes are to changes in the polarity of the environment. Figure 67 collects the measured and calculated Stokes shifts of the complexes (1), (2) and (3), and Table 20 summarizes the numerical values of the L-M slopes. In all cases we found a negative slope and also the relative size of the experimental slopes is correctly reproduced - although the calculated L-M slopes are smaller than the experimental ones by a factor of four. The computational strategy is a compromise between accuracy and efficiency; more sophisticated computational schemes can bring the absolute value of the slopes in

closer agreement with the experimental data, but this would drastically reduce the efficiency of the screening procedure. The correct reproduction of both sign and relative magnitude of the slopes validates the computational strategy followed in this study to select promising Ru(II)-polypyridyl candidates for polarity probes.

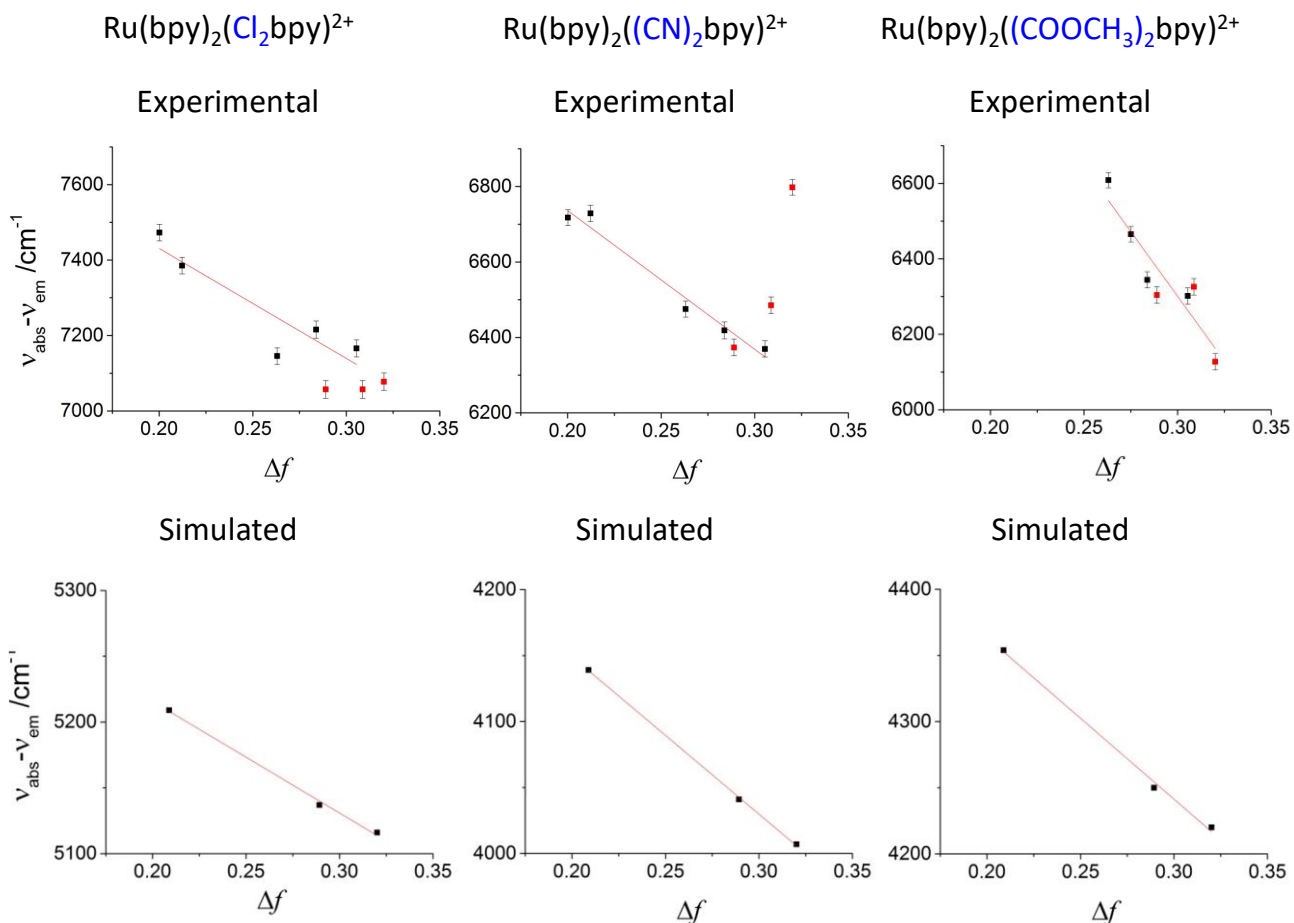


Figure 67. Experimental (already reported in **Figure 42**, **Figure 43**, and **Figure 44**) and calculated Lippert-Mataga plots for the heteroleptic Ru(II) dyes in **Figure 64**. The uncertainties in the experimental plots are the maximum estimated uncertainties derived from the choice of the maximum absorption and emission wavelengths. The data points in red correspond to the protogenic solvents (EtOH, MeOH and H₂O); they have not been included in the linear fits to determine the experimental L-M slope (see text).

Table 20. Comparison of the computed and experimental Lippert-Mataga slopes (in cm^{-1}) for the synthesized $[\text{Ru}(\text{bpy})_2(\text{G}_2\text{bpy})]^{2+}$ complexes

Complex	Computed	Experimental
3 ($\text{G} = \text{CO}_2\text{CH}_3$)	-1223	-6900 ± 1300
2 ($\text{G} = \text{CN}$)	-1192	-3700 ± 400
($\text{G} = \text{H}$)	-976	-3600 ± 1000
1 ($\text{G} = \text{Cl}$)	-855	-2900 ± 800

To analyze the different L-M slopes extracted from the experimental Stokes shifts and the calculated ones, we first consider how the absorption varies with the polarity of the solvent. The systematic study by Meyer and co-workers of the absorption energy of $[\text{Ru}(\text{bpy})_3]^{2+}$ complexes versus the solvent polarity shows an increase of the transition energy as the polarity increases [Kober 1984, Thompson 2013]. However, the changes are rather small, never exceeding 1 kcal/mol ($\sim 350 \text{ cm}^{-1}$). To the best of our knowledge, there are no other recent experimental data for that compound, and little has been published on the absorption spectra dependence on solvent polarity for other complexes. For example, for $[\text{Ru}(\text{dppz})(\text{phen})_2]^{2+}$ the influence on the emission spectra of the solvent has been extensively studied given to its particular luminescent behavior (it is not photoluminescent in water but does emit in non-aqueous solvents, see for example references [Nair 1997] and [McKinley 2013]), while its absorption spectra does not show a significant influence by the nature of the solvent, showing that the MLCT absorption band is at slightly longer wavelengths in H_2O than in CH_3CN [Nair 1997, Olson 1997]. Similar behavior is found for related compounds [Sun 2010]. From the computational point of view, some works have been published on this issue. TD-DFT studies report absorption wavelengths for the MLCT band of $[\text{Ru}(\text{dppz})(\text{phen})_2]^{2+}$ in different solvents: in vacuum, acetonitrile and water the maxima of the absorption bands are located at 417, 445 and 449 nm respectively in reference [Fantacci 2004] and at 423, 450 and 454 nm in reference [Ambrosek 2010]. These results are in partial agreement with the experimental data reported in [Olson 1997], which show that the MLCT absorption band is observed at longer wavelengths in H_2O than in CH_3CN . Less clear conclusions were extracted from the TD-DFT study of $[\text{Ru}(\text{bpy})_2(\text{bpy-E-Ph-E-Ipa})]^{2+}$ (E = ethynylene, Ph = *p*-phenylene, Ipa = isophthalic acid) [Lundqvist 2007]. Increasing polarity from benzene ($\epsilon = 2.27$) to ethanol ($\epsilon = 24.5$), the maximum absorption wavelength decreases, while it slightly increases from ethanol to acetonitrile ($\epsilon = 37.5$). Regarding the fulfillment of the Lippert-Mataga equation, some authors have reported cases in which dyes display a behavior that is opposite to the predicted by this equation. For example, authors of references [Castro 2005] and [Lundqvist 2007] describe a hypsochromic shift of the Ru(II) polypyridyls

emission with increasing solvent polarity in a wide range, while changes in the absorption energy are reported to be small and no predominant trend has been established.

In their analysis of the solvent effects on the absorption and emission energies, Lippert and Mataga placed the solute in a spherical cavity surrounded by a continuous polarizable medium. The dipole moments of the ground state (μ_G) and of the excited state (μ_E) were assumed to remain approximately constant when the solute relaxes to the optimal excited state geometry. Under this assumption, the fast component of the solvent stabilization (electronic rearrangement of the solvent molecules) does not contribute to the Stokes shift. Therefore, the latter exclusively depends on the slow component due to the reorientation of the solvent molecules around the solute. The resulting expression predicts a linear dependency of the Stokes shift on the solvent polarity Δf with a positive slope given by $(\mu_E - \mu_G)^2$ (see eq. [5]). In the Ru complexes studied here, we indeed observe a linear dependence of the Stokes shift on the solvent polarity, but the slope of the plot is negative, both computationally and in the experimental measurements.

Despite being a rather successful model, the L-M equation only covers part of the solvent-solute interactions. In addition to the aforementioned approximation of constant dipole moments, the L-M model does not consider intersystem crossing from the initially populated singlet excited state: the excited state populated by the photon absorption is also the state that originates the emission, the differences being only the orientation of the solvent molecules around the solute. To start with the latter approximation, this is obviously not the case for the Ru complexes studied here. The strong spin-orbit coupling promoted by the heavy metal core causes a rapid intersystem crossing from S_1 to T_1 and subsequent relaxation of the triplet state brings the system to the emitting (3MLCT) species. The assumption of negligible changes in the dipole moment of ground and excited state upon the geometry relaxation does not seem to be justified, as the dipole moments of the S_0 , S_1 and T_1 states in the Franck-Condon region and at the relaxed geometry change significantly. Other effects such as hydrogen bonding cannot be used to explain the discrepancy between the L-M equation and the calculated results, as they are not included in the computational approach. Such interactions are likely to be the reason for the underestimation of the calculated slopes compared to the experimental ones.

Deviations from the Lippert-Mataga relationship

Vertical absorption energy of the complex in the ground state geometry:

$$\Delta E_{abs} = E_{exc}(gs) - E_{gs}(gs)$$

Vertical emission energy of the complex in the relaxed excited state geometry:

$$\Delta E_{\text{em}} = E_{\text{exc}}(\text{exc}) - E_{\text{gs}}(\text{exc})$$

Stokes shift:

$$\Delta E_{\text{abs,em}} = \Delta E_{\text{abs}} - \Delta E_{\text{em}}$$

Energy of a solute in a cavity (of radius α) surrounded by a dielectric continuum:

$$E = E_{\text{vac}} + \mu R = 2\mu \cdot \Delta f / \alpha^3$$

being μ the dipole moment of the solute, R the reaction field induced in the dielectric by the dipole and Δf the polarity parameter defined in eq. [6].

The reaction field is a sum of the electronic reorganization (fast, polarization) and the reorientation of the solvent molecules (slow, dipole orientation):

$$R = R^{\text{el}} + R^{\text{dip}}$$

Then, the four energies become:

$$\begin{aligned} E_{\text{gs}}(\text{gs}) &= E_{\text{gs,vac}}(\text{gs}) - \mu_{\text{gs}}(\text{gs}) R_{\text{gs}}^{\text{dip}} - \mu_{\text{gs}}(\text{gs}) R_{\text{gs}}^{\text{el}} \\ E_{\text{exc}}(\text{gs}) &= E_{\text{exc,vac}}(\text{gs}) - \mu_{\text{exc}}(\text{gs}) R_{\text{gs}}^{\text{dip}} - \mu_{\text{exc}}(\text{gs}) R_{\text{exc}}^{\text{el}} \\ E_{\text{gs}}(\text{exc}) &= E_{\text{gs,vac}}(\text{exc}) - \mu_{\text{gs}}(\text{exc}) R_{\text{exc}}^{\text{dip}} - \mu_{\text{gs}}(\text{exc}) R_{\text{gs}}^{\text{el}} \\ E_{\text{exc}}(\text{exc}) &= E_{\text{exc,vac}}(\text{exc}) - \mu_{\text{exc}}(\text{exc}) R_{\text{exc}}^{\text{dip}} - \mu_{\text{exc}}(\text{exc}) R_{\text{exc}}^{\text{el}}, \end{aligned}$$

The absorption and emission energies:

$$\begin{aligned} \Delta E_{\text{abs}} &= \Delta E_{\text{abs,vac}} - [\mu_{\text{exc}}(\text{gs}) - \mu_{\text{gs}}(\text{gs})] R_{\text{gs}}^{\text{dip}} - \mu_{\text{exc}}(\text{gs}) R_{\text{exc}}^{\text{el}} - \mu_{\text{gs}}(\text{gs}) R_{\text{gs}}^{\text{el}} \\ \Delta E_{\text{em}} &= \Delta E_{\text{em,vac}} - [\mu_{\text{exc}}(\text{exc}) - \mu_{\text{gs}}(\text{exc})] R_{\text{exc}}^{\text{dip}} - \mu_{\text{exc}}(\text{exc}) R_{\text{exc}}^{\text{el}} - \mu_{\text{gs}}(\text{exc}) R_{\text{gs}}^{\text{el}} \end{aligned}$$

And the Stokes shift, assuming that $\mu_{\text{gs}}(\text{gs}) \approx \mu_{\text{gs}}(\text{exc})$ and $\mu_{\text{exc}}(\text{gs}) \approx \mu_{\text{exc}}(\text{exc})$:

$$\begin{aligned} \Delta_{\text{abs,em}} &= (\Delta E_{\text{abs}} - \Delta E_{\text{em}})_{\text{vac}} - (\mu_{\text{exc}} - \mu_{\text{gs}})(R_{\text{gs}}^{\text{dip}} + R_{\text{exc}}^{\text{dip}}) = \\ &= (2\Delta f / \alpha^3)(\mu_{\text{exc}} - \mu_{\text{gs}})^2 + \Delta \Delta E_{\text{vac}} \end{aligned}$$

In addition to the assumption that the dipole moments of the ground state and excited state do no change too much when the geometry relaxes, it is also assumed that the nature of the state does not change, i.e. no internal conversion (IC) or intersystem

crossing (ISC) occur during relaxation from the Franck-Condon geometry to the excited state minimum.

In general, the effect of the solvent polarity on the excitation and emission energies depend on the differential stabilization of the ground and excited states by solvation (Chen 1998). An important factor that determines the interaction between solvent and solute is the magnitude of the dipole moment. It is then expected that a large dipole moment difference ($\Delta\mu$) between the ground and excited states will provoke a larger variation of the Stokes shift with increasing polarity of the solvent. According to this, the possible variation of the Stokes shift with Δf in the simplest cases is schematically represented in **Figure 68**.

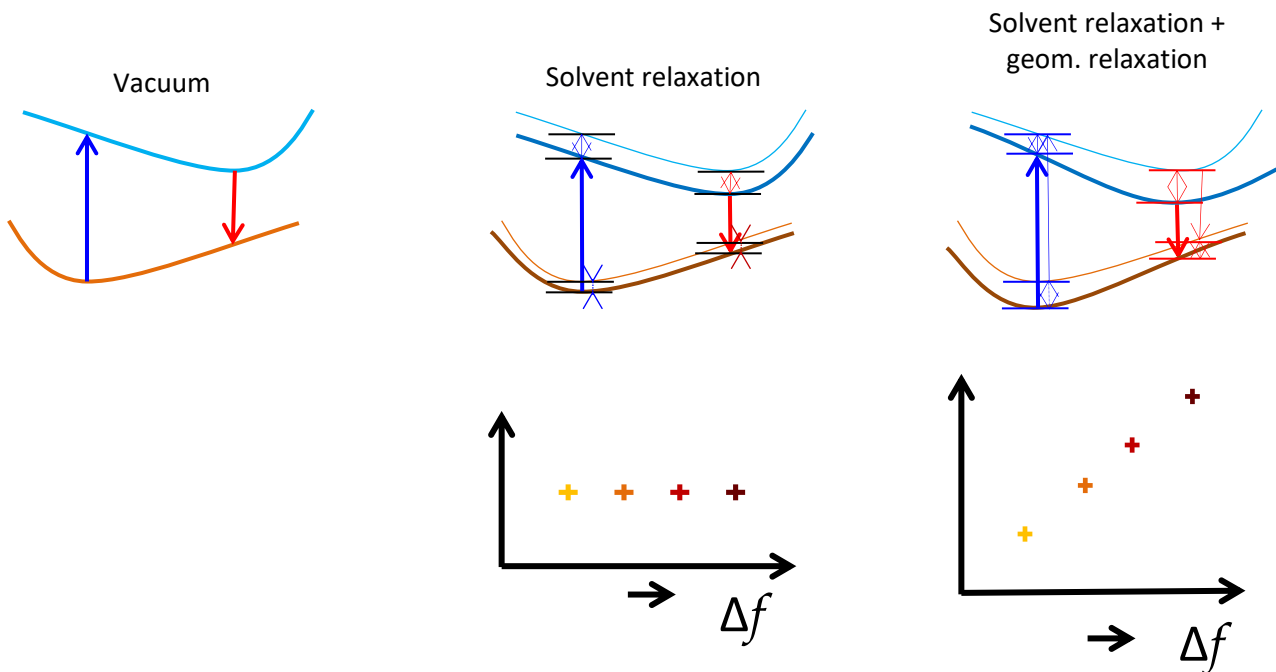


Figure 68. Schematic representation of the solvent effect on the potential energy surfaces of the states involved in a luminescent event and the possible dependences of the Stokes Shift on Δf in these cases.

However, if intersystem crossing occurs, the change between the state populated by the excitation and the emitting state can lead to rather large differences in the electronic reorganization and consequently in the effect of the environment on the absorption and emission. In the polarity probes studied here based on Ru(II) complexes, where the excited state involved in the absorption is S1 while the one involved in the emission is T1, additional factors should be considered. Consequently, the relation between the dipole moment difference and the Stokes shift may not be so simple so not even the sign of the slope of the Lippert-Mataga equation can be predicted *a priori*. This situation is depicted in **Figure 69**.

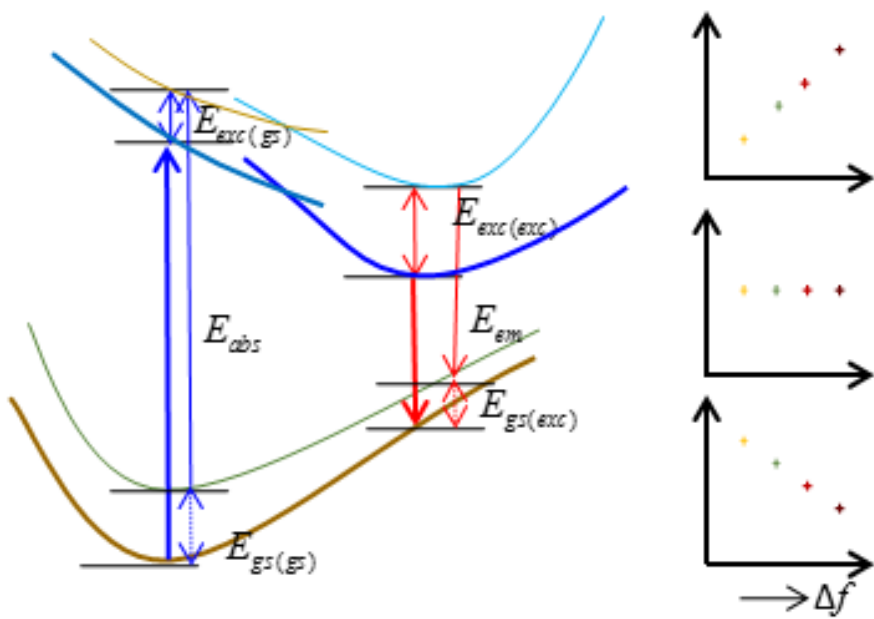


Figure 69. Schematic representation of the solvent effect on the potential energy surfaces of the states involved in a luminescent event where ISC takes place, and possible dependence of the Stokes Shift on Δf in this case.

3.6. References

Abdel-Shafi	2007	Abdel-Shafi, A. A.; Ward, M. D.; Schmidt, R. Mechanism of Quenching by Oxygen of the Excited States of Ruthenium(II) Complexes in Aqueous Media. Solvent Isotope Effect and Photosensitized Generation of Singlet Oxygen, O ₂ (1Δg), by [Ru(diimine)(CN) ₄] ²⁻ complex ions. <i>Dalton Trans.</i> 2007 , 24, 2517–2527.
Adamo	1999	Adamo, C.; Barone, V. Toward Reliable Density Functional Methods Without Adjustable Parameters: The PBE0 Model. <i>J. Chem. Phys.</i> 1999 , 110, 6158–6170.
Ambrosek	2010	Ambrosek, D.; Loos, P. F.; Assfeld, X.; Daniel, C. A Theoretical Study Of Ru(II) Polypyridyl DNA Intercalators Structure And Electronic Absorption Spectroscopy Of [Ru(Phen) ₂ (Dppz)] ²⁺ And [Ru(Tap) ₂ (Dppz)] ²⁺ Complexes Intercalated In Guanine-Cytosine Base Pairs. <i>J. Inorg. Biochem.</i> 2010 , 104, 893–901.
Antoine	1888	Antoine, C. "Tensions des Vapeurs; Nouvelle Relation Entre les Tensions et les Températures" [Vapor Pressure: A New Relationship Between Pressure and Temperature], <i>Comptes Rendus des Séances de l'Académie des Sciences</i> (in French) 1888 , 107, 681–684, 778–780, 836–837.
Arnold	1911	Arnold, J.P. Origin and History of Beer and Brewing: From Prehistoric Times to the Beginning of Brewing Science and Technology. <i>Alumni Assn. of the Wahl-Henius Institute</i> 1911 .
Askerov	2009	Askerov, N. A.; Zhogun, V. N.; Magomedov, Z. A. Acousto-Optical Alcohol Meters. <i>Meas. Tech.</i> 2009 , 52, 884–889.
Bains	2011	Bains, G.; Patel, A. B.; Narayanaswami, V. Pyrene: A Probe To Study Protein Conformation And Conformational Changes. <i>Molecules</i> 2011 , 16, 7909–7935.
Bay	1972	Bay, H. W.; Blurton, K. F.; Lieb, H. C.; Oswin, H. G. Electrochemical Measurements of Blood Alcohol Levels. <i>Nature</i> , 1972 , 240, 52.
Blum	2001	Blum, P.; Mohr, G. J.; Matern, K.; Reichert, J.; Spichiger-Keller, U. E.; Optical Alcohol Sensor Using Lipophilic Reichardt's Dyes In Polymer Membranes. <i>Anal. Chim. Acta</i> 2001 , 432, 269–275.
Brandes	2007	Brandes, E.; Mitu, M.; Pawel, D. The Lower Explosion Point: A Good Measure for Explosion Prevention: Experiment and Calculation for Pure Compounds and Some Mixtures. <i>J. Loss Prevent. Process Ind.</i> 2007 , 20, 536–540.
Brereton	2003	Brereton, P.; Hasnip, S.; Bertrand, S.; Wittkowski, R.; Guillou, C. Analytical Methods for the Determination of Spirit Drinks, <i>Trends Analyt. Chem.</i> 2003 , 22, 19–25.

Bustamante	2018	Bustamante, N.; Ielasi, G.; Bedoya, M.; Orellana, G. Optimization of Fiber-Optic Temperature Sensing with Polymer-Embedded Luminescent Ru(II) Complexes. <i>Polymers</i> 2018 , <i>10</i> , 234.
Campagna	2007	Campagna S, Puntoriero F, Nastasi F, Bergamini G, Balzani V. Photochemistry and Photophysics of Coordination Compounds: Ruthenium. In: <i>Photochemistry and Photophysics of Coordination Compounds I</i> , Balzani V., Campagna S. (Eds), Springer, Berlin, 2007; pp. 117-214.
Capek	2002	Capek, I. Fate of excited probes in micellar systems. <i>Adv. Colloid Interface Sci.</i> 2002 , <i>97</i> , 91-149.
Carturan	2009	Carturan, S.; Tonezzer, M.; Quaranta, A.; Maggioni, G.; Buffa, M.; Milan, R. Optical Properties of Free-Base Tetraphenylporphyrin Embedded in Fluorinated Polyimides and Their Ethanol and Water Vapours Sensing Capabilities. <i>Sens. Actuator B-Chem.</i> 2009 , <i>137</i> , 281-290.
Caspar	1983	Caspar, J. V.; Meyer, T. J. Photochemistry of Ru(bpy) ₃ ²⁺ . Solvent Effects. <i>J. Am. Chem. Soc.</i> 1983 , <i>105</i> , 5583-5590.
Castro	2005	Castro, A. M.; Delgado, J.; Orellana, G. Hydrocarbon in Water Sensing with PTFE Membranes Doped with a Luminescent Ru(II) Poly(Pyridyl) Complex. <i>J. Mater. Chem.</i> 2005 , <i>15</i> , 2952-2958.
Cerón-Carrasco	2014	Cerón-Carrasco, J. P.; Jacquemin, D.; Laurence, C.; Planchat, A.; Reichardt, C.; Sraïdi, K. Solvent polarity scales: determination of new ET(30) values for 84 organic solvents. <i>J. Phys. Org. Chem.</i> 2014 , <i>27</i> , 512-518.
Chang	1997	Chang, Q.; Lakowicz, J. R.; Rao, G. Fluorescence Lifetime-based Sensing of Methanol. <i>Analyst</i> 1997 , <i>122</i> , 173-177
Chen	1998	Chen, P.; Meyer, T. J. Medium Effects on Charge Transfer in Metal Complexes. <i>Chem. Rev.</i> 1998 , <i>98</i> , 1439-1477.
Craggs	1974	Craggs, A.; Moody, G. J.; Thomas, J. D. R. PVC Matrix Membrane Ion-Selective Electrodes. <i>J. Chem. Educ.</i> 1974 , <i>51</i> , 541-544.
L138 HSE Books	2003	Dangerous Substances and Explosive Atmospheres. Dangerous Substances and Explosive Atmospheres Regulations 2002. Approved Code of Practice and guidance L138 HSE Books 2003 . ISBN 0 7176 2203 7
Demchenko	2015	Demchenko, A. P.; Duportail, G.; Oncul, S.; Klymchenko, A. S.; Mély, Y. Introduction to Fluorescence Probing of Biological Membranes. <i>Methods Mol. Biol.</i> 2015 , <i>1232</i> , 19-43; b) Zhou, J.; Ma, H., Design Principles of Spectroscopic Probes for Biological Applications. <i>Chem. Sci.</i> 2016 , <i>7</i> , 6309-6315.

Chapter 3 - Optode for EtOH sensing based on Ru(II) indicator dyes

Dimroth	1963	Dimroth, K.; Reichardt, C.; Siepmann, T.; Bohlmann, F. On pyridinium N-phenol betaines and their use for characterizing the polarity of solvents. <i>Liebigs Ann. Chem.</i> 1963 , 661, 1.
DIRECTIVE EU PARLIAMENT	2014	DIRECTIVE 2014/34/EU OF THE EUROPEAN PARLIAMENT AND OF THE COUNCIL of 26 February 2014 on the harmonization of the laws of the Member States relating to equipment and protective systems intended for use in potentially explosive atmospheres. Retrieved from http://eur-lex.europa.eu/legal-content/EN/TXT/?uri=celex:32014L0034 .
Dong	1982	Dong, D. C.; Winnik, M. A. The Py scale of solvent polarities. <i>Photochem. Photobiol.</i> 1982 , 35, 17–21.
Drysdale	1999	Drysdale, D. Fire safety engineering in the process industries [online]. <i>Chemeca 99: Chemical Engineering: Solutions in a Changing Environment</i> . Institution of Engineers: Barton, A.C.T (Australia), 1999 , pp. 22–34. Retrieved from https://search.informit.com.au/documentSummary;dn=944830315328896;res=IELENG ISBN: 0858257203.
Dubowski	1975	Dubowski, K. M. Studies in breath-alcohol analysis: biological factors. <i>Z Rechtsmed.</i> 1975 , 76, 93–117. doi: 10.1007/BF00200555.
Fantacci	2004	Fantacci, S.; De Angelis, F.; Sgamellotti, A.; Re, N. A. TDDFT Study Of The Ruthenium(II) Polyazaaromatic Complex [Ru(Dppz)(Phen)2]2+ In Solution. <i>Chem. Phys. Lett.</i> 2004 , 396, 43–48.
Freys	2012	Freys, C.; Gardner, J. M.; D'Amario, L.; Brown, A. M.; Hammarström, L. Ru-Based Donor-Acceptor Photosensitizer that Retards Charge Recombination in a P-Type Dye-Sensitized Solar Cell. <i>Dalton Trans.</i> 2012 , 41, 13105–13111.
Furche	2014	Furche, F.; Ahlrichs, R.; Hättig, C.; Klopper, W.; Sierka, M.; Weigend, F. Turbomole. <i>WIREs Comput. Mol. Sci.</i> 2014 , 1, 91–100;
García-Fresnadillo	1996	García-Fresnadillo, D.; Georgiadou, Y.; Orellana, G.; Braun, A. M.; Oliveros, E. Singlet-Oxygen ($1\Delta g$) Production by Rutheniurn(II) Complexes Containing Polyazaheterocyclic Ligands in Methanol and in Water. <i>Helv. Chim. Acta</i> 1996 , 79, 1222–1238.
Gay-Lussac	1824	Gay-Lussac, J.L. Instruction pour l'usage de l'alcoomètre centésimal et des tables qui l'accompagnent. Paris, France: Chez M. Collardeau, 1824 .
George	2001	George, S. C.; Thomas, S. Transport Phenomena through Polymeric Systems. <i>Prog. Polym. Sci.</i> 2001 , 26, 985–1017.
González-Velasco	2002	González-Velasco, J. R.; González-Marcos, J. A.; López-Dehesa, C. Pervaporation of Ethanol – Water Mixtures through Poly(1-

		Trimethylsilyl-1-Propyne) (PTMSP) Membranes. <i>Desalination</i> 2002 , <i>149</i> , 61-65.
Hall	2013	Hall, J.; Beer, H.; Buchner, K.; Cardin, D.; Cardin, C. Preferred Orientation in an Angled Intercalation Site of a Chloro-Substituted Lambda- [Ru(TAP) ₂ (dppz)] ²⁺ Complex Bound to d(TCGGCCGCA) ₂ . <i>Philos. Trans. Royal Soc. A</i> 2013 , <i>371</i> .
Hernaez	2017	Hernaez, M.; Zamarreno, C. R.; Melendi-Espina, S.; Bird, L. R.; Mayes, A. G.; Arregui, F. J. Optical Fibre Sensors Using Graphene-Based Materials: A Review. <i>Sensors</i> 2017 , <i>17</i> .
Heymann	2017	Heymann, H.; Ebeler, S.E. Uses and Good Practices of Sensory Evaluation in the Alcoholic Beverage Industry. In <i>Sensory and Instrumental Evaluation of Alcoholic Beverages</i> , Academic Press: San Diego, 2017 . Ch. 2, pp. 24-33.
Ielasi	2019	Ielasi, G.; Alcover, G.; Casellas, J.; de Graaf, C.; Orellana, G.; Reguero, M. Computer-aided design of short-lived phosphorescent Ru(II) polarity probes. <i>Dyes Pigm.</i> 2019 , <i>162</i> , 168-176.
Iodice	2017	Iodice, P.; Senatore, A.; Langella, G.; Amoresano, A. Advantages of Ethanol-Gasoline Blends as Fuel Substitute for Last Generation SI Engines. <i>Environ. Prog. Sustain. Energy</i> 2017 . https://doi.org/10.1002/ep.12545 .
Jung	2016	Jung, H. S.; Verwilst, P.; Kim, W. Y.; Kim, J. S. Fluorescent and colorimetric sensors for the detection of humidity or water content. <i>Chem. Soc. Rev.</i> 2016 , <i>45</i> , 1242-1256.
Juris	1988	Juris, A.; Balzani, V.; Barigelli, F.; Campagna, S.; Belser, P.; von Zelewsky, A. Ru(II) Polypyridine Complexes: Photophysics, Photochemistry, Eletrochemistry, and Chemiluminescence. <i>Coord. Chem. Rev.</i> 1988 , <i>84</i> , 85-277.
Kamlet	1976	Kamlet, M. J.; Taft, R. W. The Solvatochromic Comparison Method. I. The b-Scale of Solvent Hydrogen-Bond Acceptor (HBA) Basicities. <i>J. Am. Chem. Soc.</i> 1976 , <i>98</i> , 377-383.
Klamt	1993	Klamt, A.; Schürmann, G. COSMO: A New Approach To Dielectric Screening In Solvents With Explicit Expressions For The Screening Energy And Its Gradient. <i>J. Chem. Soc. Perkin Trans. 2</i> 1993 , 799-805.
Klini	2015	Klini, A.; Pissadakis, S.; Das, R. N.; Giannelis, E. P.; Anastasiadis, S. H.; Anglos, D. ZnO-PDMS Nanohybrids: A Novel Optical Sensing Platform for Ethanol Vapor Detection at Room Temperature, <i>J. Phys. Chem. C Nanomater. Interfaces</i> 2015 , <i>119</i> , 623-631.
Klymchenko	2013	Klymchenko, A. S.; Mely, Y. Fluorescent Environment-Sensitive Dyes as Reporters of Biomolecular Interactions. <i>Prog. Mol. Biol. Transl. Sci.</i> 2013 , <i>113</i> , 35-58.

Kober	1984	Kober, E. M.; Sullivan, B. P.; Meyer, T. J. Solvent Dependence Of Metal-To-Ligand Charge-Transfer Transitions. Evidence For Initial Electron Localization In MLCT Excited States Of 2,2'-Bipyridine Complexes Of Ruthenium(II) And Osmium(II), <i>Inorg. Chem.</i> 1984 , 23, 2098–2104;
Kudo	2010	Kudo, H.; Sawai, M.; Suzuki, Y.; Wang, X.; Gessei, T.; Takahashi, D.; Arakawa, T.; Mitsubayashi, K. Fiber-Optic Bio-Sniffer (Biochemical Gas Sensor) for High-Selective Monitoring of Ethanol Vapor Using 335 nm UV-LED. <i>Sens. Actuator B-Chem.</i> 2010 , 147, 676–680.
Laha	2002	Laha, A. K.; Das, P. K.; Bagchi S. Study of Preferential Solvation in Mixed Binary Solvent as a Function of Solvent Composition and Temperature by UV-Vis Spectroscopic Method. <i>J. Phys. Chem. A</i> 2002 , 106, 3230–3234.
Lai	2012	Lai, C.-L.; Fu, Y.-L.; Chen, J.-T.; An, Q.-F.; Liao, K.-S.; Fang, S.-C.; Hu, C.-C.; Lee, K.-R. Pervaporation Separation of Ethanol/Water Mixture by UV/O ₃ -Modified PDMS Membranes. <i>Sep. Purif. Technol.</i> 2012 , 100, 15–21.
Lam	2009	Lam, H.; Kostov, Y. Optical Instrumentation for Bioprocess Monitoring. <i>Adv. Biochem. Eng. Biotechnol.</i> 2009 , 116, 1–28.
Lee	2011	Lee, Y. E.; Kopelman, R. Nanoparticle PEBBLE Sensors in Live Cells. <i>Meth. Enzymol.</i> 2012 , 504, 419–470; b) Baù, L.; Tecilla, P.; Manzin, F. Sensing with Fluorescent Nanoparticles. <i>Nanoscale</i> 2011 , 3, 121–133.
Li	2010	Li, J.; Fan, H. Q.; Jia, X. H.; Yang, W. W.; Fang, P. Y. Enhanced Blue-Green Emission and Ethanol Sensing of Co-Doped ZnO Nanocrystals Prepared by a Solvothermal Route. <i>Appl. Phys. A Mater. Sci. Process.</i> 2010 , 98, 537–542.
Liaw	2010	Liaw, H.-J.; Gerbaud V.; Wu H.-T. Flash-Point Measurements and Modeling for Ternary Partially Miscible Aqueous-Organic Mixtures. <i>J. Chem. Eng. Data</i> 2010 , 55, 3451–3461.
Lippert	1957	Lippert, E. Spectroscopic Determination of the Dipole Moment of Aromatic Compounds in the First Excited Singlet State. <i>Z. Elektrochem., Ber. Bunsenges. Phys. Chem.</i> 1957 , 61, 962–975.
Lundqvist	2007	Lundqvist, M. J.; Galoppini, E.; Meyer, G.J.; Persson, P. Calculated Optoelectronic Properties Of Ruthenium Tris-Bipyridine Dyes Containing Oligophenylenethynylene Rigid Rod Linkers In Different Chemical Environments. <i>J. Phys. Chem. A</i> 2007 , 111, 1487–1497.
Machado	2014	Machado, V. G.; Stock, R. I.; Reichardt, C. Pyridinium N-Phenolate Betaine Dyes. <i>Chem. Rev.</i> 2014 , 114, 10429–10475.
Magnusson	2014	Magnusson, B.; Örnemark, U. Eurachem Guide: The Fitness for Purpose of Analytical Methods – A Laboratory Guide to

Method Validation and Related Topics, 2nd ed., 2014 . ISBN 978-91-87461-59-0. Available from www.eurachem.org .		
Mariammal	2012	Mariammal, R. N.; Ramachandran, K.; Renganathan, B.; Sastikumar, D. On the Enhancement of Ethanol Sensing by CuO Modified SnO ₂ Nanoparticles Using Fiber-Optic Sensor. <i>Sens. Actuator B-Chem.</i> 2012 , <i>169</i> , 199–207.
Mariammal	2012 b	Mariammal, R. N.; Susila, V. M.; Renganathan, B.; Sastikumar, D.; Ramachandran, K. Ethanol Sensor Using Zn _{1-x} CdxO (x = 0.00 and 0.10) Nanorods by Fiber-Optic Technique. <i>Sens. Lett.</i> 2012 , <i>10</i> , 18–25.
Masuda	1990	Masuda, T.; Tang, B.-Z.; Higashimura, T. Pervaporation of Organic Liquid-Water Mixtures through Substituted Polyacetylene Membranes. <i>J. Memb. Sci.</i> 1990 , <i>49</i> , 69–83
Masuda	1998	Masuda, A.; Kaizu, Y. Specific Role of Water in Radiationless Transition from the Triplet MLCT States of Tris(polypyridine) Complexes of Osmium(II). <i>Inorg. Chem.</i> 1998 , <i>3713</i> , 3371–3375.
Mataga	1956	Mataga, N.; Kaifu, Y.; Koizumi, M. Solvent Effects upon Fluorescence Spectra and the Dipole moments of Excited Molecules. <i>Bull. Chem. Soc. Jpn.</i> 1956 , <i>29</i> , 465–470.
McKinley	2013	McKinley, A. W.; Lincoln, P.; Tuite, E. M. Sensitivity Of [Ru (Phen)2(Dppz)] ²⁺ Light Switch Emission To Ionic Strength, Temperature, And DNA Sequence. <i>Dalton Trans.</i> 2013 , <i>42</i> , 4081–4090.
Mohr	2001	Mohr, G. J.; Klimant, I.; Spichiger-Keller, U. E.; Wolfbeis, O. S. Fluoro Reactands and Dual Luminophore Referencing: A Technique to Optically Measure Amines. <i>Anal. Chem.</i> 2001 , <i>735</i> , 1053–1056.
Mohr	2005	Mohr, G. J. Covalent Bond Formation as an Analytical Tool to Optically Detect Neutral and Anionic Analytes. <i>Sens. Actuator B-Chem.</i> 2005 , <i>107</i> , 2–13.
Nagamura	2010	Nagamura, T.; Tanaka, H.; Matsumoto, R. High Performance Optical Sensing of Alcohol by Guided Wave Mode Geometry. <i>Sens. Actuator B-Chem.</i> 2010 , <i>146</i> , 253–259.
Nair	1997	Nair, R. B.; Cullum, B. M.; Murphy, C. J. Optical Properties Of [Ru (Phen)2(Dppz)] ²⁺ As A Function Of Nonaqueous Environment. <i>Inorg. Chem.</i> 1997 , <i>36</i> , 962–965.
Nakajima	1971	Nakajima, A. Solvent Effect on the Vibrational Structures of Fluorescence and Absorption Spectra of Pyrene. <i>Bull. Chem. Soc. Jpn.</i> 1971 , <i>44</i> , 3272–3277.
NIOSH	1992	NIOSH: Recommendations for Occupational Safety and Health - Compendium of Policy Documents and Statements. NIOSH Publication No. 92-100: Cincinnati, OH, 1992 .
NIOSH	1995	Documentation for Immediately Dangerous to Life or Health Concentrations (IDLHs). <i>National Institute of Occupational Safety</i>

		<i>and Health (NIOSH)</i> 1995 . Retrieved from http://www.cdc.gov/niosh/idlh/64175.html
Olson	1997	Olson, A. J. C.; Hu, D.; Hörmann, A.; Jonkman, A. M.; Arkin, M. R.; Stemp, E. D. A.; Barton, J. K.; Barbara, P. F. First Observation of the Key Intermediate in the “Light-Switch” Mechanism of [Ru(phen) ₂ dppz] ²⁺ . <i>J. Am. Chem. Soc.</i> 1997 , <i>119</i> , 11458–11467.
Onsager	1936	Onsager, L. Electric Moments of Molecules in Liquids. <i>J. Am. Chem. Soc.</i> 1936 , <i>58</i> , 1486–1493.
Orellana	1988	Orellana, G.; Alvarez Ibarra, C.; Santoro, J. ¹ H and ¹³ C NMR Coordination-Induced Shifts in a Series of Tris(a-diimine)ruthenium(II) Complexes Containing Pyridine, Pyrazine, and Thiazole Moieties, <i>Inorg. Chem.</i> 1988 , <i>27</i> , 1025–1030.
Orellana	1995	Orellana, G.; Gomez-Carneros, A. M.; de Dios, C.; Garcia-Martinez, A. A.; Moreno-Bondi, M. C. Reversible Fiber-Optic Fluorosensing of Lower Alcohols. <i>Anal. Chem.</i> 1995 , <i>67</i> , 2231–2238.
Orellana	1998	Orellana, G.; García-Fresnadillo, D.; Marazuela, M.D.; Moreno-Bondi, M.C.; Delgado, J.; Sicilia, J.M. Fiber-Optic Chemical Sensors: From Molecular Engineering to Environmental Analytical Chemistry in the Field, in <i>Monitoring of Water Quality: The Contribution of Advanced Technologies</i> , F. Colin, P. Quevauviller (Eds.), Elsevier, Amsterdam, 1998 ; pp 103–116.
Orellana	2011	Orellana, G.; Cano-Raya, C.; López-Gejo, J.; Santos, A. R. Online Monitoring Sensors. In: <i>Treatise on Water Science</i> , Vol. 3, Wilderer, P. (Ed.) 2011 ; Elsevier: Oxford, UK. Ch. 59, pp. 221–262.
Orellana	2004 a	Orellana, G. Luminescent optical sensors. <i>Anal. Bioanal. Chem.</i> 2004 , <i>379</i> , 344–346.
Orellana	2004 b	Orellana, G.; García-Fresnadillo, D. Environmental and Industrial Optosensing with Tailored Luminescent Ru(II) Polypyridyl Complexes. In: <i>Optical Sensors: Industrial, Environmental and Diagnostic Applications</i> , Narayanaswamy, R.; Wolfbeis, O. S. (Eds) 2004 (Springer, Berlin Heidelberg), Ch. 13, pp. 309–357.
Palmer	2006	Palmer, J. J. How to Brew. Brewers Publications, 2006 .
Papkovsky	1997	Papkovsky, D. B.; Mohr, G. J.; Wolfbeis, O. S. New Polar Plasticizers for Luminescence-Based Sensors. <i>Anal. Chim. Acta</i> 1997 , <i>337</i> , 201–205.
Petrov	2001	Petrov, N. K.; Wiessner, A.; Staerk, H. A Simple Kinetic Model of Preferential Solvation in Binary Mixtures. <i>Chem Phys Lett.</i> 2001 , <i>349</i> , 517–520.

Piñeiro	2015	Piñeiro, L.; Novo, M.; Al-Soufi, W. Fluorescence emission of pyrene in surfactant solutions. <i>Adv. Colloid Interface Sci.</i> 2015 , <i>215</i> , 1–12.
Regulation (EU) No 1169/2011	2011	REGULATION (EU) No 1169/2011 OF THE EUROPEAN PARLIAMENT AND OF THE COUNCIL of 25 October 2011, Annex XII. Retrieved from https://eur-lex.europa.eu/legal-content/EN/TXT/?uri=celex:02011R1169-20140219 .
Reichardt	2010	Reichardt, C.; Welton, T. Solvents and Solvent Effects in Organic Chemistry, 4th ed, Wiley-VCH, 2010 .
Runge	1984	Runge, E.; Gross, E. K. U. Density-Functional Theory For Time-Dependent Systems, <i>Phys. Rev. Lett.</i> 1984 , <i>52</i> , 997–1000;
Sebok	2012	Sebok, D.; Janovák, L.; Kovács, D.; Sápi, A.; Dobó, D. G.; Kukovecz, A.; Kónya, Z.; Dékány, I. Room Temperature Ethanol Sensor with Sub-Ppm Detection Limit: Improving the Optical Response by Using Mesoporous Silica Foam. <i>Sens. Actuator B-Chem.</i> 2012 , <i>243</i> , 1205–1213.
Sen Gupta	2016	Sen Gupta, S. K. Proton Transfer Reactions in Apolar Aprotic Solvents. <i>J. Phys. Org. Chem.</i> 2016 , <i>29</i> , 251–264.
Sharifpour-Boushehri	2015	Sharifpour-Boushehri, S.; Hosseini-Golgoo, S. M.; Sheikhi, M.-H. A Low Cost and Reliable Fiber Optic Ethanol Sensor Based on Nano-Sized SnO ₂ . <i>Opt. Fiber Technol.</i> 2015 , <i>24</i> , 93–99.
Simon	1995	Simon, D.N.; Czolk, R.; Ache, H.J. Doped Sol-Gel Films for the Development of Optochemical Ethanol Sensors. <i>Thin Solid Films</i> 1995 , <i>260</i> , 107–110.
Somerharju	2002	Somerharju, P. Pyrene-labeled lipids as tools in membrane biophysics and cell biology. <i>Chem. Phys. Lipids</i> 2002 , <i>116</i> , 57–74.
Sullivan	1978	Sullivan, B. P.; Salmon, D. J.; Meyer, T. J. Mixed phosphine 2,2'-bipyridine complexes of ruthenium. <i>Inorg. Chem.</i> 1978 , <i>17</i> , 3334–3341.
Sun	2010	Sun, Y.; Turro, C. Highly Solvent Dependent Luminescence from [Ru (bpy) _n (dppp2)3-n]2 ⁺ (n = 0-2). <i>Inorg. Chem.</i> 2010 , <i>49</i> , 5025–5032.
Thungon	2017	Thungon, P.D.; Kakoti, A.; Ngashangva, L.; Goswami, P. Advances in Developing Rapid, Reliable and Portable Detection Systems for Alcohol, <i>Biosens. Bioelectron.</i> 2017 , <i>97</i> , 83–99.
Tolbert	2002	Tolbert, L. M.; Solntsev, K. M. Excited-State Proton Transfer: From Constrained Systems to “Super” Photoacids to Superfast Proton Transfer. <i>Acc. Chem. Res.</i> 2002 , <i>35</i> , 19–27.
Tomasi	2005	Tomasi, J.; Mennucci, B.; Cammi, R. Quantum Mechanical Continuum Solvation Models. <i>Chem. Rev.</i> 2005 , <i>105</i> , 2999–3094.
Valeur	2001	Valeur, B. Effect of Polarity on Fluorescence Emission. Polarity Probes. In: <i>Molecular Fluorescence: Principles and Applications</i> , 1st ed, Wiley-VCH, 2001; pp. 200–225.

Valeur	2012	Valeur, B.; Berberan-Santos, M. N. Environmental Effects on Fluorescence Emission, in <i>Molecular Fluorescence: Principles and Applications</i> , Second Edition, Wiley-VCH Verlag GmbH & Co KGaA: Weinheim, Germany, 2012 , pp. 109–140.
Vane	2008	Vane, L. M.; Namboodiri, V. V.; Bowen, T. C. Hydrophobic Zeolite–Silicone Rubber Mixed Matrix Membranes for Ethanol–Water Separation: Effect of Zeolite and Silicone Component Selection on Pervaporation Performance. <i>J. Memb. Sci.</i> 2008 , <i>308</i> , 230–241.
Wallin	2005	Wallin, S.; Davidsson, J.; Modin, J.; Hammarström, L. Femtosecond Transient Absorption Anisotropy Study on [Ru(bpy) ₃] ²⁺ and [Ru(bpy)(py) ₄] ²⁺ . Ultrafast Interligand Randomization of the MLCT State. <i>J. Phys. Chem. A</i> 2005 , <i>109</i> , 4697–4704.
Wang	1991	Wang, K.; Seiler, K.; Haug, J. P.; Lehmann, B. West, S.; Hartman K.; Simon, W. Hydration of Trifluoroacetophenones as the Basis for an Optical Humidity Sensor. <i>Anal. Chem.</i> 1991 , <i>63</i> , 970–974.
Weigend	2005	Weigend, F.; Ahlrichs, R. Balanced Basis Sets Of Split Valence, Triple Zeta Valence And Quadruple Zeta Valence Quality For H To Rn: Design And Assessment Of Accuracy. <i>Phys. Chem. Chem. Phys.</i> 2005 , <i>7</i> , 3297–3305.
Winnik	1993	Winnik, F. M. Photophysics of preassociated pyrenes in aqueous polymer solutions and in other organized media. <i>Chem. Rev.</i> 1993 , <i>93</i> , 587–614.
Wypych	2004	Wypych, G. Plasticizers Use and Selection for Specific Polymers, in <i>Handbook of plasticizers</i> . ChemTec Publishing, 2004 , Ch. 11.
Zabetakis	1965	Zabetakis, M. G. Flammability Characteristics of Combustible Gases and Vapors. <i>Technical Report Archive and Image Library</i> . U.S. Department of the Interior, Bureau of Mines, 1965 . Vol. 627–629.
Zelinskii	1956	Zelinskii, V. V.; Kolobkov, V.P.; Piimlik, L. G. <i>Opt. i Spekt.</i> 1956 , <i>1</i> , 161–167.
Zeng	1994	Zeng, H.-H.; Wang, K.-M.; Li, D.; Yu, R.-Q. Development of an Alcohol Optode Membrane Based on Fluorescence Enhancement of Fluorescein Derivatives. <i>Talanta</i> 1994 , <i>41</i> , 969–975.
Zhou	2016	Zhou, J.; Ma, H. Design principles of spectroscopic probes for biological applications. <i>Chem. Sci.</i> 2016 , <i>7</i> , 6309–6315.

4. APPLICATION OF LUMINESCENCE-BASED MICROSENSORS TO MICROFLUIDIC CELL CULTURES AND ORGAN-ON-A-CHIP DEVICES

Like the furtive collectors of stolen art, we [cell biologists] are forced to be lonely admirers of spectacular architecture, exquisite symmetry, dramas of violence and death, mobility, self-sacrifice and, yes, rococo sex.

— Lorraine Cudmore

Chapter 4 - Application of Luminescence-Based Microsensors For Microfluidic Cell Cultures and Organ-On-A-Chip Devices

4.1. Introduction

This chapter deals with two projects. The first one, developed in the Pharmaceutical Analysis group in the Rijksuniversiteit Groningen (The Netherlands), concerned **developing dioxygen sensors for human umbilical vein endothelial cells (HUVECs) cultured in microfluidic PDMS - glass chips**. The second one, carried out in Micronit Microtechnologies B.V. (Enschede, The Netherlands), regarded **manufacturing dioxygen and temperature sensors for glass organ-on-a-chip (OOAC) devices**. Additionally, the aim was using cheap and compact luminescence lifetime-based monitoring instrumentation for both applications, achievable through measurements in the frequency domain [Lakowicz 2006]. Hence, the indicator dyes used were polyazaaromatic ruthenium complexes which luminescence can be monitored by a portable phase-shift based multichannel luminometer. The instrument, tuned towards the excitation - emission wavelength and luminescence lifetime of these metal complexes, was equipped with optical fibers for remote sensing.

Cell culture is of paramount importance in many fields, like cellular and molecular biology, medicine and pharmacology. Many vaccines (e.g., against polio and chickenpox) are obtained thanks to mass culture of animal cell lines [Milián 2015, Perdue 2011], and tissue engineering allows development of biological substitutes for biological tissue or whole organs [Lanza 2000, MacArthur 2005, Phelan 2017]. For growing cells in vitro, control of culture conditions is of great importance in order to recreate in vivo-like environment, because they affect cellular function and behavior. Microfluidic cell cultures are especially interesting because they permit close mimic of in vivo conditions, for example allowing continuous perfusion of the culture, creating physical or chemical gradients, controlling cells number and volume available, and growing different cells in close contact to allow exchanging material or signals [Huh 2012, Bhatia Halldorsson 2015]. Moreover, it is possible to continuously perfuse living cells arranged in 3D structures to simulate tissue- and organ-level physiology, in the so-called organ-on-a-chip (OOAC) devices [Bhatia 2014]. This is especially important when dealing with preclinical drug testing, for which traditional 2D cell-cultures, even though able to provide valid information about the substance efficacy and toxicity, fail to represent precisely cells function and physiology [Breslin 2013, Edmondson 2014]. The 3D structures found in an intact organ or its simulation can instead add fundamental information about tissue-tissue interactions [Huh 2012].

One of the most important parameters in cell culture is dioxygen (O_2) tension [Semenza 2007, Jagannathan 2016]. While it is known since long time that atmospheric dioxygen pressure is not the “normal” condition for human cells [Cooper 1958, Jagannathan 2016], cell cultures are still kept majorly under 19.95-21% O_2 . These values are much higher than in the human body, where O_2 varies between 0.5 to 16%. In the case of endothelial cells, for example, normoxia is considered about 10% O_2 for

arterial environment and 5% O₂ for venous environment [Tsai 2003], and hence in these conditions cells should be cultured for biologically relevant results. Another fundamental cell culture parameter is temperature (T) [Kretzmer 1998], which is known since the 1960s to have a dramatic effect on cells growth kinetics [Watanabe 1967]. While human cells are always cultured in incubators at 37 °C, the required handling is usually done at about 20 °C. These mild temperature shocks are commonly neglected, but recent studies revealed that changes in gene expression could be detected after one hour already at 32 °C, without recovery at 37 °C [Fujita 1999]. And further undesired effects are induced when cells are exposed to lower temperatures [Kaufmann 1999, Neutelings 2013]. For all these reasons, there is a growing interest in inspecting O₂ and T in cell cultures. Microfluidic chip-based cell cultures enable control of these parameters at a microscopic level, although their monitoring can be challenging due to the chips small size. Moreover, real time measurements as well as high spatial resolution of PO₂ and T are usually necessary [Abaci 2014, Brennan 2014, Oomen 2016]. Optical O₂ and T sensors are thus the most suitable, giving their aptness for miniaturization, imaging, and lack of analyte consumption [Sun 2015]).

Many luminescent-based sensors designed for microfluidic chips have been described in the literature. The majority are constituted of a sensitive spot incorporated inside the chip microstructures, monitored with a (spectro)luminometer, plate reader, or microscope [Nock 2013, Brennan 2014, Sun 2015, Pfeiffer 2015, Oomen 2016, Pfeiffer 2017]. However, it is often complex to transfer these kind of sensors – designed to proof the sensitive layer operation – in chips truly optimized for cell cultures [Lin 2009, Skolimowski 2010, Krabbe 2015, Mousavi Shaegh 2016]. In addition, the luminescent sensitive polymer is usually deposited onto the glass side of the chip [Grate 2012, Ungerboeck 2013, Gitlin 2013, Wang 2013, Lasave 2015], which should be devoted to cell attachment. The microchips predominantly used for research purposes, in fact, are constituted of a glass slide attached to a patterned polydimethylsiloxane (PDMS) part containing the microfluidic structures (**Figure 70**). The PDMS is a less than optimal material for cells attachment. It can be functionalized for improving cell adhesion, but it implies further complexity [Qiu 2014, Halldorsson 2015].

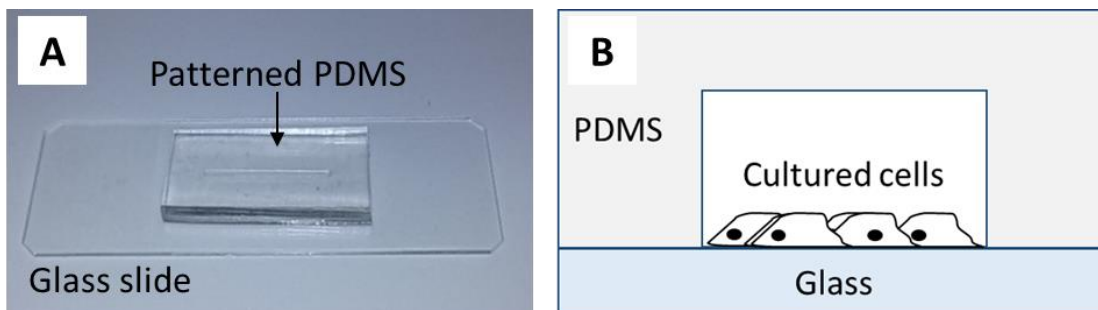


Figure 70. A: picture of a typical PDMS-glass microfluidic chip. B: artistic depiction of cells cultured into the microchannels of the microfluidic chip.

4.2. Dioxygen sensors for HUVECs culture in PDMS-glass microfluidic chips

4.2.1. Aim of the study

Regarding the first sub-project, the aims of this work were

- I. to prepare an O₂-sensitive layer which can be effortless deposited into the small-sized structures of microfluidic chip cultures, adapting the sensor to the design of the microchip culture. Preferentially, the O₂-sensitive layer had to coat the PDMS side of the chip, in order to leave the glass side for cells attachment;
- II. to culture cells in the chip, in order to verify the O₂-sensitive layer biocompatibility; and
- III. to use an instrument for contactless sensing the pO₂ in the microchannels where cells were grown.

4.2.2. Materials and methods

4.2.2.1. Reagents

- Water (purified with a Millipore Direct-Q system, Bedford, MA)
- Solvents (Fisher Scientific, Loughborough, UK), HPLC grade, used without further purification
- Silica particles AEROSIL® R 812s (Evonik Industries AG, Essen, DE)
- Trihexyl(tetradecyl)phosphonium dicyanamide (shortened as [C₂N₃]-[P_{14,6,6,6}]⁺, Sigma Aldrich)
- PR-1204 RTV Prime Coat (Dow Corning, Midland, MI)
- Tris(4,7-diphenyl-1,10-phenanthroline)ruthenium(II) bis(hexafluorophosphate) (shortened as [RD3]²⁺ [2(PF₆)²⁻] and tris[(1,10-phenanthroline-4,7-diyl)bis(benzenesulfonate)]-ruthenate (shortened as [Na₄]⁴⁺[Ru(S₂D)₃]⁴⁻), synthesized as described elsewhere [García-Fresnadillo 1996, García-Fresnadillo 2001]
- Negative photoresist SU-8 3025 (Micro Resist Technology GmbH, Berlin, DE)
- Two-part PDMS Sylgard 184 (Dow Corning, Midland, MI)
- 200 µm-thick glass slide (Thermo Fisher Scientific, Waltham, MA)
- Primary HUVECs, from the University Medical Center (Groningen)
- Endothelial culture medium (ECM), consisting of RPMI 1640 supplemented with 20% heat-inactivated fetal calf serum (FCS), 2 mM L-glutamine, 5 IU/mL

heparin, 100 IU/mL penicillin, 100 µg/mL streptomycin, and 50 µg/mL endothelial cell growth factor supplement extracted from bovine brain

- Trypsin-EDTA solution (Sigma Aldrich)
- Gelatin (from porcine skin, gel strength 300, Type A, Sigma Aldrich)
- Glutaraldehyde (Sigma Aldrich)
- Calcein AM (Sigma Aldrich)
- One component, room temperature curing, solvent free Poly-(dimethylsiloxane)-based coating Dow-Corning 3140 (Wiesbaden, Germany)

4.2.2.2. O₂-sensitive material

The sensitive layers were prepared by depositing a “sensor cocktail”, i.e. a mixture containing matrix precursor, O₂-sensitive luminescent Ru(II) dye, solvent and additives. Two sensor cocktails were prepared. *Sensor cocktail 1* was designed to be biocompatible, while *Sensor cocktail 2* was designed to be cytotoxic (see 4.2.2.5 Biocompatibility of the O₂-sensitive coatings). The biocompatible sensitive coating was meant to allow monitoring the O₂ concentration close to the cells, while the cytotoxic sensitive coating was designed to monitor O₂ concentration but avoiding cells to grow near it.

Sensor cocktail 1. [RD3]²⁺ [2(PF₆)]²⁻ was dissolved in CHCl₃ and added over silica (0.15 wt% dye/silica). The mixture was sonicated for 5 minutes and then the solvent was evaporated in a rotary evaporator (40° C, atmospheric pressure). Finally, the dyed powder was added to the silane solution PR-1204 (1 wt% dyed silica/silane solution) and suspended via sonication for 5 minutes.

Sensor cocktail 2. 1 mg [Na₄]⁴⁺ [Ru(S₂D)₃]⁴⁻ was dissolved in 1 mL H₂O. [C₂N₃]⁻[P_{14,6,6,6}]⁺ (6 eq) and 1 mL CHCl₃ were added to the solution and the mixture was left stirring overnight. The water was removed, and the obtained RTIL (<{[P_{14,6,6,6}]⁺}₄ [Ru(S₂D)₃]⁴⁻}) was dissolved in toluene (1 ml). The organic phase was washed 3 times with water and then mixed with the silane solution PR 1204 (1 ml).

The two mixtures were kept in sealed vials inside a desiccator with silica gel, protected from light, until use. The O₂-sensitive layer obtained from the deposition of the cocktails 1 and 2 will be hereafter named “coating 1” and “coating 2”, respectively.

Additionally, a reference was used to verify the O₂ tension inside the measuring chamber (see **Figure 76**), close to the microfluidic chips. The reference was a polymer film prepared from a commercial poly-(dimethylsiloxane)-based formulation (Dow-Corning 3140, Wiesbaden, Germany) filled with 10% (by weight) of silica AEROSIL® R 812s, dyed via immersion in a 4 mM RD3 in CHCl₃ solution (following the procedure detailed in [Navarro-Villoslada 2001]).

4.2.2.3. Microfluidic chips fabrication

Microchips were manufactured following the usual steps for soft lithography processes, summarized afterwards.

- a) Designing the mask. Because our aim was to adapt to an existing microfluidic HUVECs culture, it was used a chip design already chosen and tested for this purpose (kindly provided by M. Xu, P. Mulder and Prof. S. Verpoorte), reported in **Figure 71**.

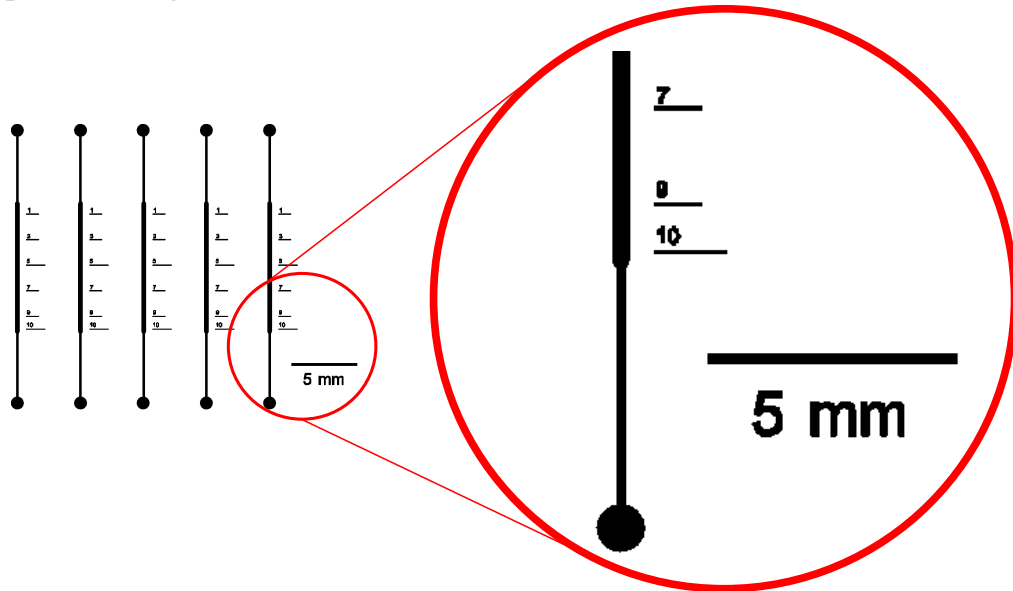


Figure 71. Design of the mask for patterning the photoresist SU-8

One chip consists of five structures. Each one is composed of an introduction channel (width 180 µm, height 100 µm) before and after the cell-seeding channel. The seeding channel (length 1 cm, width 360 µm, height 100 µm) is in the middle, marked with a ruler.

- b) Manufacturing the mold (**Figure 72**).
 1. The glass substrate was spin-coated with the negative photoresist and then exposed to UV light through the mask.
 2. The UV-treated SU-8 was heated at 95°C, in order to promote crosslinking.
 3. The uncured SU-8 was washed away with solvents.

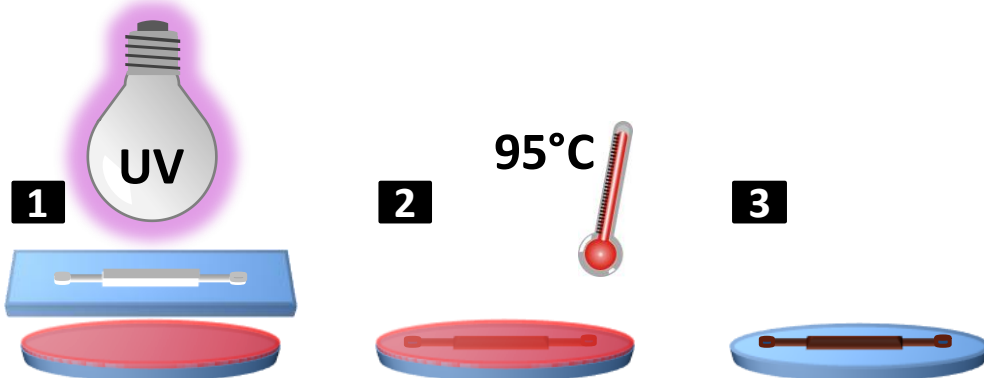


Figure 72. Steps for manufacturing the SU-8 mold.

- c) Making the PDMS-glass chips starting from the SU-8 master mold (**Figure 73**):
1. 30 g of PDMS:crosslinker mixture 10:1 was stirred ($t = 3$ min) and then left in vacuum desiccator ($t = 30$ min) to eliminate bubbles. Afterwards, the mixture was poured onto the master mold, which was kept flat on a leveled hotplate. The hot plate was set to 55°C for 2 hours.
 2. The PDMS negative replica was cut and removed from the mold.
 3. 1 mm holes were punched as microfluidic inlet and outlet.
 4. The sensor cocktail ($V = 2 \mu\text{l}$) was manually pipetted in the microchannels and then left curing for 48 hours. This step was skipped when preparing uncoated chips.
 5. The patterned PDMS piece and a 200 μm -thick glass slides were treated in the O₂-plasma machine (Plasma Cleaner equipped with a mass flow controller PDC-FMG, Harrick Plasma, NY). The plasma activation process parameters ($p\text{O}_2 = 0.47 \text{ hPa}$. RF level: "High". Time: 30 s) had been optimized previously for these chips.
 6. Activated PDMS piece and glass slide were contacted to obtain a covalently bound chip.

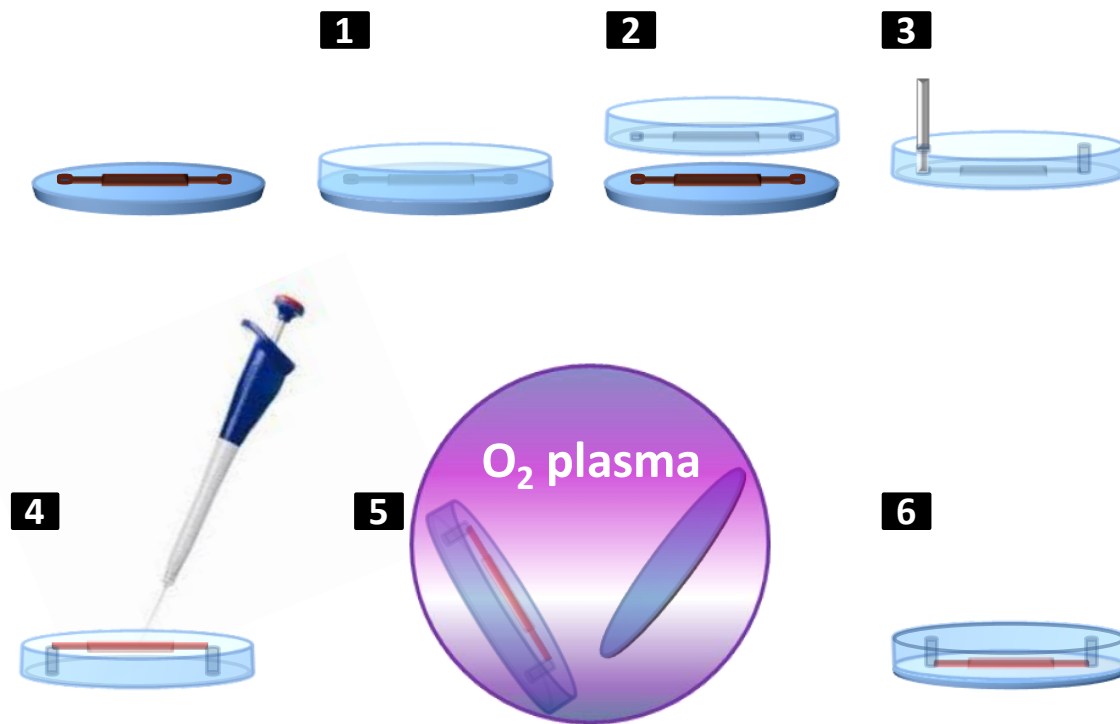


Figure 73. Scheme of the steps for making the PDMS-glass chips from the SU-8 master mold.

4.2.2.4. Cells harvesting and seeding

Primary HUVECs were cultured in ECM and harvested with a 0.25% trypsin-EDTA solution for 30 s (dissociation checked visually), stopped with addition of ECM ($V = 4.5 \text{ ml}$) and centrifugation (1800 rpm, 5 min, 4 °C). The cells were finally resuspended in ECM at a concentration of 4500 cells/ μl and kept in ice until use (max 2 hours).

1% gelatin in water solution was injected into each channel of the microfluidic chip. After 45 min, a 0.5% glutaraldehyde in PBS solution was injected, and gelatin was left crosslinking for 15 min. This step was followed by thorough rinsing with PBS (4 times) and subsequent conditioning with ECM at 37 °C. Finally, 10 μl cells suspension (4500 cells/ μl , empirically selected for obtaining 70% confluence – percentage of the surface that is covered by adherent cells – in these microchannels) were injected into each channel. The chips were incubated at 37 °C and 5% CO₂ in a non-tightly closed plastic box containing wet tissues to avoid excessive evaporation of the medium. Fresh ECM was provided after 2 hours, and then every 12 hours.

For assessing cell viability, it was used the live-cell staining dye Calcein AM (0.05% Calcein AM solution in ECM). Staining was performed to facilitate discerning between healthy cells and not healthy or dead cells, although it is possible to recognize healthy

HUVECs just observing their attachment and morphology in brightfield microscopy (see for example **Figure 81**).

For imaging, it was used a DM-IL Inverted Contrasting Microscope (Leica Microsystems AG, Wetzlar, DE), equipped with a camera Leica DFC300 FX, with 1.4 MPixel of resolution. For imaging the stained cells and the luminescent O₂-sensitive coatings, it was added a filter cube I3 with a band-pass 470-nm excitation filter, a 510-nm dichroic mirror and a 515-nm long-pass emission filter (Leica).

4.2.2.5. Biocompatibility of the O₂-sensitive coatings

Biocompatibility of the O₂-sensitive coatings was tested both in wells (24-well plates) and in microchannels. HUVECs were cultured in absence (control) and presence of coating 1 or coating 2. In all cases, starting cell concentration was selected to obtain 70% confluence. For the biocompatibility study in wells, three cultures each were used for control, coating 1 and coating 2. In the microchannels, 21 cultures were used as control, and 16 for both coatings 1 and 2. The number of live cells was observed some hours after seeding (up to 60 hours for the biocompatibility study in wells, up to 24 hours in microchannels). For estimating culture confluence, the cells density was related to a culture in which cells occupy all the available space with a monolayer, using this as a 95% confluence reference (**Figure 83A**).

4.2.2.6. Setup for cell culture in controlled atmosphere

The plastic measurement chamber for performing the experiments at controlled gas concentration was placed into a sealed workstation (**Figure 74** and **Figure 75**), which was automatically thermostated at 37 °C with 3 electric fan heaters monitored with a digital thermometer. The atmosphere composition inside the measurement chamber was set with a mass flow controller manifold (EL-FLOW® Prestige, BRONKHORST HIGH-TECH BV, NL) placed outside the workstation. CO₂ was fixed at 5 %v/v, while N₂ and O₂ were varied to the desired concentrations. The gas mixture produced with the mass flow controller was conveyed into the sealed chamber via a Teflon hose and was kept water-saturated passing through a bubbler filled with deionized water. The microfluidic chips were placed into the measurement chamber onto a custom-made 3D-printed holder (**Figure 76**). This latter allowed interfacing the optical fibers, kept fixed in position, to interrogate from the glass-side of the chips the position inside the microchannel where the O₂-sensitive layer had been deposited. Optical fibers were used in order to measure remotely the luminescence of the O₂-sensitive layer from outside the workstation. Water reservoirs were placed into the measurement chamber to avoid drying out the microfluidic cell cultures.

Chapter 4 - Application of Luminescence-Based Microsensors For Microfluidic Cell Cultures and Organ-On-A-Chip Devices

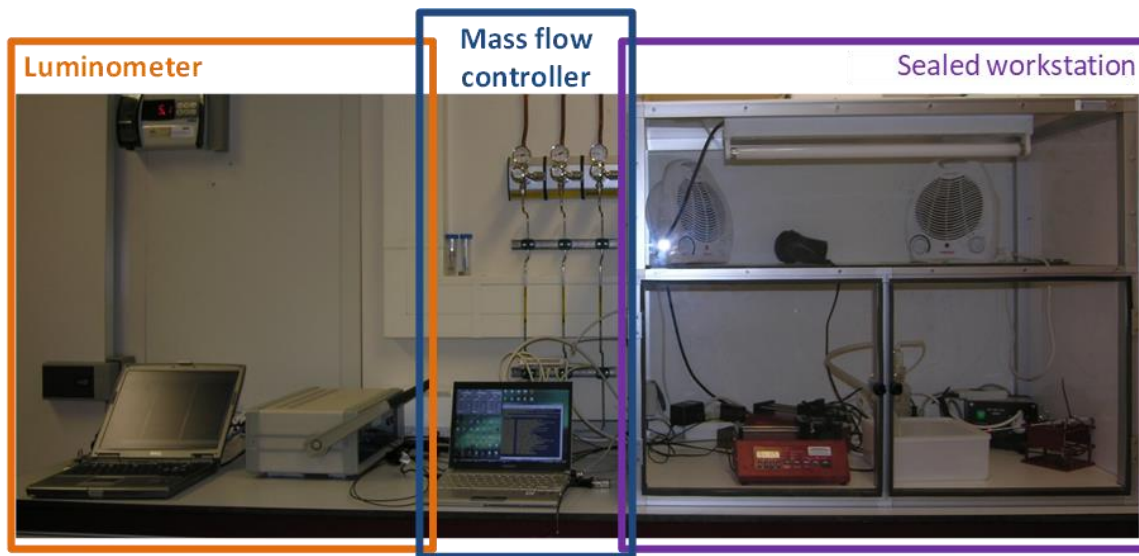


Figure 74. Picture of the luminometer, the mass flow controller and the sealed workstation for experiments at controlled O₂ concentration.



Figure 75. Particular of the measurement chamber placed inside the sealed workstation.

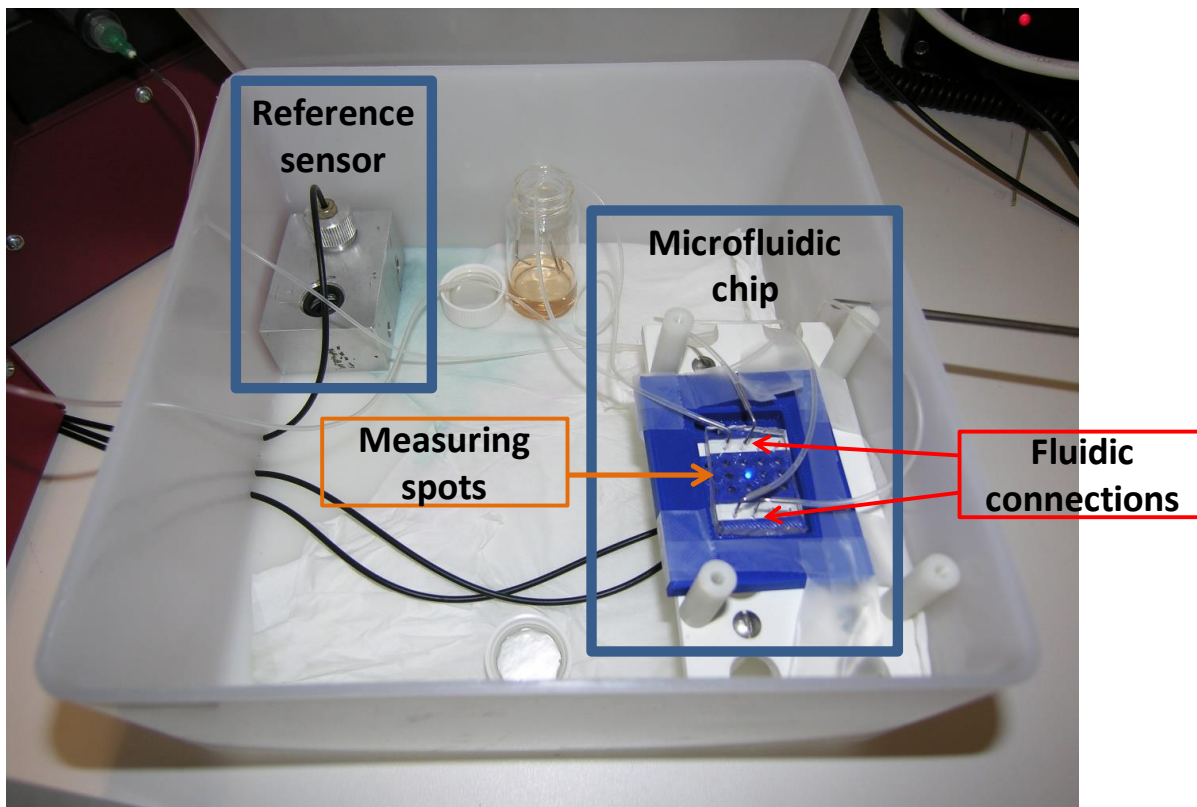


Figure 76. View of the opened plastic measurement chamber. Highlighted are shown the metal holder containing the reference optical O₂-sensitive polymer film used as reference sensor and the microfluidic chip onto the 3D-printed chip holder (in blue).

Gas composition. Although not rigorous, the gas composition is reported in % v/v. Given the small daily variation in atmospheric pressure and the low altitude of the laboratories where the project was carried out (Groningen is practically at sea level), 100% v/v can be considered equal to 1013 hPa.

4.2.2.7. O₂ quantification

The sensing working principle is frequency-domain luminometry. As already stated in the Introduction, the phase shift (ϕ), is function of the modulation frequency (f) and the luminescence probe lifetime (τ), as in eq [7]:

$$\tau = \tan \phi / 2\pi f \quad [7]$$

For these luminescent coatings, the optimum frequency – the frequency at which the phase shift was closest to 45° and thus the sensitivity was the highest – was found to be 39 kHz, and kept constant so that eq [7] could be used to calculate the (apparent)

decay time of the O₂-sensitive luminophore. From this value, it was obtained the oxygen concentration using the so-called Stern-Volmer (S-V) plot. The Stern-Volmer plot based on two-sites quenching model is frequently reported as in eq [20] [Carraway 1991]:

$$\frac{\tau_M^0}{\tau_M} = \left(\frac{f_{01}}{1 + K_{SV1}[Q]} + \frac{f_{02}}{1 + K_{SV2}[Q]} \right)^{-1} \quad [20]$$

where τ_M^0 and τ_M are the pre-exponentially weighted emission lifetimes in absence and in presence of O₂, respectively, f_{01} and f_{02} are the fractions of the total emission from the luminophore in each one of the two sites on the solid support, in absence of O₂, and K_{SV1} and K_{SV2} the Stern-Volmer quenching constants associated to each site ($K_{SV} = k_Q \tau_{M0}$ being k_Q the bimolecular quenching rate constant of the luminophore by O₂).

In order to obtain the same correlation in the phase domain, substitution of eq [7] in eq [20] leads to eq [21]:

$$\tan \phi = \tan \phi^0 \left(\frac{f_{01}}{1 + K_{SV1}[Q]} + \frac{f_{02}}{1 + K_{SV2}[Q]} \right) \quad [21]$$

4.2.3. Results and discussion

4.2.3.1. Microchips preparation and O₂-sensor coatings deposition

The soft lithographic route employed yields the structures reported in **Figure 77**.

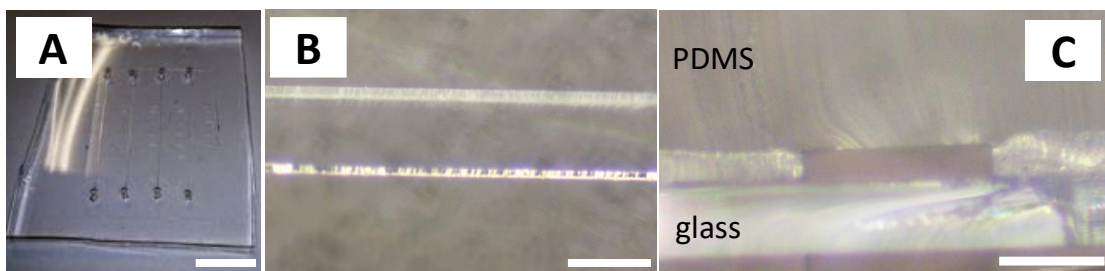


Figure 77. (A) Photograph of the entire chip (patterned PDMS attached onto glass slide), view from the PDMS side; white scale bar: 1 cm. (B) Bright-field micrograph of one seeding channel of the patterned PDMS piece (tilted of about 30°); white scale bar: 360 μ m. (C) Bright-field micrograph of a sliced chip, showing the cutaway view of a chip seeding chamber; white scale bar: 200 μ m.

Our goal was to fabricate the O₂-sensitive luminescent layers onto the PDMS-side of the microfluidic chips, pipetting the “sensor cocktail” directly into the microchannels. Because of the highly hydrophobic nature of the polydimethylsiloxane surface, we chose to follow a sol gel strategy, i.e. to assemble a siloxane coating onto the PDMS surface as the luminescent layer matrix. For this aim, we selected the PR-1204 RTV Prime Coat. This precursor is a dilute solution containing mainly a silane coupling agent (Tetrakis(2-butoxyethyl) orthosilicate) in a mixture of solvents (toluene and light aliphatic solvent naphtha). We designed two different cocktail recipes targeting opposite applications. The first one (cocktail 1) was engineered for resulting in a highly biocompatible coating apt for monitoring dioxygen adjacent to the cells, and it was prepared suspending [RD3]²⁺-dyed silica particles into the silane solution. The second one (cocktail 2) was designed to yield a cytotoxic coating layer that prevents HUVECs to attach and proliferate in its proximity. For this goal, the counter cations of the indicator dye [Na₄]⁴⁺[Ru(S₂D)₃]⁴⁻ were exchanged using [C₂N₃]⁻[P_{14,6,6,6}]⁺, known to have biocidal effects [Xue 2015]. The resulting room temperature ionic liquid (RTIL) was finally mixed with the silane precursor PR-1204.

The two different O₂-sensitive cocktails display different adhesion onto the PDMS surface: while coating 1 results in a homogeneous layer covering all the internal side of the PDMS structure (**Figure 78A**), coating 2 forms a film only on the lateral walls (**Figure 78B** and **Figure 79**).

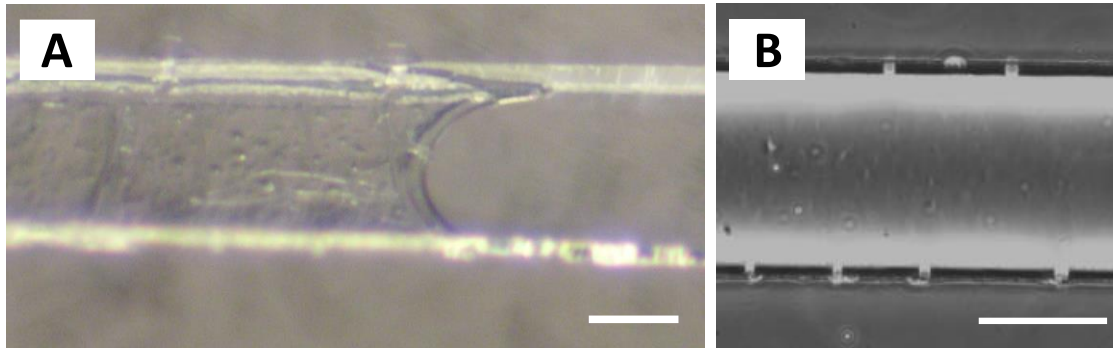


Figure 78. (A) Bright-field micrograph of one seeding channel with coating 1, taken tilting the patterned PDMS piece. White scale bar: 200 µm. (B) Phase-contrast micrograph of one seeding channel with coating 2. White scale bar: 200 µm.

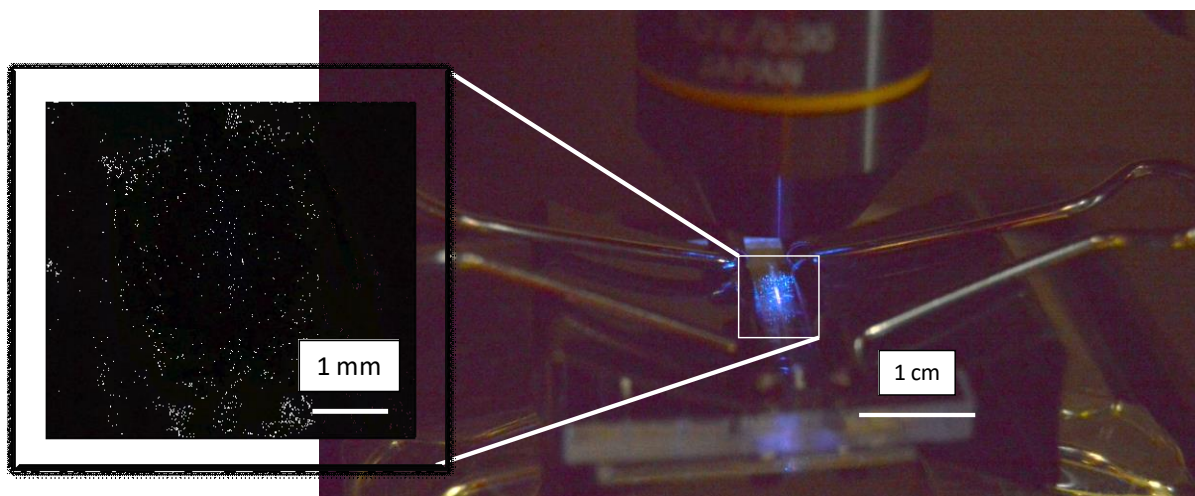


Figure 79. Photograph of a microchip with coating 2 deposited into a seeding channel. Under the blue excitation light ($\lambda_{\text{exc}} = 470 \text{ nm}$), the red emission of the Ru(II) dye is visible at naked eye. The inset shows a zoom of the chip.

4.2.3.1. Biocompatibility study

The result of the biocompatibility study is summarized in Figure 80.

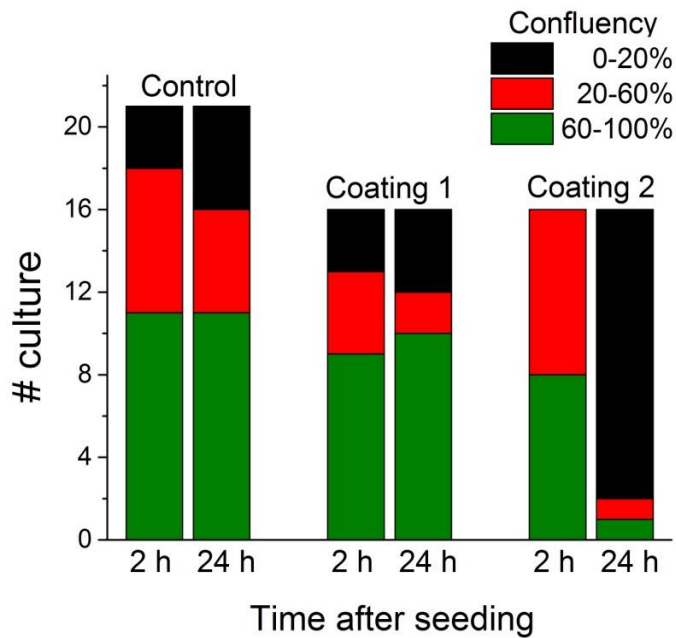


Figure 80. Biocompatibility study in the microfluidic cultures. Control: pristine microchannels (no coating deposited). Coating 1: microchannels in which cocktail 1 was deposited. Coating 2: microchannels in which cocktail 2 was deposited (see text for cocktails composition).

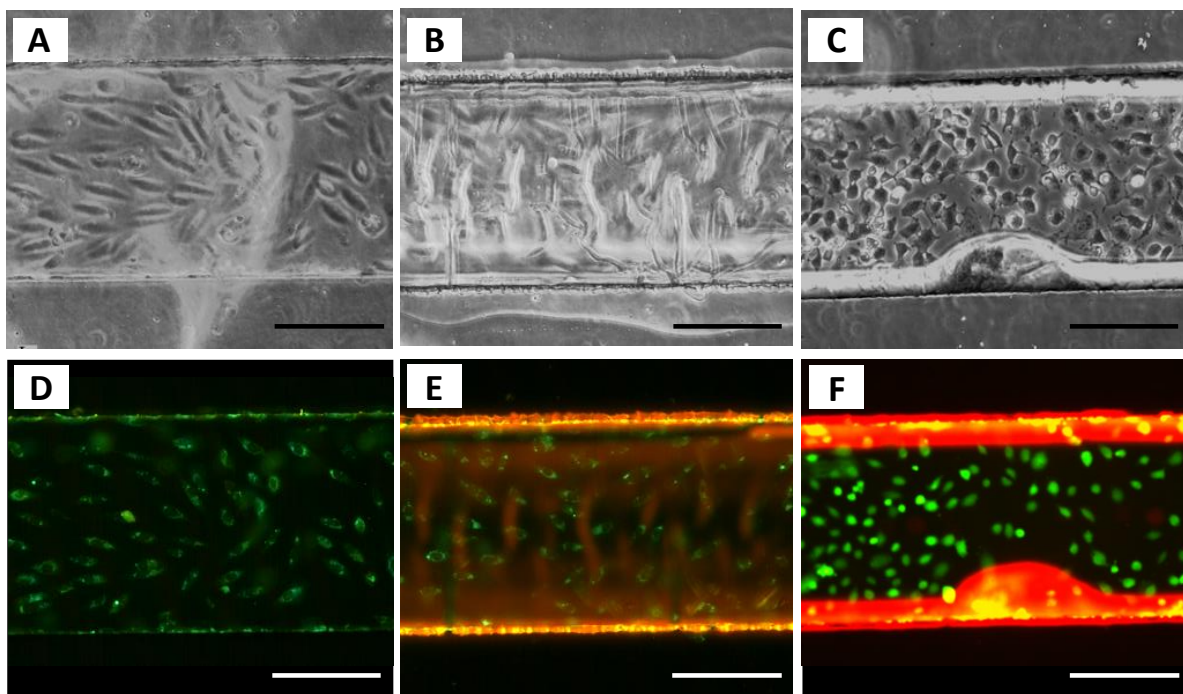


Figure 81. HUVECs stained with calcein AM, 18 hours after seeding in a microchannel. Magnification 10×. Scale bar: 200 μ m. Top three images: phase-contrast; bottom three images: luminescence ($\lambda_{\text{exc}} = 470$ nm; $\lambda_{\text{em}} > 515$ nm). Comparison between control microchannel (A and D), (healthy) cells in the microchannel functionalized with coating 1 (B and E) and (unhealthy) cells in the microchannel functionalized with coating 2 (C and F).

As stated in the “Cells harvesting and seeding” section, all microchannels were seeded with 10 μ l cells suspension at a concentration of cells of 4500 cells/ μ l, aiming to obtain about 70% confluence. ECM (10 μ l) was flushed 2 hours after seeding and then every 12 hours.

Inside the control channels (Figure 81A, D), cells attached and proliferated, reaching confluence higher than 60% in 11 cultures out of 21, and confluence between 20% and 60% in other 5 cases. Only in 3 cultures there were no or few live cells 2 hours after seeding. After 24 hours, cell confluence decreased only in 2 cultures. In the microchannels coated with the O₂-sensitive coating 1 (Figure 81B, E), the result was practically the same as the control, both after 2 and 24 hours. After this time, the confluence was higher than 60%, between 20 and 60%, and lower than 20% for 10, 2, and 4 cultures, respectively, for a total of 16 cultures. Cells attached and proliferated in the coated microchannels, both on the glass side and on the coated PDMS side. As a matter of fact, the luminescent indicator layer resulted more suitable for cell

attachment than the plain PDMS (Figure 82). On the contrary, the coating obtained from cocktail 2 resulted toxic for HUVECs (Figure 81C, F). In the majority of the functionalized microchannels, cells attached but already 18 hours after seeding they looked unhealthy (Figure 81C, F). 24 hours after seeding most cells were detached and got washed away when flushing fresh ECM.

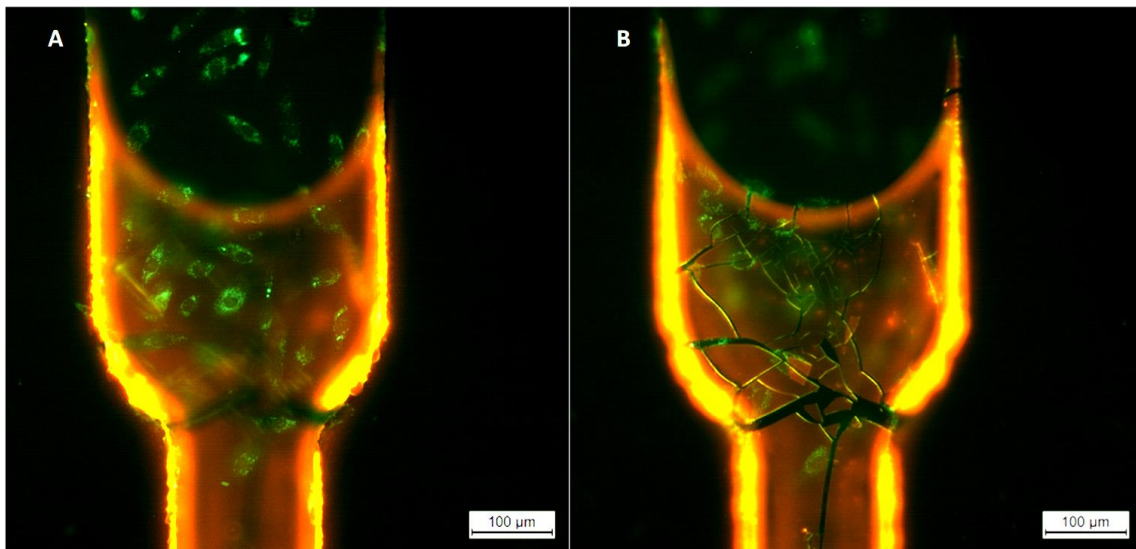


Figure 82. Stained cells, cultured in a microchannel partially coated with coating 1. Zoom of the area where the introduction channel meets the seeding channel (position of the mark n° 10, see Figure 71). Luminescence ($\lambda_{\text{exc}} = 470 \text{ nm}$; $\lambda_{\text{em}} > 515 \text{ nm}$). Magnification: 10×. A) Focus on the cells on the glass side. B) Focus on the cells on the PDMS side: the O₂-sensitive coating (orange) resulted more suitable for cell attachment than plain PDMS.

In the biocompatibility study realized in the 24-well plate, it was found that cells were able to attach and proliferate both in the proximity and onto the O₂-sensitive coating 1 (Figure 83). Conversely, when testing the coating 2, very few cells were found at a distance smaller than 300 μm from it, and they were mostly dead or detached. Cells attached further than 300 μm from coating 2 looked unhealthy (Figure 84).

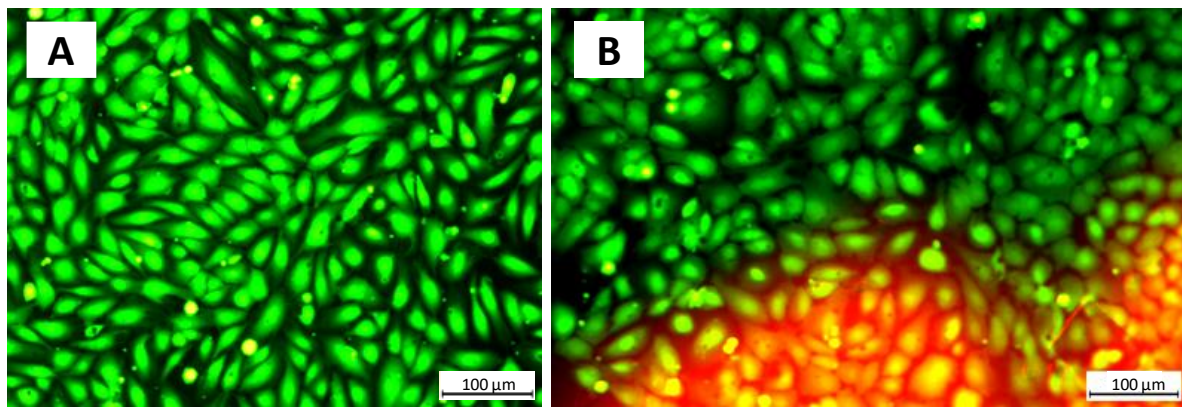


Figure 83: Toxicity study in 24-well plate. Time = 43 h. Fluorescence ($\lambda_{\text{exc}} = 470 \text{ nm}$; $\lambda_{\text{em}} > 515 \text{ nm}$). Magnification: 20 \times . A) Control well. B) Well coated with coating 1.

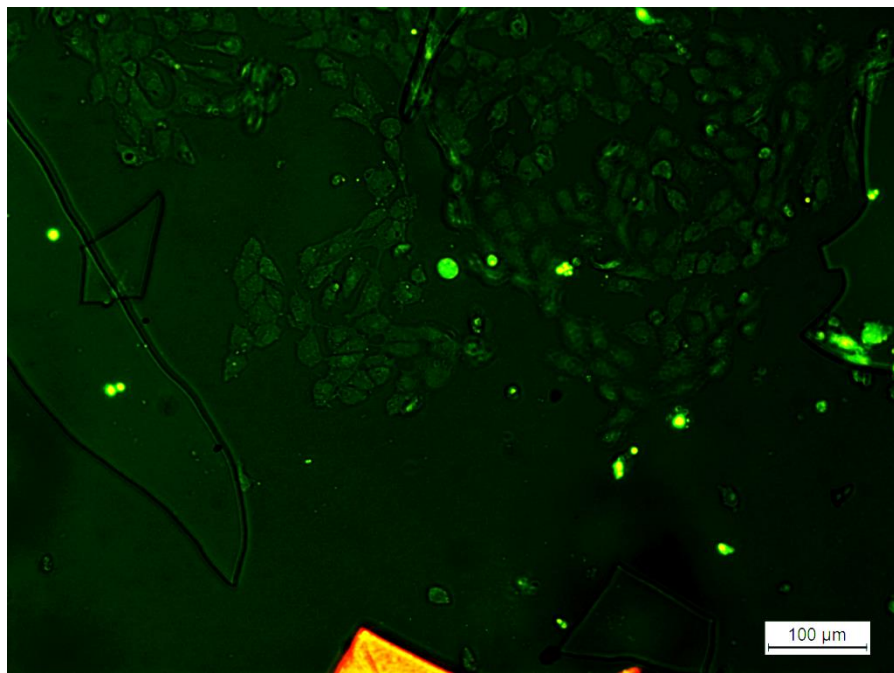


Figure 84. Toxicity study in 24-well plate. Time = 43 h. Fluorescence ($\lambda_{\text{exc}} = 470 \text{ nm}$; $\lambda_{\text{em}} > 515 \text{ nm}$). Magnification: 20 \times . Well coated with coating 2.

4.2.3.2. O₂-sensitive coatings response: measurements and corrections

Measurements based on phase shift are very robust, but there are some factors affecting the repeatability and precision of the sensor.

First, it is a lifetime-based measurement and everything that causes quenching of the luminophore is reflected in shortening of its luminescence lifetime. The O₂-sensitive coatings are inhomogeneous at the molecular level, especially those containing fillers (e.g. the silica in this particular case). A local higher concentration of the Ru(II) complex can lead to undesired effects like energy homotransfer and triplet-triplet annihilation of the photoexcited indicator dye [López-Gejo 2010]. These inhomogeneities in different regions of the same coating or between different coatings are reflected in distinct values of phase shift observed at the same O₂ pressure. To solve this first issue, a one-point calibration is required.

Secondly, also in absence of inhomogeneities, signal drift may be observed due to dye photobleaching/leaching. The phase shift is measured referencing – with the modulated excitation – the detected light; the latter is the sum of the probe luminescence and all possible interferences, for example scattering light coming from the excitation source. Because the excitation and emission filters are colored glasses, in fact, part of undesired wavelength may slip through. Scattering acts as a short lifetime component with a luminescence lifetime of the order of the LED modulation, that is about 25 ns in case of a 39 kHz modulation. The apparent lifetime depends on the relative intensities of the probe luminescence and all interferences. If the former is reduced because of photobleaching, the apparent lifetime will be reduced accordingly (a problem shared with the dual lifetime referencing – DLR – technique [Lakowicz 1998]). If the luminescent sensitive layer is thick (e.g. 200 μm, as the reference sensor used in this work), its luminescence is commonly strong enough to overwhelm the interferences, so that no drift is expected. The O₂-sensitive coatings applied in the microchips, however, are usually thinner than 20 μm, and so their luminescence is less intense. Moreover, the latter is further decreased because of some factors: the distance between optical fiber and coating (due to the necessity of interrogating the sensitive layer from outside the chip), the presence of the colored ECM, the scattering due to cells, etc. As a result, the phase shift may drift towards lower values. This deviation can be corrected using the signal drift (if present) at a fixed O₂ concentration to rectify the entire measure.

4.2.3.3. Calibration curve using the reference O₂-sensitive films

To take into account the exact O₂ pressure in the measurement box, a reference sensor was always used during the experiments. An example of the response varying from 0% to 21% O₂ (in volume, in N₂ plus 5% CO₂) is reported in Figure 85.

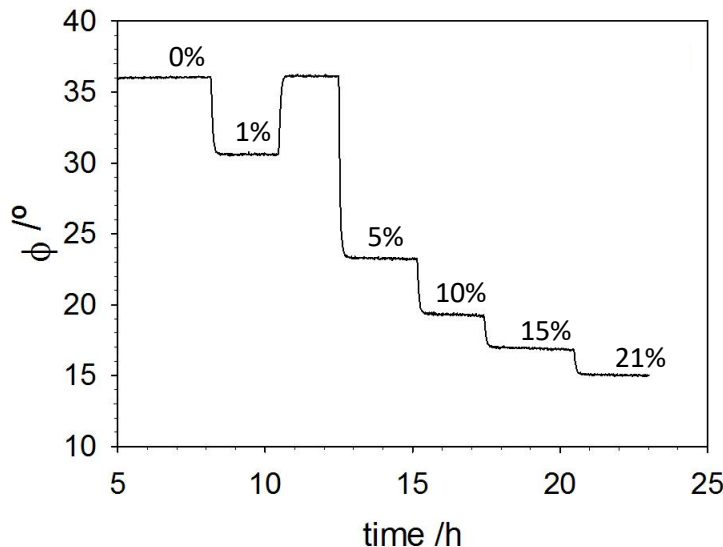


Figure 85. Response of the reference film to O₂ (in volume, in N₂ plus 5% CO₂).

The overall references response time (90% signal change, 0–1% O₂, in volume, in N₂ plus 5% CO₂) was 7.8 ± 1.2 minutes. This value corresponds to the sum of the time for filling the measuring chamber and the reference response time.

The response of three distinct reference films is reported in Figure 86. The differences between different films are larger than the measurement uncertainty for a single one, as expected (see above). For this reason, a single point calibration was needed. The best calibration plots for the references based on eq [21] led to the parameters reported in Table 21.

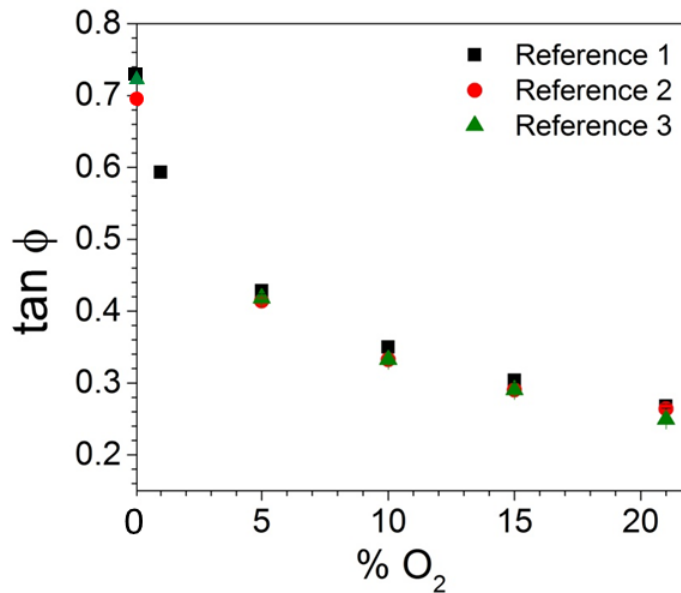


Figure 86. Phase domain Stern-Volmer plot of the three reference films.

Table 21. Parameters of the best calibration curve of the references data points based on eq [21].

f1	k1	f2	k2
0.52 ± 0.02	0.030 ± 0.004	0.48 ± 0.02	0.45 ± 0.08

The comparison between experimental S-V plots and data obtained from the calibration curve for the three different references is reported in Figure 87, Figure 88, and Figure 89.

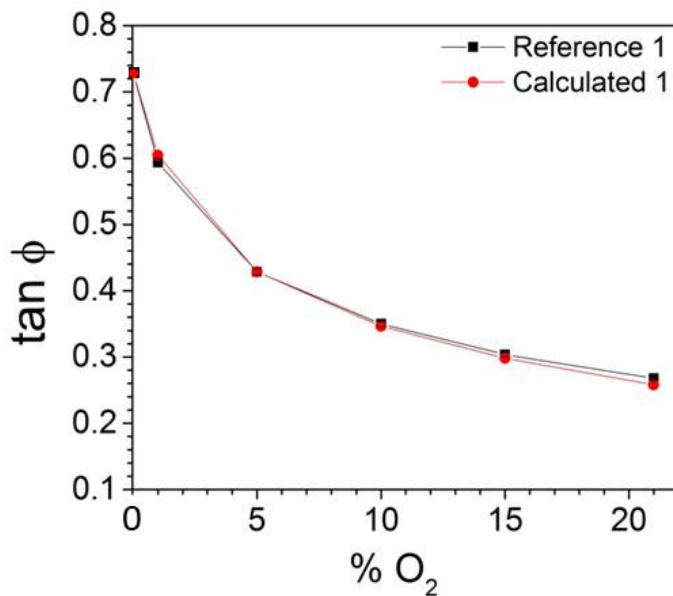


Figure 87. Phase domain S-V plot comparing experimental and calculated points for O₂-sensitive reference sensor n° 1. The modeled data were obtained using the value $\tan \phi = 0.428$ for [O₂] = 5%.

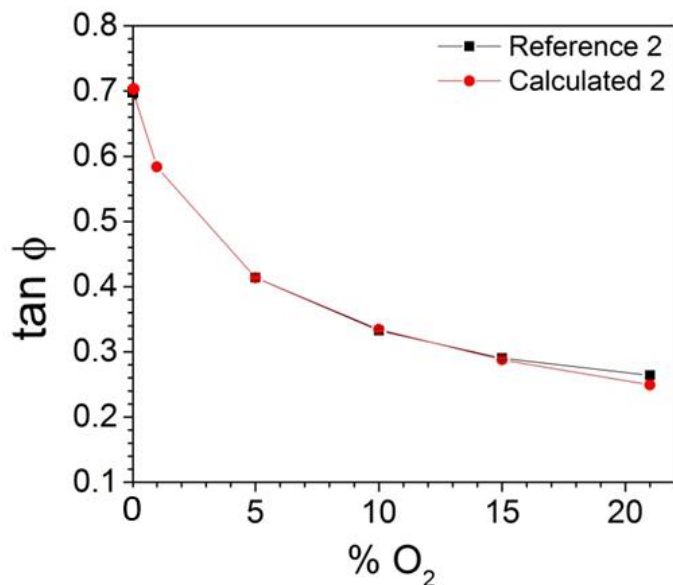


Figure 88. Phase domain S-V plot comparing experimental and calculated points for O₂-sensitive reference sensor n° 2. The modeled data were obtained using the value $\tan \phi = 0.414$ for [O₂] = 5%.

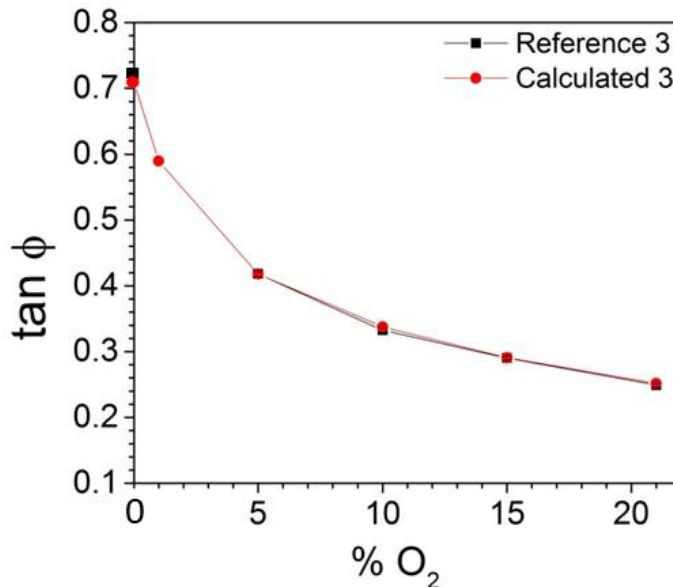


Figure 89. Phase domain S-V plot comparing experimental and calculated points for O₂-sensitive reference sensor n° 3. The modeled data were obtained using the value tanφ = 0.418 for [O₂] = 5%.

4.2.3.4. Measuring using the O₂-sensitive coating 1 into the microfluidic chips – without and with cells

Next step was changing the O₂ pressure in the measuring chamber using the gas flow controllers. The O₂ variation inside the microchannels was measured exploiting the O₂-sensitive coatings deposited. Three channels were only filled with ECM, while one was also seeded with cells (Figure 90 and Figure 91).

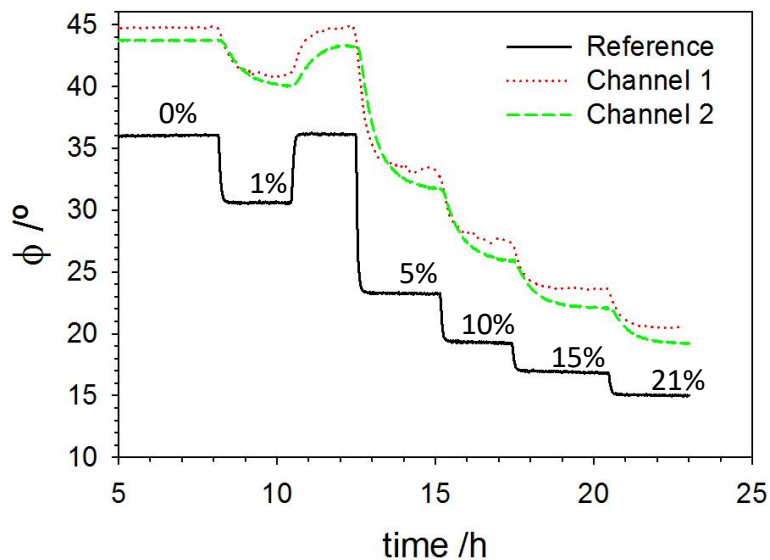


Figure 90. O₂ response of the luminescent layers (coating 1) in two separate microchannels of the chip (red dotted and green dashed lines) and the luminescent reference outside the microfluidic chip (black line). O₂ is reported as %v/v, in N₂ plus 5% CO₂. The microchannels were filled with ECM, but no cells were seeded.

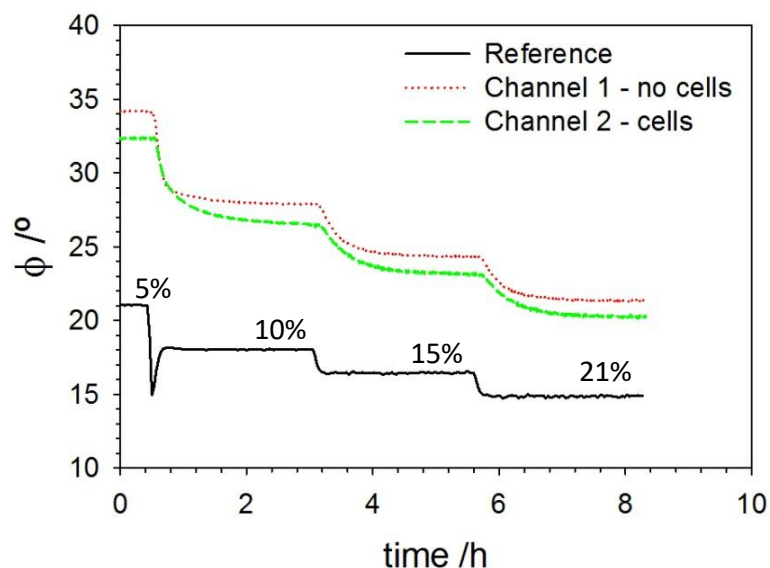


Figure 91. O₂ response of the luminescent layers (coating 1) in two separate microchannels of the chip (red dotted and green dashed lines) and the luminescent reference outside the microfluidic chip (black line). O₂ is reported as %v/v, in N₂ plus

5% CO₂. The microchannels were filled with ECM, and one of them (Channel 2, green dashed line) was seeded with cells.

There are some differences between the sensitive coatings in microchannels and the reference films. First, the response time (90% signal change) of the former ranged from 30 ± 5 minutes to 78 ± 14 minutes, much larger than the reference response time. The delay occurs because oxygen has to permeate through the PDMS and dissolve into the ECM before diffusing into the coating layer and collide with the photoexcited Ru(II) complex molecules. The large response time deviation between different O₂-sensitive coatings is due to different thickness and morphology of the coatings. Second, in some cases, signal drift was observed (see paragraph 4.2.3.2 above). The data have been corrected of 0.12°/h for channel 2 in Figure 90 and 0.073°/h for channel 2 in Figure 91 (for non-corrected data, see Figure 97 and Figure 99 of the appendix in reference to Figure 90 and Figure 91, respectively).

The O₂-sensitive coatings response is reported in Figure 92. Again, a single point calibration was used to correlate the sensors response and the O₂ pressure. The best calibration plots based on eq [21] led to the parameters reported in Table 22.

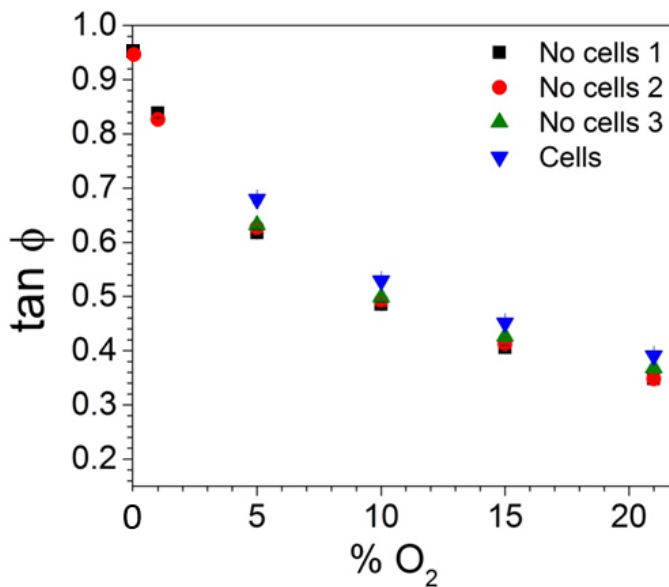


Figure 92. O₂-response of luminescent coating 1 deposited in four separate microchannels, three containing only ECM and one also seeded with HUVECs.

Chapter 4 - Application of Luminescence-Based Microsensors For Microfluidic Cell Cultures and Organ-On-A-Chip Devices

Table 22. Parameters of the best calibration curve of the O₂-sensitive coatings data points based on eq [21].

f1	k1	f2	k2
0.70 ± 0.01	0.17 ± 0.06	0.30 ± 0.05	0.019 ± 0.001

The comparison between experimental S-V plots and data obtained from the calibration curve for the four coatings is reported in Figure 93, Figure 94, Figure 95, and Figure 96.

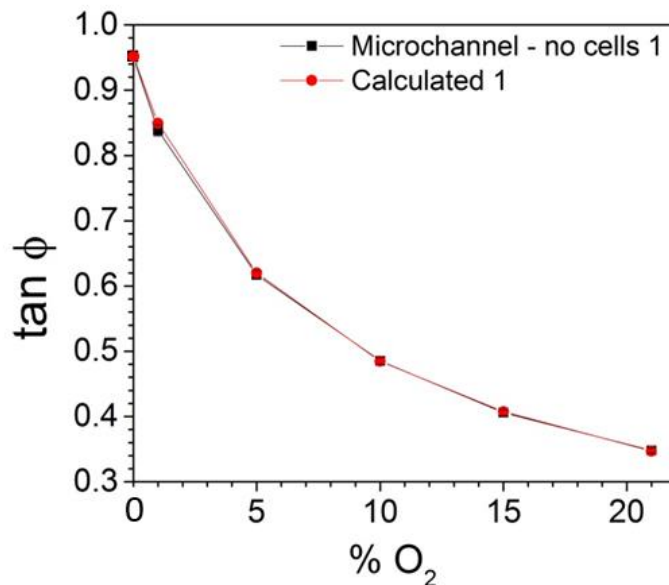


Figure 93. O₂-response of luminescent coating 1 deposited in a microchannel (microchannel 1) containing ECM but not seeded with cells. Phase domain S-V plot comparing experimental and calculated data. The modeled data were obtained using the value tanφ = 0.485 for [O₂] = 10%.

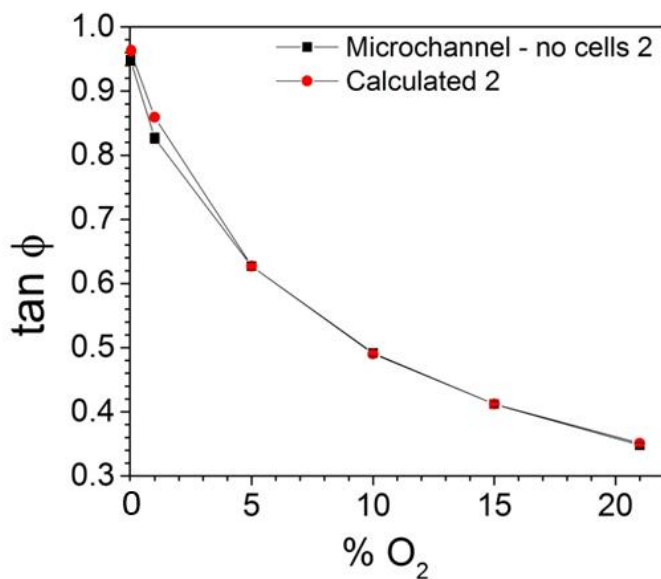


Figure 94. O₂-response of luminescent coating 1 deposited in a microchannel (microchannel 2) containing ECM but not seeded with cells. Phase domain S-V plot comparing experimental and calculated data. The modeled data were obtained using the value $\tan\phi = 0.627$ for $[O_2] = 5\%$

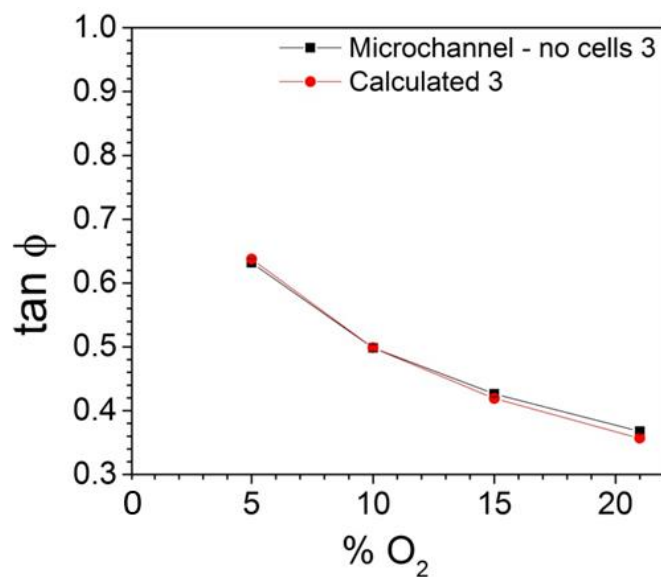


Figure 95. O₂-response of luminescent coating 1 deposited in a microchannel (microchannel 3) containing ECM but not seeded with cells. Phase domain S-V plot comparing experimental and calculated data. The modeled data were obtained using the value $\tan\phi = 0.498$ for $[O_2] = 10\%$.

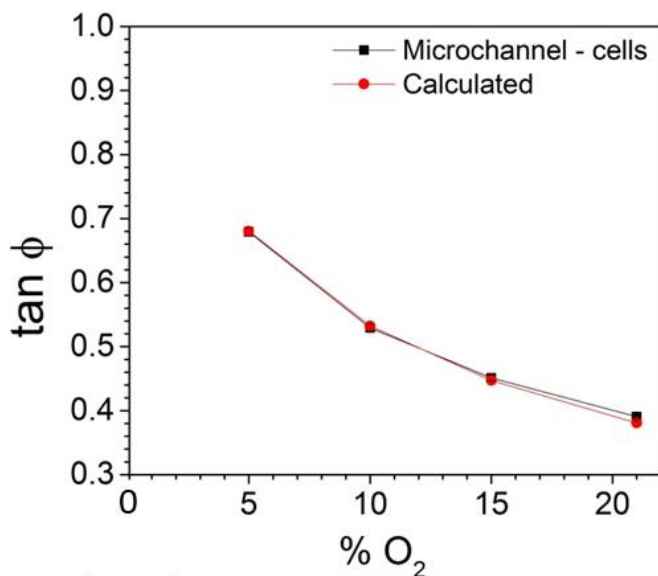


Figure 96. O₂-response of luminescent coating 1 deposited in a microchannel (microchannel 4) containing ECM and seeded with cells. Phase domain S-V plot comparing experimental and calculated data. The modeled data were obtained using the value $\tan\phi = 0.679$ for $[O_2] = 5\%$.

4.2.4. Results discussion

Cell cultures are kept majorly under 19.95-21% O₂. This condition is not correct for most cells: for endothelial cells, for example, normoxia is considered about 10% O₂ for arterial environment and 5% O₂ for venous environment [Tsai 2003]. If the PDMS-glass microchips are kept at a certain O₂ pressure, after an initial equilibration time (required for allowing dioxygen permeation through PDMS and solution into the cell medium), the internal dioxygen pressure equals the external one. For growing cells at a specific O₂ pressure is hence sufficient keeping the microfluidic chip cultures inside incubators with the desired gas composition – which should **not** be 21% O₂. Other materials (e.g. glass, polymers with lower permeability) must be used if the equilibration with external atmosphere is not desired. Cells with faster metabolism may consume dioxygen at a higher rate and lead to different results.

4.2.5. Acknowledgements

Thanks to Prof. Elizabeth Verpoorte, Ing. Patty Moulder, Jean-Paul Mulder and Dr. Maureen Xu for guidance, suggestions and providing all material, included the mold for the chips.

4.2.6. Annex I

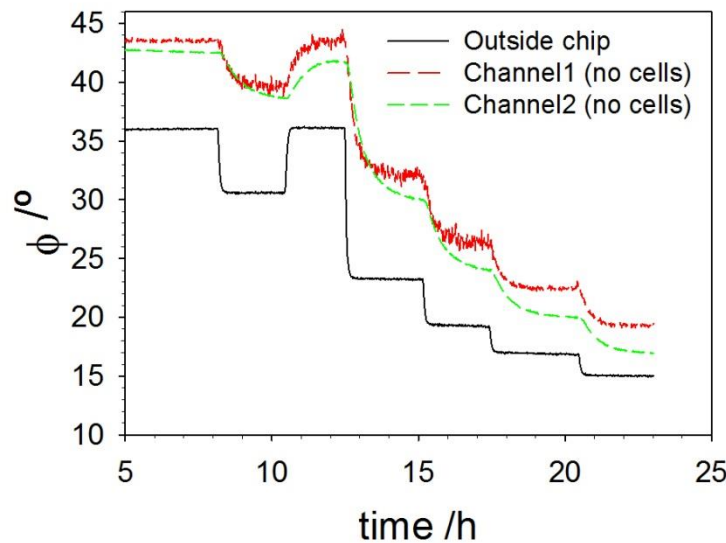


Figure 97. Original data (phase shift) related to Figure 90. The signal of the sensor spot “Channel2” drifts during the measurement. The data for the sensor “Channel2” reported in Figure 90 were corrected applying a correction factor of $0.12^\circ/\text{h}$.

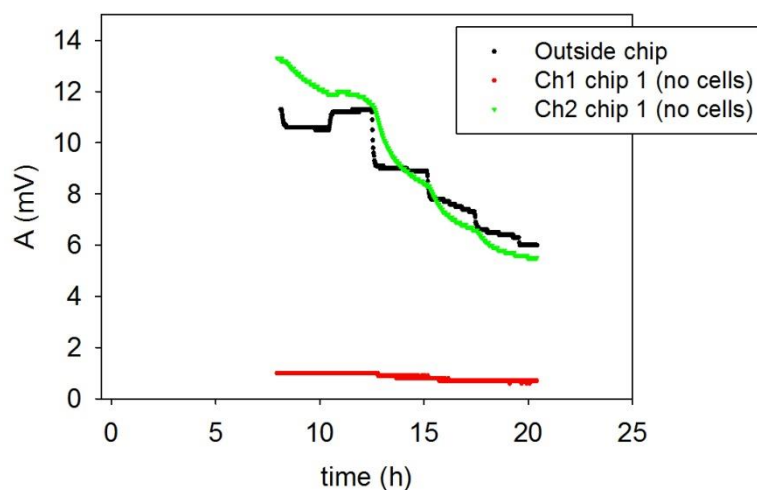


Figure 98. Original data (intensity of the signal) related to Figure 90.

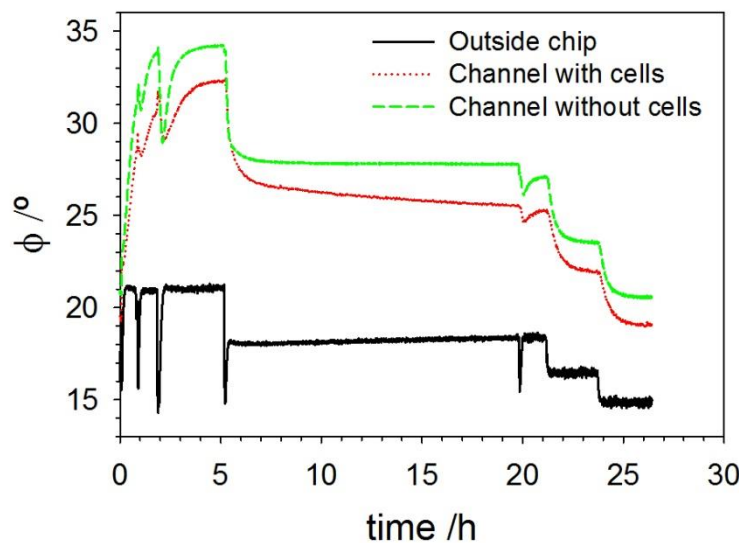


Figure 99. Original data (phase shift) related to Figure 91. Steps are: 5%, 10%, 15% and 21% oxygen (in volume, in N₂ plus 5% CO₂). The signal of the sensor “channel with cells” drifts during the measurement. The data for the sensor “channel with cells” reported in Figure 91 were corrected applying a correction factor of 0.073°/h.

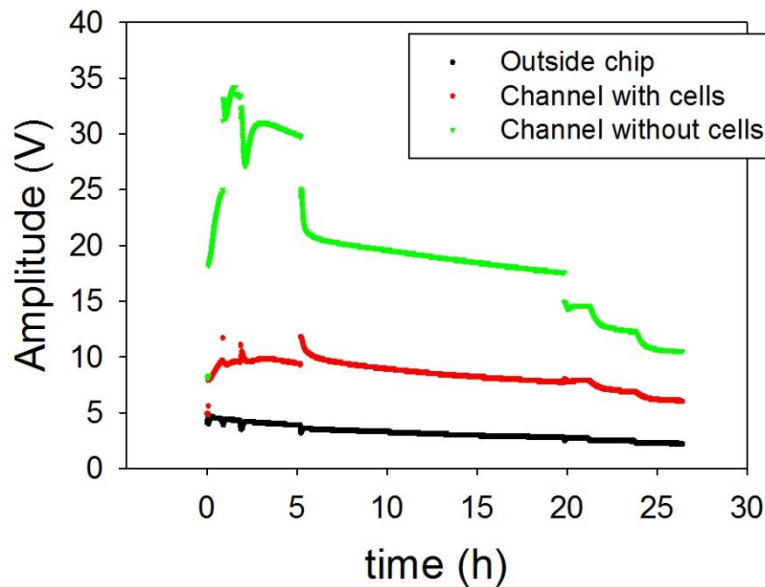


Figure 100. Original data (intensity of the signal) related to Figure 91.

4.3. Dioxygen and temperature sensors for glass organ-on-a-chip devices

Regarding the second part of the work, the aim was to integrate O₂ and T luminescence-based sensors into OOAC devices. For this, luminescent O₂- and T-sensitive spots were manufactured into the chips and optical fibers were coupled for allowing remote sensing.

One of the organs that have been simulated on-chip is the lung, or more precisely the blood-air (capillary-alveolar) barrier existing in the gas-exchanging region of the lungs [Huh 2010]. The barrier consists of an alveolar cells monolayer (of the alveolar wall), an endothelial cells monolayer (of the capillaries) and an intermediate permeable membrane (the basement membrane) in between (Figure 101). The simplified corresponding organ-on-chip can thus be built cultivating endothelial cells and alveolar cells on the opposite sides of a permeable membrane. The latter also have to separate the device into two chambers, one containing blood (or an analogous solution) and the other containing air (Figure 102).

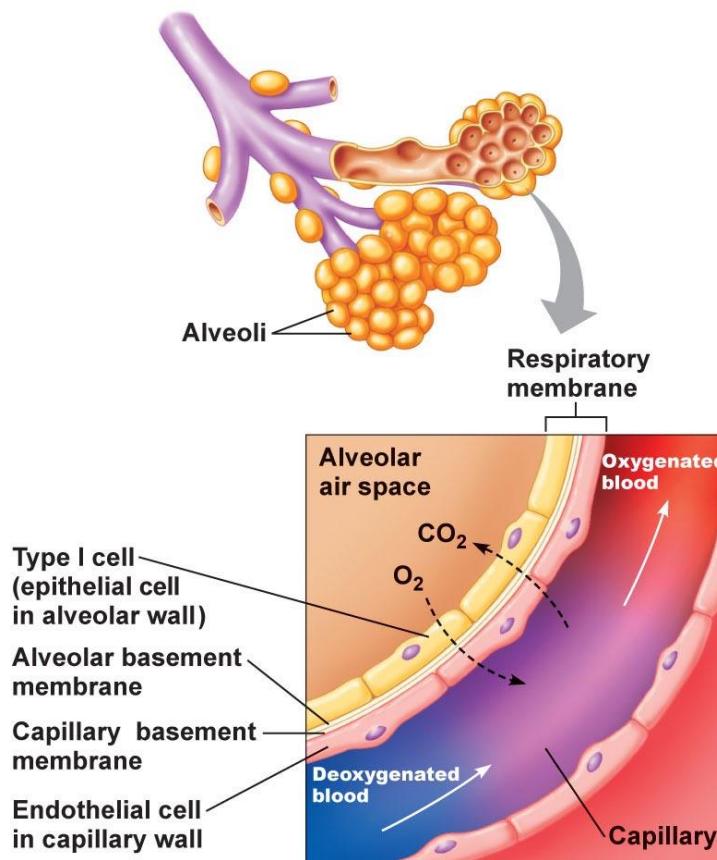


Figure 101. Depiction of blood-air (capillary-alveolar) barrier inside the alveoli.
Copyright 2013 Pearson Education, Inc., reprinted from [Stanfield 2013] with permission.

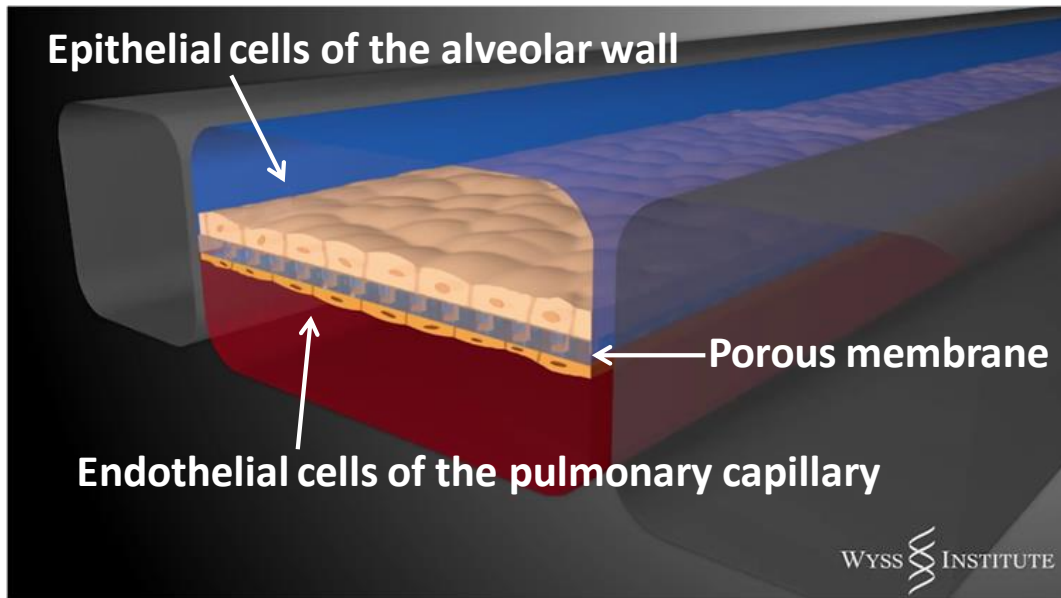


Figure 102. Representation of the organ-on-a-chip system to mimic blood–air barrier.
Wyss institute, free to use material [Prantil-Baun 2018].

Organ-on-a-chip devices utilized in this work were kindly provided by Micronit Microtechnologies (Enschede, NL) (<https://www.micronit.com/products/organ-on-a-chip.html>). These chips consist of three layers: a perforated glass slide supporting a gas-permeable PET membrane (with $0.45\text{ }\mu\text{m}$ pores), sandwiched between two glass slides equipped with perfluorinated elastomeric gaskets (Figure 103). The cells are supposed to be seeded onto the porous membrane. The flow chambers are created by mechanically compressing the three layers using the dedicated (customizable) Micronit Fluidic Connect Pro clamp (Figure 104). This sealing strategy yields flow chambers without the need of thermal or chemical processes and allows re-opening the chips at any time just by opening the clamp.

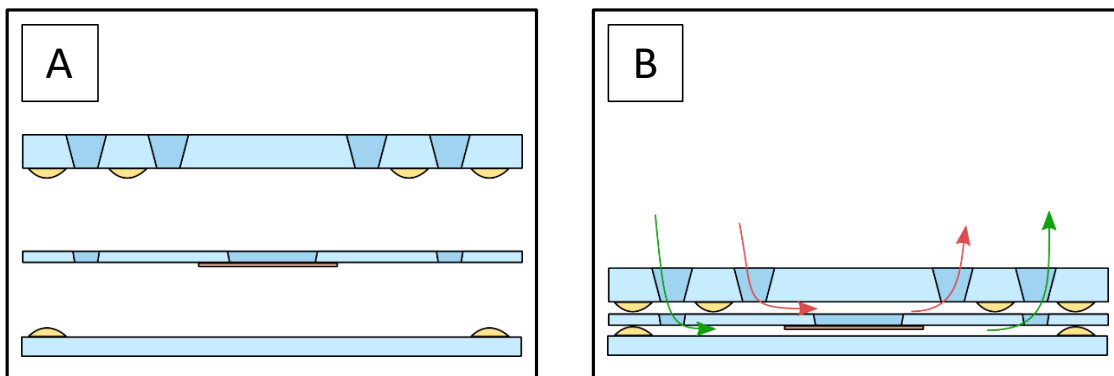


Figure 103. Three layers chip. The porous membrane attached onto the central perforated glass slide is depicted in orange. The elastomeric separator gaskets are depicted in yellow. A) Opened chip. B) Mechanically compressed chip, green and red arrows show the separated fluidic paths (for fluids that do not permeate through the porous membrane).

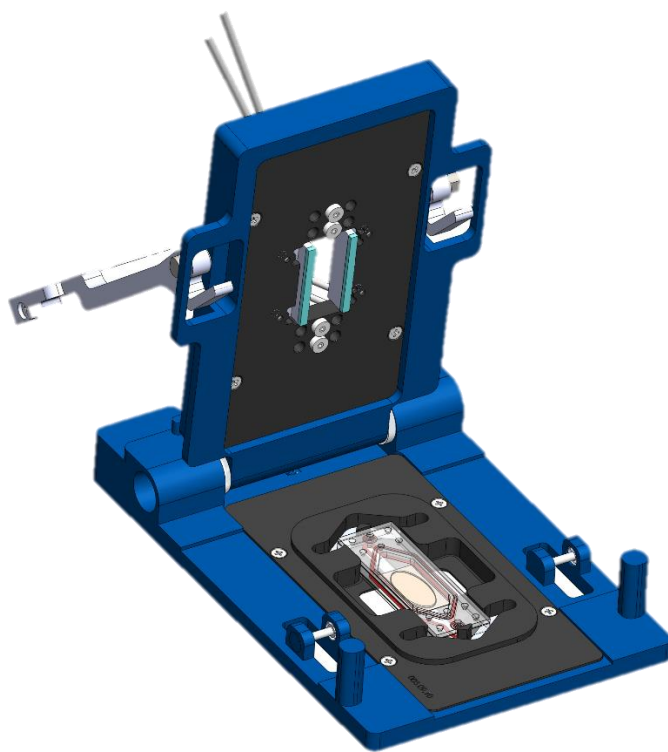


Figure 104. Micronit Fluidic Connect PRO chip holder (ref. FC_PRO_CH4515), with the three layers OOAC device.

4.3.1. Aim of the study

The aims of this study were:

- I. To test luminescent dioxygen- and temperature-sensitive microprobes in an organ-on-a-chip device, and
- II. to find the parameters to be used to mimic *in vivo* oxygenation condition in order to have biologically relevant result when growing cells within this device.

4.3.2. Materials and methods

4.3.2.1. Materials

- Solvents (Fisher Scientific, Loughborough, UK), HPLC grade, used without further purification
- Silica particles AEROSIL® R 812s (Evonik Industries AG, Essen, DE)
- Tris(4,7-diphenyl-1,10-phenanthroline)ruthenium(II) bis(hexafluorophosphate) (shortened as [RD3]²⁺ [2(PF₆)]²⁻)
- [Bis(1,10-phenanthroline)(4-chloro-1,10-phenanthroline)]ruthenium(II) dichloride (shortened as [Ru(phen)₂(4-Clp)]²⁺ [Cl₂]²⁻)
- One component poly-(dimethylsiloxane)-based coating Dow-Corning 3140 (Wiesbaden, Germany)
- Ethyl cyanoacrylate (Loctite super glue-3 professional, Henkel, Düsseldorf, DE)

4.3.2.2. Preparation of the O₂-sensitive and T-sensitive elements in the chips.

The sensor cocktail for dioxygen sensing consisted of poly-(dimethylsiloxane)-based Dow-Corning 3140 mixed with silica AEROSIL® R 812s (10 w/w %), which was previously dyed with RD3 (0.15 w/w %). The cocktail for yielding temperature sensitive spots was prepared dissolving the [Ru(phen)₂(4-Clp)]²⁺[Cl₂]²⁻ dye (67 µM) in the pure PCA monomer [Bustamante 2018]. Both dyed polymers obtained from these mixtures were tested for biocompatibility with HUVECs (see annex III).

Dioxygen- and temperature-sensitive dyed films, with a thickness lower than 100 µm in order to fit into the fluidic chamber, are deposited in the internal part of the top glass slide. For this, sheets of polyimide tape (Kapton®, DuPont) of 50 µm thickness were cut to produce the deposition masks using a cutting plotter (Graphtec CE6000-60, Irvine, CA). The masks were 15 × 45 mm. Additionally, three holes (4 mm dia.) aligned along the long axis (for precise positioning of the O₂-sensitive spots) and one 3 × 10

mm square staggered towards one side (for the positioning of the T-sensitive spot) were cut. The patterned tape sections were then transferred onto the glass slides. The O₂-sensor cocktail was knife-coated onto the three central holes, and the T-sensor cocktail onto the lateral one. The latter was furthermore covered with a piece of 15 µm-thick aluminum foil, which remained glued onto the dyed cyanoacrylate film. The Kapton® tape was immediately removed leaving behind the four spots of dyed solution. The luminescent spots were allowed to cure for 24 h (Figure 105a and b).

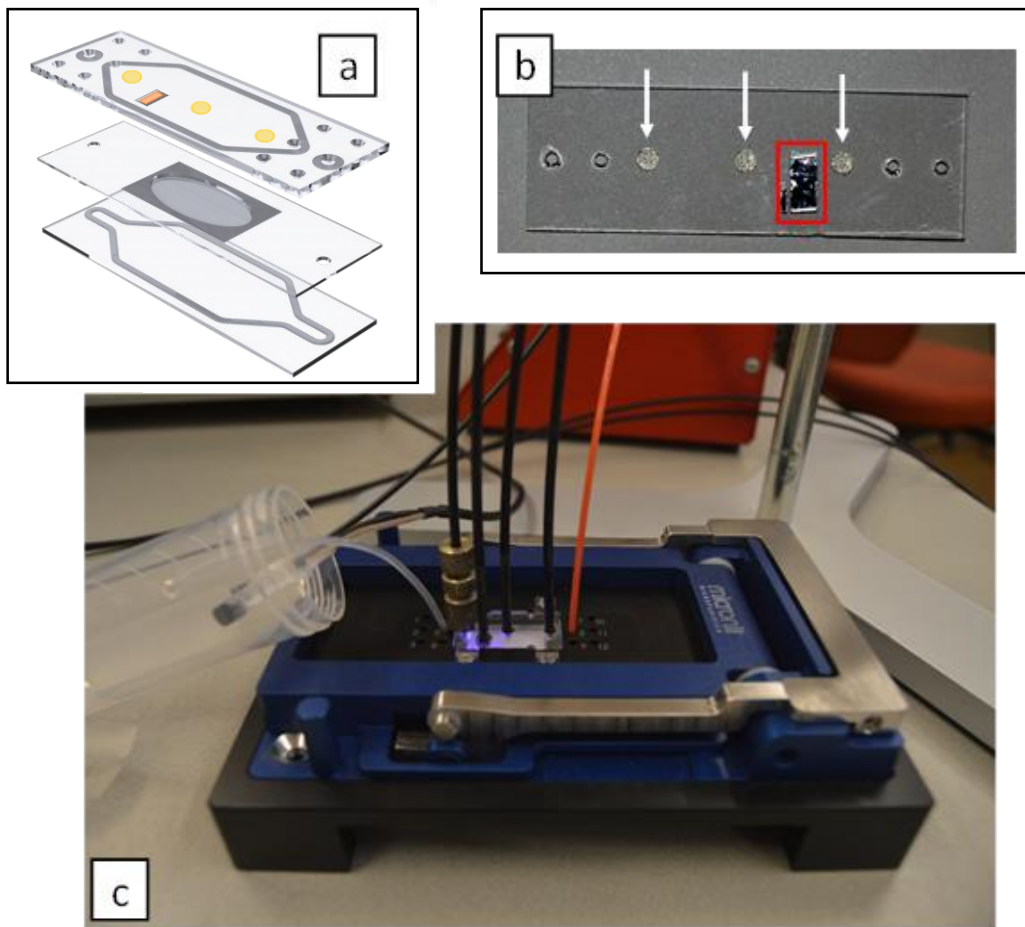


Figure 105. a) Micronit 3-slide chip scheme, with the thin glass supporting the permeable membrane sandwiched between two glass slides carrying the elastomeric gaskets. On the top slide, the three O₂-sensitive spots are depicted in yellow and the squared T sensitive patch (covered with a piece of Al foil on the opposite side) is coloured in orange. b) Internal side of the top glass slide (before the gasket deposition) with the three O₂-sensitive luminescent spots (white arrows) and the aluminium foil-covered squared T-sensitive luminescent patch (red square). c) The Micronit Fluidic Connect PRO chip holder (ref. FC_PRO_CH4515) with the fluidic inlet (orange tube) and outlet (transparent tube) and the four optical fibers attached.

Using a CNC milling machine, an expressly designed adaptor was manufactured in order to interface four optical fibers, in order to keep them in place exactly in front of the four luminescent spots previously deposited (Figure 105c).

4.3.2.3. Dioxygen response – gas phase

For characterizing the spots response to dioxygen, a calibration plot was obtained using an optical fiber for monitoring the luminescence response. The O₂-sensitive spot was deposited onto a round glass window, which was placed into a custom-made flow-through cell. This setup allows flowing N₂/O₂ mixtures from an electronic mass flow controller manifold (EL-FLOW® Prestige).

A glass slide onto which three O₂-sensitive spots had been deposited was used for studying the sensors response reproducibility. The slide was used assembling a chip with the Fluidic Connect PRO clamp. N₂ and air were then cyclically flown through, and the three spots response was collected using three optical fibers.

4.3.2.4. Temperature response – gas phase

A glass slide supporting the luminescent T-sensitive spots was held onto a heating plate (IKA RCT basic) for obtaining the spots luminescence response to temperature. The latter was varied with the plate and monitored with a commercial thermistor (LM335, Texas Instrument).

4.3.2.5. Luminescent spots response – liquid phase

For the actual application, the sensors are supposed to monitor the capillary chamber, measuring dioxygen permeation through the plastic membrane and the two cells monolayers. The capillary blood was simulated flowing deoxygenated water in the capillary chamber (although oxygen tension is around 53 hPa in pulmonary arteries blood when it reaches the alveoli, and not 0 hPa [Prantil-Baun 2018]) while the alveolus chamber was left opened to air (Figure 106).

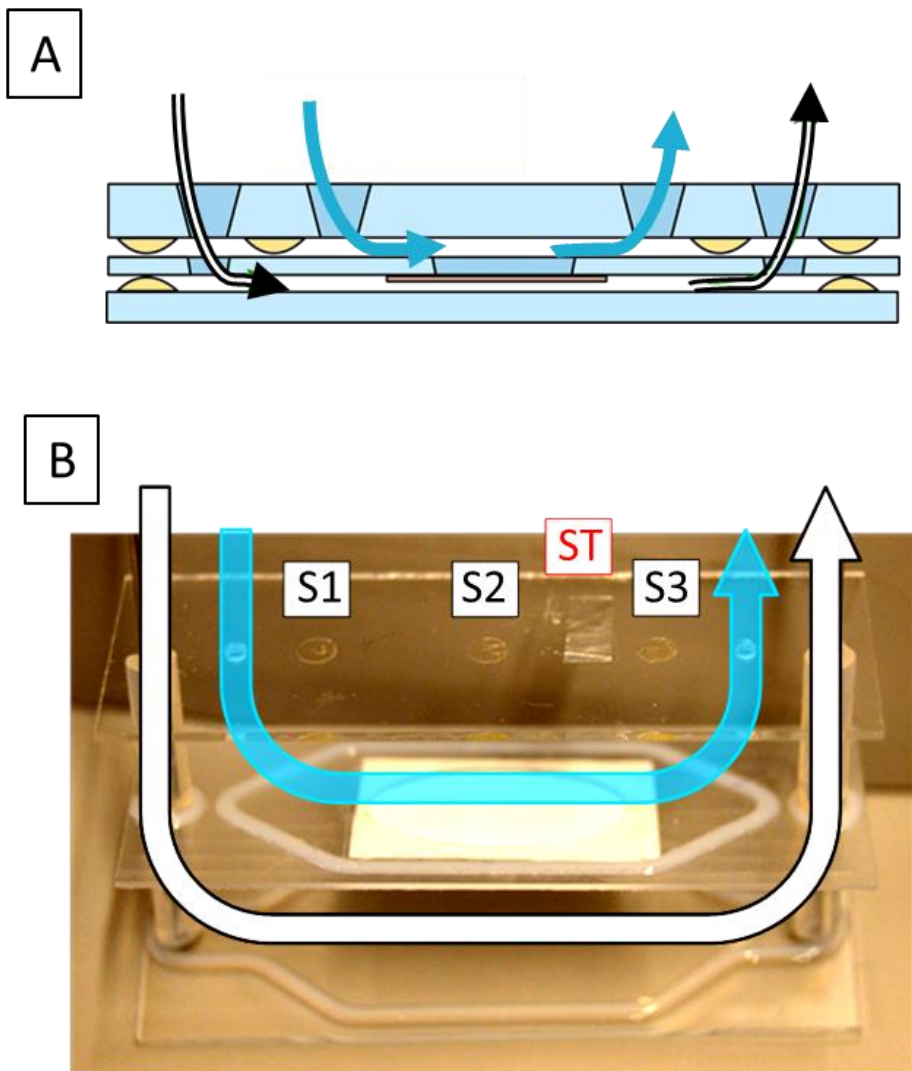


Figure 106. A: scheme of the 3-slide chip. B: picture of the 3-slide chip (kept opened with spacers for clarity). The blue and grey arrows illustrate the route of deoxygenated water and air, respectively. The three yellow polymer spots, labelled with S1, S2, and S3 are the O₂-sensitive spots. The squared labelled with ST is the Al foil-covered T-sensitive patch.

4.3.3. Results and discussion

4.3.3.1. Calibration of O₂ and T microsensors in OOAC devices

1. O₂ microsensors

For manufacturing the dioxygen-sensitive spots, it was used one of the most common combination for making O₂-sensing polymer films, i.e. tris(4,7-diphenyl-1,10-phenanthroline)ruthenium(II) in a silicone matrix containing silica [Orellana 2014]. For the temperature-sensitive patches, we used a Ru(II) dye specifically designed to display a large temperature coefficient for its luminescence intensity and lifetime, while keeping the excellent photostability that characterizes the O₂ indicator complex [Bustamante 2018]. In this case, the embedding polymer support was optimized for limiting cross-sensitivity to O₂ without slowing down the sensor response. Integrating the developed temperature-sensitive patches in the chips provides also a way to correct O₂ (and any other Ru(II)-based) optosensors for the temperature effect by employing the very same instrumentation.

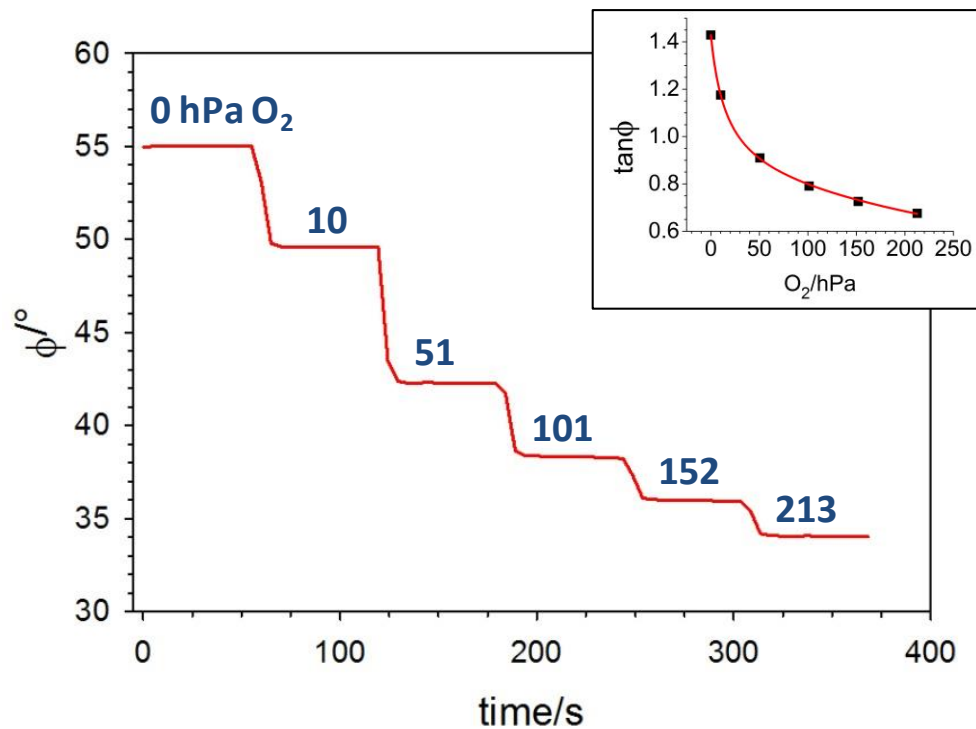


Figure 107. Dioxygen dose response of the RD3-silica-PDMS luminescent spots (sensor S3 in Figure 106). The blue values specifies to the O₂ pressure in hPa (in pure N₂). In the inset, the corresponding phase-domain Stern-Volmer plot.

The sensors were characterized in gas phase. The O₂-sensitive spots were tested at different O₂ concentration between 0 and 213 hPa (O₂ in pure N₂). The sensitivity shown was 0.54°/hPa in the 0-10 hPa range, and the response time was about 10 s (t_{90} 0-10 hPa O₂) (Figure 107). Reproducibility was studied cycling between pure N₂ and synthetic air (21% O₂ in N₂, Figure 108), and the phase shift values obtained for the three sensors are reported in Table 23.

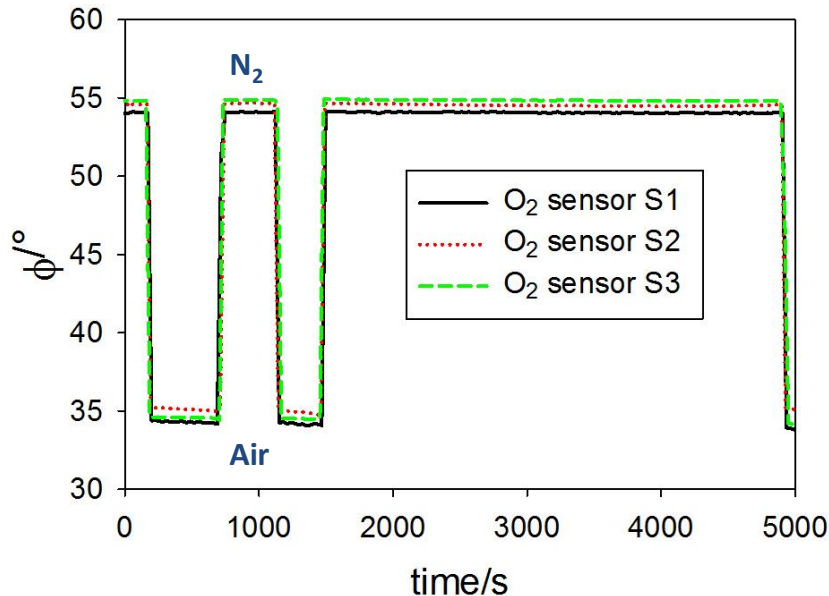


Figure 108. Response of the RD3-silica-PDMS luminescent spots cycling from pure N₂ to synthetic air (21% O₂ in N₂), using three sensors in parallel in the same chip (see Figure 106).

Table 23. Phase shift values obtained for three different RD3-silica-PDMS luminescent spots, cycling between 0 and 213 hPa O₂

Sensor	$\phi_{N_2}/^\circ$ a	$\phi_{Air}/^\circ$ a
S1	54.09 ± 0.04	34.2 ± 0.2
S2	54.54 ± 0.05	35.0 ± 0.1
S3	54.84 ± 0.03	34.5 ± 0.1

a n = 15

2. *T* microsensors

The T-sensitive spots deposited onto glass slides (without assembling the three-layer chip) were tested between ca. 27 to 52 °C (Figure 109).

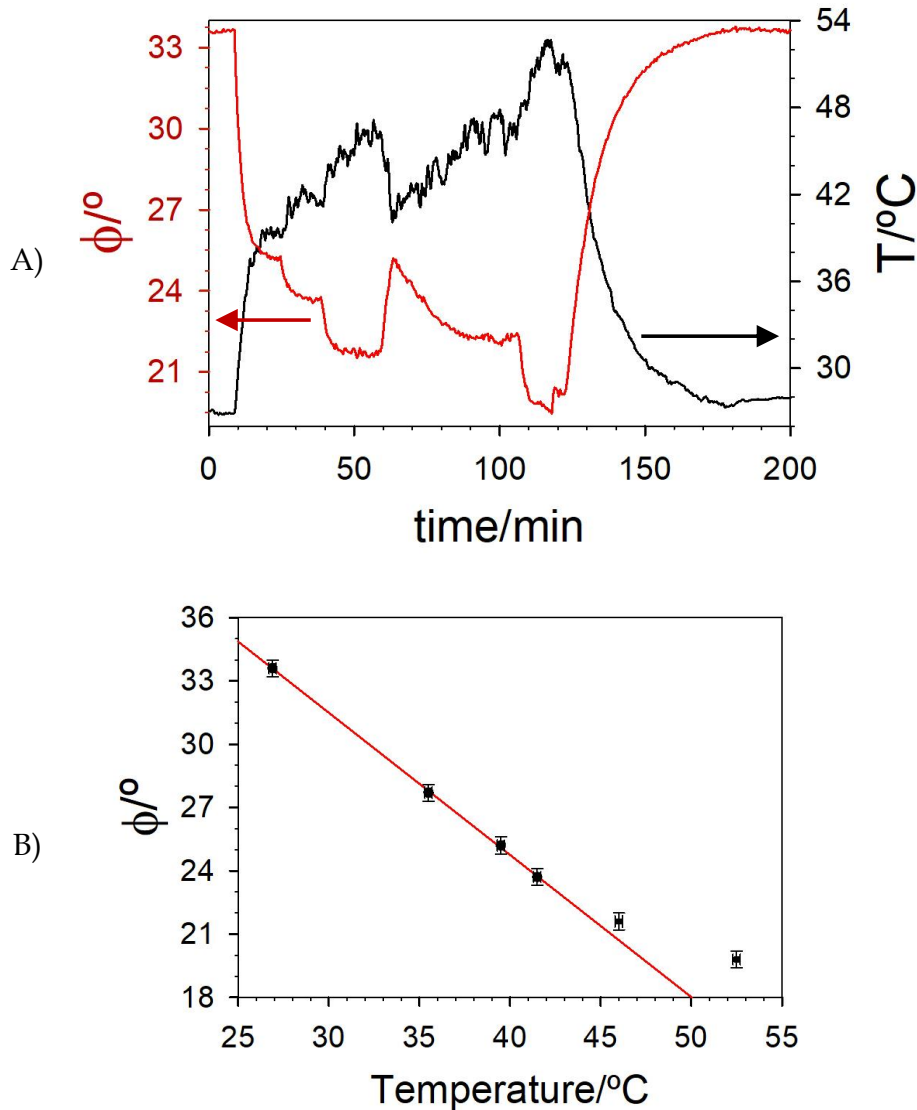


Figure 109. (A) Example of the fiberoptic luminescence-based temperature sensor response (red line). The temperature was varied with a heating plate (IKA RCT basic) and monitored with a commercially available thermistor (LM335, Texas Instrument, black line). (B) Phase-shift response with temperature. The red line is the linear fit of the experimental data between 26.9 °C and 41.5 °C (parameters of the best fit $\phi/^\circ = A + b \cdot T/^\circ\text{C}$: $A = (51.7 \pm 0.3)$; $b = (-0.674 \pm 0.009)^\circ(\text{°C})^{-1}$; $r^2 = 0.9996$). Data published in [Bustamante 2018] and reprinted with permission.

The response is linear between 27 and 43 °C, a suitable range for monitoring cell cultures [Ozturk 2005]. The response time (i.e. the delay between thermistor and optode signals) is around 5 s. The thin polymer is slightly permeable to O₂ (see Figure 110), but the interference is easily suppressed by measuring that species and temperature at the same time, something that can be readily performed in a multichannel instrument like ours. Moreover, the interference of O₂ can be further lowered by covering the dyed PCA spot with commercial aluminum foil, which blocks permeation of gases without decreasing the sensor sensitivity to temperature.

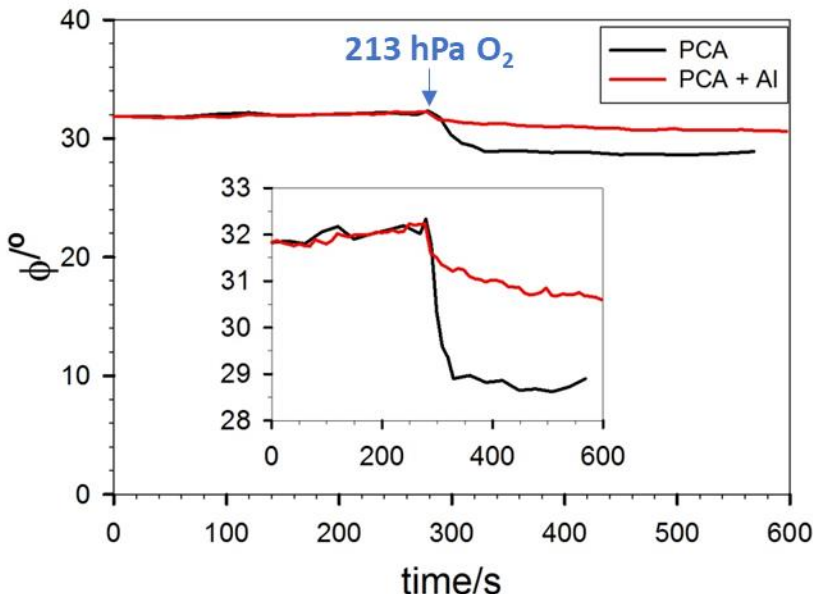


Figure 110. [Ru(phen)₂(4-Clp)]/PCA temperature-sensitive spots in the organ-on-a-chip device: response to O₂ (from 0 to 213 hPa O₂ in pure N₂) at 27 °C. Black line: naked T-sensitive luminescent film; red line: aluminum foil-covered T-sensitive luminescent film. Data published in [Bustamante 2018] and reprinted with permission.

4.3.3.2. Simulation of real operation

Finally, the OOAC devices with sensor spots (Figure 106) were tested in an experiment to simulate real operation (Figure 111). First, pure N₂ was flown inside the chip in order to calibrate the sensor response to 0% O₂ (grey areas on the left side of Figure 111). Then, while leaving the alveolus chamber opened to air, deoxygenated water was flown (25 µl/min, typical flow rate in experiments with these OOAC devices) in the capillary chamber (Figure 111, light blue area). At this flow rate, due to the chip geometry and materials, water runs initially along the capillary chamber sides,

reaching first the central spot (S2, orange line), then the first spot (S1, red line) and at last the third one (S3, light green line). Right above the porous membrane, the sensor S2 displays a phase shift that increases in about 1800 s until $\phi = 50.0^\circ$, corresponding to around 10 hPa dioxygen in the water directly contacting the dyed polymer. At the same time, water in contact with S1 and S3 contains 20 hPa O₂ (phase shift = 47.9°) and 66 hPa O₂ (phase shift = 41.9°), respectively. The temperature sensor ST, on the other hand, allows correcting the signal for the temperature variation (Figure 111).

As soon as the water flow is stopped (Figure 111, purple area), O₂ from the alveolus chamber, passing through the porous PET membrane, dissolves and diffuses into the still water in the capillary chamber. S2 shows that O₂ rapidly diffuses close to the permeable membrane.

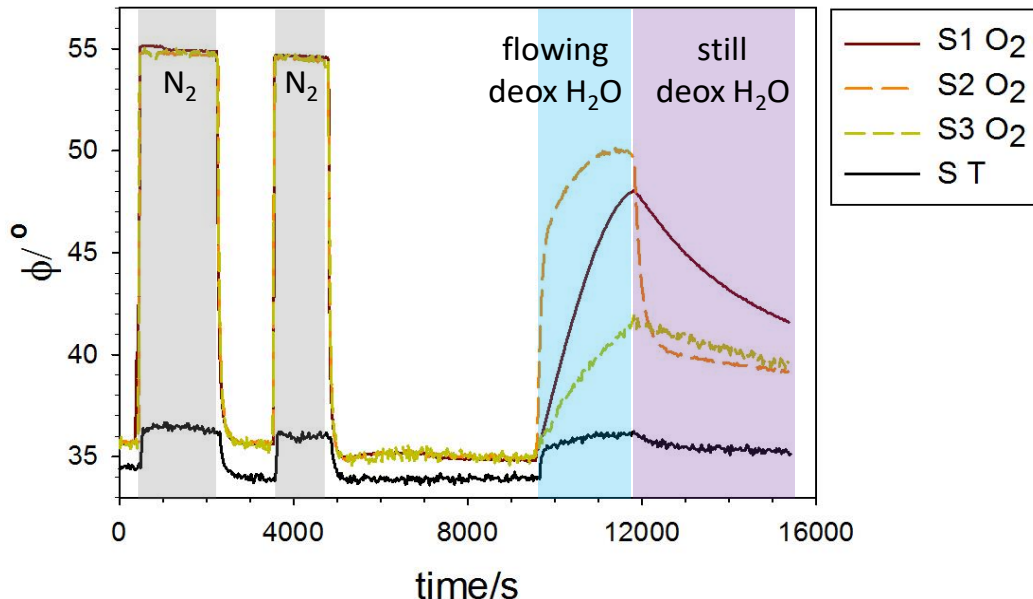


Figure 111. Response of the three O₂-sensitive spots and the T-sensitive patch to N₂ (grey area) and deoxygenated water (light blue area). Finally, water flow was stopped, leaving still water into the chip (purple area).

4.3.4. Results discussion

Dioxygen transported in pulmonary arteries and veins (i.e.: before and after the gas exchanging area, respectively) is around 53 hPa and 133 hPa, respectively [Prantil-Baun 2018]. The experimented parameters (i.e.: flowing deoxygenated water at 25 µl/min with the reported structure), **do not** correctly reproduce *in vivo* conditions (**Table 24**): the dioxygen pressure is much lower both before and after the artificial blood-air barrier.

Chapter 4 - Application of Luminescence-Based Microsensors For Microfluidic Cell Cultures and Organ-On-A-Chip Devices

In order to better simulate *in vivo* conditions, the feeding water should carry around 40 hPa O₂, but more experiments should be done for selecting the necessary water flow rate.

Table 24. Dioxygen pressure measured in the lung-on-a-chip compared to the expected one in the biological system.

	PO ₂ /hPa		
	Before the gas exchanging area	At the gas exchanging area	After the gas exchanging area
Expected in the lung [Prantil-Baun 2018]	53		133
Measured in the lung-on-a-chip (conditions described in the main text)	20	10	66

Finally, placing one O₂-sensitive spot directly onto the porous membrane (where endothelial cells will be cultivated) could be appropriate to monitor the exact O₂ that cells experiment. For this aim, a cells-compatible dioxygen-sensitive dyed polymer (as the ones shown in the first part of the chapter) must be used.

4.3.5. Acknowledgements

Thanks to Dr. Brivio Monica and Dr. Meucci Sandro for guidance, suggestions and providing all material, included the glass chips and the clamp with the optical fiber adaptors.

4.3.6. Annex II

The reported O₂- and T-sensitive polymers are meant to be used with cells. Hence, their biocompatibility was tested as described in the first part of the chapter. Both luminescent materials appeared to be compatible with cells, which looked as in the control well at a distance higher than 400 µm and only slightly less confluent at a closer distance. (Figure 112 and Figure 113).

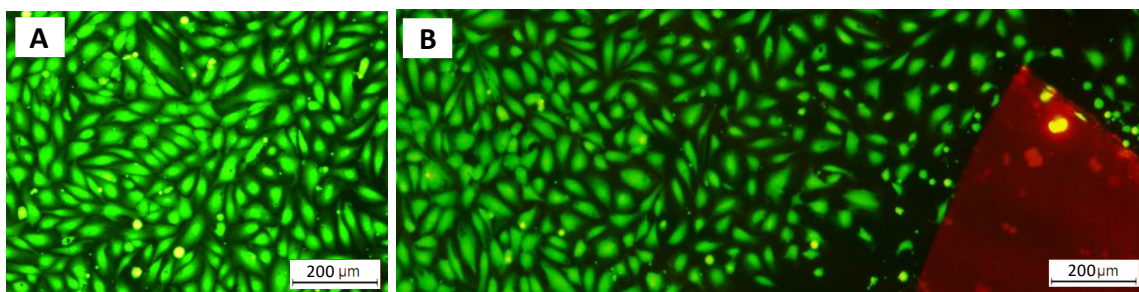


Figure 112. Toxicity study in 24-well plate, after 43 h. Fluorescence ($\lambda_{\text{exc}} = 470 \text{ nm}$; $\lambda_{\text{em}} > 515 \text{ nm}$). Magnification: 20×. A) Control well. B) Well containing the RD3-silica-PDMS 3140.

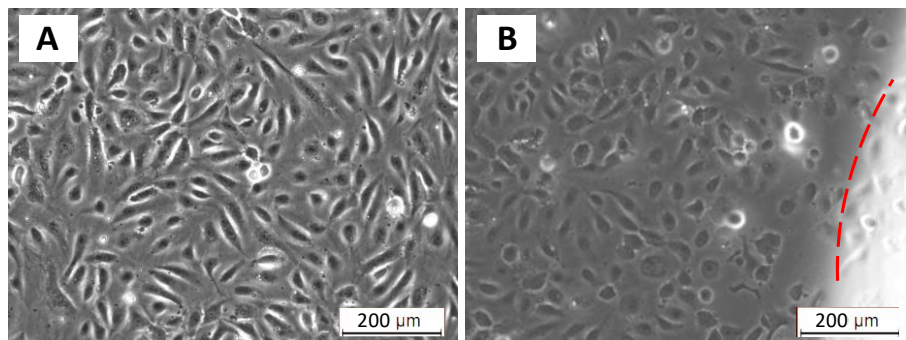


Figure 113. Toxicity study in 24-well plate, after 42 h. Bright field. Magnification: 20×. A) Control well. B) Well containing the Ru(phen)₂(4-Clp)²⁺-PCA (film edge highlighted with a red dashed line).

4.4. References

Abaci	2014	Abaci, H. E.; Shen, Y. I.; Tan, S.; Gerecht, S. Recapitulating Physiological and Pathological Shear Stress and Oxygen to Model Vasculature In Health and Disease. <i>Sci. Rep.</i> 2014 , <i>4</i> , 4951.
Bhatia	2014	Bhatia, S. N.; Ingber, D. E. Microfluidic organs-on-chips. <i>Nat. Biotechnol.</i> 2014 , <i>32</i> , 760–772.
Brennan	2014	Brennan, M. D.; Rexius-Hall, M. L.; Elgass, L. J.; Eddington, D. T. Oxygen Control with Microfluidics. <i>Lab Chip</i> 2014 , <i>14</i> , 4305–4318.
Breslin	2013	Breslin, S., O'Driscoll, L. Three-dimensional cell culture: the missing link in drug discovery. <i>Drug Discov. Today</i> 2013 , <i>18</i> , 240–249.
Bustamante	2018	Bustamante, N.; Ielasi, G.; Bedoya, M.; Orellana, G. Optimization of Fiber-Optic Temperature Sensing with Polymer-Embedded Luminescent Ru(II) Complexes. <i>Polymers</i> 2018 , <i>10</i> , 234.
Carraway	1991	Carraway, E. R.; Demas, J. N.; DeGraff, B. A. Luminescence Quenching Mechanism for Microheterogeneous Systems. <i>Anal. Chem.</i> 1991 , <i>63</i> , 332–336.
Cooper	1958	Cooper, P. D.; Burt, A. M.; Wilson, J. N. Critical Effect of Oxygen Tension on Rate of Growth. <i>Nature</i> 1958 , <i>182</i> , 1508–1509.
Edmondson	2014	Edmondson, R.; Broglie, J. J.; Adcock, A. F.; Yang, L. Three-Dimensional Cell Culture Systems and Their Applications in Drug Discovery and Cell-Based Biosensors. <i>Assay Drug Dev Technol.</i> 2014 , <i>12</i> , 207–218.
Fujita	1999	Fujita, J. Cold Shock Response in Mammalian Cells. <i>J. Mol. Microbiol. Biotechnol.</i> 1999 , <i>1</i> , 243–255.
Garcia-Fresnadillo	1996	Garcia-Fresnadillo, D.; Georgiadou, Y.; Orellana, G.; Braun, A. M.; Oliveros, E. Garcia-Fresnadillo, D.; Georgiadou, Y.; Orellana, G.; Braun, A. M.; Oliveros, E. <i>Helv. Chim. Acta</i> 1996 , <i>79</i> , 1222–1238.
García-Fresnadillo	2001	García-Fresnadillo, D.; Orellana, G. Interaction of Sulfonated Ruthenium(II) Polypyridine Complexes with Surfactants Probed by Luminescence Spectroscopy. <i>Helv. Chim. Acta</i> 2001 , <i>84</i> , 2708–2730.
Gitlin	2013	Gitlin, L.; Hoera, C.; Meier, R. J.; Nagl, S.; Belder, D. Micro Flow Reactor Chips with Integrated Luminescent Chemosensors for Spatially Resolved On-Line Chemical Reaction Monitoring. <i>Lab Chip</i> 2013 , <i>13</i> , 4134–4141.

Chapter 4 - Application of Luminescence-Based Microsensors For Microfluidic Cell Cultures and Organ-On-A-Chip Devices

Grate	2012	Grate, J. W.; Kelly, R. T.; Suter, J.; Anheier, N. C. Silicon-On-Glass Pore Network Micromodels with Oxygen-Sensing Fluorophore Films for Chemical Imaging and Defined Spatial Structure. <i>Lab Chip</i> 2012 , <i>12</i> , 4796–4801.
Halldorsson	2015	Halldorsson, S., Lucumi, E., Gómez-Sjöberg, R., Fleming, R. M. T. Advantages and Challenges of Microcell Culture in Polydimethylsiloxane Devices. <i>Biosens. Bioelectron.</i> 2015 , <i>63</i> , 218–231.
Huh	2010	Huh, D.; Matthews, B. D.; Mammoto, A.; Montoya-Zavala, M.; Hsin, H. Y.; Ingber, D. E. Reconstituting Organ-Level Lung Functions On A Chip. <i>Science</i> 2010 , <i>328</i> , 1662–1668.
Huh	2012	Huh, D.; Torisawa, Y. S.; Hamilton, G. A.; Kim, H. J.; Ingber, D. E. Microengineered Physiological Biomimicry Organs-on-Chips. <i>Lab Chip</i> 2012 , <i>12</i> , 2156–2164.
Jagannathan	2016	Jagannathan, L.; Cuddapah, S.; Costa, M. Oxidative Stress under Ambient and Physiological Oxygen Tension in Tissue Culture. <i>Curr. Pharmacol. Rep.</i> 2016 , <i>2</i> , 64–72.
Kaufmann	1999	Kaufmann, H.; Mazur, X.; Fussenegger, M.; Bailey, J. E. Influence of Low Temperature on Productivity, Proteome and Protein phosphorylation of CHO Cells. <i>Biotechnol. Bioeng.</i> 1999 , <i>63</i> , 573–582.
Krabbe	2015	Krabbe, S.; Achatz, D.E.; Nieradzik, T.; Gerhardy, C.; Schomburg, W.K. Ultrasonic Welding of Chemical Optical Sensors Supporting O ₂ , pH and CO ₂ Imaging in Microfluidic Systems. <i>Proc. Eng.</i> 2015 , <i>120</i> , 598–601.
Kretzmer	1998	Kretzmer, G.; Buch, T.; Konstantinov, K.; Naveh, D. The Temperature Effect in Mammalian Cell Culture an Arrhenius Interpretation [sic]. In: Merten OW., Perrin P., Griffiths B. (eds) <i>New Developments and New Applications in Animal Cell Technology</i> . Springer: Dordrecht, 1998 .
Lakowicz	2006	Lakowicz, J. R. Principles of Fluorescence Spectroscopy, 3rd ed.; Springer Science+Business Media, LLC: New York, NY, 2006 , Ch.2; e-ISBN 978-0-387-46312-4.
Lakowicz	1998	Lakowicz, J. R.; Castellano, F. N.; Dattelbaum, J. D.; Tolosa, L.; Rao, G.; Gryczynski, I. Low-Frequency Modulation Sensors Using Nanosecond Fluorophores. <i>Anal. Chem.</i> 1998 , <i>70</i> , 5115–5121.
Lanza	2000	Lanza, R. P.; Langer, R.; Vacanti, J. P. (eds) <i>Principles of Tissue Engineering</i> . Academic Press: New York, 2000 .
Lasave	2015	Lasave, L. C.; Borisov, S. M.; Ehgartner, J.; Mayr, T. Quick and Simple Integration of Optical Oxygen Sensors Into Glass-Based Microfluidic Devices. <i>RSC Adv.</i> 2015 , <i>5</i> , 70808–70816.

Chapter 4 - Application of Luminescence-Based Microsensors For Microfluidic Cell Cultures and Organ-On-A-Chip Devices

Lin	2009	Lin, Z.; Cherng-Wen, T.; Roy, P.; Trau, D. In-Situ measurement of Cellular Microenvironments in a Microfluidic Device. <i>Lab Chip</i> , 2009 , 9, 257–262.
Lopez-Gejo	2010	Lopez-Gejo, J.; Haigh, D.; Orellana, G. Relationship between the Microscopic and Macroscopic World in Optical Oxygen Sensing: A Luminescence Lifetime Microscopy Study. <i>Langmuir</i> 2010 , 26, 2144–2150.
MacArthur	2005	MacArthur, B. D.; Orefeo, R. O. C. Bridging the Gap. <i>Nature</i> 2005 , 433, 19.
Milián	2015	Milián, E.; Kamen, A. A. Current and Emerging Cell Culture Manufacturing Technologies for Influenza Vaccines. <i>Biomed. Res. Int.</i> 2015 , http://dx.doi.org/10.1155/2015/504831 .
Mousavi Shaegh	2016	Mousavi Shaegh, S. A.; De Ferrari, F.; Zhang, Y. S.; Nabavina, M.; Binth Mohammad, N.; Ryan, J.; Pourmand, A.; Laukaitis, E.; Banan Sadeghian, R.; Nadhman, A.; Shin, S. R.; Nezhad, A. S.; Khademhosseini, A.; Dokmeci, M. R. A Microfluidic Optical Platform for Real-Time Monitoring of pH and Oxygen in Microfluidic Bioreactors and Organ-On-Chip Devices. <i>Biomicrofluidics</i> 2016 , 10, 044111.
Navarro-Villoslada	2001	Navarro-Villoslada, F.; G. Orellana, M. C. Moreno-Bondi, T. Vick, M. Driver, G. Hildebrand, and K. Liefeth. Fiber-Optic Luminescent Sensors with Composite Oxygen-Sensitive Layers and Anti-Biofouling Coatings. <i>Anal. Chem.</i> 2001 , 73, 5150-5156.
Neutelings	2013	Neutelings, T.; Lambert, C. A.; Nusgens, B. V.; Colige, A. C. Effects of Mild Cold Shock (25°C) Followed by Warming Up at 37°C on the Cellular Stress Response. <i>PLoS One</i> 2013 , 8, e69687.
Nock	2013	Nock, V.; Blaikie, R. J.; Maan, M. A.: Optical Oxygen Sensors for Micro- and Nano-fluidic Devices. In <i>Smart Sensors for Industrial Applications</i> . Iniewski, K. (Ed.), CRC Press: Boca Raton. 2013 , ch. 9. eBook ISBN: 9781315216027.
Oomen	2016	Oomen, P. E.; Skolimowski, M. D.; Verpoorte, E. Implementing Oxygen Control in Chip-Based Cell and Tissue Culture Systems. <i>Lab Chip</i> 2016 , 16, 3394–3414.
Ozturk	2005	Ozturk, S.; Hu, W.-S. Cell Culture Technology for Pharmaceutical and Cell-Based Therapies; CRC Press: Boca Raton, FL, USA, 2005.
Perdue	2011	Perdue, M. L.; Arnold, F.; Li, S.; Donabedian, A. Cioce, V.; Warf, T.; Huebner, R. The Future of Cell Culture-Based Influenza Vaccine Production. <i>Expert Rev. Vaccines</i> 2011 , 10, 1183–1194

Chapter 4 - Application of Luminescence-Based Microsensors For Microfluidic Cell Cultures and Organ-On-A-Chip Devices

Pfeiffer	2015	Pfeiffer, S. A.; Nagl, S. Microfluidic Platforms Employing Integrated Fluorescent or Luminescent Chemical Sensors: A Review of Methods, Scope and Applications. <i>Methods Appl. Fluoresc.</i> 2015 , <i>3</i> , 034003.
Pfeiffer	2017	Pfeiffer, S. A.; Nagl, S. On-chip photothermal analyte detection using integrated luminescent temperature sensors. <i>Anal. Chem.</i> 2017 , <i>89</i> , 9400–9406.
Phelan	2017	Phelan, K.; May, K. M. Mammalian Cell Tissue Culture Techniques. <i>Curr. Protoc. Mol. Biol.</i> 2017 , <i>117</i> , A.3F.1–A.3F.23.
Prantil-Baun	2018	Prantil-Baun, R.; Novak, R.; Das, D.; Somayaji, M. R.; Przekwas, A.; Ingber, D. E. Physiologically Based Pharmacokinetic and Pharmacodynamic Analysis Enabled by Microfluidically Linked Organs-on-Chips. <i>Annu. Rev. Pharmacol.</i> 2018 , <i>58</i> , 37–64.
Qiu	2014	Qiu, W.; Wu, C.; Wu, Z. Surface Modification of PDMS in Microfluidic Devices. In <i>Concise Encyclopedia of High Performance Silicones</i> , Tiwari, A.; Soucek, M. D. (Eds.), Ch. 10, Wiley: Hoboken, New Jersey, 2014 .
Semenza	2007	Semenza, G. L. Life with Oxygen. <i>Science</i> 2007 , <i>318</i> , 62–64.
Skolimowski	2010	Skolimowski, M.; Nielsen, M. W.; Emnéus, J.; Molin, S.; Taboryski, R.; Sternberg, C.; Dufva, M.; Geschke, O._Microfluidic Dissolved Oxygen Gradient Generator Biochip as a Useful Tool in Bacterial Biofilm Studies_ <i>Lab Chip</i> 2010 , <i>10</i> , 2162–2169.
Stanfield	2013	Stanfield, C. L. <i>Principles of Human Physiology</i> , 5th ed.; Pearson Education, Inc.: London, UK. Pag. 475. ISBN-13: 978-0-321-81934-5.
Sun	2015	Sun, S.; Ungerböck, B.; Mayr, T. Imaging of Oxygen in Microreactors and Microfluidic Systems. <i>Methods Appl. Fluoresc.</i> 2015 , <i>3</i> , 034002.
Tsai	2003	Tsai, A. G.; Johnson, P. C.; Intaglietta, M. Oxygen Gradients in the Microcirculation. <i>Physiol Rev</i> 2003 , <i>83</i> , 933–963
Ungerbock	2013	Ungerbock, B.; Charwat V, Ertl P, Mayr T. Microfluidic Oxygen Imaging Using Integrated Optical Sensor Layers and a Color Camera. <i>Lab Chip</i> , 2013 , <i>13</i> , 1593–1601.
Wang	2013	Wang, L.; Liu, W.; Wang, Y.; Wang, J. C.; Tu, Q.; Liu, R.; Wang, J. Construction of Oxygen and Chemical Concentration Gradients in a Single Microfluidic Device for Studying Tumor Cell-Drug Interactions in a Dynamic Hypoxia Microenvironment. <i>Lab Chip</i> 2013 , <i>13</i> , 695–705.
Watanabe	1967	Watanabe, I.; Okada, S. Effects of Temperature on Growth Rate of Cultured Mammalian Cells (L5178Y). <i>J. Cell. Biol.</i> 1967 , <i>32</i> , 309–323.

Chapter 4 - Application of Luminescence-Based Microsensors For Microfluidic Cell Cultures and Organ-On-A-Chip Devices

Xue	2015	Xue, Y.; Xiao, H.; Zhang, Y. Antimicrobial Polymeric Materials with Quaternary Ammonium and Phosphonium Salt. <i>Int. J. Mol. Sci.</i> 2015 , <i>16</i> , 3626–3655.
-----	------	---

Chapter 4 - Application of Luminescence-Based Microsensors For Microfluidic Cell Cultures and Organ-On-A-Chip Devices

5. HIGHLIGHTS, CONCLUSIONS, AND OUTLOOK

Chapter 5 - Highlights, conclusions, and outlook

This thesis focused on most of the different facets of luminescence-based chemical sensor development:

- 1) design of luminescent indicator dyes tuned towards the sought application (polarity-based sensors – chapter 3),
- 2) synthesis of the luminescent indicator dyes (chapter 3),
- 3) manufacturing and characterization of the sensitive plastic element (consisting of dye, polymer, and additives) for two different applications (industrial ethanol sensors and sensors for organ-on-a-chip devices – chapter 3 and 4, respectively);
- 4) sensor miniaturization (through optimization of organic-inorganic hybrids for developing intrinsic chemically-sensitive micro LEDs – chapter 2);

The main results and conclusions of the research work have been summarized in the next paragraphs.

5.1. GaN-silane-dye hybrid materials for luminescent chemical sensing

5.1.1. Summary of obtained results

- For manufacturing intrinsic O₂-responsive GaN-based LEDs, we modified GaN substrates to tether a luminescent Ru(II) indicator dye. To achieve covalent attachment of the dye, the GaN surfaces were pre-activated with oxygen plasma and a ω -aminoalkyl-trialkoxysilane layer was grown on top.
- While p-doped GaN does not hinder the luminescent properties of the GaN-silane-Ru(II) dye hybrids [Lopez-Gejo 2011], n-GaN hybrids have to be properly engineered to achieve adequate photochemically-sensitive materials because the emission of the surface-bound Ru(II) dye is quenched by the semiconductor. Such quenching decreases exponentially with the silane layer thickness, thus confirming a previously suggested photoinduced electron transfer (PET) from the excited dye to the semiconductor.
- Growth of at least a 15 nm-thick silane layer onto n-doped GaN prevents the PET that diminishes its efficiency as O₂ sensor. After eliminating the disturbing PET, the modified n-doped GaN substrates allow manufacturing the O₂-responsive microLEDs, the key step for manufacturing miniature printed circuit board PCB-integrateable, optically-based, gas-sensing elements.

5.1.2. Conclusions

A versatile procedure for **attaching luminescent indicator dyes to GaN surfaces at a controlled distance** has been developed. Following this procedure, numerous dyes and semiconductors may be used for manufacturing chemically-sensitive elements.

Following the straightforward methodology described in this thesis, it is possible to manufacture oxygen-sensitive hybrid materials from basic low-cost LEDs (which have a p-GaN layer on top) and also from high efficiency and high intensity devices (power saving devices and blue LEDs for illumination having a n-type outermost surface).

Moreover, a larger selection of LED-dye pairs may be now amenable to fabricate hybrid materials based on luminescent indicators covalently attached to electroluminescent semiconductors, regardless the position of the conduction and valence bands of the latter, or the excited state redox potentials of the former.

Understanding the different factors that control formation and morphology of the intermediate silane layer is the key to foresee which surface functionalization can be used to avoid electron transfer from/to the indicator dye to/from the semiconductor. Further work is needed to boost the sensitivity of the hybrid materials for chemical sensing of other gases of interest for personal safety and environmental monitoring.

5.2. Optodes for EtOH monitoring based on polarity-sensitive Ru(II) indicator dyes

5.2.1. Summary of obtained results

- The developed polarity-sensitive dyes have been used for manufacturing an ethanol vapors sensor. After synthesis and characterization of the Ru(II)-based indicator dyes (adapting procedures from the literature; two of the luminescent indicators were never described before), we demonstrated that the luminescence response of these dyes does not always follow the widely used "Lippert-Mataga" model.
- The selection of the best indicator dye and polymer support allowed preparation of polarity-based ethanol sensors showing optimal features for practical applications in ethanol level monitoring in the gas phase for production/storage facilities (**Table 25**), which are robust and very easy to manufacture.

Table 25. Summary of the developed luminescent EtOH sensor features

LOD/ppm	400
LOQ/ppm ^a	1400
Response time/s	23
Interference from the most common VOCs ^b	None
Interference from water	Little. Huge water concentration variations could interfere with the sensor response. The interference can be corrected, if needed, using a humidity sensor.

^a Target LOQ is 3300 ppm of ethanol in air at RT, considering that ethanol vapor concentration *immediately dangerous to life and health* (IDLH) is 10% of the LEL, which is equivalent to 33000 ppm [NIOSH 1995];

^b VOCs tested: EtOH, MeOH, AcOEt, MeCN, and acetone.

- The results show that the developed sensor can be also used for monitoring alcohol content in beers, wine, and spirits –beverages with ethyl alcohol concentration usually between 4 and 40% v/v– with an accuracy of $\pm 0.26\%$. The ethanol concentration in solution is obtained measuring the ethanol vapor concentration in the bottles head space. This sensor is accurate enough for alcohol determination in Europe [Regulation (EU) No 1169/2011]. Some countries, however, require a higher accuracy in alcohol determination (for example the US, where the TTB standard requires measurement of % alcohol with 0.02% accuracy).

5.2.2. Conclusions

Selection of the best **luminescent indicator Ru(II) polypyridyl dye** into the best **perm-selective membrane** has led to robust, sensitive **ethanol vapor sensors** for industrial applications.

Heteroleptic Ru(II) polypyridyl complexes with electron-withdrawing substituents can be used as probes of the microenvironmental polarity, although they are less sensitive than elongated organic molecules that boast a lowest-lying intramolecular charge transfer (ICT) excited state with distant charge separation. Because of their phosphorescent emission, Ru(II) dyes do not behave as expected from the widely used Lippert-Mataga model. However, it is possible to predict their behavior with changes in the solvent polarity by means of theoretical calculations. Such predictions will lead to better transition metal-based phosphorescent complexes (i) to probe efficiently the polarity of sample gas or liquid mixtures after immobilization of the indicator molecule in an adequate analyte-permeable polymer film, (ii) to report on the polarity of biopolymers or cell structures to which they bind, and (iii) to sense the micropolarity of materials using both the emission intensity and lifetime of their lowest-lying excited state.

5.3. O₂ and T luminescent microsensors for microfluidic devices

This work was only a preliminary study carried out during my secondment in RUG, Groningen (in the Pharmaceutical Analysis group headed by prof. Dr. E.M.J. Verpoorte) and in Micronit Microtechnologies, Enschede. Nevertheless, important conclusions can be drawn.

5.3.1. Summary of obtained results

5.3.1.1. Development of O₂ sensors for microfluidic chips that are easy to make and bio-compatible

- A “sensor cocktail” (Cocktail 1) that is non-toxic for endothelial cells (HUVECs) has been developed, remarkably simple to prepare and straightforward to deposit into the microchannels of PDMS-based microfluidic chips. The luminescent coating obtained after depositing Cocktail 1 and curing it at room temperature is biocompatible – actually, HUVECs attach onto this coating much more readily than onto the PDMS chips themselves. Thanks to the luminescent response of the coating, a compact, phase-sensitive, portable luminometer was used to monitor molecular dioxygen inside microfluidic cell cultures.
- Conversely, the second “sensor cocktail” developed (Cocktail 2) works both for O₂ sensing and as anti-biofouling material (at least for HUVECs) due to the biocide effect of its quaternary phosphonium salt.

5.3.1.2. O₂ and T luminescent microsensors to develop a lung-in-a-chip

- Lung-in-a-chip devices are built to mimic the real blood-air barrier in the lungs. The sensors reported in this chapter can be used to assess how close the artificial model is to the biological structure in term of O₂ distribution. Moreover, in this thesis chapter a way to measure O₂ and T simultaneously inside chips, in a contactless way, is shown by exploiting a dedicated compact phase-sensitive luminometer.

5.3.2. Conclusions

Microfluidic channels endowed with the presented luminescent coatings will allow distributed, real-time, *in situ*, continuous oxygen and temperature monitoring into organ-on-a-chip devices.

Modifying the sensor cocktail recipe using indicator dyes tuned towards different analytes or physical parameters would allow obtaining coating layers for monitoring other variables of interest in cell cultures.

5.4. Outlook

We are at the verge of the 4th industrial revolution, that will be driven by the so-called Internet-of-Things (IoT) – connecting physical, digital, and biological world. It is expected that 125 billion devices will be connected by 2030 [IHS Markit 2017]. And sensors will be at the foundation of all IoT design, allowing devices to collect data and interpret the environment.

In this thesis, several aspects of sensor development and applications have been researched; the obtained results pave the way towards further exciting advancements.

- 1) **Miniaturization.** Ru(II)-silane-dye hybrids have been optimized, in order to obtain the highest possible miniaturization of light source and sensitive element. The next step would be to finalize the sensor chip, adding the detector of light. This would lead to a new challenge: to remove the contribution of the excitation light. The solution could be to select a light source that emits light with wavelength for which the detector has very low sensitivity – for example, pairing a AlGaN deep UV LED as light source, the luminescence of which is centred at 265 nm, with a silicon-based avalanche photodiode as detector, which is only sensitive to wavelengths between ~400 and 1000 nm. Both components are commercially available (see for example [Mounted LEDs \(thorlabs.com\)](#) and [Si Avalanche Photodetectors \(thorlabs.com\)](#)). Last step would be integration of the sensor chips with the smartphone-based platform we developed in 2014 (**Figure 18**, unpublished).
- 2) **Smartphone-based miniaturized ethanol sensor.** In the thesis (chapter 3), the entire process of sensor development (in this particular case, a sensor for assessing concentration of ethanol vapors in air) from design, to characterization, to the final application is shown. A straightforward advance would be to utilize the developed polarity-sensitive dyes as sensitive element in the same system described in point 1). There are two main challenges that I can foresee. First, the sensitivity to polarity of these dyes is due to their chemical structure. Modifying the structure (i.e., substituting one or more polypyridyl ligands with the ligands containing the required anchoring moieties), the dye may lose the sensitivity to the parameter of interest. Anyway, we could use the same theoretical calculation shown in chapter 3 to screen the best candidates, among all the available ligands, for developing a novel polarity-probing dye considering the new chemical structure. Second, in the O₂-sensitive chip development (chapter 2) we did not use an encapsulating polymer, while for the ethanol sensor we showed that the polymer (PVC) was actually fundamental to act as permselective barrier reducing the interference of water. The solution could be as simple as encapsulating the entire chip with the permselective plastic. Ideally the plastic of choice should not absorb light in the useful wavelength ranges (LED chip electroluminescence and indicator dye

Chapter 5 - Highlights, conclusions, and outlook

photoluminescence). A possible additional (beneficial) effect could be increasing the refractive index matching, which would increase the light extraction from the LED chip.

- 3) **Multi sensor platform.** In a work published already in 2010, Rae et al. [Rae 2010] showed a structure of 64 GaN-based LEDs bonded to an 8x8 pixels CMOS image sensor. Applying to this design the LED chip functionalization shown in chapter 2 of the present thesis would allow obtaining 64 sensors in a few cubic mm. Using several indicator dyes sensitive to different parameters would allow manufacturing a platform for 64 different analytes/parameters.

5.5. References

IHS Markit	2017	Digitalisation and the industrial IoT revolution – why should you care? (https://ihsmarkit.com/research-analysis/digitalisation.html)
Lopez-Gejo	2011	Lopez-Gejo, J.; Navarro-Tobar, A.; Arranz, A.; Palacio, C.; Muñoz, E.; Orellana, G. Direct Grafting of Long-Lived Luminescent Indicator Dyes to GaN Light-Emitting Diodes for Chemical Microsensor Development. <i>Appl. Mater. Interfaces</i> 2011 , <i>3</i> , 3846–3854.
NIOSH	1995	Documentation for Immediately Dangerous to Life or Health Concentrations (IDLHs). <i>National Institute of Occupational Safety and Health (NIOSH)</i> 1995 . Retrieved from http://www.cdc.gov/niosh/idlh/64175.html
Prantil-Baun	2018	Prantil-Baun, R.; Novak, R.; Das, D.; Somayaji, M. R.; Przekwas, A.; Ingber, D. E. Physiologically Based Pharmacokinetic and Pharmacodynamic Analysis Enabled by Microfluidically Linked Organs-on-Chips. <i>Annu. Rev. Pharmacol.</i> 2018 , <i>58</i> , 37–64.
Rae	2010	Rae, B. R.; Yang, J.; McKendry, J.; Gong, Z.; Renshaw, D.; Girkin, J. M.; Gu, E.; Dawson, M. D.; Henderson, R. K. <i>IEEE Trans Biomed Circuits Syst.</i> 2010 , <i>4</i> , 437–444.
Regulation (EU) No 1169/2011	2011	REGULATION (EU) No 1169/2011 OF THE EUROPEAN PARLIAMENT AND OF THE COUNCIL of 25 October 2011, Annex XII. Retrieved from https://eur-lex.europa.eu/legal-content/EN/TXT/?uri=celex:02011R1169-20140219 .
Tsai	2003	Tsai, A. G.; Johnson, P. C.; Intaglietta, M. Oxygen Gradients in the Microcirculation. <i>Physiol Rev</i> 2003 , <i>83</i> , 933–963

Chapter 5 - Highlights, conclusions, and outlook

“Quotation is a serviceable substitute for wit.”

— Oscar Wilde, 1890